Digital Twins for Autonomous Thermal Food Processing

Zur Erlangung des akademischen Grades Doktor-Ingenieur (Dr.-Ing.)
Genehmigte Dissertation von Maximilian Kannapinn geb. Scheid aus Siegen
Tag der Einreichung: 13.04.2023, Tag der Prüfung: 27.06.2023

1. Gutachten: Prof. Dr. rer. nat. Michael Schäfer
2. Gutachten: Prof. Dr. rer. nat. Oliver Weeger
Darmstadt, Technische Universität Darmstadt, 2023

TECHNISCHE
UNIVERSITÄT
DARMSTADT

Fachbereich Maschinenbau
Fachgebiet Numerische Berechnungsverfahren im Maschinenbau

Digital Twins for Autonomous Thermal Food Processing

Accepted doctoral thesis by Maximilian Kannapinn geb. Scheid

Date of submission: 13.04.2023
Date of thesis defense: 27.06.2023

Darmstadt, Technische Universität Darmstadt, 2023

Bitte zitieren Sie dieses Dokument als:
URN: urn:nbn:de:tuda-tuprints-243866
URL: http://tuprints.ulb.tu-darmstadt.de/24386
Jahr der Veröffentlichung auf TUprints: 2023

Preface

I am delighted to present this doctoral thesis, which represents the culmination of my research over the past four years. This work would not have been possible without the support and encouragement of many people, and I would like to express my sincere gratitude to each of them. First and foremost, I want to thank my family, especially my wife, for their unwavering support and understanding throughout this journey.

I would like to thank Prof. Dr. rer. nat. Michael Schäfer, who supervised this thesis and gave me the freedom to pursue the presented research idea. I am grateful to Prof. Dr. rer. nat. Oliver Weeger for supervising this thesis and also my master students. His feedback was instrumental in improving the quality of my work. I would also like to express my gratitude to Dr. Florian Löw, who mentored me during our joint research projects from 2017 to 2020. His insights and practical experience have been valuable in shaping my research and understanding the needs of the industry. Besides, I thank Prof. Ashim Datta [55], Prof. Dr.-Ing. Oliver Nelles [174], Dr. Chandan Kumar [149], Christoph Petre and Dr. Valery Morgenthaler [8] and Emilien Dupont [74] for pleasant correspondence.

I thank my colleagues at FNB and CPS for a great time together and for their support. Special thanks go to Felix for our joint research project. I want to express my appreciation to Monika, Michael, Christian, Markus, Carina, and others who have helped me on the administrative side. I am also grateful to everyone who proofread parts of my thesis, particularly Dominik, Juan, Konstantin, Zach, Mauricio, Helge and Felix. Last but not least, I am indebted to Dr. Lauren Scholz for superb English language proofreading.

I hope this thesis will contribute to not only food science and technology and inspire future research. I genuinely believe the findings presented here can help the industry to design autonomous processes with physics-based, data-driven digital twins.

The research presented here has been published in parts in:

I. M. Kannapinn. *The digital twin for thermal fluid-structure interaction in the context of cooking modeling – concept paper.* Tech. rep. Technical University of Darmstadt, Graduate School Computational Engineering, 2018.
II. M. Kannapinn and M. Schäfer. *"Endeavouring intelligent process self-control by employing digital twin methodology: Proof-of-concept study for cooking applications".* In: CADFEM ANSYS Simulation Conference, Kassel, 2019.
III. M. Kannapinn and M. Schäfer. *"Autonomous cooking with digital twin methodology".* In: 14th World Congress on Computational Mechanics (WCCM) and ECCOMAS Congress, Paris, 2020. Ed. by F. Chinesta et al., 2021.
IV. M. Kannapinn, M. K. Pham, and M. Schäfer. *"Physics-based digital twins for autonomous thermal food processing: efficient, non-intrusive reduced-order modeling".* In: Innovative Food Science & Emerging Technologies 81 (2022), p. 103143.

The topic was accepted for oral presentation at:

I. CADFEM ANSYS Simulation Conference, Kassel, 2019. Won the best paper award.
II. 14th World Congress on Computational Mechanics (WCCM) and ECCOMAS Congress, Paris (virtual), 2020.
III. 36th EFFoST International Conference, Lausanne, 2021.
IV. 21st IUFoST World Congress of Food Science & Technology, Singapore, 2022.

Some code was developed in supervised master theses at the Technical University of Darmstadt:

I. M. K. Pham. "Untersuchung transienter reduzierter Modelle zur Realisierung digitaler Zwillinge thermodynamischer Probleme". MA thesis. Technical University of Darmstadt, 2022.
II. D. Dorer. "Echtzeit modellprädikative Regelung zur Realisierung autonomer Prozesse". MA thesis. Technical University of Darmstadt, 2022.

Abstract

Developing sustainable and efficient food processing technologies is paramount to reducing greenhouse gas emissions and food waste. Autonomous food processing technologies, driven by artificial intelligence, offer a promising solution for achieving these goals while maintaining high-quality standards. In this context, digital twins have emerged as a powerful tool to model and optimize complex systems, providing accurate predictions of the system behavior to allow optimization of the process variables live during operation. This work proposes a software framework that combines multi-physical, conjugate simulations and data-driven reduced-order modeling to develop physics-based, data-driven digital twins for autonomous thermal food processing. The framework is independent of the modeling approach and simulation software and aims at the immediate application in the industry.

Physics-based, data-driven digital twins are highly accurate and fast-solving virtual replications of a physical product or process, giving information on the current processing variables that cannot easily or feasibly be measured during operation. Generally, the concept of digital twins stands for a paradigm shift in computational engineering. In past decades, knowledge gained from simulations remained in the hands of highly skilled product and process development experts. Digital twins attempt to provide access to this knowledge even during operation to enable potential process autonomy. This work demonstrates how multi-physical simulation models of realistic size and dimension form the basis for physics-based, data-driven digital twins. To model thermal food processing inside a convection oven, non-isothermal flow and thermal radiation are coupled with mechanistic food processing models in one setup. This approach captures the couplings between the food process variables and the heat transfer mechanisms much better than heat- and mass-transfer-coefficient-based modeling approaches that still dominate within food science.

A challenge for modern-day computational engineering is that computing power does not keep pace with the progressively increasing complexity and computational cost of multi-physical simulation models. So far, real-time simulations of such models are not feasible, especially when the models should be executed on low-end processors. In this work, neural ODEs, a novel data-driven reduced-order modeling technique, are applied to generate an accurate and fast-solving surrogate of simulation models, which also exhibit low computational cost. The resulting reduced-order models are stored in an encrypted container format to protect the developer's intellectual property when deployed in the final appliance. The container files are executed at the device level without cluster, edge or cloud computing. For the presented generation of a digital twin for a convection oven, fewer errors are caused by the reduced-order models than by the underlying food processing models. As coupled, multi-physical models of realistic dimensions still require considerable solution times on modern cluster PCs, generating many data sets for data-driven reduced-order modeling is not economically feasible. This work proposes an efficient design of experiments that enables data-driven reduced-order modeling with only one-to-two training data sets. Finally, the performance of fast-solving and highly accurate digital twins is demonstrated within a model predictive control algorithm. The latter autonomously handles two scenarios during thermal food processing in a convection oven.

Zusammenfassung

Die Entwicklung nachhaltiger und effizienter Technologien für die Lebensmittelverarbeitung ist von entscheidender Bedeutung für die Reduzierung von Treibhausgasemissionen und Abfällen. Autonome Technologien für die Lebensmittelverarbeitung, die durch künstliche Intelligenz vorangetrieben werden, bieten eine vielversprechende Lösung, um diese Ziele zu erreichen und gleichzeitig hohe Qualitätsstandards zu wahren. In diesem Zusammenhang haben sich digitale Zwillinge als leistungsstarkes Werkzeug zur Modellierung und Optimierung komplexer Systeme erwiesen. Digitale Zwillinge können das zukünftige Systemverhalten genau vorhersagen, um so die Optimierung der Prozessvariablen während des Betriebs zu ermöglichen. In dieser Arbeit wird ein Software-Framework vorgeschlagen, das multiphysikalische, konjugierte Simulationen und datengesteuerte Modellierung reduzierter Ordnung kombiniert, um physikbasierte, datengesteuerte digitale Zwillinge für die autonome thermische Lebensmittelverarbeitung zu entwickeln. Das Framework ist unabhängig vom Modellierungsansatz und der Simulationssoftware und zielt auf unmittelbare Anwendbarkeit in der Industrie ab.

Physikalisch basierte, datengesteuerte digitale Zwillinge sind hochpräzise und schnell lösende virtuelle Replikationen eines physischen Produkts oder Prozesses, die Informationen über die aktuellen Prozessvariablen liefern, welche während des Betriebs nicht einfach oder praktikabel gemessen werden können. Generell steht das Konzept der digitalen Zwillinge für einen Paradigmenwechsel in der Simulationstechnik. In den vergangenen Jahrzehnten blieben die aus Simulationen gewonnenen Erkenntnisse in den Händen von hoch qualifizierten Experten im Bereich der Produkt- und Prozessentwicklung. Digitale Zwillinge versuchen, dieses Wissen auch während des laufenden Betriebs zugänglich zu machen, um Prozessautonomie potenziell zu ermöglichen. Diese Arbeit zeigt, wie multiphysikalische Simulationsmodelle von realistischer Größe und Dimension die Grundlage für physikbasierte, digitale Zwillinge bilden. Um die thermische Verarbeitung von Lebensmitteln in einem Konvektionsofen zu modellieren, werden erzwungene Konvektion und Wärmestrahlung mit mechanistischen Modellen der Lebensmittelverarbeitung in einem Setup gekoppelt. Dieser Ansatz erfasst die Kopplungen zwischen den Prozessvariablen der Lebensmittel und den Mechanismen der Wärmeübertragung viel besser als die auf Wärme- und Stoffübergangskoeffizienten basierenden Modellierungsansätze, die immer noch die Lebensmittelwissenschaft dominieren.

Eine Herausforderung für moderne Computertechnik besteht darin, dass die Rechenleistung nicht mit der zunehmenden Komplexität und dem Rechenaufwand von multiphysikalischen Simulationsmodellen Schritt hält. Bislang sind Echtzeitsimulationen solcher Modelle nicht möglich, insbesondere wenn die Modelle auf Low-End-Prozessoren ausgeführt werden sollen. In dieser Arbeit wird eine neuartige datengetriebene Modellierungstechnik reduzierter Ordnung vom Typ der *neuronalen ODE* angewandt, um ein genaues und schnelles Ersatzmodell von Simulationsmodellen zu generieren, das zudem einen geringen Rechenaufwand aufweist. Die resultierenden Modelle reduzierter Ordnung werden in einem verschlüsselten Containerformat gespeichert, um das geistige Eigentum des Entwicklers zu schützen, wenn sie auf den Endgeräten ausgeliefert werden. Diese können auf der Geräteebene ohne Cluster-, Edge- oder Cloud-Computing ausgeführt werden. Bei der vorgestellten Entwicklung eines digitalen Zwillings für einen Umluftofen sind die zusätzlichen Fehler, die durch die Modelle reduzierter Ordnung verursacht werden, geringer als die Fehler der zugrunde liegenden Modelle für die Lebensmittelverarbeitung. Da gekoppelte, multiphysikalische Modelle realistischer Dimensionen immer noch beträchtliche Berechnungszeiten auf modernen Cluster-PCs erfordern, ist die Erzeugung vieler Datensätze für die datengesteuerte Modellierung reduzierter Ordnung wirtschaftlich nicht machbar. In dieser Arbeit wird ein effizientes Design von Experimenten vorgeschlagen, das eine datengetriebene Modellierung reduzierter Ordnung mit nur ein bis zwei Trainingsdatensätzen ermöglicht. Abschließend wird die Leistungsfähigkeit schnell lösender und hochpräziser digitaler Zwillinge in Verbindung mit einem modellprädiktiven Kontrollalgorithmus demonstriert. Letzterer bewältigt autonom zwei Szenarien während der thermischen Lebensmittelverarbeitung in einem Umluftofen.

Contents

Abbreviations

Short form	**Long form**
1D	One-dimensional
2D	Two-dimensional
3D	Three-dimensional
APRBS	Amplitude-modulated pseudo-random binary sequence
ARMAX	Auto-regressive moving average with exogenous inputs
BDF	Backward differentiation formula
CFD	Computational fluid dynamics
CPU	Central processing unit
CVP	Control vector parameterization
FEM	Finite element method
FMU	Functional mock-up unit
GCI	Grid convergence index
LTI	Linear time-invariant
MPC	Model predictive control
NARX	Nonlinear auto-regressive with exogenous inputs
ODE	Ordinary differential equation
PDE	Partial differential equation
POD	Proper orthogonal decomposition
RANS	Reynolds-averaged Navier–Stokes
RAM	Random-access memory
REV	Representative elementary volume
RNN	Recurrent neural network
ROM	Reduced-order model
SVD	Singular value decomposition

1. Introduction

In the decades to come, one of the greatest challenges for humankind is the introduction of sustainable and climate-neutral products and processes. Our food system, for example, accounts for nearly 21–37% of greenhouse gas emissions, whereas 8–10% can be attributed to food wastage [129]. To address these emerging issues, international institutions such as the European Union have already launched transformative initiatives to promote sustainable and resilient economies. Policy frameworks, such as the *Green Deal* and the *Farm to Fork Strategy*, aim to make the food economy more sustainable, inclusive, and climate-neutral by 2050 [80]. Among the most promising technology trends that can provide such paradigm shifts are autonomous processes that utilize artificial intelligence [212]. Autonomous processes potentially enhance process quality, safety and energy efficiency.

For the public eye, visible progress towards autonomous procedures is made, for example, within the transportation sector. Autonomous vehicles can significantly reduce emissions and traffic congestion by optimizing driving behavior and improving road safety by reducing human error [163, 210]. Additionally, less stressful driving is a welcomed enhancement in the quality of life. Similar improvements in energy consumption, waste reduction and quality of life can be conjectured concerning autonomous food processing. However, a less pronounced pace of transformation is observable in this respect. Already in 2008, a joint brainstorming session of academia and industry concluded: *"As a general comment, the food industry is seen to be one with a great deal of inertia as compared to other industries"* [58].

Preparing food with heat is presumably one of the oldest activities of humankind. By now, we have replaced the fire with more refined forms of heat supply. However, we still lack innovative methods in processing our foods — we still follow the *cook and look* approach without the help of potentially intelligent cooking appliances. Datta, a renowned computational food scientist, concluded: *"[computer-aided engineering] and model-based understanding of food processes can enable the building of highly intelligent food processing machines"* [55]. The quality of processed foods might take a *"quantum leap through development of intelligent ovens"* [57].

1.1. Motivation

Food scientists worldwide agree that intelligent thermal food processing equipment can optimize process control, reducing food waste and improving quality and energy savings. A recent pan-European review [211] within food science concluded in 2016: *"There are optimization needs* *for a good understanding of efficient process monitoring and control methods. These methods are often lacking [...]. Such methods offer a chance of reducing the overprocessing given to foods while maintaining required product safety. Better understanding of how processes work and use of knowledge for improved process control will minimize waste through energy recovery and better use of by-products."* Similarly, Rakesh et al. [199] commented on the potential of combination heating appliances: *"[I]n the cooking process, the quality of the final product such as texture (e.g., sogginess) or flavor (e.g., browning) is a multifaceted attribute that depends on the temperature and moisture distribution and their time-histories. Through improved understanding of the combination heating process, overheating, underheating, overdrying and sogginess of food can be minimized while enhancing its quality. Reliable prediction of food quality factors will in turn enable increased automation and efficiency in food product and process development."*

Summarizing the statements above, intelligent thermal food processing appliances can assist in preparing large quantities of safe and high-quality meals just in time. Potential use cases are community catering, such as in hospitals, schools, universities, diners, and canteens, or for crisis response. The cooking operations in these sectors are mainly carried out by less-trained staff. There have been recent staffing shortages in the food service industry caused by the COVID-19-related shutdowns of public life. Even before the coronavirus pandemic, Germany's top six least popular jobs were chefs and sous-chefs [180]. Hence, adequate supervision and decision support are required in kitchens to ensure food safety. Langsrud [151] disclosed deficits in judging the doneness of food, as approximately 30% of foodborne illnesses can be related to eating undercooked poultry. Rabeler et al. [198] have demonstrated how the absence of pink color, a widespread indicator of doneness, is reached at a temperature of 59 °C. Conversely, safe consumption of chicken meat can only be guaranteed for core temperatures of at least 74 °C [247].

Besides in community catering, transformation can significantly impact our food system when applied at scale, e.g., in industrial processing. Our food system is critical in ensuring food security, nutrition, and livelihoods for billions of people. However, it is also a significant contributor to climate change. Recent studies by Clark [44] indicate a 67% probability of endangering the 2 °C greenhouse gas reduction target if no transformation is undertaken within the food system by 2050. Estimates for the United States imply that proper technological innovations in food production, processing, packaging, transportation, and consumption can save up to 50% of energy in food chains [211]. Data for the United Kingdom in 2011 [211], for example, reveals the major impact of the food system: 160 Mt of the total 470 Mt [206] of CO_2 is relatable to the food chain, from which 13 Mt can be attributed to food processing. The food service sector emits approximately 5.3 Mt of CO_2. More than 10% (42 TWh) of the total industrial energy use is related to the food and drink industry, from which 68% is used for process and space heating. 15 Mt of food is wasted annually, which corresponds to an avoidable amount of 30 Mt of CO_2 emissions.

Even at home, intelligent food processing can combine reduced wastage, energy savings and proper pathogen inactivation with increased comfort. In the United Kingdom [211], 8.4 Mt CO_2 is emitted by domestic cooking. In terms of scaling potential, the energy savings are manifold: In

2018, 94% of households in Germany owned an electric stove [113]. Approximately 15% energy can be saved through timely removal and switching off the appliance and 10–20% by dispensing with preheating and using the residual heat for cooking. Not opening the door during baking or roasting can save up to 25% energy [111].

Last but not least, autonomous thermal food processing can be considered a step towards a smarter, connected home that enriches living quality. Of course, the preparation of meals brings people together as a ritual, hobby, or to perform the art of haute-cuisine. However, living in a fast-paced world, we sometimes do not have the privilege of spending one-to-two hours in the kitchen after a long workday. Then, it might be welcome to ask our future kitchen to prepare our food to be safe, maybe crusty, but tender inside and have ready-to-eat temperatures at a specific time in the evening.

Many renowned food science and technology researchers demand further interdisciplinary research efforts to advance food processing. In 2016, Datta [55] summarized: *"Coupling the predictive power of models with a mathematical optimization technique and making it part of powerful decision support systems would substantially enhance the usefulness of models. However, not nearly as much work has been done in the area of optimization as in modeling."* In 2020, Verboven et al. [253] found holistic digital twin frameworks capable of advancing food science: *"So, as with for the modeling approaches themselves, more holistic frameworks will be required for optimization, allowing model reduction and multi-criteria decision making."*

Acknowledging the need to transform our food system, this work aims at contributing an interdisciplinary, technological building block to advance thermal food processing. It proposes a computational framework to enable the autonomy of thermal food processing with digital twin methodology. Process autonomy can be attained by making the insights of coupled, multi-physical simulations accessible to the thermal processing appliance. Considering that the transformation of our processes should be realized promptly, the digital twin framework is designed to be readily applicable within the industry.

1.2. Physics-based, data-driven digital twin framework

This section presents the proposed framework to generate digital twins for autonomous thermal food processing. It defines key terms, identifies requirements and formulates research hypotheses. A review of the state of the art can be found in Sec. 1.3.

First, it is instructive to define digital twins precisely as they are essential to this work. Michael Grieves developed the notion of digital twins in 2003 as the *mirrored spaces model* for his university lectures [95]. Years later, Vickers inspired the pseudonym digital twin [95]. Many efforts have been made since then to define and standardize the digital twin idea [2, 132, 232], and it has been designated as an active research area by articles in renowned journals [177, 238]. Common features found in the literature that characterize a digital twin are summarized in Tab. 1.1. A digital twin is a virtual set of information (labeled F1 in Tab. 1.1) replicating its physical

Table 1.1. Common features of the digital twin concept in literature [137].

Common Feature	Description	Sources
F1: Digital mirror	Consists of a simulation model / a virtual domain	[2, 95, 201]
F2: Speed-up	Must reflect the physical process in real-time	[90, 159, 201]
F3: High-fidelity	Must reflect the physical process at utmost accuracy	[90, 95, 201]
F4: Symbiosis	Synergies of physics-based and data-based modeling	[177, 201, 253]
F5: Bi-directionality	Mutual data exchange of digital and physical twin	[2, 90, 159, 177]
F6: Persistence	Evolves during the product life-cycle and reflects changes	[2, 95, 201]
F7: Robustness	Reliable / accounts for uncertainty / validated	[177, 201]
F8: Explorative	Allows for monitoring, automation or autonomy	[2, 95, 177, 212]

counterpart at the utmost fidelity (F3). Digital and physical twin benefit from bi-directional data exchange (F4, F5), in real time (F2) and over the whole life-cycle of the process or product (F6). To date, experts in the design phase have predominantly employed simulation and data science technologies in *what-if* simulations to optimize products or processes. Digital twins symbolize the endeavor to provide those insights also to the process in operation (F6), such that the process control algorithms might make better-informed decisions (F8) [177, 201]. Thus, digital twins might act as catalysts for developing autonomous processes [212], which can be considered a novel thrust in digital twin research and technology. So far, around 85% of digital twin studies concentrated on product life-cycle management, whereas 11% focused on factory or manufacturing planning [159]. Niederer et al. [177] identify that novel mathematical, numerical, and computational methodologies must be created to reliably implement digital twins at scale (F7).

1.2.1. Requirements and hypotheses to attain thermal food processing autonomy

Several requirements must be fulfilled to attain thermal food processing autonomy with digital twins. Table 1.2 clusters conceptualized requirements, relates them to the standard features (F1–F8) of digital twins and presents the corresponding solution proposition of this work. Three working hypotheses are formulated that aim to address the requirements within the scope of the presented work.

First, digital twins must replicate their "physical siblings" accurately (F1). Science has a proven track record of successfully deriving equations describing physical phenomena. In food science literature, physics-based models, also called mechanistic models, exceed observation-based models in insights and predictive capability [55, 58]. Not many decades ago, the mathematical toolboxes limited the solution of physical models such that analytical solutions could only be found for particular, simplified problems. During the age of computerization, we have witnessed an unprecedented rise of numerical methods, continuously improving accuracy and efficiency [177]. Allowing to solve more complex models, the trend of past decades lies in modeling across scales and disciplines: multi-physical models couple relevant physical fields of the problem, such as fluid mechanics and thermodynamics. In light of the advancement in computational engineering, the first working hypothesis of this work is: *Physics-based models should be the foundation of digital* *twins. Conjugate heat and mass transfer simulations that couple food processing models with the non-isothermal flow and thermal radiation of a thermal process are needed. Such simulation models better capture the product-process interrelationship between primary process variables and heat transfer mechanisms.*

Second, digital twins must replicate their physical counterparts at least in real-time (F2). This requirement shows that the concept of digital twins is much more sophisticated than that of a simulation model. However, digital twins are still often mistakenly treated as such [159, 238]. Digital twins based on highly accurate, multi-physical simulation models face the dilemma of modern computational engineering. The solution of such simulations for large-scale industrial problems will not be achievable in real time in the coming years, maybe even decades — despite a spectacular growth of feasible computing power over past years, still following Moore's law [41]. Since the 1990s, scientific computing and computational engineering researchers have identified reduced-order models (ROM), whose generation is also called model order reduction or surrogate modeling, as a potential solution to the dilemma [17]. For food science as well, they are considered as useful [58]. Particularly, data-driven ROMs adapt well to the reality of model development in many open-source, commercial or custom codes. Data-driven ROMs solely require the output data of the simulation model. Nonetheless, some data-driven ROMs still need much training data, which is not feasible. The question of how to select a small set of appropriate training data for ROMs leads to the second working hypothesis: *Given the significant simulation times of sophisticated full-order models, data-driven ROMs of thermal food processing need to be trained with only one-to-two training data sets while preserving sufficient accuracy. A proposed efficient design of experiments provides decision support to select training data that ensures low test error of the ROMs on representative test data. Combining the notion of highly-accurate simulation models with data-driven reduced-order modeling shall be conveyed in the coined term "physics-based, data-driven digital twin".*

Third, intelligent decision-making of processes requires an advanced control algorithm, such as the industry-standard *model predictive control* (MPC) [72, 108]. During operation, the algorithm queries the model multiple times to determine the optimal trajectory of the control variables. A comparison between the virtual and the real world also enables a reaction to unforeseen disruptions or desired changes while the execution is still in progress. Aiming to realize multi-query optimizations during operation leads to the following statement: *MPC-based autonomous decision-making requires surrogate models that are solvable several orders faster than real time. Besides, one can hypothesize that physics-based, data-driven digital twins increase the accuracy and efficiency of MPC approaches.* This work presents an MPC approach based on accurate physical models encapsulated in the functional-mockup unit (FMU) format [168]. The latter is a cross-platform, intellectual-property-protected data format to store and deploy ROMs. The presented algorithm that combines MPC and FMUs has a significantly low computational cost, allowing for execution on low-end processors, e.g., those of processing devices.

Table 1.2. Requirements and solution proposition for a digital-twin-enabled process autonomy [137].

Requirement	Relates to	Description	Solution proposition
R1: Physics-based modeling	F3	First principle models provide a profound understanding of the cause-and-effect relationships, which enables control over the process.	Conjugate heat and mass transfer models better capture product-process interrelationship of thermal food processing inside a convection oven.
R2: Minimum physical sensors	F1, F5,	Focus on easy-to-measurable quantities that are used as boundary conditions for the simulation.	
R3: Faster than real-time	F2	Process autonomy based on digital twin methodology requires faster-than-real-time simulations.	Data-driven reduced-order modeling furnishes high speed-ups, and it is non-intrusive to the model equations. A proposed efficient design of experiments provides decision support to select on-to-two training data sets of the full-order model to train ROMs with low test errors.
R4: Reflect modeling reality in industry and academia	F3, F4, F6, R1	Modeling takes place in various software. Seldom, there is code access to solvers in commercial simulation software. Even for available source code, sometimes intrusive ROMs are considered too time-consuming [185].	
R5: Data determines ROM quality	F3, F7, R4	Data-based ROM methods require sophisticated excitation signal design to accomplish ROM accuracy.	
R6: On-device operation	F2, F3	For execution at the device level, the simulation's computational cost must be minimal.	Autonomous decision-making with FMU-based model predictive control. The FMUs impose meager computational costs and store the ROMs in an encrypted format.
R7: Cyber-security	F5, F7, R6	On-device operation increases cyber-security, especially for automating system-critical processes.	
R8: Intellectual property	F3, F4, F5, R6	Modeling know-how is the core intellectual property of companies and should not be left unprotected.	
R9: Open access	F6	The generation and distribution of digital twins should be open-source-based to enable an application at scale.	TwinLab — A MATLAB code framework for digital twin generation from COMSOL and ANSYS simulation data.

Lastly, the generation and distribution of digital twins requires open-source platforms to enable an application at scale. In 2021, Niederer et al. [177] concluded on deploying digital twins: *"however, analogous open-source platforms—which have been so influential in finite element analysis, optimization and machine learning—are not widely available for digital-twin applications."* To meet this requirement to a certain extent, the software termed *TwinLab* was developed for this thesis. It seeks to contribute to efforts toward applying digital twins at scale. The code connects simulation models, data science and control techniques into one framework and, at its current state, offers interfaces for two major commercial simulation software packages.

1.2.2. Overview of the proposed digital twin framework

Imagine a convection oven that performs autonomous thermal food processing. Food quality variables, such as core temperature, moisture content, or texture, are difficult to evaluate by the cooking appliance without additional equipment. A digital twin may offer knowledge of unknown conditions using a detailed and accurate multi-physical model. Faster-than-real-time solution times enable the ROM of the simulation model to return multiple future scenarios. The device can plan its oven temperature trajectory to meet the user requirements of specific moisture content, safe core temperatures, or texture at the end of the process at one particular point in time. Three building blocks form the digital twin framework for autonomous thermal food processing.

Within the first building block, a conjugate heat and mass transfer model for thermal food processing is derived, see upper block of Fig. 1.1. Conjugate product and process modeling entail non-isothermal computational fluid dynamics (CFD) simulations coupled to a food processing model. The individual components of the model are validated step-by-step. For non-isothermal fluid flow inside a convection oven, the benchmark cases *flow over a flat plate*, *flow over a cylinder* and *surface-to-surface radiation inside a cavity* are evaluated. Two food processing models are implemented and investigated: the *hygroscopic, capillary-porous media model* [53–55] and a *soft-matter model* for chicken meat [83, 84, 196, 228]. Both models are tested against synthetic and experimental data, depending on availability. Next, the sensitivities of the model parameters are investigated. Of particular interest is the potential of the model to be extended to a conjugate simulation model. Finally, all relevant parts of the selected food model are coupled to the physics of thermal food processing within a simulation model of reduced size — a so-called *forerunner* model. The ultimate *full-order model* is characterized not only by the application of all relevant physics but also capturing geometric features. Comparable operating conditions and identically applied physics render the two models similar.

Data-driven reduced-order modeling starts with synthesizing special excitation signals that vary the oven temperature at the inlets of the simulation models, see the second block in Fig. 1.1. A full-order model is considered too computationally expensive for multiple preliminary simulations, as it typically may take days or weeks to solve. The proposed efficient design of experiments consists of two major steps. Step 1: The forerunner model generates a basis of simulation data sets with different excitation signals. One data set consists of a unique combination of excitation signal and simulation output data. The Pearson correlation matrix reveals correlations between training data set properties and corresponding ROM prediction errors. Testing of the ROMs is performed on special *fair* data sets that are selected with a χ^2 test. Step 2: With the knowledge of correlations, one-to-two excitation signals are selected to simulate the full-order model. From this data, the final ROM is trained and saved as an FMU.

The emulation of an operational phase is the third building block of the framework, see the lowest block in Fig. 1.1. Simple measurements of the current oven temperature form the initial condition of the ROM. A control algorithm employs the control vector parameterization (CVP) approach, which systematically varies the amplitudes of a hypothetical oven temperature trajectory. In such a way, the algorithm gains insight into the sensitivities of the model concerning a target function that includes the desired cooking objectives. An optimization problem is solved at discrete points during the operation to determine the optimal trajectory of oven temperatures to reach the objectives. Repetitive comparisons of the actual oven temperature with the planned trajectory mitigate the model–process mismatch by recalculating the residual trajectory.

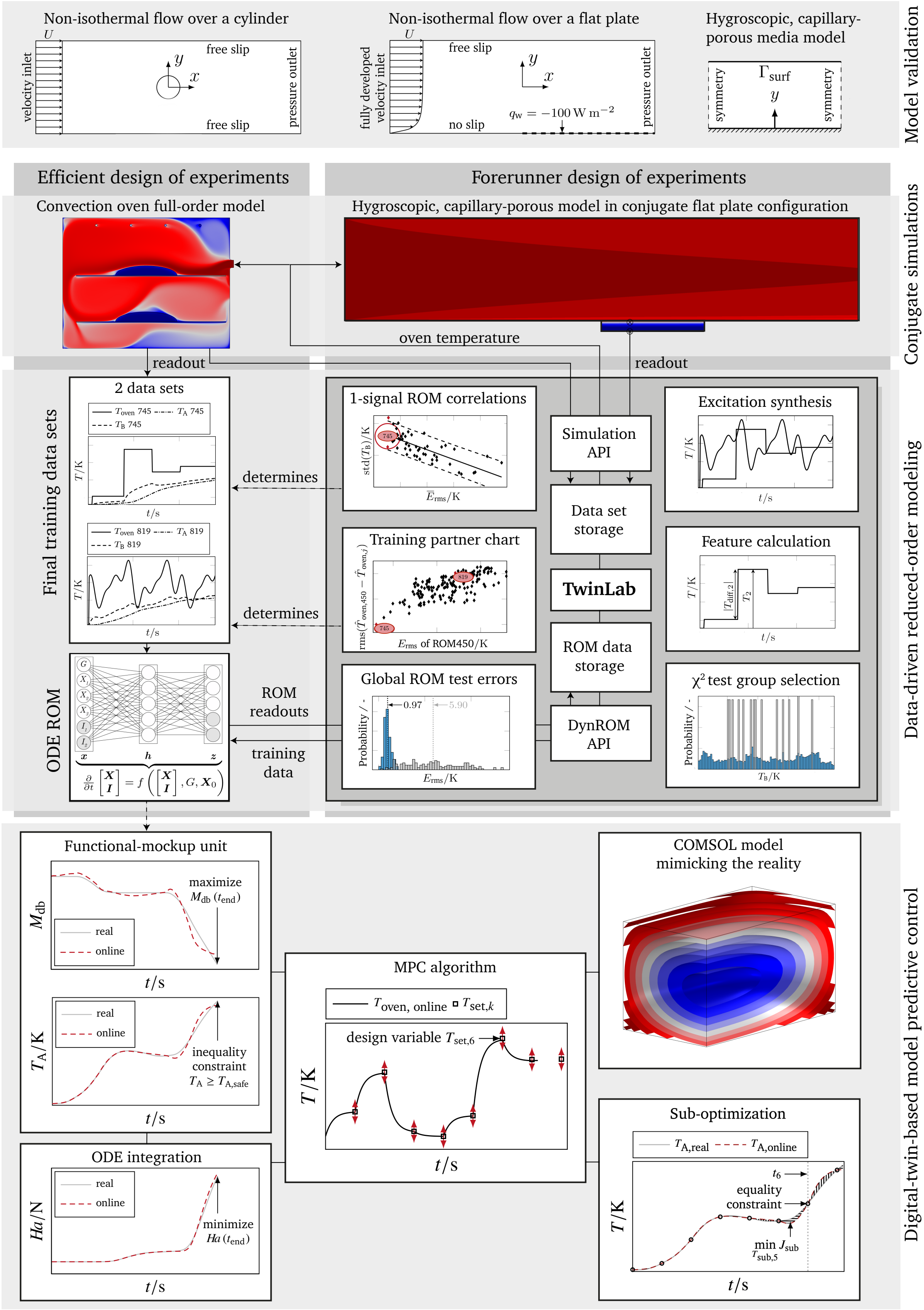

Figure 1.1. The proposed physics-based, data-driven digital twin framework.

1.3. State of the art

Research within the food science and technology community has not yet addressed many of the abovementioned concepts. The following literature review focuses on three categories in food science: (1) intelligence for thermal food processing, including digital twins and advanced control algorithms, (2) data-driven reduced-order modeling as well as (3) conjugate thermal food processing models. The articles are evaluated against the standard criteria of digital twins and the derived requirements for processing autonomy. In comparison to this thesis, many of the presented works lack either conjugate modeling, state-of-the-art mechanistic food processing models, proper radiation consideration, a ROM to obtain significant speed-ups and reduced computational cost, a highly accurate surrogate model within intelligent control algorithms, or a surrogate model that can run live during operation.

1.3.1. Intelligence for thermal food processing

In 2018, the concept report for the present thesis work [134] was one of the first works envisioning the application of digital twin methodology within food science and technology. The latest publication derived from this thesis work [137] covers many of the concepts presented in Tab. 1.1. To date, no publication in the field fulfills all required criteria.

Digital twins in food science

Only in the last three years have we have seen the emergence of digital twins in food science and technology, which explains why relevant literature is still rare. The potential of digital twins has recently been highlighted in several review articles [68, 117, 253]. Whereas mechanistic models were recommended in [68, 253], it was thought that only simple models would be viable for application as digital twins. Complex physics-based models were considered not solvable in real time. The assessment of digital twins in [253] concentrated on big data, cloud computing, the internet of things and sensorization. Instead of identifying the predictive power of digital twins for process autonomy, a real-time augmented-reality monitoring system was envisioned. Henrichs et al. [117] concentrated their review on the food value chain and shop floor production planning. The work by Koulouris et al. [146] is a good example of this perspective on digital twins. Furthermore, according to the review [117], few food science studies explored process autonomy. Just eight of 84 pieces of research focused on digital-twin-enabled process autonomy, and only two of these eight were peer-reviewed studies. Guo et al. [103] developed a cyber–physical system that monitors and controls the soil and plant parameters in greenhouses with robots. Eppinger et al. [76] presented two application examples in brief: ketchup production optimization and a spray-drying method for making milk powder. However, this work appears to serve marketing rather than academic research purposes.

Some manuscripts partially cover the common features of digital twins, as summarized in Tab. 1.1.

Several studies on digital twins within the post-harvest sector [67, 224, 225, 236] see the latter as a simulation model for processing temperature profiles of physical equivalents that have been pre-recorded. Concepts like bi-directional linkages, interactive decision-making, and mirroring across the product life cycle are not yet addressed. Real-time simulations are necessary, as has been envisioned recently [68, 192]. In [192], the computational hardware (8-core Intel Core i7 processor with 32 GB RAM) required a simulation time of 20 h to predict the solar drying of one-eighth of one apple ring in a non-conjugate setting. Consequently, the presented speed-ups (compared to real time) of factor three are not enough for online decision-making with advanced control algorithms. Considering additionally the computational cost, it would be unfeasible to predict multiple scenarios even for just one fruit. Here, the need for reduced-order modeling becomes obvious.

Advanced process control in food science

Modern model-based control techniques are a popular approach to control the future behavior of systems [152, 153]. *Optimal control* entails solving an optimization problem to obtain the ideal control parameters of the system in an offline stage. The actual process then incorporates this control signal. *Model predictive control* entails repeating the optimization at regular intervals live during operation. This enables a response to differences between system reaction and model prediction [152]. Employing contemporary control techniques for the food sector was encouraged in a review by Kondakci et al. [145]. Madoumier et al. [161] identified the following research gaps concerning surrogate models within their review: *“The main advantage of these black box models is probably the calculation speed, which enables use of a wide variety of optimization algorithms. Nonetheless, these modelling approaches are often very data-hungry [...]. To develop [food engineering process] simulators, it should be defined what is expected of a model tailored to optimization, especially in terms of compromise between calculation speed and accuracy of results.”* Both reviews concluded that fast and precise models are essential for model-based control techniques and require further research in the upcoming years.

The works closest to the concepts presented within this thesis are the ones by Alonso et al. [4, 5]. Without naming it digital twins, the works contain many elements that classify them as such: a physics-based simulation model, a ROM and an MPC algorithm. Alonso et al. [5] modeled the batch sterilization of food in cans. The authors stated that ignoring the dynamics of the process would lead to unfeasible solutions during the MPC of the process. However, the process and the product were realized in a non-conjugate fashion. The processing plant was described with macroscopic ordinary differential equations (ODEs). In contrast, the temperature of the product was modeled with Fourier’s law and heat transfer coefficients. The final set of equations was Galerkin-projected to a smaller subspace to create a ROM. One disadvantage of the work is the equation-invasive nature of the employed proper orthogonal decomposition (POD) [34, 118, 244] and the need for handling the nonlinear terms [34, 207]. A large share of simulation models is developed in commercial software [253], where root-level access to the equations for custom modifications is seldom possible. Consequently, the POD approach excludes the use of commercial software. The study in [5] relied mainly on a pre-computed optimal control policy realized with conventional controllers. Only for unexpected deviations were these policies recomputed live during operation. For six and ten MPC steps for a total process time of 60–70 min, the maximum solve time of the optimization was approximately 3 min and 6 min per MPC time step, respectively. Within a more recent study [4], which extended the model with robust control elements, the authors indicated that the solve times of their approach must be significantly decreased to achieve actual real-time optimal control. The underlying optimization routine was programmed to stop after 5 min and then proceed with the following MPC time step.

A recent article by Vilas et al. [254] demonstrated the MPC of a freeze-drying process. It is modeled with constant transfer coefficients that are estimated from experimental data. Radiation was not modeled explicitly but was accounted for as a boundary condition. Instead of employing a ROM, the problem was simulated on a one-dimensional (1D) domain. The recalculation time of optimal policies required “several minutes” for one control step with a duration of 1 h. Other works that developed MPC approaches based on simple food models are [219, 235, 261]. Outside of food science and especially within the Modelica community, several researchers performed MPC with FMUs [18, 85, 93, 94, 127, 264]. However, the surrogate models presented in these works were only derived from macroscopic system models.

Several studies that aim at the optimal control of thermal processing can be found. Hadiyanto et al. [104] presented an optimal control approach for baking optimization. The model, realized with heat and mass transfer coefficients, was discretized with 10 1D elements resulting in 108 ODEs to replicate 9000 s of real time. In the best-case scenario, the control vector parameterization optimization required a solve time of 4243 s. Arias-Mendez et al. [9] modeled a 2D quarter section of an axisymmetric potato chip with heat and mass transfer coefficients estimated to match experimental data. As no ROM was employed within the optimal control algorithm, the problem was coarsely discretized with 200 elements, which required 40 s to simulate 90 s of real time within COMSOL Multiphysics. Ousegui et al. [184] presented an optimal control study of a baking process using adjoints of the non-conjugate simulation model.

Intelligent food processing appliances

Based on marketing claims by several brands, one may get the impression that intelligent thermal processing devices are already developed, e.g., for the consumer [255]. Although these and other appliances automate the cooking process, they merely follow pre-defined cooking paths or simple logic designed upfront for the individual end-product. For a closer discussion of automated cooking appliances, the interested reader is referred to [73].

1.3.2. Data-driven reduced-order modeling in food science

Data-driven reduced-order modeling can be considered an essential block to derive digital twins from simulation data independent of the software or custom code. Few works covered this aspect in food science and technology literature. Generally, developing surrogate models is not new to food science. Within the early work of Brescia and Moreira [28], linear auto-regressive moving average models with exogenous input (ARMAX) were trained from experimental data to develop an online controller. Bottani and Volpi [25] deduced analytical formulas from diffusive heat equation simulations of a steam oven to predict trend curves for meat temperatures with 4.6% relative errors compared to experimental data. However, nonlinear, transient ROMs for field data are scarce in food science. The two works by Rivas et al. [207] and Alonso et al. [5] are rare exceptions, as discussed above.

Only very few studies in food science consider ROMs that employ machine-learning approaches to predict transient model behavior. Broyart and Trystram [31] trained recurrent neural networks (RNNs) to predict macroscopic quantities during biscuit baking from experimental data. Similarly, Isleroglu and Beyhan [130] predicted the browning index of cookies. Khan et al. [142] recently reviewed the state of the art of machine-learning-based modeling in food processing. The authors conclude: *"The development of a machine learning (ML)-based approach to food processing applications is an exciting and innovative idea for optimizing process parameters and process kinetics to reduce energy consumption, processing time, and ensure better-quality products; however, developing such a novel approach requires significant scientific effort."* Two of the 31 presented studies were transient ROMs: Huang et al. [125] developed a nonlinear, autoregressive system equation with exogenous input (NARX) employing an RNN to predict only a few future steps of macroscopic properties of snack food during frying; and Li et al. [154] trained a recurrent self-evolving fuzzy neural network to predict red maple's temperature and moisture content from data of an effective diffusion model. The ROM was consecutively used within an MPC environment. The residual studies in [142] reveal that many machine-learning models in food science are steady-state. The findings of experiments or simulations are utilized for training feed-forward neural networks. Owing to the lack of dynamics, process parameters cannot be influenced within the run of the surrogate model.

The employed reduced-order modeling software within this work is ANSYS Dynamic ROM builder. It is a neural-ODE-type of data-driven ROM method. The motivation to employ it and details of the approach are discussed in Sec. 3.2. Since its introduction in 2018, few works employed the method [24, 36, 143] other than publications stemming from this thesis work [135–137]. This thesis intends to investigate the method in depth regarding speed-up and the impact of ODE augmentation parameters on accuracy.

Within the discipline of system identification, tailored excitation signals are utilized to extract information from a physical model during tailored virtual or real experiments. The excited transient behavior of the physical problem can be determined from the recorded output data [23, 157, 174]. A few notable works inspired the excitation signal design in this thesis [96, 115, 116, 174, 237]. However, those articles only provide suggestions for the design of experiments for NARX models, local model networks and recurrent neural networks. To date, no published work has been found that considers the training data generation and selection for data-driven reduced-order modeling of food models. In general, the selection of data sets to train neural ODE ROMs with low test errors has not been reported. This thesis and the related publication [137] try to close these gaps by proposing an efficient design of experiments. Moreover, [137] demonstrates that suggestions to uniformly cover the models' input space [174] or output space [237] to ensure good ROM training does not hold for the presented food model. An input and output space coverage measure for the food model was implemented. High coverages did not correlate with low test errors [137].

1.3.3. Conjugate thermal food processing models

For the simulation of thermal food processing, there has been a notable trend towards more mechanistic and multi-disciplinary models over the past years. After predominantly employing simple lumped diffusion models until the 1990s, more mechanistic models for moisture and temperature were used during the 2000s [53]. From 2010 onward, additional physics, such as electromagnetic heating and deformations [102], were added. Today, research additionally focuses on finding remaining model parameters [50, 51]. However, models that couple the process and the food, e.g., conjugate heat and mass transfer models, are still scarce in food science and technology literature.

Convective heating

A large share of food science research on convective heating applied constant transfer coefficients to model the interaction of food with its surrounding process. Early studies of convective heating of potato slabs assumed laminar flow and employed standard empirical correlations for the Nusselt number to obtain constant heat transfer coefficients. Based on analogy assumptions of heat and mass transfer, the Lewis relation was used to derive the corresponding mass transfer coefficient [175, 176]. The details of the procedure are explained in Sec. 2.3.2. Other works estimated the heat transfer coefficients from experimental heat flux and temperature measurements [172] or simply *"estimated [the coefficient] to minimize the prediction error"* [40]. The latter statement reflects the mindset toward considering the heat transfer coefficient as a convenient tuning parameter.

The common practice of deriving constant values from correlations can be found in many works. Sman employed constant coefficients for the modeling and validation of roasting beef inside an oven [228] and chicken meat inside a tunnel oven [229]. Feyissa and Rabeler obtained constant coefficients from experiments with aluminum blocks to model the roasting of meat [84] and chicken meat [196] inside a convection oven. The four models can be grouped within the class of *soft-matter models for meats* owing to their similarity and common roots. The models contain fitting parameters such that their output matches experimental data. A closer discussion of the implications can be found in Sec. 4.2. Goni et al. [91] modeled meat roasting inside an oven with constant transfer coefficients that were compiled with measured air velocities. Isleroglu et al. [131] investigated steam-assisted beef cooking. The convective heat transfer coefficients were obtained from experiments using the lumped capacity method. A separate radiative portion using the Stefan–Boltzman law was added as a macroscopic boundary condition without modeling radiative heat transfer explicitly. Various other works modeled bread baking and validated the model with constant transfer coefficients [262, 263]. Ousegui et al. [183] enhanced this baking model and demonstrated a strong dependence of the heat transfer coefficient on the surface temperatures.

Within several works, radiation is considered at a macroscopic level but is not simulated explicitly. Rakesh et al. [199] investigated microwave heating with additional radiant and convective influx. Convection and radiation were sub-summarized in a constant heat transfer coefficient derived from temperature and heat flux measurements. During cycled microwave operation, the heat influx by radiation and convection was larger by a factor of 5.8 compared to the microwave heat input. Other research models used separate but macroscopic boundary conditions in variants of the Stefan–Boltzmann law [182, 183]. For the investigation of convection oven roasting, Feyissa et al. [84] argued that *“[r]adiation plays only a little role at the temperature applied (at 175 °C) and the contribution from radiation is further reduced because the oven walls are of polished stainless steel.”* Similar arguments can be found in later works [196]. However, expecting low radiative input to the food because of low wall emissivities is a misconception. From energy conservation and Kirchhoff’s law (refer to Sec. 2.2.2), it becomes evident that low wall emissivities imply large reflective portions of energy. Hence, lower wall emissivities effectively increase the radiative heat flux to a food item. For example, Dhall et al. [70] showed that lower wall emissivities imply higher (and locally variable) radiative heat input of more than 50% of the total heat flux to the food sample inside a convection oven. The work explicitly models the radiative heat exchange inside an oven with infrared heating and non-participating air. However, the results are slightly impacted by neglecting convective effects, which might be a reason for the under-prediction of heat losses observed. Moreover, no food-specific model was included in the investigation. The food was treated as a solid, heat-conducting object.

Some works simulated the fluid flow inside a convection oven [189, 251]. Verboven et al. [252] investigated the convection and radiation effects inside a microwave oven without considering electromagnetic radiation or modeling a particular food. Radiative effects were found to be in the same order of magnitude as the convective heat transfer effects. Only one research article partially approached conjugate thermal food processing modeling: The work by Halder and Datta [106] investigated the so-called blowing out of a porous medium by employing a two-dimensional (2D) conjugate heat and mass transfer setup. A channel flow of air with a velocity of $0.1\,\mathrm{m\,s^{-1}}$ over a partially porous plate was modeled. However, no thermal radiation has been considered. The derived convective heat transfer coefficient showed substantial temporal and spatial variance.

Drying and cooling

In the absence of holistic, conjugate heat and mass transfer models for convective heating that include radiation and a mechanistic food processing model, this literature review is extended to the sectors of more specialized food treatment, e.g., food drying and cooling. Within this sector, many publications employ constant transfer coefficients until today. Various works simulate conventional food drying [1, 100, 148], combined convective and microwave or infrared drying of food [133, 147, 149, 181, 217] and microwave vacuum drying [155, 173, 239]. More specific examples include rice puffing [101] and a microwave drying model including deformations [102]. For the former model, the simulation time for a 2D, axisymmetric quarter model of one rice corn (10 800 elements) was 64 h on a 12-core Intel Xeon CPU with 32 GB of RAM to resolve 15 s of real time.

Conjugate drying models are scarce. Defraeye et al. [66] summarized that mostly non-conjugate models can be found in the literature. If a model is conjugate, it is mainly 2D, and radiation is usually left unaccounted. If radiation were to be accounted for, the analogy between heat and mass transfer, e.g., the Lewis relation, is not valid anymore. In a review on drying modeling, Defraeye [61] denotes that *"[w]ithin the field of food engineering, the group of Datta is at the forefront of such multiphysics modelling of dehydration processes [...] Future perspectives in multiphysics modelling should be directed towards developing more complete multiphysics models for drying, i.e. models which couple heat and mass transport within the material simultaneously with multiple other physical processes (e.g. deformation, airflow, radiation), instead of with only a single one (e.g. as in conjugate modelling, [...]). Particularly for food, such next-generation dehydration models should also include (bio)chemical or biological (degradation) processes to be able to address quality and safety parameters."*

Ateeque et al. [10] developed a pseudo-conjugate model of potato drying. First, a cuboid was immersed in a channel flow with velocities of 0.1–$4\,\mathrm{m\,s^{-1}}$. The local heat transfer coefficient varied significantly: $\alpha(x_i) \in [65, 210]\,\mathrm{W\,m^{-2}\,K^{-1}}$ for the front facing face and $\alpha(x_i) \in [20, 155]\,\mathrm{W\,m^{-2}\,K^{-1}}$ for the side faces. The local mass transfer coefficient was determined with the Lewis relation. A purely diffusion-based food model was simulated once with local transfer coefficients and once with averaged coefficients per face. The authors argued that similar *average* results were obtained with averaged transfer coefficients, such as average food temperature or average moisture content. The *local* impacts of the strongly spatially variable heat input remained uninvestigated, as the authors favored the usage of constant transfer coefficients in the end. On the contrary, Defraeye et al. [62] demonstrated considerable differences in the average drying rate of a porous flat plate when comparing a conjugate approach and a heat-transfer-coefficient-based variant. Erriguible et al. [78, 79] developed a conjugate model for drying pine wood by coupling ANSYS Fluent to a custom 2D FORTRAN code for the porous medium. Other research groups developed their own conjugate code [140, 141] or utilized COMSOL Multiphysics [35, 60, 162] to develop conjugate drying models. However, radiation was not considered.

Defraeye and coworkers presented several drying or cooling models in recent years [63, 64, 97, 236] that also advocated the usage of conjugate simulation models. In [63], the impact of spatial and temporal variable transfer effects was captured with a conjugate model. Radiation was not modeled explicitly but was considered with a boundary condition. Some models focus on deformation and resort to semi-conjugate couplings through pre-computed transfer coefficients [64]. Others focus on the fruit shape and random stack modeling [97], but unexpectedly use mesh resolutions within the boundary layer ($y^+ \in [6, 19]$) that lie far above recommended values of $y^+ \approx 1$ to capture the local heat transfer effects accurately [7]. In [225], the authors state: *"[w]e used wall functions to model the near-wall regions and built a corresponding mesh with a desired y^+ value of 1."* The usage of wall functions is only recommended for mesh resolutions of $y^+ > 30$ [218], and wall functions considerably reduce the resolution accuracy of the near-wall effects. Other models [236] employed an effective diffusion ansatz to model heat and mass transfer within the porous medium, an approach often criticized by experts in the field [53, 55].

Outside of food science, Selimefendigil et al. [222, 223] published a series of articles on porous objects that are immersed within a channel flow. Although no foodstuff was simulated, the approach is comparable to the models on drying. The implementation was performed in COMSOL Multiphysics, and no radiation was considered. Notable particularities of the model are a moving-boundary formulation and a subsequent compression of the field data.

1.4. Identified research gaps, objectives and outline of this work

Summarizing the state of the art, the following gaps can be identified: Within food science and technology, many typical features that qualify a digital twin have not yet been combined in one comprehensive approach. A conjugate heat and mass transfer model comprising non-isothermal flow, thermal radiation and a hygroscopic, capillary-porous media approach has not yet been explored. In particular, the local effects of convection and radiation have not yet been considered in detail. Moreover, the requirements for achieving processing autonomy with digital twins have not yet been adequately addressed. Neither non-intrusive ROMs that reproduce field data nor systematic investigations on selecting only a few data sets to train accurate ROMs could be found in food science literature. Advanced control algorithms that perform intelligent decision-making live during operation have so far relied only on macroscopic, strongly simplified models or ROMs of simplified models. MPC algorithms with access to highly accurate and computationally lean ROMs of comprehensive, physical models have not yet been covered in food science. Process autonomy based on digital twins can be seen as a novel thrust, as digital twins have so far been seen as a monitoring tool rather than a potential core of process intelligence. This research initiative aims to close the abovementioned gaps, proposing a physics-based, data-driven digital twin framework for autonomous thermal food processing. It aims to match the standard features of digital twins in Tab. 1.1 and to fulfill the requirements in Tab. 1.2.

The outline of this work follows the order of the framework in Fig. 1.1. Chapter 2 presents the fundamentals of modeling food processing inside a convection oven from first principles. Chapter 3 then motivates the selection of the numerical methods and introduces the latter. Chapter 4 covers the first building block of the proposed framework in-depth. It presents the analysis of two food processing models and investigates their potential to be included in a conjugate model. After benchmarks of all required model components, a conjugate heat and mass transfer model for thermal food processing is derived and investigated. Of particular interest is the local influence of the conjugate model, particularly of radiation and convection, on the food temperature and moisture saturation. Chapter 5 covers the subsequent data-driven reduced-order modeling. An efficient design of experiments is proposed and investigated in detail for point data ROMs of a soft-matter model for meat roasting. Consecutively, the approach is applied for a conjugate convection oven model comprising non-isothermal flow, radiation and a hygroscopic, capillary-porous media model. This work proposes a procedure to develop digital twins for autonomous thermal food processing. The focus is on conjugate modeling and data-driven reduced-order modeling. To deliver a holistic picture of the concept, Chapter 6 briefly presents how the digital-twin-based autonomy may be accomplished with MPC. The algorithm encounters scenarios that require autonomous decision-making during food processing inside a convection oven. Detailed syntheses can be found at the end of Chapter 4–6. Chapter 7 summarizes the major findings of this work and contextualizes them from a more global perspective. It also outlines the novelties and contributions to food science and beyond and refers to potential future research that can follow this work.

2. Fundamentals on physical modeling

The introductory chapter motivated the derivation of multi-physically coupled simulation models for thermal food processing. This chapter introduces the relevant physical foundations to do so. Figure 2.1 illustrates qualitatively the two main domains that require modeling of the physical effects, namely the cavity of a convection oven filled with hot air Ω_{cavity} and the domain of one or multiple food items $\Omega_{\text{porous},i}$ that are treated as porous solids within this work. Their union forms the problem domain $\Omega = \Omega_{\text{cavity}} \cup \Omega_{\text{porous},1} \cup \Omega_{\text{porous},2}$. The modeling of the relevant physical phenomena involves conserving the mass, momentum and energy of the concerned fluids and solids in the domains. Consequently, a system of coupled partial differential equations (PDEs) and ODEs arises, which requires the specification of boundary and initial conditions. The boundary Γ_{cavity} can be subdivided into sections where Dirichlet Γ_{D} (specification of the variable values), Neumann Γ_{N} (specification of the normal fluxes) and Robin Γ_{R} (mixed formulations of variable values and fluxes) boundary conditions are imposed, and $\Gamma_{\text{D}} \cup \Gamma_{\text{N}} \cup \Gamma_{\text{R}} = \Gamma_{\text{cavity}}$ holds. Section 2.1 describes the modeling of non-isothermal turbulent fluid flow on Ω_{cavity}. Section 2.2 focuses on specialties in heat transfer modeling, namely the description of conjugate heat transfer, the coupling conditions at the fluid–solid interface $\Gamma_{\text{porous},i} \equiv \Gamma_{\text{interf},i}$, thermal radiation and the description of moist air. Section 2.3 is devoted to modeling the food's thermal processing in $\Omega_{\text{porous},i}$. Following an overview of the approaches in food science, two food processing models based on the porous media approach are presented. The introduction of sensory quality models of food concludes this section.

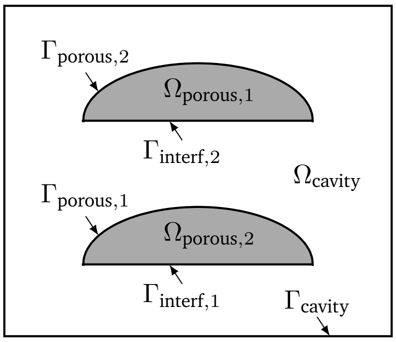

Figure 2.1. Stylized domain setup for the thermal processing of food items in a convection oven.

Note that units of variables only are given when they are considered helpful for better comprehension of derivations. Hence, if not stated otherwise, the reader can expect the standard units of the given quantities within the SI system.

2.1. Non-isothermal fluid flow

Non-isothermal turbulent flow is modeled with the Navier–Stokes equations, which are presented in this section. The efficient numerical solution of the fluid flow problem requires employing a turbulence model. The Reynolds-averaged Navier–Stokes (RANS) equations and the k–ω shear stress transport (SST) model are introduced in this context.

2.1.1. Navier–Stokes equations

Describing the single-phase non-isothermal flow of a fluid involves the derivation of conservation of mass, momentum and energy. From a continuum mechanics perspective, the respective conservation laws are formulated for a small fluid parcel (Lagrangian description). Transforming the equations to Eulerian description (e.g., with Reynolds transport theorem) and switching from integral to differential form yields the Navier–Stokes equations

$$\frac{\partial \rho}{\partial t} + \frac{\partial (\rho\, v_i)}{\partial x_i} = 0\,, \tag{2.1}$$

$$\frac{\partial (\rho\, v_i)}{\partial t} + \frac{\partial (\rho\, v_i\, v_j)}{\partial x_j} = -\frac{\partial p}{\partial x_i} + \frac{\partial \tau_{ij}}{\partial x_j} + \rho\, g_i\,, \tag{2.2}$$

$$\frac{\partial (\rho\, h)}{\partial t} + \frac{\partial (\rho\, h\, v_i)}{\partial x_i} = \frac{\partial p}{\partial t} + \frac{\partial (\tau_{ij}\, v_j)}{\partial x_i} + \rho\, g_i\, v_i - \frac{\partial q_i^{\mathrm{S}}}{\partial x_i}\,, \tag{2.3}$$

where x_i are cartesian coordinates, v_i are fluid velocities, ρ represents density, p is pressure, h is total enthalpy and g_i is the gravitational acceleration [11, 19, 218, 231]. Fourier's law models the surface heat fluxes q_i^{S}

$$q_i^{\mathrm{S}} = -\kappa\, \frac{\partial T}{\partial x_i}\,, \tag{2.4}$$

where κ denotes the isotropic thermal conductivity and T the absolute temperature. The viscous stress tensor τ_{ij} of a Newtonian fluid reads

$$\tau_{ij} = \mu \left(\frac{\partial v_i}{\partial x_j} + \frac{\partial v_j}{\partial x_i} \right) - \frac{2}{3}\, \mu\, \frac{\partial v_k}{\partial x_k}\, \delta_{ij}\,, \tag{2.5}$$

where μ denotes dynamic viscosity and δ_{ij} is the Kronecker delta [170]. Besides this constitutive material law and relations for the material parameters μ and κ, the thermal and caloric equations of state are required to close the system of equations describing non-isothermal fluid flow [19]:

$$\rho = \rho(p, T)\,, \tag{2.6}$$

$$c_p = c_p(p, T)\,, \tag{2.7}$$

where c_p denotes the heat capacity at constant pressure that relates temperature and enthalpy (see Eq. (2.24)). Viscous heating $\frac{\partial}{\partial x_i}(\tau_{ij}\, v_j)$ can be neglected in Eq. (2.3) for flows without enormous velocity gradients [19], which is expected to hold for the scope of this work. The closed set of PDEs becomes solvable with given boundary and initial conditions, which are presented in Chapter 4.

2.1.2. Turbulence modeling

The Reynolds number is a dimensionless measure that relates inertial and viscous forces in a flow. It reads

$$Re = \frac{\rho U L}{\mu} = \frac{U L}{\nu}\,, \tag{2.8}$$

where U and L are characteristic velocity and length scales of the problem, and $\nu = \mu/\rho$ is the kinematic viscosity. Exceeding a critical Reynolds number, the flow becomes turbulent. Turbulence is characterized by a broad spatial and temporal range of inherently three-dimensional (3D), unsteady eddies [82]. The fluctuations might appear chaotic to an observer. Richardson and Kolmogorov introduced the idea of an energy cascade to describe the mechanisms of turbulence [191]. The largest eddies of a flow have a characteristic length similar to those length scales of the geometric problem (energy-containing range). These turbulent eddies are unstable and break down into smaller structures (inertial subrange) until the size is small enough that viscous forces dominate, and consequently, the energy is dissipated (dissipation range). This energy cascade's lowest statistical length scale is called Kolmogorov length [191]. Although Eq. (2.1) to (2.3) can describe these phenomena, the necessary numerical resolution in space $\sim (Re^{3/4})^3$ and in time $\sim Re^{1/2}$ becomes unfeasible for typical engineering problems at elevated Reynolds numbers [82, 218].

A well-established approach to this problem is to derive the RANS equations. The RANS equations solve for the mean values of the dependent variables of the Navier–Stokes equations, and additional terms arise that have to be modeled. The following derivation is presented for an incompressible, steady-state case, as found in numerous literature [82, 218, 260]. The concluding remarks of this section discuss the applicability to transient, compressible and non-isothermal flows in a convection oven.

To derive the RANS equations, the fluid quantities are split into mean value $\overline{\Phi}$ and fluctuation Φ' in the first step. Inserting this split into Eq. (2.1)–(2.3) and then averaging the equations over time furnishes the RANS equations. The Reynolds stress tensor $-\rho\,\overline{v_i'\,v_j'}$ arises from the averaging of the momentum equation, specifically from the nonlinear convective term. The Reynolds stress tensor correlates the velocity fluctuations in the three spatial directions. The modeling of the six new unknowns of this symmetric tensor accomplishes turbulence closure. The class of eddy viscosity models assumes that the Reynolds stress tensor can be modeled in analogy to the viscous stress tensor, see Eq. (2.5), by introducing a turbulent viscosity μ_t (Boussinesq approximation):

$$\tau_{\mathrm{t},ij} = -\rho\, \overline{v_i' \, v_j'} = 2\,\mu_\mathrm{t}\, \overline{S_{ij}} - \frac{2}{3}\,\rho\, k\, \delta_{ij}\,, \tag{2.9}$$

where $\overline{S_{ij}} = \frac{1}{2}\left(\frac{\partial \overline{v_i}}{\partial x_j} + \frac{\partial \overline{v_j}}{\partial x_i}\right)$ is the mean strain rate tensor. One conceptional idea is to derive transport equations for further turbulent quantities, which can provide information on the turbulent length and time scales to find expressions for $\nu_\mathrm{t} = \mu_\mathrm{t}/\rho$. For example,

$$\nu_\mathrm{t} \sim \frac{k^2}{\varepsilon}\,, \tag{2.10}$$

$$\nu_\mathrm{t} \sim \frac{k}{\omega}\,, \tag{2.11}$$

where $k = 1/2\, \overline{v_i' \, v_i'}$ is the turbulent kinetic energy, $\varepsilon = \nu \overline{\frac{\partial v_i'}{\partial x_k}\frac{\partial v_i'}{\partial x_k}}$ is the turbulent dissipation rate and ω is the specific turbulent dissipation rate. Two equation turbulence models, such as the k–ε or the k–ω models, are frequently used in research and engineering applications [260]. The solution of two further transport equations is a reasonable trade-off between increased computational cost and loss of accuracy, as the fluid field is only represented by its mean quantities, and turbulent eddies are fully modeled. However, both models display unwanted behavior in specific applications. Standard k–ε models under-predict the size of recirculation zones when adverse pressure gradients are present. Moreover, corrections in the form of damping functions are required in the vicinity of walls. The k–ω model may be used to describe wall-bounded flow accurately but shows sensitivity to its free stream values. The latter, in return, is not as pronounced for k–ε models [260]. Menter [165, 166] proposed a blending between the two models within the logarithmic boundary layer to combine the benefits of the two models. The transport equations for k and ω read

$$\frac{\mathrm{D}k}{\mathrm{D}t} = P - \beta^*\,\omega\, k + \frac{\partial}{\partial x_j}\left[(\nu + \nu_t\,\sigma_k)\,\frac{\partial k}{\partial x_j}\right], \tag{2.12}$$

$$\frac{\mathrm{D}\omega}{\mathrm{D}t} = \gamma\,\frac{\omega}{k}\,P - \tilde{\beta}\,\omega^2 + \frac{\partial}{\partial x_j}\left[(\nu + \nu_t\,\sigma_\omega)\,\frac{\partial \omega}{\partial x_j}\right] + 2\,(1-F_1)\;\sigma_{\omega_2}\,\frac{1}{\omega}\,\frac{\partial k}{\partial x_j}\,\frac{\partial \omega}{\partial x_j}\,, \tag{2.13}$$

where $\frac{\mathrm{D}}{\mathrm{D}t}$ is the material derivative and $P = \min(2\,\nu_t\,\overline{S_{ij}}\,\overline{S_{ij}}, 10\,\rho\,\beta^*\,k\,\omega)$ is the limited version of the production term of the Wilcox k–ω model [166, 260]. Table 2.1 summarizes the model parameters that are blended by a factor F_1 via $\phi = F_1\,\phi_1 + (1-F_1)\;\phi_2$ for $\phi \in \{\sigma_k, \sigma_\omega, \tilde{\beta}, \gamma\}$.

The blending factor F_1 is essentially a tangent hyperbolicus and additional $\max()$ and $\min()$ operators account for well-posedness of the transition to $F_1 = 1$ for near-wall solutions:

$$F_1 = \tanh\left[\min\left(\max\left(\frac{\sqrt{k}}{\beta^*\omega\, l_\mathrm{W}}; \frac{500\,\nu}{l_\mathrm{W}^2\,\omega}\right); \frac{4\,\rho\,\sigma_{\omega 2}\,k}{\mathrm{CD}_{k\omega}\,l_\mathrm{W}^2}\right)^4\right], \tag{2.14}$$

$$\mathrm{CD}_{k\omega} = \max\left(2\,\rho\,\sigma_{\omega 2}\,\frac{1}{\omega}\,\frac{\partial k}{\partial x_j}\,\frac{\partial \omega}{\partial x_j}, 10^{-10}\right), \tag{2.15}$$

Table 2.1. Model parameters of the k–ω SST model [46, 165].

model	ϕ_i :	$\sigma_{k\,i}$	$\sigma_{\omega\,i}$	$\tilde{\beta}_i$	β^*	$\tilde{\kappa}$	γ_i
k–ω	$(i = 1)$	0.85	0.5	0.0750	0.09	0.41	5/9
k–ε	$(i = 2)$	1.0	0.856	0.0828	0.09	0.41	0.44

where l_w is the distance to the closest wall and $\mathrm{CD}_{k\omega}$ represents the positive portion of cross-diffusion term between k and ω. The last term acts as an additional safeguard against a free-stream-dependent solution [165]. So far, the equations are closely similar to the k–ω baseline (BSL) model reported by Menter [165]. Within the same publication, he proposed a shear stress transport (SST) extension of the model. The name suggests the solution of a transport problem for turbulent shear stresses, which is relevant to more accurately describe flows with adverse pressure gradients [165, 260]. However, no such transport problem is solved. In return, a correction of the turbulent viscosity is introduced with a blending factor F_2:

$$\nu_t = \frac{0.31\,k}{\max\left(0.31\,\omega,\, \sqrt{2\,\overline{S_{ij}}\,\overline{S_{ij}}}\,F_2\right)}\,, \tag{2.16}$$

$$F_2 = \tanh\left[\max\left(2\frac{\sqrt{k}}{\beta^*\,\omega\,l_\mathrm{w}};\, \frac{500\,\nu}{l_\mathrm{w}^2\,\omega}\right)^2\right]. \tag{2.17}$$

Boundary and initial conditions

The underlying k–ω model is a so-called low Reynolds model. In contrast to standard k–ε models, it holds its validity in the boundary layer of the flow without further corrections. Here, the Reynolds number refers to the viscous sublayer, where velocities are low to obey the no-slip condition ($v_i = 0$) at the wall. The integration through the viscous sublayer is necessary to estimate quantities, such as friction or heat transfer coefficients, accurately. From the no-slip condition, it can be concluded $k = 0\,\mathrm{m}^2\,\mathrm{s}^{-2}$ for the turbulent kinetic energy at the boundary. Taking the limit of Eq. (2.13) for the normal wall distance, the resulting equation is fulfilled for

$$\lim_{l_\mathrm{w}\to 0} \omega = \frac{6\,\mu}{\rho\,\tilde{\beta}\,l_\mathrm{w}^2}\,, \tag{2.18}$$

where l_w is the generalized normal wall distance. Accurate solutions employing the low Reynolds approach require the dimensionless distance $l_\mathrm{w}^+ = \rho\,v_\tau\,l_\mathrm{w}/\mu$ to be close to unity, where v_τ is the friction velocity [46]. At inlets, the values of k and ω can be estimated

$$k = \frac{3}{2}(U I_{\mathrm{T}})^2 \,, \tag{2.19}$$

$$\omega = \frac{\sqrt{k}}{\beta^{*1/4} L_{\mathrm{T}}} \,, \tag{2.20}$$

where I_{T} is the turbulent intensity and L_{T} is a turbulent length scale. For fully turbulent channel flows one can estimate $I_{\mathrm{T}} \approx 5\text{–}10\%$ and $L_{\mathrm{T}} \approx 0.07L$, where L is the channel width [46, 82]. The initial values can be estimated with approximate mixing length approaches; for example, from [46, 150]

$$k_0 = \left(\frac{\mu}{\rho\, L_{\mathrm{ref}}}\right)^2 \,, \tag{2.21}$$

$$\omega_0 = \frac{\sqrt{k_0}}{L_{\mathrm{ref}}} \,, \tag{2.22}$$

where L_{ref} is chosen to be the shortest side of the geometry bounding box [46].

Applicability to compressible, non-isothermal and transient fluid flow problems

In general, eddy viscosity models are plagued by several known problems, round-/plane-jet or stagnation point anomaly, to name a few [260]. Considering the application of a convection oven, free stream jets from the inlets, favorable and adverse pressure gradients during flow over food items, and impingement on walls are to be expected. Nonetheless, a variant of the RANS approach is employed in this work. Previous comparisons with empirical data have shown that the k–ω SST model provides the most accurate behavior compared to other eddy viscosity models in the context of food drying [65]. In this spirit, this thesis solves several standard test cases in Sec. 4.3 as a confidence-building measure.

RANS-equations equivalents for compressible fluid flow can be derived with slight modifications. It involves taking a Favre (mass) average of the compressible Navier–Stokes equations. This simplifies the derivation mathematically and yields a similar structure for the Reynolds stress tensor and all subsequent turbulent quantities [260]. The k–ω model only needs minor adjustments to be applicable for compressible problems, such as a multiplication with ρ of ν, ν_{T}, and k/ω in Eq. (2.12) and Eq. (2.13), whereas the closure coefficients remain identical to the incompressible case [260]. From the analogy between momentum and heat transfer, the supplementary turbulent heat-flux vector can be derived for the energy equation

$$q_{\mathrm{t},i} = -\frac{\mu_{\mathrm{t}}\, c_p}{Pr_{\mathrm{t}}} \frac{\partial \overline{T}}{\partial x_i} \,, \tag{2.23}$$

where Pr_{t} is the turbulent Prandtl number [260]. It can be described reasonably well with the Kays–Crawford model (see [138] for more information).

For transient flow scenarios, the mean quantities can generally vary over time. The standard split can be replaced by an ensemble average and again yields very similar equations to the RANS equations. The time step of the simulation is required to be large compared to the lower turbulent time scales, but small compared to the time scale of the dominant coherent structures that are to be resolved (e.g., of a vortex street). Although unsteady RANS (URANS) today does not stand on the most solid theoretical foundations, it is practiced frequently with satisfactory results. The more sophisticated, fully transient resolution of large eddies, as practiced in large eddy simulations, has considerable mesh and time step requirements. The resulting size of the discretized model and the required resolution of long physical time spans with sufficiently small time steps lie outside the computing power at hand.

2.2. Heat transfer

This thesis considers three heat transfer mechanisms inside a convection oven: conduction, convection and thermal radiation. Conduction and convection are inherently covered within the non-isothermal formulation of the Navier–Stokes equations. Fourier's law models the conduction (Eq. (2.4)). Natural convection is covered by the inclusion of the body force term $\rho\, g_i$ in Eq. (2.2) and forced convection can be related to the second term in Eq. (2.3). When evaluating heat fluxes at a boundary, the effects of conduction and convection are, in some sense, lumped. The fluid flow obeys the no-slip condition at the wall. Hence, essentially, the fluid's heat transfer is pure conduction. However, the effective heat flux is strongly influenced by the fluid's bulk speed and accompanying, possibly turbulent mixing in the boundary layer. Referencing the convective heat flux at a fluid boundary includes the effect of conduction naturally.

2.2.1. Conjugate heat transfer

Within the CFD community, conjugate heat transfer typically stands for the coupled solution of the energy equation for both liquid and solid domains of a problem. Occasionally, it is convenient to recast the total enthalpy equation in terms of temperature. COMSOL Multiphysics, the employed finite element solver within this work, solves the non-conservative form of the energy equation, as the total enthalpy is claimed to be prone to numerical oscillations [48]. The recast of Eq. (2.3) to a non-conservative form for temperature employs a variant of the Gibbs fundamental equation [11]

$$\mathrm{d}h = c_p\,\mathrm{d}T + \frac{1}{\rho}\left[1 + \frac{T}{\rho}\left(\frac{\partial \rho}{\partial T}\right)_p\right]\mathrm{d}p\,, \tag{2.24}$$

and invokes Eq. (2.1) to furnish

$$\rho\, c_p\,\frac{\mathrm{D}T}{\mathrm{D}t} = \beta\, T\,\frac{\mathrm{D}p}{\mathrm{D}t} + \frac{\partial(\tau_{ij}\, v_j)}{\partial x_k} + \frac{\partial}{\partial x_k}\left(\kappa\,\frac{\partial T}{\partial x_k}\right)\,, \tag{2.25}$$

where $\beta = -\frac{1}{\rho}\left(\frac{\partial\rho}{\partial T}\right)_p$ is the bulk expansion coefficient and $\frac{\mathrm{D}}{\mathrm{D}t}$ is again the material derivative [19, 170]. For a conjugate problem, such as the introductory example of Fig. 2.1, continuity of temperature T and normal heat fluxes q at a fluid–solid interface $\Gamma_{\text{porous}} \equiv \Gamma_{\text{interf}}$ reads

$$T_{\text{porous}}(x_i, t) = T_{\text{cavity}}(x_i, t)\,, \tag{2.26}$$

$$q_{\text{porous}}(x_i, t) = -q_{\text{cavity}}(x_i, t)\,. \tag{2.27}$$

Numerically solving the resulting coupled system requires stabilization methods that are discussed in Sec. 3.1.2. Note that food heating in a convection oven can be considered a particular variant of conjugate heat transfer, as the foodstuff is not modeled as a purely solid, but as a porous object. Unique forms of Eq. (2.25) are derived in the context of food-specific models in Sec. 2.3. Another particularity of this work is that the heat flux q_{cavity} at the fluid–solid interface also comprises contributions by surface-to-surface radiation. The following section introduces its foundations.

2.2.2. Thermal radiation

Thermal radiation represents the third mode of heat transfer, in addition to convection and conduction. Every body with a temperature T emits and absorbs electromagnetic radiation. For an ideal black body, the total hemispherical emissive power E_{b} ($\mathrm{W\,m^{-2}}$) follows from Stefan–Boltzmann law:

$$E_{\text{b}} = \int_0^\infty E_{\text{b},\lambda}(\lambda^*)\;\mathrm{d}\lambda^* = \sigma T^4\,, \tag{2.28}$$

where $E_{\text{b},\lambda}(\lambda)$ is the spectral emissive power distribution following Planck's law, λ is the wavelength, and σ is the Stefan–Boltzmann constant [11]. The multiplication of E_{b} with an emissivity $\epsilon\,(T, \lambda)$ accounts for the observation that natural bodies emit with a reduced emissive power distribution owing to surface and material properties. Grey bodies represent the conceptual simplification that the deviation from a black body does not depend on the wavelength λ. Incident radiation can be absorbed, reflected or transmitted. For the respective fractions of energy, a conservation reads $\mathcal{A} + \mathcal{R} + \mathcal{T} = 1$, where the fractions are termed absorptivity $\mathcal{A}$, reflectivity $\mathcal{R}$ and transmissivity $\mathcal{T}$. Opaque surfaces do not transmit electromagnetic waves ($\mathcal{T} = 0$). Kirchhoff's law states $\mathcal{A} = \epsilon$ [128]. Hence, the bodies absorb and emit the same fraction of energy of E_{b}.

In the absence of a participating medium, a conservation equation for the net radiative heat flux q_{rad} between participating surfaces can be derived. Consider a surface m with a temperature T. Let G_m ($\mathrm{W\,m^{-2}}$) be the irradiation, the incoming radiative heat flux from all other surfaces. J_m ($\mathrm{W\,m^{-2}}$) is the radiosity, the total radiative heat flux leaving the surface

$$J_m = \epsilon_m\, E_{\text{b},m} + \mathcal{R}_m\, G_m\,, \tag{2.29}$$

where the first term is the grey body emissive power and $\mathcal{R}_m$ is the fraction of irradiation that is diffusely reflected by the surface. The irradiation G_m on the surface m again depends on the radiosity of all other surfaces. The fraction of the emitted energy of a surface j that reaches surface m is represented by a view factor F_{jm}. For view factors, the reciprocity relation

$$A_j\, F_{jm} = A_m\, F_{mj} \tag{2.30}$$

holds [128].

Coming back to the derivation of a conservation equation, the total energy $Q_{m,\text{in}}$ (W) irradiated on m by all other surfaces reads

$$Q_{m,\text{in}} = \sum_{j=1}^{N} F_{jm}\, Q_{j,\text{out}} \tag{2.31}$$

$$\Leftrightarrow A_m\, G_m = \sum_{j=1}^{N} A_j\, F_{jm}\, J_j\,. \tag{2.32}$$

Note that this case also includes self-irradiation of a concave surface m. Applying Eq. (2.30) yields

$$G_m = \sum_{j=1}^{N} F_{mj}\, J_j\,. \tag{2.33}$$

Inserting Eq. (2.33) in Eq. (2.29) results in a linear system of equations

$$\boldsymbol{F}\boldsymbol{J} = \boldsymbol{E}\,, \tag{2.34}$$

that can be solved with conventional numerical methods. The derived procedure to obtain the radiative heat flux at the surface is sometimes referred to as the radiosity method [45]. The difference between irradiation and radiosity is the net incoming radiative heat flux

$$q_{m,\text{rad}} = G_m - J_m = G_m - \epsilon_m\, E_{\text{b},m} - \mathcal{R}_m\, G_m\,. \tag{2.35}$$

Applying the conservation relation $\mathcal{A}_m = 1 - \mathcal{R}_m$ and Kirchhoff's law $\mathcal{A} = \epsilon$ yields

$$q_{m,\text{rad}} = \mathcal{A}_m\, G_m - \epsilon_m\, E_{\text{b},m} = \epsilon_m \left(G_m - E_{\text{b},m}\right). \tag{2.36}$$

The found relation for $q_{m,\text{rad}}$ is included in the boundary condition of the energy conservation equation (Eq. (2.25)).

2.2.3. Moist air and evaporation

The thermal processing of food often induces accelerated evaporation of water stored in the food. It requires the calculation of partial pressures and the vapor's fraction in the food and in the surrounding air for exact modeling. Consider the imaginative experiment of a vacuum chamber that is partially filled with water. At any temperature above absolute zero, molecules start to overcome cohesion forces and surface tension of the liquid phase owing to increased (molecular) motion. Vapor, denoted with index v, is called the gaseous phase of water that is formed in the vacuum chamber. At thermal equilibrium, one can measure the saturation water vapor pressure $p_{\text{v,sat}}(T)$ in the gas phase. The saturation pressure can be derived from the Clausius–Clapeyron equation for water vapor. Alternatively, various approximation equations have been derived, such as the Magnus or Goff–Gratch equation.

Resuming the imaginative experiment, this time for multiple components, the effective pressure of the gaseous phase is the sum of the partial pressures of the individual components. At atmospheric pressures, air–steam mixtures follow the Gibbs–Dalton law closely [226]:

$$p_{\text{tot}} = p_{\text{air,partial}} + p_{\text{v,partial}} \,. \tag{2.37}$$

Note that a component's partial pressure differs from its saturation vapor pressure. Raoult's law relates the former with the latter:

$$p_{\text{k,partial}} = \chi_{\text{k}} \, p_{\text{k,sat}} \,, \tag{2.38}$$

where $p_{\text{k,partial}}$ is the partial pressure of the component k in the gaseous mixture, $p_{\text{k,sat}}$ is the saturation vapor pressure of the pure component k, and χ_{k} is the mole fraction of the component k [187]. For better readability of the forthcoming formulae, the index partial is omitted, and only saturated pressures are marked with an index sat.

It is often convenient to relate partial pressures of components to their mass, mole and volume fractions in the mixture. The ideal gas equations for dry air and water vapor (k $\in \{\text{air}, \text{v}\}$) reads

$$p_{\text{k}} V = n_{\text{k}} \, R T \,, \tag{2.39}$$

where n_{k} is the amount of substance (mol), R is the universal gas constant and V is volume. Dividing the ideal gas equation for air by the summation of the equations for air and water vapor yields [226]

$$\frac{p_{\text{air}}}{p_{\text{air}} + p_{\text{v}}} = \frac{n_{\text{air}}}{n_{\text{air}} + n_{\text{v}}} = \chi_{\text{air}} \,, \tag{2.40}$$

where the right-hand side equals the definition of mole fracture χ_{air}. The mole fraction of a component is now related to its partial pressure and the total pressure of the mixture. The mass fraction of a component can be related to its mole fraction as

$$\omega_{\text{k}} = \frac{m_{\text{k}}}{m_{\text{tot}}} = \frac{n_{\text{k}} \, M_{\text{k}}}{\sum_{\text{i}} n_{\text{i}} \, M_{\text{i}}} \,, \tag{2.41}$$

where m_{k} is the respective mass of a component, m_{tot} is the effective mass of the mixture, M_{k}

is the molar weight of a component, an N is the total number of components. Expanding and employing $n_\mathrm{i}/\sum_\mathrm{j} n_\mathrm{j} = \chi_\mathrm{i}$ yields

$$\omega_\mathrm{k} = \frac{n_\mathrm{k}\, M_\mathrm{k}}{\sum_\mathrm{j} n_\mathrm{j}} \frac{\sum_\mathrm{j} n_\mathrm{j}}{\sum_\mathrm{i} n_\mathrm{i}\, M_\mathrm{i}} = \frac{\chi_\mathrm{k}\, M_\mathrm{k}}{\sum_\mathrm{i} \chi_\mathrm{i}\, M_\mathrm{i}} \,. \tag{2.42}$$

The molar concentration c_k ($\mathrm{mol\,m^{-3}}$) of a component can be derived from its mass fraction as

$$c_\mathrm{k} = \frac{n_\mathrm{k}}{V_\mathrm{tot}} = \frac{m_\mathrm{k}/M_\mathrm{k}}{\sum_\mathrm{i} m_\mathrm{i}/\rho_\mathrm{tot}} = \omega_\mathrm{k} \frac{\rho_\mathrm{tot}}{M_\mathrm{k}} \,, \tag{2.43}$$

and it can be easily transformed to a mass concentration ($\mathrm{kg\,m^{-3}}$) when M_k is omitted. The volume fraction of a component is defined as

$$\phi_\mathrm{k} = \frac{V_\mathrm{k}}{V_\mathrm{tot}} = \frac{m_\mathrm{k}/\rho_\mathrm{k}}{m_\mathrm{tot}/\rho_\mathrm{tot}} = \omega_\mathrm{k} \frac{\rho_\mathrm{tot}}{\rho_\mathrm{k}} \,. \tag{2.44}$$

At a certain temperature and pressure, the relative humidity of the air can be given as the ratio of the mole fraction of water vapor in the current air sample to the mole fraction in a saturated air sample [226]:

$$\mathrm{RH} = \frac{\chi_\mathrm{v}}{\chi_\mathrm{v,sat}} = \frac{p_\mathrm{v}}{p_\mathrm{v,sat}} \,, \tag{2.45}$$

where the recast is accomplished by applying Eq. (2.40).

2.3. Porous media multiphase modeling of thermal food processing

The previous sections summarize the principles of non-isothermal flow, radiation and moist air. Their physical effects are required to model the thermal processing environment (e.g., a convection oven). This section focuses on the physical modeling of thermal food processing of the foodstuff itself. After giving some classifications, definitions and general assumptions, two models for the thermal processing of potatoes and chicken meat are introduced in detail.

Definitions and categorizations in the context of thermal food processing

One can identify four major heating modes in conventional thermal processing of food: using hot air, steam, thermal radiation, or microwave radiation [57]. This work's scope lies in heating with hot air, which also involves thermal radiation. Whereas a roasting process implies the dry heating of food with an open flame (e.g., in a barbecue), broiling corresponds to employing more controlled heat sources (e.g., electrical heating coils or gas burners). During roasting or broiling, the heat intake is realized mainly through thermal radiation of the energy source from one direction. It requires the process or operator to turn the food. Dominant heat input from convection is referred to as baking [57].

Generally, the history (or trajectory) of heat input into the food influences various parameters. A temperature rise induces enhanced evaporation and moisture changes, mechanical stress (shrinkage, swelling), and variation in electro-dynamical and thermo-physical properties and biochemical changes [57]. One can subdivide primary and secondary quantities of interest. The former are temperature, pressure, moisture and vapor concentration, which can be obtained from models involving PDEs. Secondary quantities are sensory or safety-related properties, such as texture, color, flavor (created by enzymatic reactions, caramelization, and Maillard reactions), or the inactivation rates of organisms causing foodborne diseases (e.g., *Salmonella typhimurium*, *Listeria monocytogenes* or *Escherichia coli* O157:H7) [6, 71]. Secondary properties can be modeled as temperature or moisture-dependent analytical formulas or ODEs [167, 195, 249]. The relevant models to this work are introduced at the end of this section.

Modeling food as porous media

The modeling of food processing with porous media approaches can be traced back to the second half of the last century [32, 87, 160]. One can subdivide phenomenological and mechanistic approaches to model the thermal processing of food. During the advent of numerical methods, thermal processing simulations mainly utilized effective diffusion models. The mass and thermal diffusion rates were adjusted such that simulations matched experimental data [38, 40, 160]. Those so-called phenomenological models have an observed phenomenon as a starting point, and relations are found to reproduce measurable features [53]. In contrast, mechanistic models start from fundamental laws to derive models of an observed phenomenon. A mechanistic framework for treating food as hygroscopic capillary-porous media has been proposed by Datta [53–55]. *Porous media* can be defined as solids with voids that can be filled by a fluid [15, 53, 120]. Heat and mass transfer may occur within the porous medium [19, 53]. *Capillary-porous media* can be characterized by pore sizes that are less than 10^{-7} m [32]. *Hygroscopic materials* do not exclusively have water present in the voids but are also physically bound to the solid matrix. This difference from non-hygroscopic matter implies changes to the water–vapor equilibrium, as the bound water cannot be easily removed from the solid matrix at lower water saturations [53].

The continuum hypothesis allows the treatment of fluids as continuous media, given sufficiently small Knudsen numbers ($Kn < 0.01$) [14, 178, 191]. On the other hand, the interactions of the molecules with solid walls have to be accounted for (Knudsen diffusion) when the mean free path of the molecules is larger than the characteristic lengths of the pores. For soil systems, Knudsen diffusion has been reported to become dominant for permeabilities less than $10^{-14}\,\mathrm{m}^2$ [81], and is usually not accounted for in food models [53–55]. Ni [175] reports permeabilities of $15\text{–}46 \times 10^{-14}\,\mathrm{m}^2$ for meats.

Assumptions and model selection for this work

The upcoming trends of plant-based or insect-based products shift the focus to more or less homogeneous mixtures as the primary food composition. On the other hand, as meats are expected to become rarer and more valuable, processing quality should also be guaranteed here. Hence, this work considers one model for a homogenous foodstuff (potato) and one for a more heterogenous foodstuff (chicken meat). The former, introduced by Datta [53–55], can be considered well-known and has been validated and applied in a multitude of scenarios within the last two decades for convective heating [175], infrared heating [56], microwave heating and drying [102, 147, 149], frying and deep-fat frying [107, 257], rice puffing [101], or vacuum cooling [200].

The employed soft-matter approach for chicken meat, as presented in [228, 229] and recommended in [59], comprises a model for the shrinkage-induced liquid flow, which can be rather contextualized as being phenomenological. This work applies a variant by [196], as the researchers provided matching models for texture and color [195, 198]. Furthermore, the model is representative of popular phenomenological models in the industry owing to more pragmatic modeling approaches [54]. Its analysis and application in the proposed digital twin framework follow the goals of providing industry-applicable research. The explicit shrinkage modeling lies outside this work's scope. Its impact has been demonstrated in [100, 102, 171].

2.3.1. Hygroscopic, capillary-porous media model

As the terms thermal food processing and porous media are now defined, this section presents the theoretical foundations of the modeling framework for hygroscopic, capillary-porous media by Datta [53, 55].

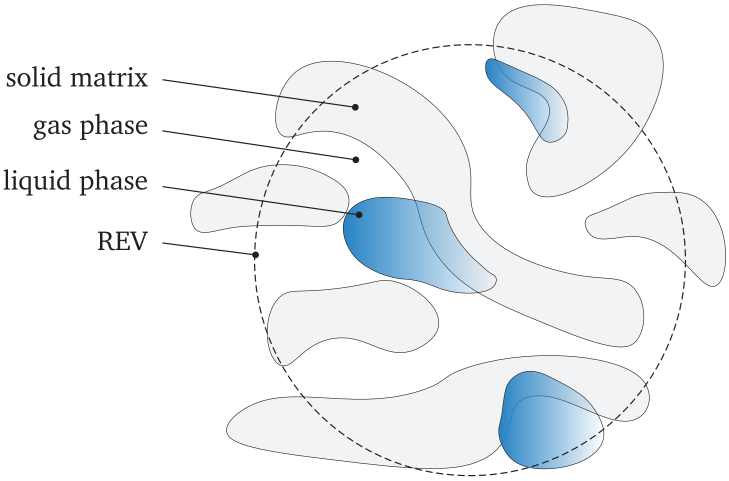

Figure 2.2. Concept of a representative elementary volume (REV) for hygroscopic, capillary-porous media, where water is also bound to the solid matrix.

Simulating fluid flow in exact representations of a porous medium is not feasible, especially on larger domains [14]. Similar to the continuum approach, but on a larger scale, all quantities of interest are averaged on a sufficiently large representative elementary volume (REV) [14, 259], see Fig. 2.2 for an illustration. To formulate the model analogous to non-hygroscopic porous media equations, a constant equivalent porosity

$$\varphi = \varphi_\mathrm{g} + \varphi_\mathrm{w} = \frac{V_\mathrm{g}}{V_\mathrm{tot}} + \frac{V_\mathrm{w}}{V_\mathrm{tot}} \,, \tag{2.46}$$

is introduced as the sum of gas and water porosity. *Porosity* is defined as the ratio of the gas (index g) and water (index w) volumes V_k to the total volume V_tot of the REV. To account for porosity changes caused by thermal processing, equivalent variable water and gas saturations

$$S_\mathrm{w} = \frac{V_\mathrm{w}}{V_\mathrm{w} + V_\mathrm{g}} = \frac{V_\mathrm{w}}{\varphi\, V_\mathrm{tot}}, \tag{2.47}$$

$$S_\mathrm{g} = \frac{V_\mathrm{g}}{V_\mathrm{w} + V_\mathrm{g}} = \frac{V_\mathrm{g}}{\varphi\, V_\mathrm{tot}}, \tag{2.48}$$

are defined. The saturations represent the relative volume fraction of the corresponding fluid in the void, implying $S_\mathrm{w} + S_\mathrm{g} = 1$. The concentrations ($\mathrm{kg\,m^{-3}}$) of water, gas (vapor + air) and vapor (index v) are defined as

$$c_\mathrm{w} = S_\mathrm{w}\, \varphi\, \rho_\mathrm{w} \,, \qquad c_\mathrm{g} = S_\mathrm{g}\, \varphi\, \rho_\mathrm{g} \,, \qquad c_\mathrm{v} = S_\mathrm{g}\, \varphi\, \rho_\mathrm{v} \,, \tag{2.49}$$

where the gas densities are determined employing ideal gas and Dalton's law (Eq. (2.37)). The corresponding mass conservation laws for gas, vapor and water read

$$\frac{\partial c_{\mathrm{g}}}{\partial t} + \frac{\partial J_{i,\mathrm{g}}}{\partial x_i} = \dot{I} \,, \tag{2.50}$$

$$\frac{\partial c_{\mathrm{v}}}{\partial t} + \frac{\partial J_{i,\mathrm{v}}}{\partial x_i} = \dot{I} \,, \tag{2.51}$$

$$\frac{\partial c_{\mathrm{w}}}{\partial t} + \frac{\partial J_{i,\mathrm{w}}}{\partial x_i} = -\dot{I} \,, \tag{2.52}$$

where $J_{i,\mathrm{k}}$ (k $\in$ {g,v,w}) are mass fluxes and $\dot{I}$ is the evaporation rate, which are introduced later.

Given sufficiently small velocities ($Re \ll 1$) in sufficiently small pores, fluid flow in porous media can be modeled with Darcy's law [15, 53, 120, 178] as

$$J_{i,\mathrm{g}} = -\rho_{\mathrm{g}} \frac{k_{\mathrm{g}}}{\mu_{\mathrm{g}}} \left(\frac{\partial p}{\partial x_i} - \rho_{\mathrm{g}} \, g_i \right) , \tag{2.53}$$

where k is permeability, μ is the dynamic viscosity, and p is pressure. This assumption covers most food processing conditions of plant- or animal-based food matter [53]. Observe that Eq. (2.50) can be recast to a PDE for pressure when Eq. (2.53) is inserted, and the ideal gas law is invoked.

The vapor mass flux likewise considers pressure-driven flow and additionally accounts for the binary diffusion of vapor in the gas

$$J_{i,\mathrm{v}} = \underbrace{-\rho_{\mathrm{v}} \frac{k_{\mathrm{g}}}{\mu_{\mathrm{g}}} \left(\frac{\partial p}{\partial x_i} - \rho_{\mathrm{g}} \, g_i \right)}_{\text{Darcy flux}} \underbrace{- \frac{\tilde{c}_{\mathrm{g}}^2}{\rho_{\mathrm{g}}} \, M_{\mathrm{v}} \, M_{\mathrm{a}} \, D_{\text{eff,g}} \, \frac{\partial \chi_{\mathrm{v}}}{\partial x_i}}_{\text{binary flux}}, \tag{2.54}$$

where χ_{v} is the mole fraction of vapor, $\tilde{c}_{\mathrm{g}}$ is the molar concentration of the gas and M_{a} and M_{v} are the molar weights of air and vapor [19], respectively. The effective gas diffusion coefficient $D_{\text{eff,g}} = D_{\text{va}}(S_{\mathrm{g}} \, \varphi)^{4/3}$ accounts for the binary diffusion in the porous cavities, which differs from the binary diffusion in free air $D_{\text{va}} = 2.6 \times 10^{-5} \, \mathrm{m}^2 \, \mathrm{s}^{-1}$ [175].

The unsaturated capillary flow of water tends to move from locations with higher concentrations to ones of lower concentrations. The capillary attraction p_{cap} of the solid counteracts gas pressure-driven flow, which is reflected in the water mass flux as

$$\begin{aligned}
J_{i,\mathrm{w}} &= -\rho_\mathrm{w} \frac{k_\mathrm{w}}{\mu_\mathrm{w}} \left(\frac{\partial p_\mathrm{w}}{\partial x_i} - \rho_\mathrm{w}\, g_i \right) \\
&= -\rho_\mathrm{w} \frac{k_\mathrm{w}}{\mu_\mathrm{w}} \left(\frac{\partial}{\partial x_i} \left(p_\mathrm{g} - p_\mathrm{cap}(c_\mathrm{w}, T) \right) - \rho_\mathrm{w}\, g_i \right) \\
&= -\rho_\mathrm{w} \frac{k_\mathrm{w}}{\mu_\mathrm{w}} \left(\frac{\partial p_\mathrm{g}}{\partial x_i} - \frac{\partial p_\mathrm{cap}}{\partial c_\mathrm{w}} \frac{\partial c_\mathrm{w}}{\partial x_i} - \frac{\partial p_\mathrm{cap}}{\partial T} \frac{\partial T}{\partial x_i} - \rho_\mathrm{w}\, g_i \right) \\
&= \underbrace{-\rho_\mathrm{w} \frac{k_\mathrm{w}}{\mu_\mathrm{w}} \left(\frac{\partial p_\mathrm{g}}{\partial x_i} - \rho_\mathrm{w}\, g_i \right)}_{\text{Darcy flux}} \underbrace{- D_{\mathrm{w},c_\mathrm{w}} \frac{\partial c_w}{\partial x_i}}_{\text{capillary flux}} \underbrace{- D_{\mathrm{w},T} \frac{\partial T}{\partial x_i}}_{\text{Soret effect}} ,
\end{aligned} \tag{2.55}$$

where $D_{\mathrm{w},c_\mathrm{w}}$ is the capillary diffusivity regarding concentration gradients and $D_{\mathrm{w},T}$ is the capillary diffusivity regarding temperature gradients (Soret effect). The latter and gravitational effects are considered negligibly small compared to the remaining driving mechanisms [53]. Thus, they are not accounted for.

The conservation of energy for all phases reads

$$\frac{\partial}{\partial t} \left(c_\mathrm{g}\, h_\mathrm{g} + c_\mathrm{w}\, h_\mathrm{w} + c_\mathrm{s}\, h_\mathrm{s} \right) + \frac{\partial}{\partial x_i} \left(J_{i,\mathrm{g}}\, h_\mathrm{g} + J_{i,\mathrm{w}}\, h_\mathrm{w} \right) = \frac{\partial}{\partial x_i} \left(\kappa_\mathrm{eff} \frac{\partial T}{\partial x_i} \right) , \tag{2.56}$$

where index s denotes the solid matrix. For $c_p = \text{const.}$, the equation can be recast to a non-conservative form for temperature T [175]:

$$(\rho\, c_p)_\mathrm{eff} \frac{\partial T}{\partial t} + \left(J_{i,\mathrm{g}}\, c_{p,\mathrm{g}} + J_{i,\mathrm{w}}\, c_{p,\mathrm{w}} \right) \frac{\partial T}{\partial x_i} = \frac{\partial}{\partial x_i} \left(\kappa_\mathrm{eff} \frac{\partial T}{\partial x_i} \right) - H_\mathrm{evap}\, \dot{I} , \tag{2.57}$$

where $H_\mathrm{evap} = 2.435 \times 10^6\,\mathrm{J\,kg^{-1}}$ is the latent heat of evaporation, and effective transport coefficients are averaged as

$$(\rho\, c_p)_\mathrm{eff} = \rho_\mathrm{s}\, (1 - \varphi)\, c_{p,\mathrm{s}} + \rho_\mathrm{g}\, S_\mathrm{g}\, \varphi\, c_{p,\mathrm{g}} + \rho_\mathrm{w}\, S_\mathrm{w}\, \varphi\, c_{p,\mathrm{w}} , \tag{2.58}$$

$$\kappa_\mathrm{eff} = \kappa_\mathrm{s}\, (1 - \varphi) + \kappa_\mathrm{g}\, S_\mathrm{g}\, \varphi + \kappa_\mathrm{w}\, S_\mathrm{w}\, \varphi . \tag{2.59}$$

Closure of the boundary value problem of mass and energy conservation is furnished with the provision of boundary and initial conditions together with a non-equilibrium formulation for distributed evaporation [20, 53]

$$\dot{I} = K_\mathrm{evap}\, (p_\mathrm{v,equ} - p_\mathrm{v}) \frac{M_\mathrm{v}}{R\, T}\, S_\mathrm{g}\, \varphi , \tag{2.60}$$

where the evaporation constant K_evap can be interpreted as the inverse of the time to reach thermodynamical equilibrium in a REV [107]. This explicit formulation of an evaporation rate enables a facilitated implementation in transport equations of commercial software [102].

Water activity

The vapor pressure at thermal equilibrium $p_{\text{v,equ}}$ in Eq. (2.60) differs from the vapor saturation pressure $p_{\text{v,sat}}$. A fraction of a food matrix's total amount of water is firmly chemically bound [246]. Similar to the relative humidity, water activity a_{w} is a measure of how much water is available (or "active") to participate in the exchange with the food's surroundings. It is defined as the ratio of the vapor pressure of food in equilibrium with its surroundings to the saturated vapor pressure of distilled water

$$a_{\text{w}} = \frac{p_{\text{v,equ}}}{p_{\text{v,sat}}} \,. \tag{2.61}$$

Water activity is usually measured experimentally [13]. It is often given as a function of moisture concentration on a dry basis

$$M_{\text{db}} = \frac{m_{\text{w}}}{m_{\text{s}}} = \frac{\omega_{\text{w}}}{1-\omega_{\text{w}}} \,. \tag{2.62}$$

Ratti derived an empirical relationship for potatoes [202], which is employed in the context of this work:

$$\ln \frac{p_{\text{v,equ}}}{p_{\text{v,sat}}} = -0.0267\, M_{\text{db}}^{-1.656} + 0.0107\, \exp(-1.287\, M_{\text{db}})\, M_{\text{db}}^{1.513}\, \ln p_{\text{v,sat}} \,. \tag{2.63}$$

Permeability and capillary diffusivity

The permeability k of a porous medium describes its ability to allow for fluid flow through the porous matrix. One can subdivide contributions of the solid properties as intrinsic permeability k_{in} and of the fluid as relative permeability k_{rel} [14]: $k = k_{\text{in}}\, k_{\text{rel}}$. For food matter, there has been limited success in relating intrinsic permeabilities to the structure of the material [54, 99], and the Datta group typically chooses $k_{\text{g,in}} = 5 \times 10^{-14}\,\text{m}^2$ for gas permeability at arid conditions and liquid permeability $k_{\text{w,in}} = 10 \times 10^{-14}\,\text{m}^2$ at very wet stages since the early works by Ni [175]. Common analytical relations for the relative permeabilities of gas and water are

$$k_{\text{g,rel}} = \begin{cases} 1 - 1.1\, S_{\text{w}}, & \text{if } S_{\text{w}} < 1/1.1 \\ 0, & \text{if } S_{\text{w}} \geq 1/1.1 \end{cases} \tag{2.64}$$

$$k_{\text{w,rel}} = \begin{cases} \left(\frac{S_{\text{w}} - S_{\text{ir}}}{1 - S_{\text{ir}}}\right)^3, & \text{if } S_{\text{w}} > S_{\text{ir}} \\ 0, & \text{if } S_{\text{w}} \leq S_{\text{ir}} \end{cases} \tag{2.65}$$

and were borrowed by Ni and Datta for food matter [54, 175], where $S_{\text{ir}} = 0.09$ is the irreducible moisture saturation.

As discussed in this subsection, the capillary diffusivity of water is not a diffusion process in the

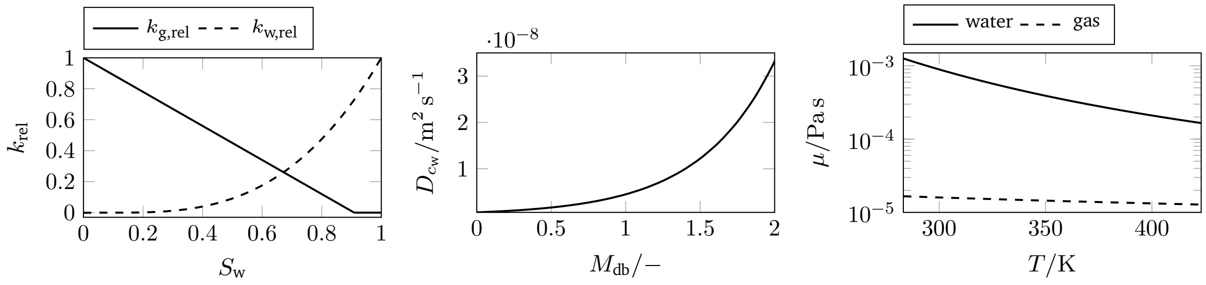

(a) Relative permeabilities. **(b)** Capillary diffusivity. **(c)** Dynamic viscosities.

Figure 2.3. Variable relative permeabilities [54, 175], capillary diffusivity [54, 175] and dynamic viscosities [164].

classical sense but a flow of water owing to capillary forces. In [175], the semi-empirical relation

$$D_{\text{w},c_{\text{w}}} = 1 \times 10^{-8} \exp\left(-2.8 + 2.0\, M_{\text{db}}\right)\ \text{m}^2\,\text{s}^{-1} \tag{2.66}$$

was derived by comparisons with experimental data of effective moisture diffusivities at very wet states, where vapor diffusion becomes negligible. Figure 2.3 illustrates the relations for permeability and capillary diffusivity in Eq. (2.64)–(2.66) and the dynamic viscosities required in Darcy's law. The reader is referred to works by Datta and Ni [53, 55, 175] for further details.

2.3.2. Soft-matter model for meats

The soft-matter approach has been successfully applied to model the thermal processing of meats [83, 84, 196, 228]. It assumes a water-saturated foodstuff, the absence of a gas phase, and capillary pressure is considered zero [59]. The governing equations are the conservation of mass and energy

$$\frac{\partial c_{\text{w}}}{\partial t} + \frac{\partial}{\partial x_i}\left(c_{\text{w}}\, u_i\right) = \frac{\partial}{\partial x_i}\left(D_{\text{w,cb}}\, \frac{\partial c_{\text{w}}}{\partial x_i}\right) , \tag{2.67}$$

$$\rho_{\text{cb}}\, c_{p,\text{cb}}\, \frac{\partial T}{\partial t} + \rho_{\text{w}}\, c_{p,\text{w}}\, u_i\, \frac{\partial T}{\partial x_i} = \frac{\partial}{\partial x_i}\left(\kappa_{ij}\, \frac{\partial T}{\partial x_j}\right) , \tag{2.68}$$

where u_i are water velocities, $D_{\text{w,cb}}$ is the effective water diffusivity, c_p and ρ denote the specific heat capacities and densities. The additional indices w and cb mark the corresponding water parameters and the chicken's effective quantities. The effective specific heat capacity $c_{p,\text{cb}}$ is the mass averaged sum of the components

$$c_{p,\text{cb}} = \sum_{\text{k}} \omega_{\text{k}}\, c_{p,\text{k}} , \tag{2.69}$$

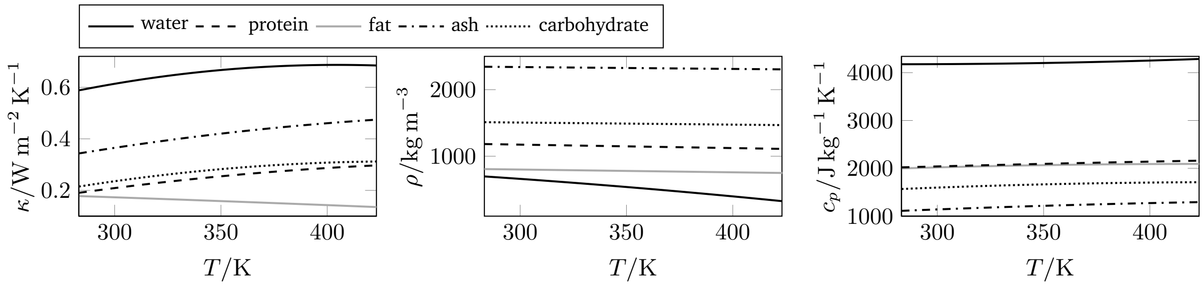

(a) Thermal conductivities. **(b)** Densities. **(c)** Heat capacities.

Figure 2.4. Temperature-dependent transport properties taken from [6, 42].

where ω_k (k $\in$ {ash, protein, fat, water}) is the respective mass fraction of a component [6]. The orthotropic thermal conductivity of the fillet fibers is accounted for with the parallel and serial models. The effective thermal conductivities in parallel and perpendicular directions with respect to the main fiber direction are

$$\kappa_\mathrm{para} = \sum_\mathrm{k} \phi_\mathrm{k}\, \kappa_\mathrm{k} \,, \tag{2.70}$$

$$\frac{1}{\kappa_\mathrm{perp}} = \sum_\mathrm{k} \frac{\phi_\mathrm{k}}{\kappa_\mathrm{k}} \,, \tag{2.71}$$

where ϕ_k is the respective volume fraction of a component. The specific heat capacities $c_{p,\mathrm{k}}$ and thermal conductivities κ_k of the food components can be modeled with empirical temperature-dependent formulas from [6, 42]. Figure 2.4 illustrates the temperature-dependence of the transport properties.

The boundary conditions of the transport equations are governed by the rate of water evaporation $\dot{m}_\mathrm{evap}$ (kg m^{-2} s^{-1}) and the heat intake modeled with a constant heat transfer coefficient α_tot (W m^{-2} K^{-1}):

$$\boldsymbol{N}_\mathrm{w}|_\mathrm{surf} = -\dot{m}_\mathrm{evap} \,, \tag{2.72}$$

$$\boldsymbol{N}_\mathrm{e}|_\mathrm{surf} = \alpha_\mathrm{tot}\,(T_\mathrm{oven} - T_\mathrm{surf}) - \dot{m}_\mathrm{evap}\, H_\mathrm{evap} \,, \tag{2.73}$$

where H_evap is the latent heat of evaporation, $\boldsymbol{N}_\mathrm{k}$(k $\in$ {w,e}) are the normal, total water and energy fluxes at the boundary, and $\cdot|_\mathrm{surf}$ is an evaluation of the former in the normal direction of the boundary. The evaporation rate $\dot{m}_\mathrm{evap}$ can be derived from the driving difference of the water-vapor concentration in the oven $c_\mathrm{v,oven}$ (kg m^{-3}) and the water-vapor concentration on the surface $c_\mathrm{v,surf}$ (kg m^{-3}) [226] as

$$\dot{m}_\mathrm{evap} = \beta_\mathrm{tot}\left(c_\mathrm{v,surf} - c_\mathrm{v,oven}\right) , \tag{2.74}$$

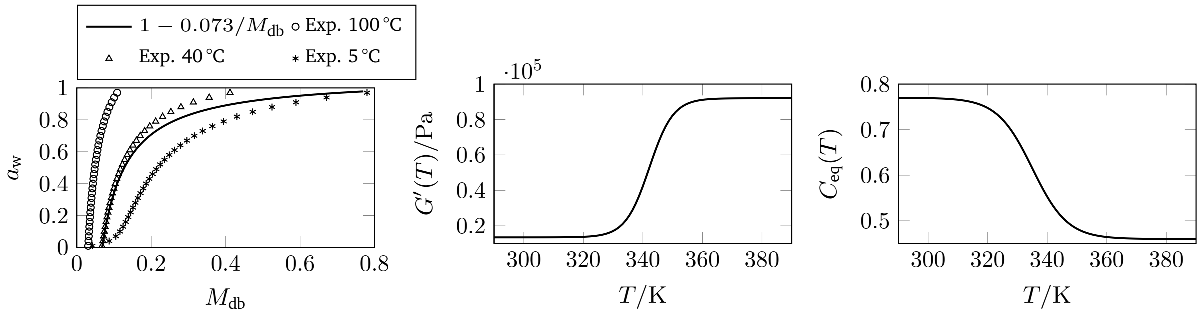

(a) Water activity. **(b)** Storage modulus. **(c)** Water holding capacity.

Figure 2.5. Modeled parameters in the swelling pressure model in [196]. Empirical data (markers) by [205] is added for comparison.

where β_{tot} is the total mass transfer coefficient. Invoking the ideal gas law for the vapor concentration at the food surface and relating the partial vapor pressure to the product of water activity a_{w} and saturated vapor pressures $p_{\text{v,sat}}(T)$ yields

$$c_{\text{v,surf}} = \frac{M_{\text{w}}}{R\,T_{\text{surf}}}\,p_{\text{v,surf}} = \frac{M_{\text{w}}}{R\,T_{\text{surf}}}\,a_{\text{w}}\,p_{\text{v,sat}}(T_{\text{surf}})\,, \tag{2.75}$$

where R is the universal gas constant. The water activity of the chicken breast is modeled as an empirical formula by [196, 228]. Figure 2.5a compares the employed empirical formulation with experimental data of Rimkate [205]. The water vapor concentration in the oven is derived from the measurements of the vapor mass fraction in ambient air, which can be expressed as a mass concentration with Eq. (2.43), resulting in

$$c_{\text{v,oven}} = \frac{M_{\text{w}}\,p_{\text{atm}}}{R\,T_{\text{oven}}}\,\omega_{\text{v}}\,, \tag{2.76}$$

where p_{atm} is the atmospheric pressure under standard conditions.

The total mass transfer coefficient β_{tot} is determined with a serial model

$$\beta_{\text{tot}} = \frac{1}{\frac{1}{\beta_{\text{ext}}} + \frac{1}{\beta_{\text{skin}}}}\,. \tag{2.77}$$

The external mass transfer coefficient is determined from the Chilton–Colburn relation [196, 227, 228]:

$$\beta_{\text{ext}} = \frac{\alpha_{\text{tot}}}{\rho_{\text{air}}\,c_{p,\text{air}}}\,Le^{-2/3}\,, \quad Le = \frac{Sc}{Pr} \approx 0.91\,, \tag{2.78}$$

where Le, Sc and Pr are the Lewis, Schmidt, and Prandtl numbers. All quantities are evaluated for air at a film temperature $T_{\text{film}} = (T_{\text{surf}} + T_{\text{oven}})/2$. The skin coefficient

$$\beta_{\text{skin}} = 0.04\, \omega_{\text{w}}^{b(T)} \,, \tag{2.79}$$

accounts for surface resistance to evaporation owing to the skin of the food product [6, 196, 227]. A function $b(T) \in [3, 5]$ modifies the exponent to lower values when the boiling temperature is reached [229]. As will be seen later, the serial model for the total mass transfer coefficient gives dominant weight to β_{skin} for small ω_{w} (dry surfaces) and reduces the total mass transfer coefficient to a value considerably less than β_{ext}. The skin coefficient β_{skin} is a modeled quantity, that is discussed more in detail in Sec. 4.1.2.

Swelling pressure approach

Darcy's law is used to relate the velocity u_i to a pressure gradient:

$$u_i = -\frac{k}{\mu_w} \frac{\partial p}{\partial x_i} \,, \tag{2.80}$$

where k is the permeability of the food matrix and μ_{w} is the dynamic viscosity of water. The permeability of chicken meat was experimentally determined by Datta [52] to be $k \in [1 \times 10^{-17}, 1 \times 10^{-19}]\,\text{m}^2$. Feyissa [84] tested values of $k \in [1 \times 10^{-16}, 1 \times 10^{-17}]\,\text{m}^2$ and suggested $k = 1 \times 10^{-17}\,\text{m}^2$ as a suitable value for raw meat. Rabeler [196] employs $k = 3 \times 10^{-17}\,\text{m}^2$ for a simulation of chicken meat.

Protein denaturation induces shrinkage during a roasting process, which results in a substantial water loss at the surface [243]. A similar phenomenon models the Flory–Rehner theory [86], which describes the swelling or shrinking in polymer gels [193, 228]. Similar to the derivation of the capillary diffusivity in Eq. (2.55), the pressure mechanisms acting on the water read

$$p_{\text{w}} = p_{\text{g}} - p_{\text{cap}} + p_{\text{swell}} \,, \tag{2.81}$$

where p_{swell} is the newly introduced swelling (and shrinking) pressure. Assuming a nearly saturated state, the contributions of capillarity and gas pressure can be neglected [53, 59]. The adaptation of the theory for thermal processing of meats models p_{swell} in relation to a driving difference of water concentrations [84, 196, 228, 229] as

$$p = G'(T) \left(C - C_{\text{eq}}(T)\right) \,. \tag{2.82}$$

The induced pressure is proportional to the difference between the local water mass fraction $C \equiv \omega_{\text{w}}$ and the equilibrium water mass fraction $C_{\text{eq}}(T)$:

$$C_{\text{eq}}(T) = C_0 - \frac{0.31}{1 + 30\, \exp\left(-0.17\, (T - T_\sigma)\right)} \,, \tag{2.83}$$

Table 2.2. Constants of the thermal processing model for chicken meat from [196].

Parameter	Value	Parameter	Value
T_σ	$315\,\mathrm{K}$	H_{evap}	$2.3 \times 10^6\,\mathrm{J\,kg^{-1}}$
$\overline{T}$	$342.15\,\mathrm{K}$	G'_0	$13.5 \times 10^3\,\mathrm{Pa}$
ΔT	$4\,\mathrm{K}$	$G'_{\max}$	$92 \times 10^3\,\mathrm{Pa}$
D_{cb}	$3 \times 10^{-10}\,\mathrm{m^2\,s^{-1}}$	a_{w}	$1 - 0.073/M_{\text{db}}$

where C_0 is the initial water mass fraction. The model constants are given in Tab. 2.2 and are taken from [196, 229]. $G'(T)$ is the storage modulus

$$G'(T) = G'_{\max} + \frac{G'_0 - G'_{\max}}{1 + \exp\left(\frac{T - \overline{T}}{\Delta T}\right)}, \tag{2.84}$$

which is a measure of the viscoelastic material elasticity [243]. Both quantities are modeled with sigmoidal functions that were fitted to experimental data [195, 228, 229] (see Fig. 2.5b and Fig. 2.5c for a graphical representation). The required model constants are summarized in Tab. 2.2. For a more extended discussion of the model, the reader is referred to [196, 229].

2.3.3. Sensory quality models

Although taste is, of course, a subjective perception, food science tried to derive objective quantities to characterize it scientifically. Four main properties can be found to describe the quality of food: appearance (e.g., color, size or gloss), flavor (e.g., taste or odor), texture (e.g., tactile sensing of the food or sound), and nutrition (e.g., carbohydrates, fat, protein or minerals) [26]. Obtaining the desired texture determines the perceived value of food (e.g., tough or dry beef sells at a much lower price than tender). As a consequence, the processing of food has to account for sensory attributes that the customer desires. Heating of meat introduces microstructural changes that lead to increased perceived hardness [243]. *Texture profile analysis* (TPA) is an experimental method pioneered by Szczesniak [234] that emulates a chewing motion. Several textural parameters have been derived from the force–time curve that describe the mouthfeel of food in the human mouth during mastication. Table 2.3 summarizes the mechanical characteristics relevant to this work's scope. Chewy, for example, may be defined as *"[t]ending to remain in the mouth without rapidly breaking up or dissolving. Requiring mastication [...]"* and hardness can be described as *"the perceived force required to break the sample into several pieces during the first bite by the molars [...]"* [26].

Besides a change of mechanical properties, the heating of meat induces the change of its color (e.g., from a light rose to white for temperature above 55 °C). The change is related to the denaturation of myoglobin proteins [98]. Further heating induces the Maillard reactions that govern the flavor and browning of meat [33]. The color of meat can be described in standardized color spaces (e.g., the $L^*a^*b^*$ color space defined by [75]). The 3D color space is spanned by the

Table 2.3. Texture parameters derived from texture profile analysis [26, 234].

Mechanical property	Origin	Units	Descriptions
hardness	TPA experiment	N	soft → firm → hard
adhesiveness	TPA experiment	Nm	sticky → tacky → gooey
springiness	TPA experiment	m	
cohesiveness	TPA experiment	-	
→ brittleness	TPA experiment	N	crumbly → crunchy → brittle
→ chewiness	gumminess × springiness	Nm	tender → chewy → tough
→ gumminess	hardness × cohesiveness	N	short → mealy → pasty → gummy

color intensity, type — a^* (varying from green to red), b^* (varying from blue to yellow) — and color brightness L^*.

A general rate law can describe the changes of a sensory quality Q in the form

$$\frac{\partial Q}{\partial t} = -k\, Q^n \,, \tag{2.85}$$

where the reaction rate constant k and the reaction order n have to be adjusted to match experimental data. Arrhenius' law

$$k = k_0 \exp\left(-\frac{E_\mathrm{a}}{R\,T}\right) \,, \tag{2.86}$$

has proven capable to describe a multitude of reaction kinetics [249], where k_0 is the pre-exponential factor, E_a is the activation energy and R is the universal gas constant. A modified rate law that accounts for non-zero equilibrium conditions of the parameters after long process durations has been proposed by [195]:

$$\frac{\partial Q}{\partial t} = k_0 \exp\left(-\frac{E_a}{RT}\right) (Q_\infty - Q)^n \,, \tag{2.87}$$

$$Q_\infty(T) = Q_\mathrm{max} + \frac{Q_0 - Q_\mathrm{max}}{1 + \exp\left(\frac{T-T^*}{\Delta T^*}\right)} \,, \tag{2.88}$$

where Q_0 is the initial quality value, Q_∞ is the final non-zero equilibrium quality value, whereas T^* and ΔT^* are fitting parameters of the sigmoid function. Data of the parameters are given in the validation test case in Sec. 4.1.3.

The description of sensory qualities finalizes the set of PDEs and ODEs employed in modeling thermal food processing within a convection oven. Before the models can be investigated closer in Chapter 4, the following chapter provides the required methods for their numerical simulation.

3. Numerical methods

The previous chapter introduced the physical models to describe thermal food processing inside a convection oven. This chapter provides the numerical methods to solve the model equations and derive the digital twin framework for autonomous thermal food processing. Section 3.1 focuses on the numerical solution of PDEs and ODEs. Then, Sec. 3.2 introduces reduced-order modeling techniques that derive lightweight and yet accurate surrogate models of the multi-physical full-order models.

3.1. Numerical solution of partial and ordinary differential equations

Data-driven reduced-order modeling methods are principally independent of the software in which the problem is modeled and solved. The following section clarifies the choice of modeling software and methods. The fundamentals of the numerical methods for solving PDEs and ODEs are presented thereafter.

3.1.1. Selection of the modeling platform

Developing a conjugate heat and mass transfer model requires the possibility of implementing mechanistic food models. In addition, it must be possible to couple the relevant fields of non-isothermal flow and thermal radiation with those of the thermal food processing model. Historically, finite volume methods were often preferred to solve fluid flow problems because of their inherently conservative properties. Based on a survey within the industry, the commercial software tools ANSYS Fluent and Simcenter STAR-CCM+ are the commercial market leaders for CFD problems [203]. In contrast to Simcenter STAR-CCM+, ANSYS Fluent offers the implementation of user-defined scalar transport equations. However, preliminary tests showed that additionally modeled fluxes, other than those driven from the fluid flow, are identified as "parasitic" and are automatically removed during the solving. ANSYS confirmed this problem upon request but did not elaborate on plans for changes. Datta concluded on food modeling in ANSYS Fluent: *"Some of the complications that need to be addressed for food processing include multiphase capability, coupled liquid and vapor phases (i.e., liquid to vapor and vice versa), and unsaturated (capillary) flow. Adapting a problem having these features to the available formulations in a typical commercial CFD software (e.g., Fluent) is non-trivial"* [54]. Within the open-source domain, OpenFOAM is a potential modeling platform. Considering the number of new couplings and customizations to the solvers *chtMultiRegionFoam*, *viewFactor* and *scalarTransportFoam*, this is considered an endeavor on its own by experts in the field. From the food science perspective, Datta commented in 2007: *"For research purposes, code development from scratch is the preferred route, but it is typically a multi-year project"* [54]. In 2016, he concluded on the choice of modeling platform: *"There has never been a tool as close to the needs of the food process modeling community as is the software COMSOL"* [55]. Not by chance, most of the computational works presented in the literature review were conducted within COMSOL Multiphysics. Indeed, the software distinguishes itself through its high flexibility. Its modules for fluid flow, heat and mass transfer and thermal radiation can be coupled to the user's liking. Moreover, it provides universal modules that allow the implementation of custom PDEs or ODEs. In summary, COMSOL Multiphysics met the requirements of this work and enabled the model developments within reasonable timeframes. It was therefore chosen to be the modeling platform.

COMSOL Multiphysics employs the finite element method (FEM). It is a well-established method to numerically solve boundary value problems, such as the non-isothermal fluid flow, conjugate heat transfer and porous media problems introduced in Sec. 2.1–2.3. However, special attention must be paid to stabilizing the FEM for advection-dominated problems, as discussed in Sec. 3.1.2. The FEM is typically applied to provide a spatial discretization of PDEs, resulting in nonlinear ODE systems in time. Section 3.1.3 outlines the numerical time integration of those systems with explicit Euler, Runge–Kutta, and implicit backward-differencing formulas. Large systems of equations arise from the implicit temporal discretization and the radiosity method for surface-to-surface radiation. Standard numerical solution approaches for systems of equations are briefly discussed in Sec. 3.1.5.

3.1.2. Spatial discretization

The fundamental ideas of the FEM, as presented in this section, are based on standard text books [218, 266, 267], where the reader is referred to for further background reading. The finite element semi-discretization in space of a generic advection–diffusion initial-boundary value problem is demonstrated hereafter. The representative model problem reads

$$\frac{\partial \Phi}{\partial t} + v_i \frac{\partial \Phi}{\partial x_i} = \frac{\partial}{\partial x_i}\left(\kappa \frac{\partial \Phi}{\partial x_i}\right) + S\,, \tag{3.1}$$

where $\Phi(x_i, t)$ is a scalar valued variable, v_i is a divergence-free velocity field, κ some representative diffusion and S is a source term on a problem domain Ω. The initial conditions are $\Phi(x_i, 0) = \Phi^{\mathrm{IC}}(x_i)$ and the time-dependent boundary conditions can be, for example, of Dirichlet or Neumann type

$$\Phi = \Phi^{\Gamma} \quad \text{on} \quad \Gamma_{\mathrm{D}}\,, \tag{3.2}$$

$$-\kappa \frac{\partial \Phi}{\partial x_i}\, n_i = q_{\mathrm{n}}^{\Gamma} \quad \text{on} \quad \Gamma_{\mathrm{N}}\,, \tag{3.3}$$

where Φ^Γ and q_n^Γ are given values of the primary variable or its boundary flux in the normal direction. Furthermore, the general requirements for boundary value problems hold, as presented in the introduction to Chapter 2.

The FEM is a particular method of weighted residuals, which involves deriving a so-called weak form. Inserting an approximative solution $\tilde{\Phi}$ into Eq. (3.1) introduces an imbalance termed the residual, the difference between the left- and right-hand side. The residual is multiplied by weight functions ω_j $(j = 1, \dots, n)$. The integral of this product over the problem domain Ω must vanish for each weight function ω_j:

$$\int_\Omega \left(\frac{\partial \tilde{\Phi}}{\partial t} + v_i \frac{\partial \tilde{\Phi}}{\partial x_i} - \frac{\partial}{\partial x_i} \left(\kappa \frac{\partial \tilde{\Phi}}{\partial x_i} \right) - S \right) \omega_j \, \mathrm{d}\Omega \overset{!}{=} 0 \quad \forall j = 1, \dots, n \,. \tag{3.4}$$

Integrating the third term by parts yields

$$\int_\Omega \left(\frac{\partial \tilde{\Phi}}{\partial t} \omega_j + v_i \frac{\partial \tilde{\Phi}}{\partial x_i} \omega_j + \kappa \frac{\partial \tilde{\Phi}}{\partial x_i} \frac{\partial \omega_j}{\partial x_i} - S \, \omega_j \right) \mathrm{d}\Omega - \int_\Gamma \kappa \frac{\partial \tilde{\Phi}}{\partial x_i} \omega_j \, \mathrm{d}\Gamma = 0 \quad \forall j = 1, \dots, n \,. \tag{3.5}$$

As the weight functions must vanish on Dirichlet boundaries, the integration over Γ can be recast to

$$\int_\Omega \left(\frac{\partial \tilde{\Phi}}{\partial t} \omega_j + v_i \frac{\partial \tilde{\Phi}}{\partial x_i} \omega_j + \kappa \frac{\partial \tilde{\Phi}}{\partial x_i} \frac{\partial \omega_j}{\partial x_i} - S \, \omega_j \right) \mathrm{d}\Omega + \int_{\Gamma_\mathrm{N}} q_n^\Gamma \, \omega_j \, \mathrm{d}\Gamma = 0 \quad \forall j = 1, \dots, n \,, \tag{3.6}$$

which is the weak form of Eq. (3.1), where the Dirichlet boundary conditions still need to be imposed for completeness. The term *weak* originates from the vanishing of the weighted residual representing a less strict requirement to the ansatz in Eq. (3.7) than fulfilling the original PDE. Moreover, the partial integration has loosened the differentiability requirements for the ansatz.

The first key idea of the FEM is the approximation of the unknown variable Φ by a linear combination of n yet unknown parameters $\tilde{\Phi}_k(t)$ and basis functions $N_k(x_i)$, such that

$$\Phi \approx \tilde{\Phi} = \sum_{k=1}^{n} \hat{\Phi}_k \, N_k \,. \tag{3.7}$$

Following the Galerkin method, $\omega_j = N_j$ gives the discretized system of equations in space

$$\boldsymbol{M} \frac{\partial \hat{\boldsymbol{\Phi}}}{\partial t} + \boldsymbol{H} \, \hat{\boldsymbol{\Phi}} + \boldsymbol{f} = \boldsymbol{0}, \tag{3.8}$$

for the unknown vector $\hat{\boldsymbol{\Phi}} \in \mathbb{R}^n$, where

$$M_{jk} = \int_\Omega N_k \, N_j \, \mathrm{d}\Omega \,, \tag{3.9}$$

$$H_{jk} = \int_{\Omega} \left(N_j \, v_i \, \frac{\partial N_k}{\partial x_i} + \kappa \, \frac{\partial N_j}{\partial x_i} \frac{\partial N_k}{\partial x_i} \right) \mathrm{d}\Omega \,, \tag{3.10}$$

$$f_j = - \int_{\Omega} N_j \, S \, \mathrm{d}\Omega + \int_{\Gamma_\mathrm{N}} q_\mathrm{n}^\Gamma \, N_j \, \mathrm{d}\Gamma \,. \tag{3.11}$$

The second key idea of the FEM is the discretization of the problem domain into discrete subdomains Ω_e, the finite elements, such that $\cup \, \Omega_e = \hat{\Omega} \approx \Omega$. On each finite element Ω_e, a local ansatz for the approximative solution of Φ is formulated as

$$\tilde{\Phi}^e = \sum_{m=1}^{p} \hat{\Phi}^e_m \, N^e_m \,, \tag{3.12}$$

where $\hat{\Phi}^e$ are called the p degrees of freedom of a finite element. From selecting $\hat{\Phi}^e_m$ to represent the approximative solution at suitable positions $\boldsymbol{x}^e_r$ ($r = 1, \ldots, p$) inside of Ω_e follows linear independent ansatz functions that fulfill $N^e_m(\boldsymbol{x}^e_r) = \delta_{mr}$. The systematic assembly of the local approximations in Eq. (3.12) for all elements yields the global ansatz of Eq. (3.7). One particularity of the FEM is the calculation of Eq. (3.9)–(3.11) on the finite elements individually owing to the local stencil of $N_k(x_i)$. For spatial numerical integration, e.g., with the Gauss–Legendre quadrature, it is beneficial to project the arbitrary elements onto a unit element. The concept of isoparametric elements utilizes the same parent variables $-1 \leq \xi_i \leq 1$ for the geometric element description in local coordinates and the unified shape function $N(\xi_i)$ [218, 267].

Stabilization for advection-dominated problems

The standard Galerkin FEM produces decent results for diffusion-dominated problems, such as pure heat conduction. However, the method shows considerable inaccuracies and instabilities for advection-dominated problems [266]. Introducing the element Peclet number $Pe_h = |\boldsymbol{v}| \, h/(2\,\kappa)$ for the model problem in Eq. (3.1), where h is a characteristic element length, it can be shown that the finite element solution with standard Galerkin methods becomes unstable once Pe_h exceeds unity [266]. The cause lies in negative diffusion introduced by the numerical scheme, similar as it can be observed for standard central difference schemes [29]. *Upwinding* is a technique that includes the advection direction into the numerical discretization. In this spirit, various approaches have been proposed over the past three decades to accomplish an upwinding effect for Galerkin finite element methods. Indeed, the "upwinded", semi-discretized equations of a 1D model problem can be interpreted as a central-difference scheme with added artificial diffusion [29]. However, such a balancing diffusion does not modify transient and source terms, which leads to inaccuracies, see [29] or [266] for examples. Likewise, adding artificial diffusion isotropically for multi-dimensional problems corrupts the solution quality. A consistent method, applicable for all terms in the weighted residual approach, and adding only anisotropic diffusion in the direction of the flow field is the streamline upwind Petrov–Galerkin (SUPG) weighting, proposed by Hughes and Brooks [29]. The essential idea is to increase the weighting function N_j at the upwind side and decrease it at the leeward side of the element, such that an adjusted weight function W_j reads

$$W_j = N_j + \alpha W_j^* \equiv N_j + \alpha \, \frac{h}{2} \, \frac{v_i}{|\boldsymbol{v}|} \, \frac{\partial N_j}{\partial x_i} \,, \tag{3.13}$$

for example. An optimal α can be determined for each element as

$$\alpha = \alpha_{\text{opt}} = \coth Pe_h - \frac{1}{Pe_h} \,. \tag{3.14}$$

It should be noted that the method introduces additional terms to the weighted residual approach that must be integrated appropriately. An extended version for compressible flows [109] is implemented in the FEM solver COMSOL Multiphysics to stabilize advection-dominated problems. The extension also adds consistent cross-wind diffusion to regions that are not aligned with the streamline direction of the flow, e.g., to capture shocks, sharp boundary or shear layers without numerical oscillations [47].

3.1.3. Time discretization

After having performed an exemplary semi-discretization in space in the previous section, a discretization in time can be performed to achieve an approximate solution to Eq. (3.8). To align the presentation of the time discretization methods in this section with standard textbooks, such as [105, 218, 266, 267], Eq. (3.8) can be recast to

$$\frac{\partial \hat{\boldsymbol{\Phi}}}{\partial t} = \mathscr{L}\left(t, \hat{\boldsymbol{\Phi}}(t)\right) \,, \tag{3.15}$$

utilizing an operator $\mathscr{L}$ that sub-summarizes all other terms. Initial values t_0 and $\boldsymbol{\Phi}(t_0)$ uniquely characterize this initial value problem. Note that the operator $\mathscr{L}$ might be nonlinear or linear in $\hat{\boldsymbol{\Phi}}$ in general. It is linear in the case of the generic advection–diffusion equation in Eq. (3.1).

Similar to the discretization in space, numerical methods solve the initial value problem at discrete points in time $t_0, t_1, \dots, t_N$. The integration of Eq. (3.15) yields

$$\int_{t_j}^{t_{j+1}} \frac{\partial \hat{\boldsymbol{\Phi}}}{\partial t} \, \mathrm{d}t = \int_{t_j}^{t_{j+1}} \mathscr{L}\left(t, \hat{\boldsymbol{\Phi}}(t)\right) \mathrm{d}t \tag{3.16}$$

$$\Rightarrow \hat{\boldsymbol{\Phi}}(t_{j+1}) = \hat{\boldsymbol{\Phi}}(t_j) + \int_{t_j}^{t_{j+1}} \mathscr{L}\left(t, \hat{\boldsymbol{\Phi}}(t)\right) \mathrm{d}t \,. \tag{3.17}$$

One common approach is the interpolatory quadrature of the integral on the right-hand side. Using, for example, the left Riemann sum yields the explicit Euler formula

$$\hat{\boldsymbol{\Phi}}_{j+1} = \hat{\boldsymbol{\Phi}}_j + \Delta t \mathscr{L}\left(t_j, \hat{\boldsymbol{\Phi}}_j\right) \,, \tag{3.18}$$

where $\Delta t = t_{j+1} - t_j$ is called time step and $\hat{\mathbf{\Phi}}_{j+1}$ now denotes the numerical approximation of $\hat{\mathbf{\Phi}}(t_{j+1})$. Applying the concept at multiple points in time between t_j and t_{j+1} without including the yet unknown solution $\hat{\mathbf{\Phi}}(t_{j+1})$ yields the Runge–Kutta methods. Because of their efficiency, these methods are utilized in the context of neural ODEs later in this chapter. With the variation of the interpolatory quadrature scheme and including the yet unknown solution $\hat{\mathbf{\Phi}}(t_{j+1})$, e.g., applying the right Riemann sum or the trapezoidal rule, the implicit Euler and the Crank–Nicolson method are derived. Methods that include the evaluation of the yet unknown solution $\hat{\mathbf{\Phi}}(t_{j+1})$ are characterized as *implicit*, as they require the solution of an additional system of equations to solve for $\hat{\mathbf{\Phi}}(t_{j+1})$.

Another common implicit approach is the approximation of $\hat{\mathbf{\Phi}}(t)$ with a polynomial P_k of order k through the past k approximate solutions $\hat{\mathbf{\Phi}}_{j-1}, \dots, \hat{\mathbf{\Phi}}_{j-k}$ and requiring $\frac{\partial P_k}{\partial t} = \mathscr{L}(t_{j+1}, \hat{\mathbf{\Phi}}_{j+1})$. This is the essential idea of the backward-differencing formulas BDF(k) [89]. For constant time steps, BDF(2) reads

$$3\hat{\mathbf{\Phi}}_{j+1} - 4\hat{\mathbf{\Phi}}_j + \hat{\mathbf{\Phi}}_{j-1} = 2\Delta t \, \mathscr{L}(t_{j+1}, \hat{\mathbf{\Phi}}_{j+1}) \,. \tag{3.19}$$

It is an unconditional stable integrator in time with a consistency order of 2. Its advantage over other second-order methods, such as the Adams–Moulton class of integrators, is the more accurate solution of numerically stiff ODE systems [105]. BDF(k) is the default time integrator in COMSOL Multiphysics. Particularly, a version of the IDA solver of Lawrence Livermore National Laboratory [119] is implemented in the software [47]. IDA employs a variable-order, variable-coefficient BDF [27], that comprises the core ideas outlined above. Note that the recast of Eq. (3.15) was performed for demonstration purposes. As it implies an inversion of $\boldsymbol{M}$ in Eq. (3.8), this recast is not performed explicitly during the solution of the FEM problem, see Sec. 3.1.5 for more details on the solution procedure.

3.1.4. Hemi-cube view factor calculation for radiative heat exchange

The radiative heat flux contribution $q_{m,\text{rad}}$, see Eq. (2.36), in the boundary condition for the energy conservation of Eq. (2.3) is the last remaining puzzle piece that needs numerical treatment before the approximative solution of the overall set of equations can be addressed. The radiosity method for surface-to-surface radiative heat exchange, as derived in Sec. 2.2.2 for topological surfaces, also holds for a discretized version of the problem. During the finite element discretization, each topological surface is discretized with triangular or quadrilateral surface patches. To calculate $q_{m,\text{rad}}$ on each surface patch, the view factors $\boldsymbol{F}$ are required in Eq. (2.34). The numerical approximation of those view factors is provided with the hemi-cube method, described hereafter.

For two arbitrarily positioned patches j and m in space, the view factor can be obtained by solving the fundamental photometric law [11]

$$F_{jm} = \frac{1}{A_j} \int_{A_j} \int_{A_m} \frac{\cos\beta_j \cos\beta_m}{\pi r^2} \, \mathrm{d}A_j \, \mathrm{d}A_m \,, \tag{3.20}$$

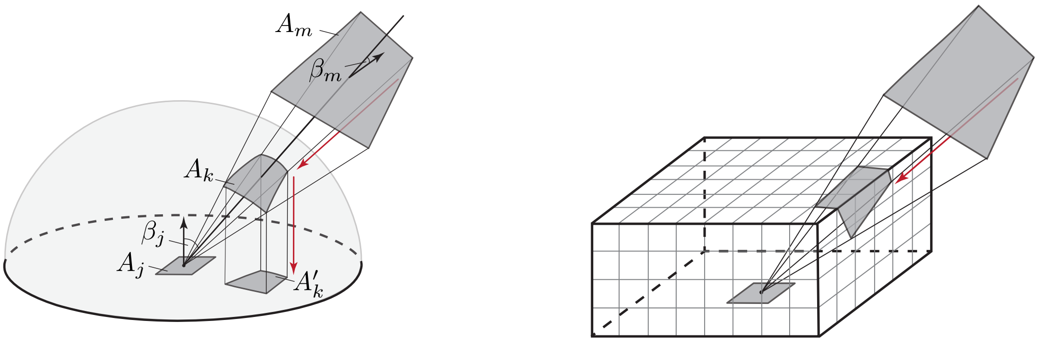

(a) Projection onto a hemisphere. **(b)** Projection onto a hemicube.

Figure 3.1. Projection methods for view factor calculations.

where A is the respective surface area of a patch, r is the distance between the centers of the patches, and β is the polar angle at which the surfaces mutually appear to each other, see Fig. 3.1a for an illustration. For simple shapes, view factors can be obtained analytically; see [11, 128, 169] for examples. For more complex geometries, the view factors could be determined from the numerical integration of the analytical relation. However, this approach is computationally intensive for a large number of surface patches and requires the absence of obstructions in the domain [45].

Nusselt [179] proposed one of the first practical approaches to estimate the view factors between two surfaces. He formulated the analogy that two patches k and m have the same view factors $F_{jk} = F_{jm}$, where k is a projection of m on a half-sphere with radius R that surrounds the center of patch j, see Fig. 3.1a for an illustration. Hence, the first step of the practical approach is a projection of an arbitrary outer patch onto the unit sphere. The integration of the view factor of the patch k is replaced by a second projection of the area A_k onto the base of the half-sphere. The view factor can be recast to the simple fraction of areas $F_{jm} = A'_k/(\pi R^2)$.

As the Nusselt analogy holds for any shape of an enclosing box, Cohen [45], a pioneer in computer graphics, enhanced the approach utilizing a hemispherical cube, see Fig. 3.1b. The so-called hemi-cube is evenly pixelated with square patches. COMSOL Multiphysics, for example, utilizes 256 pixels as default. The view factor F_k of a surface patch k can be pre-calculated analytically in advance. In the first step of the approach, an outer patch m is projected onto the pixelated surface. Secondly, every patch that is “illuminated”, contributes to the overall view factor. The summation of all partial view factors yields the total view factor $F_{jm} = \sum_k F_{k,\text{illum}}$.

Shadowing in complex geometries is efficiently captured with z-buffer algorithms that are well-known in computer graphics [37]. The z-buffer algorithm checks if multiple outside patches are projected on the same surface patch k. The patch with the smallest distance to j is taken into account, and all other patches are not included in the view factor calculation.

3.1.5. Solution algorithms

Within this work, COMSOL Multiphysics 5.6 is utilized to provide numerical solutions to the PDEs presented in Chapter 2. Details on settings and utilized modules to realize the various multi-physical couplings are given in the context of the studies of Chapter 4. One simulation run typically comprises the following steps: Calculating the view factors with the hemi-cube method is performed once during the initialization of a simulation. During each time step, the radiative heat flux $q_{m,\text{rad}}$ on each surface patch is calculated by solving the linear system of equations in Eq. (2.34) with the updated surface temperatures of the current time step. The non-isothermal, compressible Navier–Stokes equations of Eq. (2.1)–(2.3) and the porous media multi-phase PDEs of Sec. 2.3 are discretized in space and time with SUPG-stabilized FEM and BDF(2). While the software employs the core ideas of the methods as presented in the previous sections, the implementation is more elaborate. For example, when discretizing the nonlinear convective term of the momentum conservation in Eq. (2.2), a nonlinear, semi-discretized set of equations arises from the FEM. It is linearized with a Newton–Raphson method [47].

The linear systems of equations arising during one Newton iteration and from the radiosity method are solved with standard approaches. Whereas direct methods are preferable for small systems, iterative solvers should be used for large-scale systems [218]. The generalized minimal residual (GMRES) algorithm [215] is a well-established, iterative solver that is implemented COMSOL Multiphysics [47, 119]. Notably, Krylov subspace methods, such as GMRES, require appropriate preconditioning, as they are often otherwise inefficient [30]. Good selections of preconditioners are often problem-dependent; see [30, 47, 119] for further background reading.

3.2. Reduced-order modeling

As motivated in the introduction, the digital twin methodology must go hand-in-hand with reduced-order modeling approaches that replicate the large-scale, multi-physical problems within reasonable simulation time and with lean computational cost. Section 3.2.1 motivates employing ANSYS Dynamic ROM builder for this thesis. The method is explained in Sec. 3.2.2 for point data and is extended to field data in Sec. 3.2.3. An overview of error measures concludes this chapter in Sec. 3.2.4.

3.2.1. Selection of the reduced-order modeling method

Various perspectives can be shed on ROMs, as the problem is addressed in many disciplines. A common classification criterion is the intrusiveness of the ROM generation method [17, 244]. Access to and modification of the underlying set of PDEs can be called an *intrusive* approach. Conversely, methods that do not modify the underlying equations are called *non-intrusive* [17, 185].

Within the discipline of computational engineering, the PDE-centric, intrusive approaches utilize the formulated PDE of the physical model as a starting point. After a numerical discretization in space and time, the resulting equation is projected onto a reduced-order space, where an accelerated solution to the problem is targeted [17]. Commercial simulation software companies protect their solution algorithms as intellectual property. They do not grant users root-level access to the underlying algorithms. Hence, intrusive ROM methods are not a feasible option. This work resorts to non-intrusive ROM methods to preserve universality in employed simulation software.

Within the discipline of system identification, researchers have developed many methods to derive surrogates of dynamical systems [12, 157, 174]. Either generic (black-box) or problem-specific (gray-box) ansatz equations are formulated that should describe the system dynamics [23]. The unknown model parameters are fitted such that the output is close to the actual output of the problem in the sense of some error measure. Linear time-invariant (LTI) systems, represented in either time or frequency domain, have a long tradition in system identification [157, 174]. As demonstrated in [135, 188], LTIs are unsuitable for replicating strong non-linearities of coupled problems per design. Also, nonlinear approaches such as NARX models are only optimized for one-step-ahead *predictions* while measuring the actual output signal of the full-order model (or the natural experiment). NARX predictors are not designed for stand-alone *simulations* over a larger time span [157, 174, 221], as also shown in [188].

Within the discipline of machine learning, time series are usually replicated with RNNs [92]. Neural networks are known to be highly flexible, universal [124], nonlinear function approximators [92]. *Recurrent* neural networks, more specifically long short-term memory neural networks (LSTMs) [122], are characterized by recursive calls of a neural network with a discrete temporal delay to invoke the progress of the variables in time. Through the back-propagation through time algorithm, the neural network is trained to replicate input-to-output relations over time. Exemplary implementations of RNNs and discussions on how to overcome difficulties with learning long-term dependencies can be found in [121, 233].

Recently, hybrid approaches have come into focus that combine the concept of identifying system dynamics with machine-learning techniques. Dupont et al. [74] illustrate the similarity of deep feed-forward neural networks, more specifically residual networks [110], with differential equations: The mapping of a hidden state $\boldsymbol{h}_t \in \mathbb{R}^d$ at layer t to its next layer is

$$\boldsymbol{h}_{t+1} = \boldsymbol{h}_t + \boldsymbol{f}_t(\boldsymbol{h}_t)\,, \tag{3.21}$$

where $\boldsymbol{f}_t : \mathbb{R}^d \to \mathbb{R}^d$ is a differentiable function that projects from one hidden state to the next. Forming a difference quotient and taking the limit of an imaginary time step clarifies the similarity to an ODE system:

$$\lim_{\Delta t \to 0} \frac{\mathbf{h}_{t+\Delta t} - \mathbf{h}_t}{\Delta t} = \frac{\mathrm{d}\mathbf{h}(t)}{\mathrm{d}t} = \mathbf{f}(\mathbf{h}(t), t)\,. \tag{3.22}$$

An input is mapped to the output by solving an ODE over multiple time steps. A feed-forward neural network represents the right-hand side operator $\boldsymbol{f}_t$ of the ODE, which inspired the name of the approach: *neural ODEs*. Recent publications indicate that neural ODEs outperform RNNs or tree-based algorithms, e.g., in [158] for predicting pharmacokinetics or in [186] for predicting the remaining state of health of batteries. The success of neural ODEs is conjectured to be the learning of underlying dynamics instead of just input-to-output relations [123, 186].

The software package *ANSYS Dynamic ROM Builder* (ANSYS Inc. [8, 248]; termed DynROM hereafter) can provide a non-intrusive, nonlinear, transient ROM by employing a method that is quite similar to neural ODEs. Given the promising results during preliminary testing and considering the lack of in-depth investigations of the method in the literature, it was decided to employ DynROM within this work. Nonetheless, future work could also examine the applicability of the proposed efficient design of experiments for other variants of transient ROMs, such as augmented neural ODEs by Dupont et al. [74] or Runge–Kutta neural networks [265].

3.2.2. Data-driven reduced-order modeling for point data

Consider the idealized illustration of porous food items inside a convection oven cavity, as depicted in Fig. 3.2. The procedure to generate a ROM for data probed at selected points can be characterized as follows: The multi-physical model of thermal food processing, hereafter called a full-order model, is simulated within COMSOL Multiphysics. Discretized oven temperatures $\hat{\boldsymbol{G}} = [T_{\text{oven},1}, \ldots, T_{\text{oven},N}]$ are the external excitation for the full-order over time, where N is the total number of time steps. Virtual probes can read out temperatures, for example, $T_{\text{A},k}$, $T_{\text{B},k}$ and $T_{\text{C},k}$ at discrete points in space and time, which are stored in an array $\hat{\boldsymbol{Y}} \in \mathbb{R}^{n\times N}$ ($n = 3$ here, see Fig. 3.2). Now, the ROM is likewise excited by the oven temperatures $\hat{\boldsymbol{G}}$ at its input. During a training phase, the parameters of the ROM are optimized such that the discretized ROM output $\hat{\boldsymbol{X}}$ replicates the full-order model output: $\hat{\boldsymbol{Y}} \overset{!}{\approx} \hat{\boldsymbol{X}}$.

Figure 3.2 (right half) illustrates the core principle of the DynROM method. One input $G = G(t)$ is mapped to the output $\boldsymbol{X} = \boldsymbol{X}(t)$ by solving the ODE

$$\frac{\partial}{\partial t}\begin{bmatrix}\boldsymbol{X}\\ \boldsymbol{I}\end{bmatrix} = \boldsymbol{f}\left(\begin{bmatrix}\boldsymbol{X}\\ \boldsymbol{I}\end{bmatrix}, G, \boldsymbol{X}_0\right), \tag{3.23}$$

$$\boldsymbol{X}(t=0) = \boldsymbol{X}_0\,, \tag{3.24}$$

where the state vector $\boldsymbol{X} \in \mathbb{R}^n$ is prolonged by a special vector $\boldsymbol{I} \in \mathbb{R}^i$ — introduced later — and $\boldsymbol{X}_0 \in \mathbb{R}^{n+i}$ contains the initial conditions for both. The right-hand side operator $\boldsymbol{f}$ is modeled with a three-layer feed-forward neural network. The neural network consists of an input layer $\boldsymbol{x} \in \mathbb{R}^{n+i+1}$, a hidden layer $\boldsymbol{h} \in \mathbb{R}^{n+i}$ and an output layer $\boldsymbol{z} \in \mathbb{R}^{n+i}$, see Fig. 3.2. Linear transformations of the values of the input layer $\boldsymbol{x}$ with weight matrices $\boldsymbol{W}_1$ and the superposition with a bias vector $\boldsymbol{b}_1$ are the basic operations to calculate the values of the neurons on the hidden layer $\boldsymbol{h}$. The new values are found by applying a sigmoid activation function $\mathscr{S}$, which renders the relationship between the layers nonlinear [92]. Repeating this procedure for the output layer

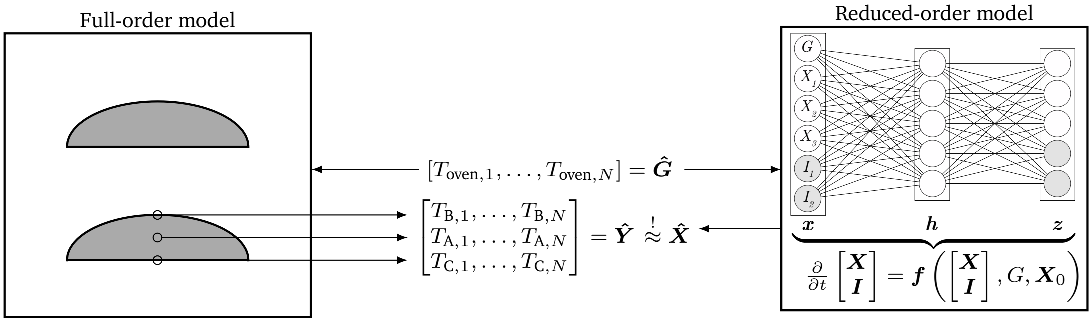

Figure 3.2. Reduced-order modeling with ANSYS Dynamic ROM Builder of discretized readout matrix $\hat{\boldsymbol{Y}}$ from a full-order model.

with different weights and biases yields the calculation from the input to the output layer:

$$\boldsymbol{h} = \mathscr{S}(\boldsymbol{W}_1 \boldsymbol{x} + \boldsymbol{b}_1)\,, \tag{3.25}$$

$$\boldsymbol{z} = \mathscr{S}(\boldsymbol{W}_2 \boldsymbol{h} + \boldsymbol{b}_2)\,. \tag{3.26}$$

To find the desired relation between the input and output layer, training data with known input $\hat{\boldsymbol{G}}$ and output $\hat{\boldsymbol{Y}}$ is introduced to the neural network. This procedure is referred to as supervised learning. Fourth-order Runge–Kutta schemes are implemented in DynROM to integrate the ODE system in time. The loss function for the neural network's training error is the mean squared error

$$E_{\text{mse}} = \frac{1}{n} \sum_{j=1}^{n} \left(\frac{1}{N} \sum_{k=1}^{N} (\hat{X}_{jk} - \hat{Y}_{jk})^2 \right)\,, \tag{3.27}$$

which is averaged for all learning scenarios. To minimize the loss function, gradient descent algorithms are combined with the back-propagation algorithm [34, 214]. This optimization procedure tries to find optimal values of the weights and biases in all layers, such that the discrete output $\hat{\boldsymbol{X}}$ of the numerical integration of Eq. (3.23) can replicate the output of the full-order model: $\hat{\boldsymbol{Y}} \overset{!}{\approx} \hat{\boldsymbol{X}}$.

The nature of ODEs is that the right-hand side can be interpreted as a vector field, where trajectories from two different initial conditions cannot cross. Dupont [74] demonstrated how neural ODEs cannot learn crossing paths from input to output without special augmentation. The limitation was elegantly eliminated with the addition of other free variables $\boldsymbol{I}$ to $\boldsymbol{X}$ by Dupont [74], which he called augmented neural ODEs. The augmentation adds extra channels to the layers, which allows to lift trajectories into other dimensions where they no longer need to cross. The number i of added free variables is called the complexity of the augmentation in this work. Like the augmentation of neural ODEs by Dupont [74], DynROM adds i free variables to the state vector as long as it further decreases the training error [8]. One particularity of the method is that only little training data is required, e.g., one-to-two simulations over time that each contains a moderate number of time steps, e.g., $N = 280$ for the studies of Chapter 5. On the contrary, in machine learning, it is not uncommon to have data set sizes on the order of 10^3–10^7 [221]. The particularity raises the question of which data can successfully convey the system properties to the ROM. The studies in Chapter 5 strive to answer that question.

3.2.3. Extension to field data

In general, one may be interested not only in replicating the values of selected points in the full-order model but of the entire solution field as well. In thermal food processing, such a ROM may serve to investigate local temperature or moisture concentration peaks. Using all n nodal temperatures of the full-order model as rows in $\hat{\boldsymbol{Y}} \in \mathbb{R}^{n \times N}$ would render the neural ODE ROM considerably high-dimensional and inefficient to train. However, many complex systems can be described by dominant low-dimensional patterns without considerable loss of accuracy. For field data, DynROM employs the singular value decomposition (SVD), one of the workhorses in the era of data-driven computational engineering [34], to generate a matrix decomposition of $\hat{\boldsymbol{Y}}$, from which a low-dimensional representation of the problem can be found. Note that the matrix dimensions are given as subscripts in the following derivation for better comprehension. For every matrix $\hat{\boldsymbol{Y}}_{n,N} \in \mathbb{C}^{n \times N}$, a unique SVD can be found that reads

$$\hat{\boldsymbol{Y}}_{n,N} = \boldsymbol{U}_{n,n} \boldsymbol{\Sigma}_{n,N} \boldsymbol{V}^*_{N,N} \,, \tag{3.28}$$

where $\boldsymbol{U}_{n,n}$ and $\boldsymbol{V}^*_{N,N}$ are unitary matrices that consist of orthonormal columns and * denotes the complex conjugate transpose and $\boldsymbol{\Sigma}_{n,N}$ is a diagonal matrix [34]. The real-valued singular values σ_k can be ordered by decreasing magnitude on the main diagonal. It can be shown that setting $\sigma_k = 0 \quad \forall k > r$ results in a optimal rank-r representation of $\hat{\boldsymbol{Y}}_{n,N}$ in least-square sense [34]:

$$\hat{\boldsymbol{Y}}_{n,N} \approx \tilde{\boldsymbol{Y}}_{n,N} = \boldsymbol{U}_{n,r} \boldsymbol{\Sigma}_{r,r} \boldsymbol{V}^*_{r,N} = \boldsymbol{U}_{n,r} \boldsymbol{C}_{r,N} \,. \tag{3.29}$$

$\boldsymbol{U}_{n,r}$ contains the first r left singular vectors (exclusively spatial mode shapes) of $\hat{\boldsymbol{Y}}_{n,N}$ and $\boldsymbol{C}_{r,N}$ contains r time-dependent mode shape coefficients on its rows. It is now a much more efficient task for DynROM to approximate the mode shape coefficients $\boldsymbol{C}_{r,N} \overset{!}{\approx} \hat{\boldsymbol{C}}_{r,N}$ instead of all outputs $\hat{\boldsymbol{Y}}_{n,N}$, as $r \ll n$. The decompression of the SVD

$$\hat{\boldsymbol{X}}_{n,N} = \boldsymbol{U}_{n,r} \hat{\boldsymbol{C}}_{r,N} \tag{3.30}$$

generates the approximation $\hat{\boldsymbol{Y}} \overset{!}{\approx} \hat{\boldsymbol{X}}$ that is sought.

3.2.4. Error measures

Error measures are utilized throughout this work to assess either the accuracy of a full-order model compared to experimental data or the quality of a ROM compared to the full-order model. An accuracy measure should be interpretable, indifferent to over- and under-predictions, scale-independent, insensitive to outliers and stable for zero crossings of the observation variable [39]. The root mean square error

$$E_{\text{rms}} = \sqrt{\frac{1}{N}\sum_{k=1}^{N}(\hat{X}_k - \hat{Y}_k)^2} \tag{3.31}$$

is a popular, scale-dependent error measure, facilitating interpretability. Here, $\hat{X}_k$ is the discrete prediction for one readout $\hat{Y}_k$ of the full-order model. The mean absolute percentage error

$$E_{\text{map}} = \frac{1}{N}\sum_{k=1}^{N}\frac{|\hat{X}_k - \hat{Y}_k|}{|\hat{Y}_k|}\,. \tag{3.32}$$

is a percentage-based variant. Both error measures are fair concerning over- and under-predictions but show sensitivity to single outliers. However, owing to the usage of deterministic models in this work, single outliers are not expected to occur. Likewise, the sensitivity of E_{map} to zero crossings of the observation $\hat{Y}_k$ and its scale sensitivity within one time series [39] only plays a minor role. The usage of E_{map} enables the comparability of all temperature errors within this work. However, the error magnitude is not comparable for differing variables. One drawback of the error measure is that relative errors may appear small, as the deviations are set in relation to the total reference value. A deviation of $20\,\text{K}$ at a reference value of $400\,\text{K}$ would result in $E_{\text{map}} = 5\%$, which appears small in contrast to an alternative relative error of 12.7% in comparison to the expected variable range of 293.15–$450.15\,\text{K} = 157\,\text{K}$. Such alternative error measure would, however, require an a priori knowledge of all variable ranges, which is considered impractical for the studies of this work. Thus, sometimes it is beneficial to assess local accuracy measures as well, for example, the maximum absolute error

$$E_{\text{max}} = \max_k |\hat{X}_k - \hat{Y}_k|\,. \tag{3.33}$$

Moreover, statistical measures of time-dependent errors, such as the median and the interquartile range of $\hat{X}_k - \hat{Y}_k$ ($k = 1, \ldots, N$), denoted as E_{med} and E_{iqr}, are considered. These measures are more robust to outliers than the mean or standard deviation. Occasionally, the root mean square, mean, standard deviation, median or interquartile range must be calculated from an array of data. The corresponding functions are denoted as $\text{rms}()$, $\text{mean}()$, $\text{std}()$, $\text{med}()$ and $\text{iqr}()$. A model's goodness-of-fit can be expressed with the coefficient of determination

$$\text{R}^2 = 1 - \frac{\sum_{k=1}^{N}(\hat{Y}_k - \hat{X}_k)^2}{\sum_{k=1}^{N}(\hat{Y}_k - \overline{Y}_k)^2}\,, \tag{3.34}$$

where an overline like in $\overline{Y}_k$ denotes the average over all items $k = 1, \ldots, N$ of a time series or array of data.

4. Physical modeling studies

This chapter aims to derive a conjugate heat and mass transfer model for thermal food processing inside a convection oven. Conjugate heat transfer typically indicates that the energy equation of a non-isothermal fluid flow is also solved on an adjacent solid body to capture mutual heat transfer effects. This work implements a conjugate energy equation for food items and oven cavity. The conjugate heat transfer covers, besides convection and conduction heat transfer, also the modeling of thermal radiation. Additional conjugate mass transfer entails continuously transporting vapor concentrations in food and oven cavity domains. Owing to scarce literature and data for validating a conjugate thermal food processing model, conjugate heat transfer and porous media models are benchmarked individually. Section 4.1 compares this work's implementation of two porous media models against synthetic and experimental data from the literature. Two subsequent studies investigate the model's working mechanisms and the model's sensitivity to parameters and modeling terms. The overall focus is on comparing the sensitivity to heat and mass transfer coefficients with the sensitivity of other food-science-specific modeling terms. Moreover, the model's applicability in a conjugate setup is of interest, which is discussed in Sec. 4.2. The conjugate heat transfer benchmarks and the conjugate simulations of food processing are described in Sec. 4.3. Section 4.4 presents the conclusions from the conjugate simulations.

4.1. Analysis of thermal food-processing models

This section aims to test the implementation of two food-processing models for plausibility and to analyze their working mechanisms. Further studies reveal sensitive modeling parameters and terms. In conclusion, a decision is made on which model is better suited for developing a conjugate heat and mass transfer model in Sec. 4.3.

4.1.1. Hygroscopic, capillary-porous media model for potatoes

The hygroscopic, capillary-porous media model for potatoes, presented in Sec. 2.3.1, was investigated in a test case by Ni [175] that also was published later by Datta [54]. The test case consists of a potato slab on a convection oven baking plate. Ni reduced the problem to a 1D domain for simplicity, see Fig. 4.1 for an illustration.

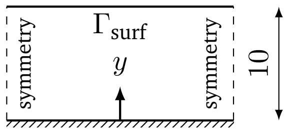

Figure 4.1. Pseudo 1D model of a potato slab (dimensions in mm).

Table 4.1. Initial conditions and model parameters from [175].

Parameter	Value	Parameter	Value
p_0	$1 \times 10^5\,\mathrm{Pa}$	ρ_s	$1419\,\mathrm{kg\,m^{-3}}$
p	$p_0 + p_\mathrm{rel}$	ρ_w	$1000\,\mathrm{kg\,m^{-3}}$
$S_{\mathrm{w},0}$	0.5	$c_{p,\mathrm{s}}$	$1566\,\mathrm{J\,kg^{-1}\,K^{-1}}$
$c_{\mathrm{v},0}$	$0.17\,\mathrm{mol\,m^{-3}}$	$c_{p,\mathrm{w}}$	$4180\,\mathrm{J\,kg^{-1}\,K^{-1}}$
T_0	$293.15\,\mathrm{K}$	$c_{p,\mathrm{v}}$	$2062\,\mathrm{J\,kg^{-1}\,K^{-1}}$
$c_\mathrm{v,oven}$	$0\,\mathrm{kg\,m^{-3}}$	$c_{p,\mathrm{a}}$	$1006\,\mathrm{J\,kg^{-1}\,K^{-1}}$
T_oven	$450.15\,\mathrm{K}$	κ_s	$0.21\,\mathrm{W\,m^{-1}\,K^{-1}}$
α_tot	$20\,\mathrm{W\,m^{-2}\,K^{-1}}$	κ_w	$0.64\,\mathrm{W\,m^{-1}\,K^{-1}}$
β_tot	$0.0125\,\mathrm{m\,s^{-1}}$	κ_g	$0.026\,\mathrm{W\,m^{-1}\,K^{-1}}$
φ	0.75	μ_g	$5.468 \times 10^{-4}\,\mathrm{Pa\,s}$
t_tot	$3600\,\mathrm{s}$	μ_w	$1.8 \times 10^{-5}\,\mathrm{Pa\,s}$

The following boundary conditions are assigned to the surface Γ_surf of the slab:

$$p_\text{rel}|_\text{surf} = 0\,\mathrm{Pa}\,, \tag{4.1}$$

$$\boldsymbol{N}_\mathrm{v}|_\text{surf} = \beta_\text{tot}\left(\varphi\, S_\mathrm{g}\,\frac{M_\mathrm{w}\,p_\text{v,surf}}{R\,T_\text{surf}} - c_\text{v,oven}\right), \tag{4.2}$$

$$\boldsymbol{N}_\mathrm{w}|_\text{surf} = \beta_\text{tot}\left(\varphi\, S_\mathrm{w}\,\frac{M_\mathrm{w}\,p_\text{v,surf}}{R\,T_\text{surf}} - c_\text{v,oven}\right), \tag{4.3}$$

$$\boldsymbol{N}_\mathrm{e}|_\text{surf} = \alpha_\text{tot}\,(T_\text{oven} - T) + H_\text{evap}\,\beta_\text{tot}\left(\varphi\, S_\mathrm{w}\,\frac{M_\mathrm{w}\,p_\text{v,surf}}{R\,T_\text{surf}} - c_\text{v,oven}\right), \tag{4.4}$$

where $\boldsymbol{N}_\mathrm{k}\ \forall\,\mathrm{k} \in \{\mathrm{v,w,e}\}$ are the total vapor, water and energy fluxes at the boundary that are driven by the differences of vapor concentration, water concentration and temperature at the top boundary facing the oven cavity. The boundary conditions assume that evaporation at the surface is intense enough to remove all excess moisture, resulting in no drip flow and representing the dominant energy losses. Zero flux conditions are assigned to the remaining boundaries. The initial conditions and additional model parameters from [175] are given in Tab. 4.1. The model implementation is realized in the *Coefficient Form PDE* module of COMSOL Multiphysics 5.6. For the spatial discretization, hexahedral elements with quadratic Lagrange (for T and p) and cubic Hermite (for c_v and c_w) polynomials are chosen. Element formulations with lower orders would result in oscillatory behavior. In contrast, Hermite ansatz functions enable to capture steep gradients in the distributed evaporation formulation, as is discussed at the end of this section.

A grid study with uniform cell sizes $h \in \{2\times10^{-4}, 1\times10^{-4}, 5\times10^{-5}\}\,\mathrm{m}$ was performed to obtain a grid-independent solution with a generalized Richardson extrapolation. The grid convergence index (GCI), calculated following [208], is $9 \times 10^{-5}\%$, $3 \times 10^{-4}\%$ and $3 \times 10^{-3}\%$ for the finest

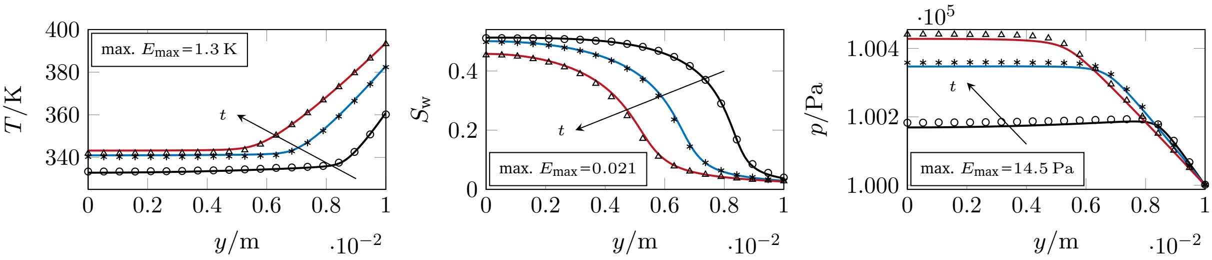

(a) Temperature **(b)** Water saturation **(c)** Pressure

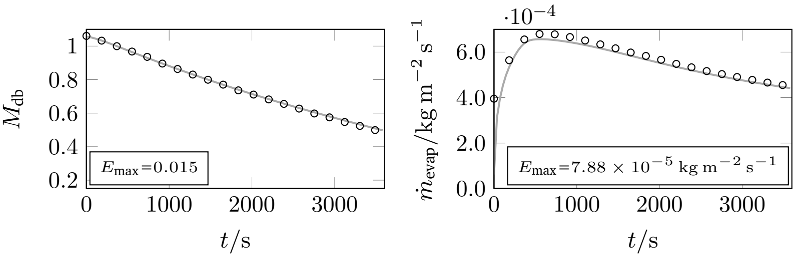

(d) Moisture content on dry basis **(e)** Evaporative mass loss

Figure 4.2. Comparison of implemented hygroscopic, capillary-porous media model (solid lines) at $t = 20\,\mathrm{min}$ (black), $t = 40\,\mathrm{min}$ (blue), $t = 60\,\mathrm{min}$ (red) with reference simulation of [175], represented with markers.

solution of T, c_{w} and p at a position of $1 \times 10^{-3}\,\mathrm{m}$ below the top surface. The finest uniform grid resolution, resulting in $179\,372$ degrees of freedom, would require a solution time of $1.5\,\mathrm{h}$ on 20 cores of a cluster of two Intel Xeon E5-2687W v4 (3.2 GHz) processors to resolve a real time of $1\,\mathrm{h}$. Consequently, the utilized mesh within the studies is manually refined to economize the grid size and solution times. The final mesh has a grid size $h = 2 \times 10^{-4}\,\mathrm{m}$, ten inflation layers with stretch factor 1.15 and a first layer height $h_0 = 2 \times 10^{-5}\,\mathrm{m}$ resolve the boundary layer in the vicinity of the wall. The spatial discretization error of this mesh is $6 \times 10^{-5}\%$, $4 \times 10^{-3}\%$ and $6 \times 10^{-4}\%$ for T, c_{w} and p compared to the grid-independent solution of the grid study outlined above. Time-stepping is performed with adaptive BDF(2) with a relative truncation error set to 0.1% for a scaled weighted root-mean-square error measure [47, 119]. The maximum time step is $10\,\mathrm{s}$, whereas the initial time step is $\Delta t = 1 \times 10^{-7}\,\mathrm{s}$. One can expect a rather stiff temporal behavior of the model in the initial phase owing to fast-rising temperatures in the surface area. During the course of the simulation, the time step is typically increased, and the maximum time step is applied after approximately $60\,\mathrm{s}$ of simulated real time.

The obtained results are in very good agreement with the reference simulation by Ni [175], see Fig. 4.2 for a comparison and the maximum differences $E_{\max}$. The maximum root-mean-square error is only $E_{\mathrm{rms}} = 0.9\,\mathrm{K}$ for the temperatures. However, there is slightly too much progress in the temperatures (Fig. 4.2a) and too few water saturation losses (Fig. 4.2b). The evaporative losses are also slightly different from the reference simulation (Fig. 4.2e). The latter has been performed on a custom code without the non-equilibrium evaporation formulation, which could be a possible source for the deviation. Moreover, Ni used a coarse, uniformly spaced grid with only 41 elements and a central differencing scheme. This grid spacing would have been insufficient in this implementation — despite a high-order ansatz — to accurately capture the steep subsurface gradients caused by evaporation. Hence, the present deviations could potentially stem from the coarse resolution in Ni's work.

Working mechanisms of the model

The heat input at the surface of the potato slab induces a rise in temperature (Fig. 4.2a). The rise in temperature leads to increased evaporation that starts to dry out the sub-surface region, which strongly determines the composition of the effective material properties, such as thermal conductivity, density and specific heat capacity (Fig. 4.3a). The reduced effective thermal conductivity hinders the heat from reaching the center of the slab. Figure 4.3b illustrates the receding evaporation front, which acts as a heat sink. The sharp stencil of the evaporation front is induced by increased vapor pressures and reduced water activity owing to low moisture concentration in the sub-surface region. Keep in mind that both parameters are multiplied to form $p_{\text{v,equ}}$ in Eq. (2.60). The dominant influences on mass fluxes are highlighted in Fig. 4.3c and Fig. 4.3d. Increased gas diffusivity and permeability allow diffusion and pressure-driven fluxes, mainly in the sub-surface region. Diffusion fluxes dominate pressure-driven gas fluxes by a factor of four to five. Similarly, capillary fluxes towards the dry surface exceed those of pressure-driven flow. The mass fluxes are confined by the receding front of the crust region where capillary diffusivity and water permeability are low.

Sensitivity study

This study investigates the sensitivity of water saturation S_{w}, temperature T and pressure p on changes to parameters and the omission of selected model terms. The aim is to compare the sensitivity of heat and mass transfer modeling to food-specific modeling terms. Additionally, the omission and variation of model terms shall give further insight into the working mechanisms and check the latter for plausibility. Table 4.2 summarizes a selection of findings of the conducted sensitivity study. It also gives identifying numbers to the individual studies and refers to figures that provide clarity. E_{map} serves as a dimensionless error measure. Note that error measures are not mutually comparable, as the three variables have their individual numerical ranges. To mitigate this shortcoming, coloring is applied individually for each variable, from white for the 10th percentile of the error measure to blue for the 45th percentile and red for the 80th percentile.

Studies 1–2 reveal the sensitivity to a variation of 20% of the mass transfer coefficient β_{tot}. It induces moderate changes of maximum $E_{\text{map}} = 2.9\%$ for the moisture saturation, $E_{\text{map}} = 3.0\%$ for the pressure and $E_{\text{map}} = 0.6\%$ for the temperature. Conversely, the model is susceptible to variations in the heat transfer coefficient, see studies 3–4. The deviations of S_{w} ($E_{\text{map}} = 16.2\%$, $E_{\text{rms}} = 0.033$, $E_{\text{max}} = 0.082$), T ($E_{\text{map}} = 1.9\%$, $E_{\text{rms}} = 6.8\,\text{K}$, $E_{\text{max}} = 13.4\,\text{K}$) and p ($E_{\text{map}} =$

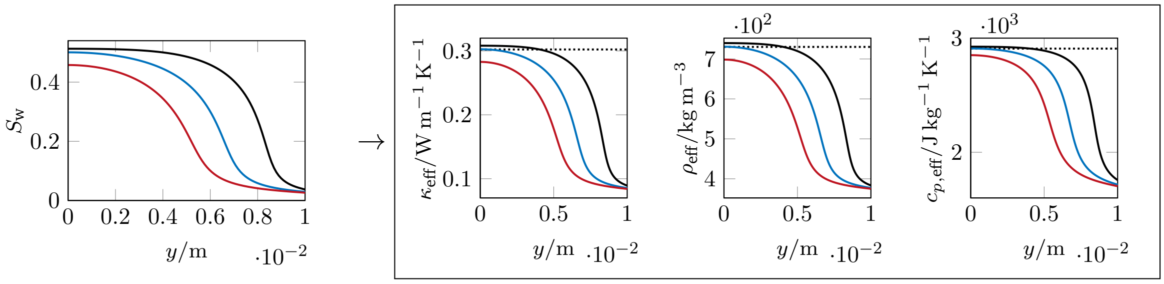

(a) Effective transport quantities are determined by water saturation.

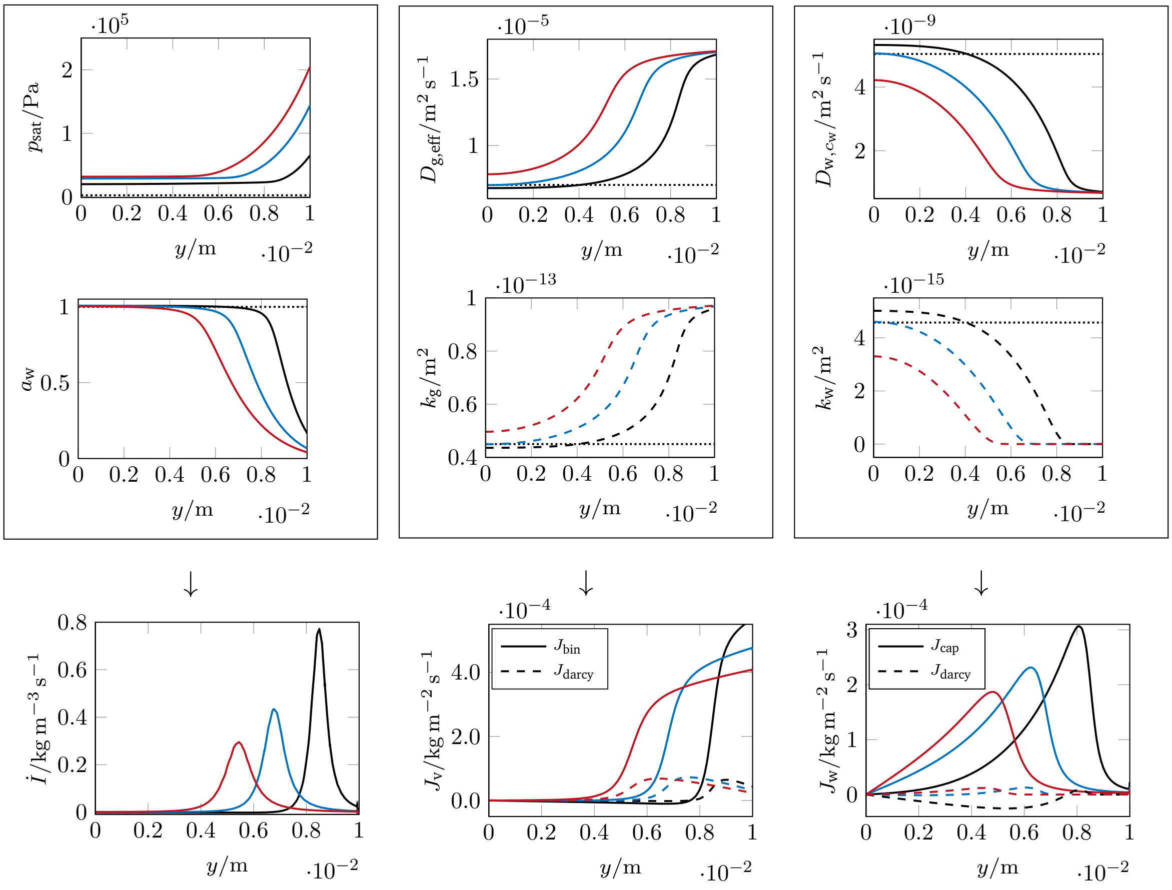

(b) Evaporation is influenced by water activity and saturation pressure.

(c) Gas fluxes are governed by effective gas diffusivity and permeability.

(d) Water fluxes are governed by capillary water diffusivity and permeability.

Figure 4.3. Working mechanisms of the hygroscopic, capillary-porous media model at $t = 20\,\text{min}$ (black), $t = 40\,\text{min}$ (blue), $t = 60\,\text{min}$ (red). Black dotted lines indicate initial conditions, where applicable.

Table 4.2. Sensitivity analysis with deviations given as E_{map} (%) in relation to the validation simulation. Coloring is applied individually for each variable, from white for the 10th percentile of the error measure to blue for the 45th percentile and red for the 80th percentile.

Study	Case	Details	Moisture saturation S_{w}			Temperature T			Pressure p		
			20 min	40 min	60 min	20 min	40 min	60 min	20 min	40 min	60 min
1	$\beta_{\mathrm{tot}} + 20\%$		1.6	1.9	2.0	0.4	0.2	0.1	1.4	0.4	0.5
2	$\beta_{\mathrm{tot}} - 20\%$		2.3	2.7	2.9	0.6	0.3	0.2	3.0	1.5	1.5
3	$\alpha_{\mathrm{tot}} + 20\%$	Fig. 4.4a	6.5	8.4	9.8	1.5	1.2	1.2	32.2	14.8	9.4
4	$\alpha_{\mathrm{tot}} - 20\%$	Fig. 4.4a	10.3	14.1	16.2	1.9	1.7	1.6	34.0	19.5	13.3
5	$\rho_{\mathrm{s}}(T),\ c_{p,\mathrm{s}}(T),\ \kappa_{\mathrm{s}}(T)$		2.3	4.7	6.5	0.3	0.5	0.7	6.0	8.7	9.7
6	$\rho_{\mathrm{s}}(T)$		1.8	3.4	4.6	0.1	0.2	0.2	2.6	1.9	1.3
7	$c_{p,\mathrm{s}}(T)$		0.1	0.2	0.2	0.0	0.0	0.0	0.7	0.2	0.1
8	$\kappa_{\mathrm{s}}(T)$		0.6	2.2	4.1	0.2	0.4	0.5	4.7	7.5	8.8
9	$\rho_{\mathrm{w}}(T),\ c_{p,\mathrm{w}}(T),\ \kappa_{\mathrm{w}}(T)$		1.8	2.4	2.6	0.0	0.1	0.1	0.8	1.1	1.3
10	$\rho_{\mathrm{w}}(T)$		1.8	2.4	2.8	0.0	0.0	0.0	0.5	0.5	0.6
11	$c_{p,\mathrm{w}}(T)$		0.0	0.0	0.0	0.0	0.0	0.0	0.0	0.0	0.0
12	$\kappa_{\mathrm{w}}(T)$		0.1	0.1	0.3	0.0	0.0	0.0	0.4	0.6	0.6
13	$\mu_{\mathrm{w}}(T)$		0.2	0.1	0.2	0.0	0.0	0.0	0.3	0.0	0.0
14	$\mu_{\mathrm{g}}(T)$		0.1	0.1	0.1	0.0	0.0	0.0	11.0	13.8	15.5
15	$D_{\mathrm{w},c_{\mathrm{w}}}(M_{\mathrm{db},0})$	Fig. 4.4b	11.0	13.9	16.3	1.1	0.9	0.8	39.5	15.5	9.9
16	$D_{\mathrm{g,eff}}(S_{\mathrm{g},0})$	Fig. 4.4b	3.4	8.5	13.3	1.4	2.3	2.3	25.8	9.0	5.3
17	$\boldsymbol{J}_{\mathrm{w,darcy}} = \boldsymbol{0}$		2.8	1.3	1.0	0.1	0.0	0.0	3.0	0.5	0.3
18	$\boldsymbol{J}_{\mathrm{g,darcy}} = \boldsymbol{0}$		0.5	1.0	1.5	0.2	0.4	0.4	3.5	2.4	1.7
19	$\boldsymbol{J}_{\mathrm{e}} = \boldsymbol{0}$		0.3	0.7	1.1	0.1	0.1	0.2	1.5	1.9	1.9
20	$(\rho c_{\mathrm{p}})_{\mathrm{eff}}(S_{\mathrm{w},0})$		0.9	2.0	2.8	0.2	0.3	0.4	4.4	4.5	4.0
21	$\kappa_{\mathrm{eff}}(S_{\mathrm{w},0})$	Fig. 4.4c	4.0	10.8	18.1	1.0	1.9	2.4	24.5	41.7	48.7
22	$\dot{I} = 0$ (global)		131.2	317.7	485.8	15.5	22.5	24.6	99.6	99.9	100.0
23	$\dot{I} = 0$ (Eq. (2.50))		3.1	1.7	0.6	0.1	0.4	0.6	100.0	100.1	100.1
24	$\dot{I} = 0$ (Eq. (2.52))		126.1	314.0	483.7	2.2	4.8	6.5	96.3	94.9	95.4
25	$K_{\mathrm{evap}} = 10\,000\,\mathrm{s}^{-1}$	Fig. 4.5	0.2	0.2	0.1	0.0	0.0	0.0	0.8	0.2	0.1
26	$K_{\mathrm{evap}} = 100\,\mathrm{s}^{-1}$	Fig. 4.5	1.5	1.1	0.9	0.2	0.1	0.0	2.3	1.1	1.0
27	$K_{\mathrm{evap}} = 10\,\mathrm{s}^{-1}$	Fig. 4.5	15.5	10.5	8.4	1.1	0.5	0.3	10.8	3.7	2.5
28	$K_{\mathrm{evap}} = 1\,\mathrm{s}^{-1}$	Fig. 4.5	92.9	103.0	65.3	5.0	2.8	1.8	60.3	13.2	6.6

34.0%, $E_{\mathrm{rms}} = 59.8\,\mathrm{Pa}$, $E_{\mathrm{max}} = 66.4\,\mathrm{Pa}$) are significantly high when α_{tot} is reduced by 20%. The results of studies 1–4 serve as a reference for the conjugate simulations in this chapter.

The reference simulation [175] assumes constant transport properties of water, denoted with index w, and carbohydrate, indicated with index s for solid matrix. A systematic switch to temperature-dependent relations by Choi and Okos [6, 42] reveals the model error of this assumption. With a maximum $E_{\mathrm{map}} = 6.5\%$ for S_{w} and $E_{\mathrm{map}} = 9.7\%$ for p, the error levels for temperature-dependent transport variables of carbohydrate, see study 9, are within the sensitivity range of study 1–4. Study 7 shows that no significant sensitivity can be found for $c_{p,\mathrm{s}}(T)$. Therefore, the main contributions can be linked to $\rho_{\mathrm{s}}(T)$ and $\kappa_{\mathrm{s}}(T)$, see studies 6 and 8. Utilizing temperature-dependent transport for water, a weak sensitivity $E_{\mathrm{map}} = 2.8\%$ can be established for $\rho_{\mathrm{w}}(T)$ on S_{w}, see studies 9–12. However, changes of $E_{\mathrm{map}} = 2.8\%$ in the water saturation do not seem to couple into temperatures and pressures. No significant influence can be linked to $\kappa_{\mathrm{w}}(T)$ and $c_{p,\mathrm{w}}(T)$.

The viscosities of water and gas are in the denominator of the Darcy velocity formulation, and smaller values induce proportionally larger fluxes. Although $\mu_{\mathrm{w}}(T) \in [1.0 \times 10^{-3}, 2.2 \times 10^{-4}]\,\mathrm{kg\,m^{-1}\,s^{-1}}$ varies by one order of magnitude, no significant change can be observed, see study 13. In contrast, the slight variation of $\mu_{\mathrm{g}}(T) \in [1.78 \times 10^{-5}, 2.15 \times 10^{-5}]\,\mathrm{kg\,m^{-1}\,s^{-1}}$ influences the pressures, see study 14. However, the pressure changes of $E_{\text{map}} = 15.5\%$ do not coordinate with the temperatures and water saturations. The influence of intrinsic gas and water permeabilities has not been investigated here, as this has already been done by Ni [175]. No visually observable deviation of temperature profiles could be found for variations of one to two orders of magnitude in $k_{\text{g,in}}$ or $k_{\text{w,in}}$.

In the description of the working mechanisms of this model, pressure-driven mass fluxes are considerably lower than capillary or binary diffusion. Omitting the Darcy mass fluxes $\boldsymbol{J}_{\text{w,darcy}} = \boldsymbol{0}$ and $\boldsymbol{J}_{\text{g,darcy}} = \boldsymbol{0}$, see studies 17–18, confirms a comparably low influence of $E_{\text{map}} = 2.8\%$ on S_{w} and $E_{\text{map}} = 3.5\%$ on p. Both omissions have insignificant influence on T ($E_{\text{map}} = 0.4\%$).

Leaving out capillary and diffusive fluxes leads to divergence. The simulation stops because of too high temperatures, resulting in steep gradients in p and S_{w} as the surface dries out. Therefore, one can assume a strong dependence of the model on capillary and binary fluxes that provide sufficient moisture to the hot surface region. Leaving $D_{\mathrm{w},c_{\mathrm{w}}}$ or $D_{\text{g,eff}}$ fixed to initial conditions, indicated by dotted lines in Fig. 4.3c and Fig. 4.3d, confirms their relatively strong influence on all variables, see studies 15–16. As the influence of the pressure equation is ruled out by study 23, discussed later in this section, the variations are likely caused by altered water saturation profiles S_{w}. Leaving $D_{\mathrm{w},c_{\mathrm{w}}}$ constant at initial moisture conditions results in increased capillary fluxes, see Fig. 4.4b. As a consequence, the saturation profiles are more diffuse. The reduced water saturations effect decreased effective thermal conductivities and, consequently, colder temperatures. Leaving $D_{\text{g,eff}}$ constant at initial gas saturations results in slightly decreased binary fluxes, see Fig. 4.3c. The transition front from dry to moist levels is slightly shifted to the right (i.e., it is delayed temporally). The delay owing to $D_{\text{g,eff}}(S_{\text{g},0})$ effects remarkably higher temperatures in the core region ($E_{\text{map}} = 2.3\%$, $E_{\text{rms}} = 8.6\,\mathrm{K}$, $E_{\text{max}} = 10.4\,\mathrm{K}$).

Studies 15 and 16 reveal a strong sensitivity of the temperatures to capillary and binary fluxes. However, leaving out all convective energy fluxes $\boldsymbol{J}_{\mathrm{e}} = \boldsymbol{0}$, leading to $\boldsymbol{J}_{\mathrm{w}} = \boldsymbol{J}_{\mathrm{g}} = \boldsymbol{0}$ in Eq. (2.57), highlights the insensitivity of the model to convective fluxes in the energy equation, see study 19. Hence, the influence of studies 15 and 16 can be related to the altered moisture profiles and not to altered convective fluxes in the energy equation. This finding aligns with findings in [175]. Study 20 investigates the transient term of the energy equation. The effective quantity $(\rho\, c_p)_{\text{eff}}$ is fixed to initial composition of the model by setting $S_{\mathrm{w}} = S_{\mathrm{w},0}$ in Eq. (2.58), indicated with dotted lines in Fig. 4.3a. Otherwise, $(\rho\, c_p)_{\text{eff}}$ varies from core to surface by one order of magnitude (2.1 to $0.6 \times 10^{6}\,\mathrm{J\,m^{-3}\,K^{-1}}$). Only a low influence on temperatures ($E_{\text{map}} = 0.4\%$) can be found for the case when this variation is omitted. Study 21 applies the same fixation to κ_{eff}. The relatively strong influence on all variables is comparable to the sensitivities of studies 4 and 16. The findings on κ_{eff} align with crust formation theories and resulting lower thermal conductivities in [54].

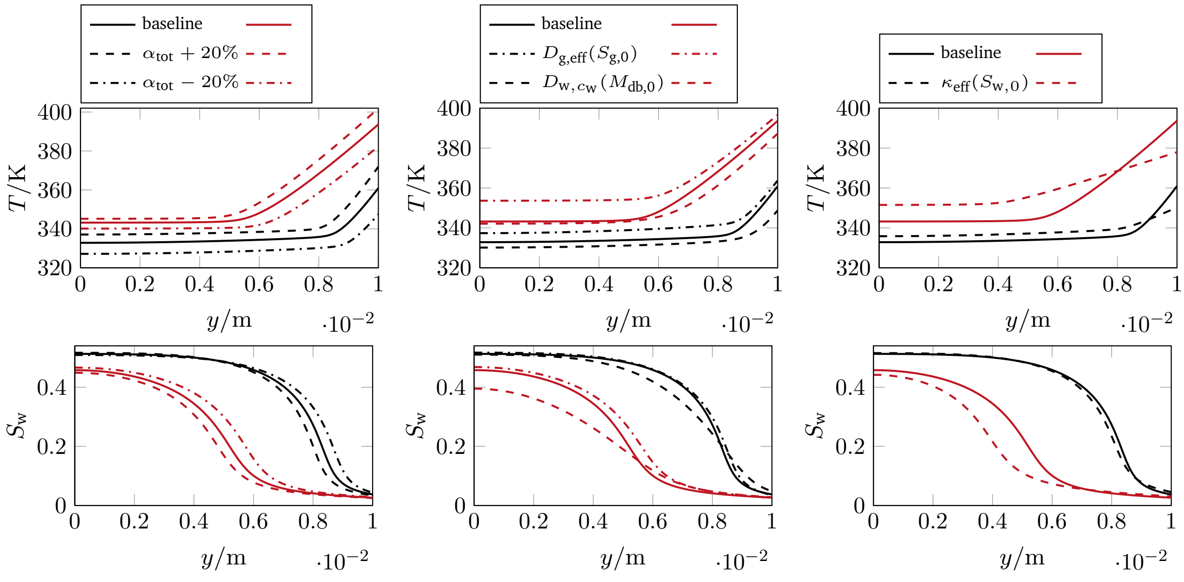

(a) Varied heat transfer coefficient by 20%.

(b) Fixed diffusivities to initial conditions.

(c) Fixed composition to initial conditions.

Figure 4.4. Selected graphs of the most sensitive parameters of the hygroscopic, capillary-porous media model at $t = 20\,\text{min}$ (black) and $t = 60\,\text{min}$ (red). Solid lines represent the baseline validation simulation. $t = 40\,\text{min}$ is omitted for a better readability.

Evaporation proves to be the most dominant mechanism. Removing $\dot{I}$ from all equations turns the model close to invalidity, as is to be expected, see study 22. More instructive is removing $\dot{I}$ from the mass balance for gas only, see study 23. It results in a quasi-deactivation of the pressure equation. Whereas pressures remain almost zero ($p \in \pm 0.5\,\text{Pa}$), the radical change in the pressures leads to only minor deviations in T ($E_{\text{map}} = 0.6\%$) and S_w ($E_{\text{map}} = 3.1\%$). The model is insensitive to pressures and pressure-driven flow at the present operational conditions. Removing $\dot{I}$ from the mass balance for vapor leads to divergence in the first step, although initial time steps are on the order of $\Delta t = 1 \times 10^{-7}\,\text{s}$. Removing $\dot{I}$ from the mass balance for water leads to its quasi-deactivation, as saturation levels mainly remain at initial conditions. Consequently, no crust region forms and temperatures rise uniformly to approximately $330\,\text{K}$. After $3600\,\text{s}$, this translates in $E_{\text{map}} = 6.5\%$, $E_{\text{rms}} = 28.0\,\text{K}$, $E_{\text{max}} = 62.8\,\text{K}$ for temperatures — a drastic, but plausible result, given the fact that the model has been stripped of its core working mechanisms.

The sensitivity study concludes with an investigation of the non-equilibrium evaporation formulation. The value of K_{evap} was set to $1 \times 10^3\,\text{s}^{-1}$ in [147] and also in this work. The value was estimated to be $1 \times 10^4\,\text{s}^{-1}$ in [107]. For a sensitivity analysis, it is changed step-wise by one order of magnitude. High values force the system to quickly transition to thermal equilibrium [53]. As noted by Datta [54] and Joardder et al. [133], this leads to numerical instabilities. The issue can be confirmed for the implementation of this work, but it was found to be much more pronounced

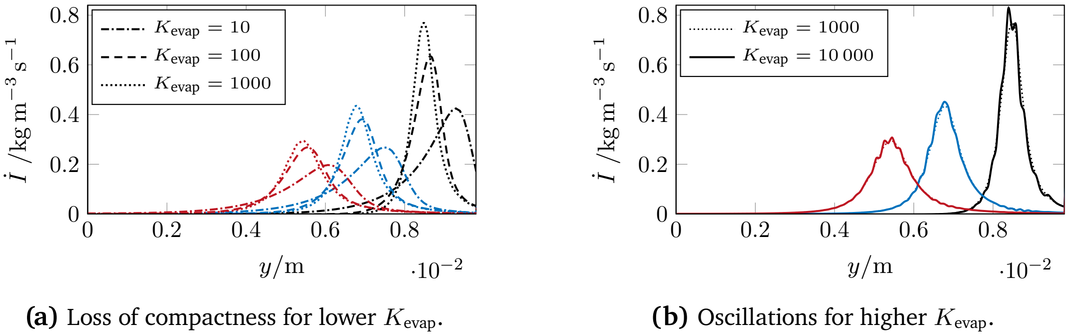

(a) Loss of compactness for lower K_{evap}.

(b) Oscillations for higher K_{evap}.

Figure 4.5. Influence of K_{evap} variations by orders of magnitude at $t = 20\,\text{min}$ (black), $t = 40\,\text{min}$ (blue) and $t = 60\,\text{min}$ (red).

only for a low-order polynomial FEM ansatz. As a consequence, cubic Hermite elements are chosen. Continuity and equality of the function value and the first derivative at the nodes of the Hermite finite elements provide smoother gradients of the primary variables. Even with a higher-order ansatz, Figure 4.5 illustrates how for $K_{\text{evap}} = 1 \times 10^4\,\text{s}^{-1}$ the evaporation rate starts to form a wave pattern superposed on the main evaporative front — a harbinger of numerical oscillations. Nonetheless, the general position and dimension of the evaporation front are already captured with $K_{\text{evap}} = 1 \times 10^3\,\text{s}^{-1}$. The front gets considerably diffuse for smaller values, significantly altering the simulation outcome in all variables, see studies 25–28. Figure 4.5a illustrates the loss of compactness of the evaporation front for lower K_{evap}. These results close the sensitivity studies of the capillary-porous media model for potatoes. Conclusions from the studies are drawn together with findings concerning the soft-matter model for meats, which is investigated hereafter.

4.1.2. Soft-matter model for meats

This section validates the implementation of the soft-matter model for chicken meat, analyses the working mechanisms and performs a sensitivity analysis. The thermal processing of chicken breast is simulated with the model presented in Sec. 2.3.2. The implementation is compared to experimental data by Rabeler and Feyissa [196]. The dimensions of the chicken fillet follow the experimental setup, where cuboids were cut out of chicken fillets. Figure 4.6 gives the model dimensions and characteristic measurement positions. Note that symmetry is exploited, and the two visible, vertical planes are the symmetry planes of the cuboid, whose total dimensions are $0.07\,\text{m} \times 0.02\,\text{m} \times 0.04\,\text{m}$. Along the surface of the food, a heat transfer coefficient α_{tot} is applied to model lumped convection and radiation effects related to the oven temperature T_{oven}. At the bottom, a higher heat transfer coefficient α_{bot} accounts for the interaction with the baking plate [196]. Table 4.3 summarizes the initial conditions and other model constants. The fibers of the chicken meat, modeled by κ_{para}, see Eq. (2.70), are oriented along the long side of the cube.

The model is implemented in the *Coefficient Form PDE* module of COMSOL Multiphysics. A quadratic Lagrange and a cubic Hermite ansatz are chosen for the spatial discretization of the

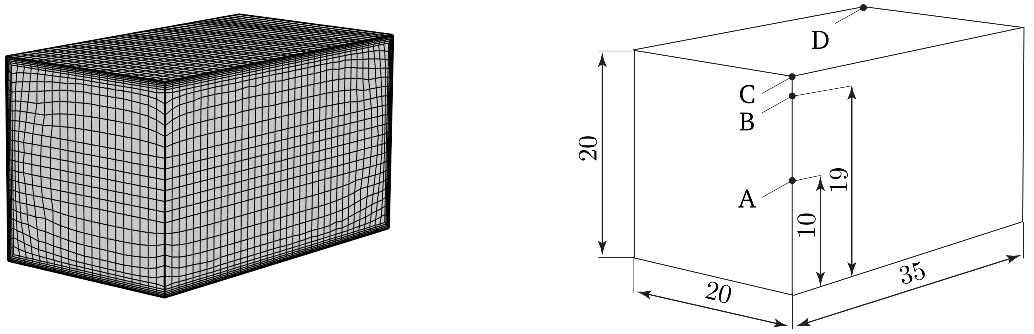

(a) Utlized mesh with inflation layers. **(b)** Dimensions (in mm) and measurement positions.

Figure 4.6. Mesh and dimensions of the quarter section model.

Table 4.3. Initial conditions and model parameters from Rabeler and Feyissa [196].

Variable	Name	Value
C_0	Initial mass fraction	0.76
T_0	Initial temperature	$279.15\,\mathrm{K}$
ρ_{cb}	Effective density of chicken	$1050\,\mathrm{kg\,m^{-3}}$
α_{tot}	Heat transfer coefficient	$44\,\mathrm{W\,m^{-2}\,K^{-1}}$
$\alpha_{\mathrm{tot,bot}}$	Heat transfer coefficient (bottom)	$50\,\mathrm{W\,m^{-2}\,K^{-1}}$
T_{oven}	Oven temperature	$443.15\,\mathrm{K}$
$\omega_{\mathrm{v,amb}}$	Ambient humidity	0.05
$\omega_{\mathrm{p,0}}$	Protein mass fraction	0.21
$\omega_{\mathrm{a,0}}$	Ash mass fraction	0.01
$\omega_{\mathrm{f,0}}$	Fat mass fraction	0.01

temperature and the moisture concentration. A grid study with uniform cell sizes $h \in \{1 \times 10^{-3}, 5 \times 10^{-4}, 2.5 \times 10^{-4}\}\,\mathrm{m}$ was performed to obtain a grid-independent solution with generalized Richardson extrapolation. The GCI, calculated following [208], is 0.04% and 0.2% for the finest solution of T and C at position B. The utilized mesh within the studies is manually refined to economize the grid size. $26\,500$ hexahedral elements, with a maximum height of $1 \times 10^{-3}\,\mathrm{m}$, are used to discretize the quarter section of the cuboid, see Fig. 4.6. Four inflation layers (stretch factor 1.2, $1 \times 10^{-4}\,\mathrm{m}$ first layer height) are designated to capture subsurface gradients. The resulting system of equations has $892\,611$ degrees of freedom. This grid has a relative discretization error of 0.02% and 0.2% for T and C compared to the grid-independent solution of the grid study outlined above. Time-stepping is performed with BDF(2) and with a maximum time step of $10\,\mathrm{s}$. The root mean square validation error is $E_{\mathrm{rms}} = 2.38\,\mathrm{K}$ for core temperatures T_{A}, $E_{\mathrm{rms}} = 3.43\,\mathrm{K}$ for surface temperatures T_{B} and $E_{\mathrm{rms}} = 0.01$ for the dry moisture content M_{db}. The corresponding percentage errors are depicted in Fig. 4.7a and Fig. 4.7b.

Working mechanisms of the model

When a chicken fillet is exposed to the hot air of temperature T_{oven} inside of a convection oven, heat is transferred to the surface by convection and radiation. As temperature rises in the surface region,

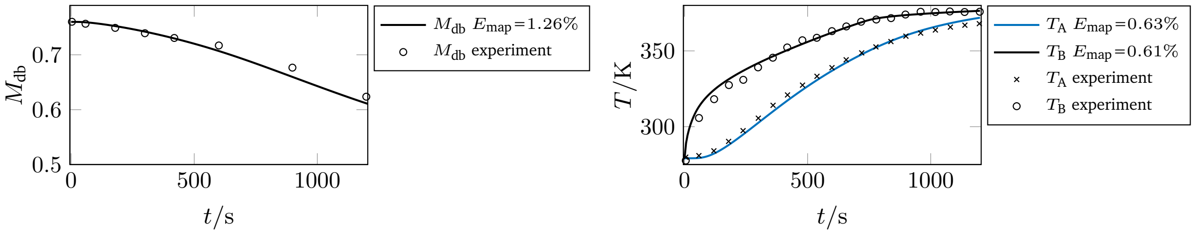

(a) Dry moisture content.

(b) Core and surface temperatures.

Figure 4.7. Validation of this work's implementation with experimental data of Rabeler and Feyissa [196].

see Fig. 4.8a, an increased water vapor saturation pressure $p_{\mathrm{v,sat}}(T)$ leads to an increased driving potential for the evaporation of water $\dot{m}_{\mathrm{evap}}$. The surface dries out, see Fig. 4.8b. Contemporarily, the protein denaturation sets in. The storage modulus G' of the food matrix increases with rising temperatures, whereas the water holding capacity C_{eq} decreases. The gradient of $C - C_{\mathrm{eq}}$, see Fig. 4.8c, induces the water velocities, see Fig. 4.8d. The excess moisture is expelled to the surface. The supplementary provision of water to the surface delays the drying of the surface and ensures further evaporative cooling.

Sensitivity study

The study of this section reveals the model sensitivity to a selection of its parameters and model terms. Besides variation of parameters in magnitude, a leave-out approach is followed for specific terms. Table 4.4 summarizes the sensitivity of the temperatures in points A and B and the moisture concentration on a dry basis M_{db}. Supplementary plots are added to Fig. 4.9 only for significant findings. The validation simulation that can be found in Fig. 4.7 serves as a baseline for comparisons and is represented by black and blue solid lines in Fig. 4.9.

The model shows more substantial sensitivities towards the surface heat transfer coefficient than towards the bottom heat transfer coefficient, see studies 1–4. Perturbing the former with a 20% magnitude, the resulting maximum temperature variation is $E_{\mathrm{max}} = +6.9\,\mathrm{K}$ to $E_{\mathrm{max}} = -8.2\,\mathrm{K}$ in the surface area. In contrast, the effective diffusivity D_{cb} had to be modified by one order of magnitude to cause variations above the level of the numerical discretization errors of the model, see studies 5 and 6. Notably, $D_{\mathrm{cb}} \times 0.1 = 3 \times 10^{-11}\,\mathrm{m}^2\,\mathrm{s}^{-1}$ does not alter the results significantly compared to the baseline simulation. This finding hints at a more pronounced sensitivity to convective than to diffusive mass fluxes of the model. This assumption is further confirmed when the water viscosity is held constant at $\mu_{\mathrm{w}} = 9.88 \times 10^{-4}\,\mathrm{kg}\,\mathrm{m}^{-1}\,\mathrm{s}^{-1}$ for one simulation, see study 7. The temperatures at point B deviate with $E_{\mathrm{max}} = +11.58\,\mathrm{K}$. The explanation can be found in Darcy's law, compare Eq. (2.80), where the viscosity is in the denominator. Within the temperature range of the model, the dynamic viscosity of water decreases from 1.5×10^{-3} to $3 \times 10^{-4}\,\mathrm{kg}\,\mathrm{m}^{-1}\,\mathrm{s}^{-1}$ in the baseline simulation. Increased fluid velocities lead to increased water exudation at the surface, which adds to the evaporative cooling.

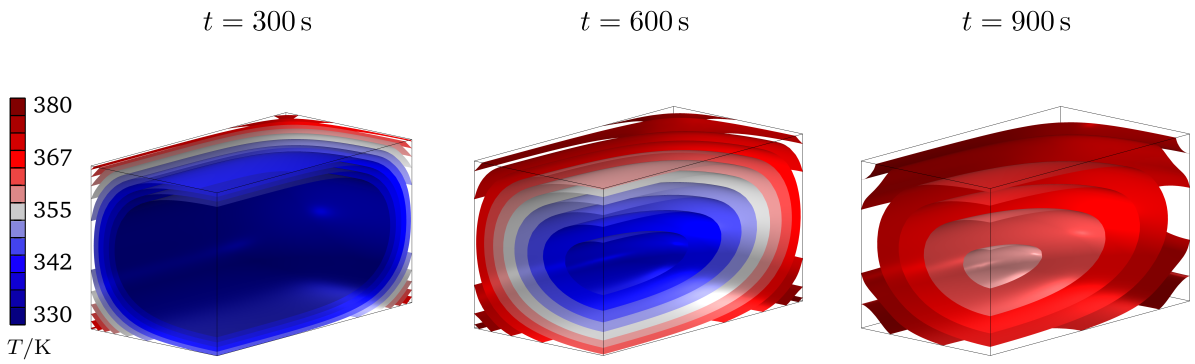

(a) Temperature.

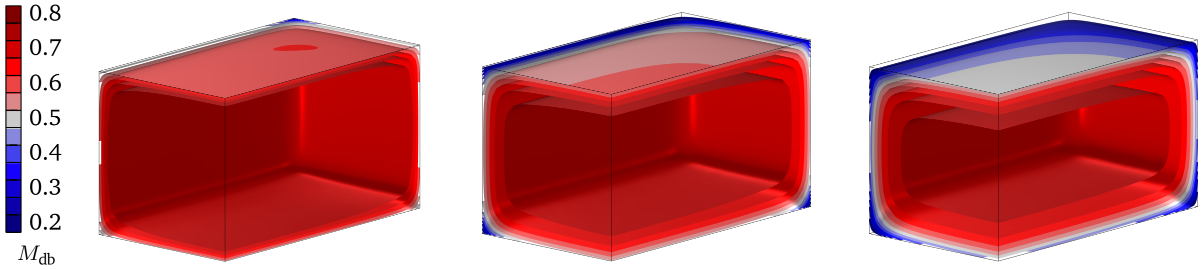

(b) Water mass concentration on a dry basis.

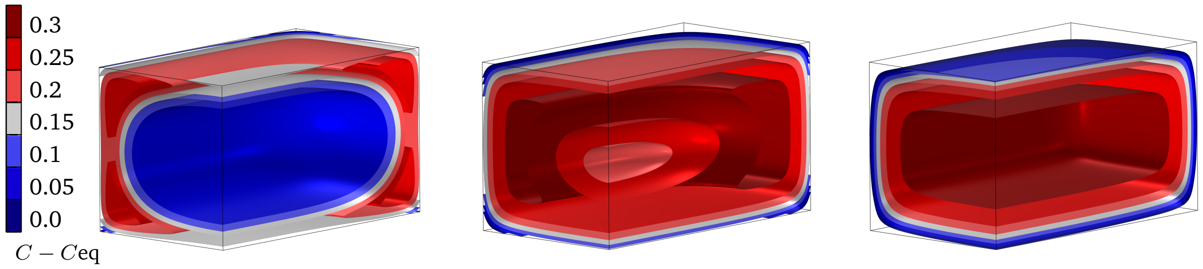

(c) $C - C_{\mathrm{eq}}$ whose gradient determines u_i.

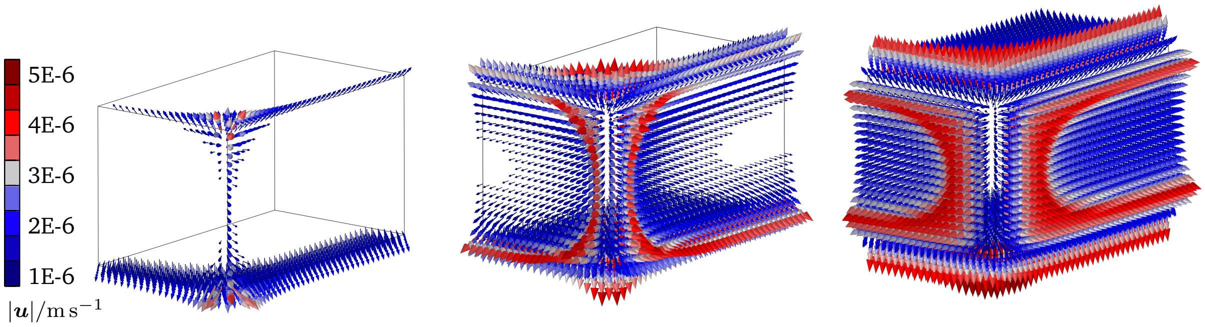

(d) Modeled water velocities u_i. Note the 180° rotation of the model to see the outside surfaces.

Figure 4.8. Spatial distribution and temporal evolution of T, C, $C - C_{\mathrm{eq}}$ and u_i.

Table 4.4. Sensitivity analysis data with deviations given by E_{map} (in $\%$) and E_{rms}, E_{max} (in K and -). Coloring is applied individually for each variable, from white for the 10th percentile of the error measure to blue for the 45th percentile and red for the 80th percentile.

Study	Case	Details	Temperature T_{A}			Temperature T_{B}			Concentration M_{db}		
			E_{map}	E_{rms}	E_{max}	E_{map}	E_{rms}	E_{max}	E_{map}	E_{rms}	E_{max}
1	$\alpha_{\text{tot,bot}} + 20\%$		1.43	1.76	2.64	0.28	0.38	0.86	0.003	0.004	0.007
2	$\alpha_{\text{tot,bot}} - 20\%$		1.76	2.18	3.28	0.34	0.47	1.04	0.004	0.005	0.009
3	$\alpha_{\text{tot}} + 20\%$	Fig. 4.9a	1.76	2.22	3.58	4.67	4.98	6.91	0.008	0.010	0.016
4	$\alpha_{\text{tot}} - 20\%$	Fig. 4.9a	2.25	2.85	4.49	5.65	6.02	8.20	0.009	0.012	0.021
5	$D_{\text{cb}} \times 10$		0.84	1.10	1.71	1.03	1.25	2.20	0.005	0.007	0.017
6	$D_{\text{cb}} \times 0.1$		0.17	0.22	0.35	0.21	0.25	0.41	0.001	0.002	0.004
7	$\mu_{\text{w}} = \text{const.}$	Fig. 4.9c	1.50	2.32	6.19	2.31	3.63	11.58	0.011	0.016	0.041
8	$a_{\text{w}} = 1$		0.13	0.18	0.31	0.17	0.19	0.33	0.001	0.001	0.003
9	$c_{p,\text{cb}}(\omega_{\text{k},0}, T)$	Fig. 4.10c	0.09	0.13	0.23	0.05	0.06	0.12	0.000	0.000	0.001
10	$\kappa_{\text{cb}}(\phi_{\text{k},0}, T)$	Fig. 4.10a	0.51	0.64	0.98	0.14	0.15	0.22	0.000	0.000	0.000
11	$\kappa_{\text{k}}(T_0)$	Fig. 4.10b	2.69	3.40	5.13	0.68	0.79	1.49	0.001	0.001	0.001
12	$c_{p,\text{k}}(T_0)$	Fig. 4.10c, 4.10b	0.17	0.23	0.37	0.08	0.10	0.23	0.000	0.000	0.001
13	$\rho_{\text{k}}(T_0)$		0.27	0.34	0.54	0.06	0.07	0.13	0.000	0.000	0.000
14	$u_i = 0$ in mass eq.	Fig. 4.9b	3.84	5.95	15.24	5.90	8.78	22.39	0.027	0.039	0.090
15	$u_i = 0$ in energy eq.	Fig. 4.9b	0.06	0.09	0.17	0.06	0.08	0.20	0.000	0.000	0.001
16	$u_i \times 2$ in energy eq.		0.06	0.09	0.17	0.06	0.08	0.19	0.000	0.000	0.001
17	$\beta_{\text{tot}} = \beta_{\text{ext}}$	Fig. 4.11b	6.86	8.87	14.12	8.59	10.08	15.51	0.030	0.036	0.052
18	$b = 5$ for β_{skin}	Fig. 4.11b	0.86	1.92	6.80	1.72	3.78	11.99	0.009	0.016	0.041
19	$b = 4$ for β_{skin}	Fig. 4.11b	0.90	1.27	3.35	1.90	2.71	8.35	0.005	0.008	0.023
20	$b = 3$ for β_{skin}	Fig. 4.11b	2.05	2.83	5.20	2.81	3.58	6.66	0.007	0.009	0.016

Opposed to the expectation, the artificial fixation of the water activity $a_{\text{w}} = 1$ does not lead to significant deviation, see study 8. Although the average water activity at the surface varies from 0.98 to 0.69 throughout one simulation, the induced deviations of temperatures and mass concentration are hardly measurable. The finding is surprising from the perspective that much attention is spent on accurately modeling water activities in food science literature [13, 205, 226]. Fixing the temporarily variable compositions of the food components ϕ_{k} and ω_{k} to fixed initial compositions in the effective thermal conductivities $\kappa_{\text{para}}, \kappa_{\text{perp}}$ and the specific heat capacity $c_{p,\text{cb}}$ does not alter the outcome of simulations above numerical error levels, see studies 9 and 10. The finding is notable, as the relative composition of chicken varies by 50% and $c_{p,\text{cb}}(\omega_{\text{k}}, T) \in [3648, 2905]\,\text{J}\,\text{kg}^{-1}\,\text{K}^{-1}$ over time, compare Fig. 4.10a and Fig. 4.10c. Similarly, the temperature-dependent transport quantities $\rho_{\text{k}}, c_{p,\text{k}}$ and κ_{k} are fixed to their value at initial temperature T_0, see studies 11–13. The model reveals only a slight sensitivity to temperature-dependent values of κ_{k} for core temperatures, see study 11. The findings on the transport parameters contradict [197], where $c_{p,\text{cb}}$ and κ_{cb} are identified as the most sensitive parameters.

The most pronounced sensitivity of E_{max} relates to the modeled fluid velocities u_i in the mass conservation. Temperatures and mass concentration differ considerably when the convective mass fluxes are omitted, see study 14. This finding hints at a strong dependence on accurate mass transport modeling. To put it differently, the model would lose its validity without the convective

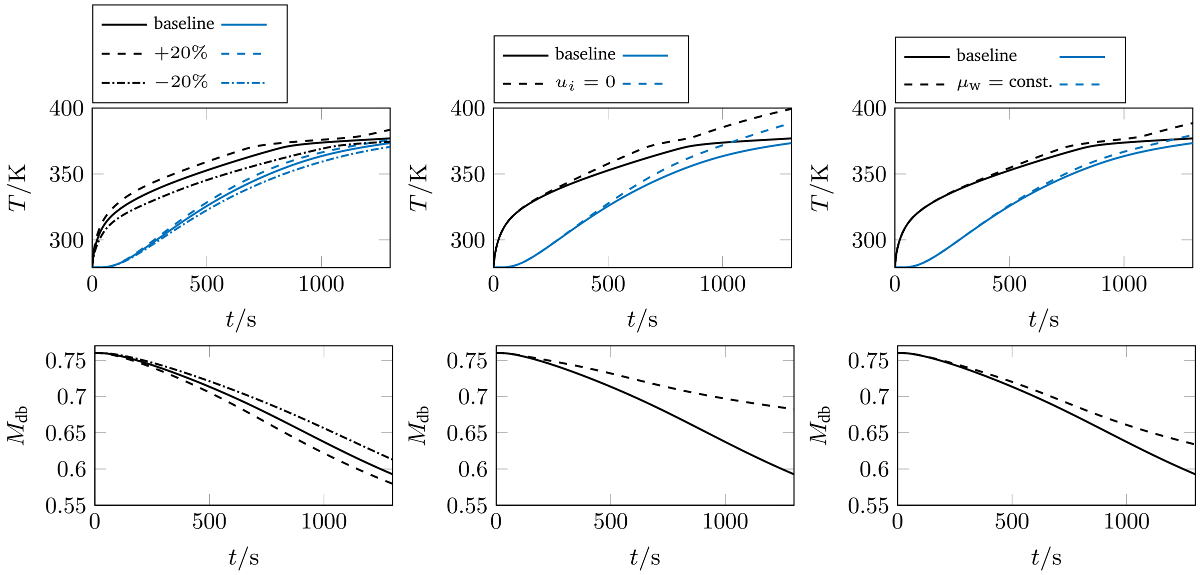

(a) Heat transfer coefficient. **(b)** Removal of water velocities. **(c)** Constant water viscosity.

Figure 4.9. Sensitivity and leave-out study of the soft-matter model. Blue and black solid lines represent the baseline simulation at positions A and B.

fluxes, which have been indirectly fitted to experimental data through G' and C_eq. Oppositely, the convective heat transport induced by u_i does not at all influence the temperatures of the model, see studies 15–16. This finding contradicts van der Sman's claims of non-negligible convective energy transport in [228]. Sman argues with an estimated Peclet number of $Pe \approx 10$. However, this study shows

$$Pe_\mathrm{avg} = \frac{|\boldsymbol{u}|\,\rho_\mathrm{w}\,c_{p,\mathrm{w}}\,H}{\kappa_\mathrm{w}} \approx 0.2\,, \tag{4.5}$$

where all quantities are averaged over space and time, and H is the height of the cube. Moreover, it could be demonstrated in this section that convective heat fluxes could be left out of the energy equation with negligible effects on the solution.

The most pronounced sensitivity of E_map and E_rms relates to neglecting the artificial mass transfer coefficient β_skin, see study 17. Omitting the latter results in a decrease in surface temperatures by 10 K on average, see Fig. 4.11b, leading to increased evaporation at the surface, which in turn can be traced back to the external heat transfer coefficient β_ext that is one order of magnitude higher than β_skin, see Fig. 4.11a. Sman [229] argues that chicken skin undergoes a glass transition that hinders moisture exudation. As a consequence, Sman introduces the artificial coefficient β_skin that is implemented in series to β_ext, compare Eq. (2.77). Figure 4.11a shows that as a consequence of the series model, the total mass transfer coefficient is almost exclusively governed by β_skin. In [229], a value of $b = 4 \pm 1.1$ in the modeling term for β_skin, compare Eq. (2.79), is proposed. A sensitivity analysis with constant exponents $b \in \{3, 4, 5\}$ reveals that temperature trajectories do not match

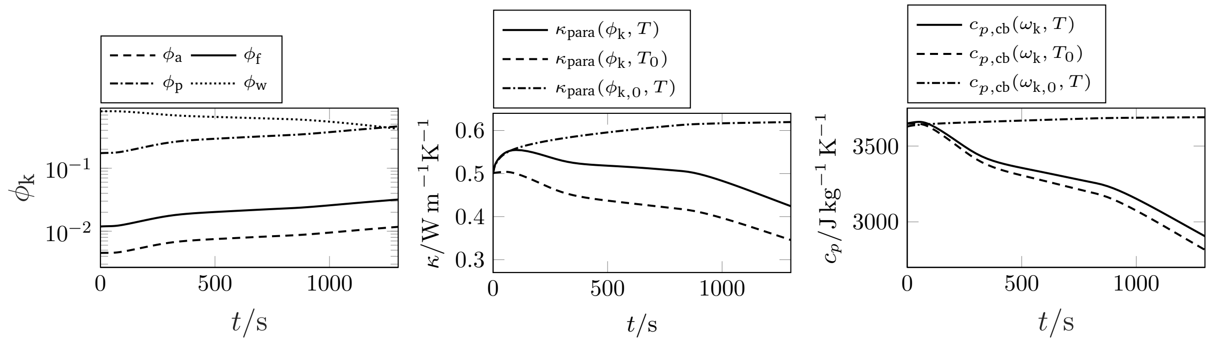

(a) $\phi_k(t)$ at position B. **(b)** κ_{para} at position B. **(c)** c_p at position B.

Figure 4.10. Variable composition determines the effective transport properties.

the baseline, see studies 18–20. Besides a wrong slope, no distinct cut-off behavior at boiling temperatures can be observed, as depicted in the upper right section in Fig. 4.11b. This finding contradicts the modeling of β_{skin} presented in [196, 197]. Rabeler [194] comments that *"different modifications to the Chilton–Colburn analogy or simple empirical approximations are used to obtain a better match with the experimental data"*, but no further details on the promoted modifications were provided. Similar studies by [21, 84] introduced a switching function f that cuts off the heat input into the model at boiling temperatures. Only when a similar approach is applied for b, e.g., the switching of $b = 5$ to $b = 3$ at boiling temperatures, the baseline temperature trajectories

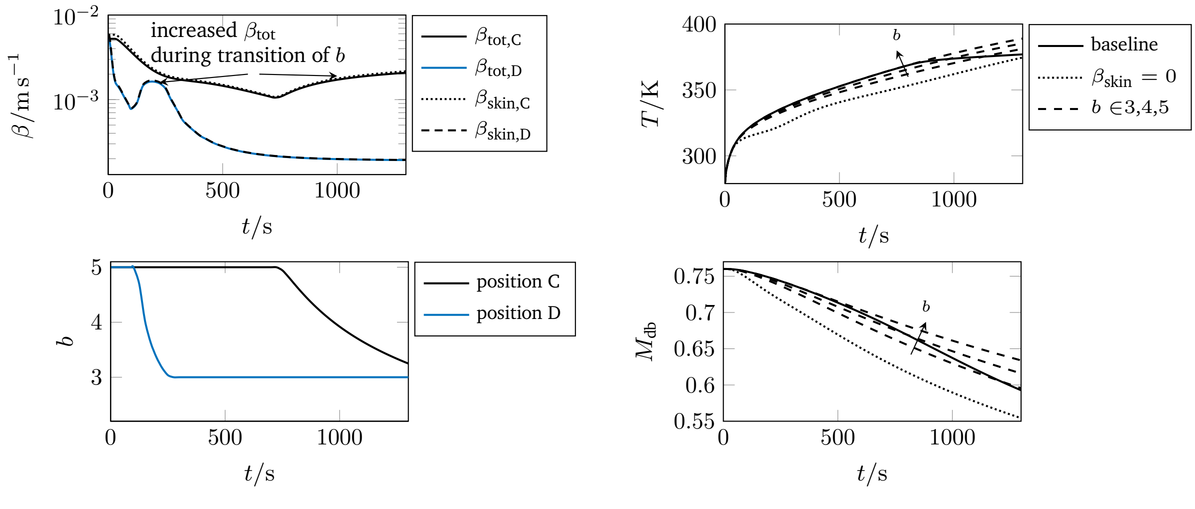

(a) Increased β_{tot} (top) during the transition of $b(T)$ (bottom). Observe the dominance of β_{skin} in β_{tot}, as $\beta_{ext} \approx 5 \times 10^{-2}\,\mathrm{m\,s^{-1}}$.

(b) Constant β_{skin} variation does not yield the baseline cut-off at boiling temperatures for T_B and to different M_{db}.

Figure 4.11. The transition of $b(T)$ at boiling temperatures induces increased total mass transfer coefficients, resulting in enhanced surface cooling.

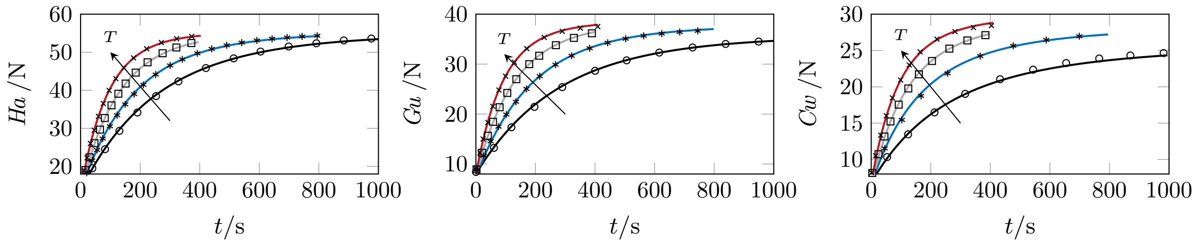

Figure 4.12. Validation of the implemented models with experimental data (markers) of [195] at constant temperatures $T = \{338.15, 348.15, 358.15, 368.15\}$ K. Modified reprint with permission of Pham [188].

can be attained. Figure 4.11a illustrates how the transition of b in β_{skin} clearly interferes with evaporative mass losses of the model. The transition of b induces a temporarily increased β_{tot}. As a consequence, increased evaporative cooling creates the characteristic "cut-off" in temperature trajectories that would not be present in the simulation data if no transition is applied.

4.1.3. Simulation of sensory quantities

The authors of the soft-matter model provided matching sensory models for the TPA quantities hardness, chewiness and gumminess in their studies [195, 196]. Within the scope of this work, an implementation by Pham [188] is utilized. Figure 4.12 depicts the validation of the model at various constant temperature levels, and Tab. 4.5 denotes the corresponding model parameters. The parameter variation given with ± indicates the value range in which the parameters are adjusted such that the model fits the experimental data provided in [195]. A good validation error of $E_{\text{map}} = 0.85\%$ is attained on average for all temperature levels and quantities.

The modified rate law of Eq. (2.87) describes a convergence of the sensory variable Q towards the final non-zero equilibrium quality value $Q_\infty(T)$. This is only valid for constant temperatures during one run. A simple test with alternating oven temperatures was performed in [188]. The core temperature T_{A} of the soft-matter model was used as an input to the sensory model for hardness Ha. Figure 4.13 reveals how decreasing food temperatures induce a questionable reversible behavior of Ha. No approach to mitigate these effects can be found in the literature to date. In response, a simple adaption was proposed together with Pham in [188], where further investigations and details can be found. The essential idea of the modification is to include a simple logic during the temporal integration of the sensory ODEs. It verifies the current value of $Q_\infty(T)$, which is the final value towards which the variable $Q(T)$ converges. In the case $Q_\infty(T) > Q(T)$, the model remains unchanged. For the case $Q_\infty(T) \leq Q(T)$, the value of $Q_\infty(T)$ is set to the current value $Q_\infty(T) = Q(T)$. Figure 4.13 illustrates how this modification effectively removes the reversible behavior. Although this change enables the usage of the model for alternating food temperature, it would need further validation with experimental data, which is beyond the scope of this work.

Table 4.5. Kinetic parameters for Ha, Gu and Cw for validation [188].

Q/N	n	$E_a/(kJ/\mathrm{mol})$	$k_0/(\mathrm{min}^{-1}[Q]^{1-n} \times 10^3)$	$Q_{\max}$/N	Q_0/N	T^*/K	ΔT^*/K
Ha	1.076 ± 0.016	39.3 ± 2.7	196 ± 8.3	55.2 ± 3.5	14 ± 1.4	318.15 ± 1.5	4 ± 1.1
Gu	1.052 ± 0.012	35.9 ± 2.2	64 ± 4.1	38.6 ± 2.2	7 ± 1.1	320.15 ± 2.1	8 ± 1.4
Cw	1.268 ± 0.088	44.6 ± 3.5	773 ± 29	28.5 ± 1.5	6.9 ± 1.5	323.15 ± 2.9	10 ± 2.1

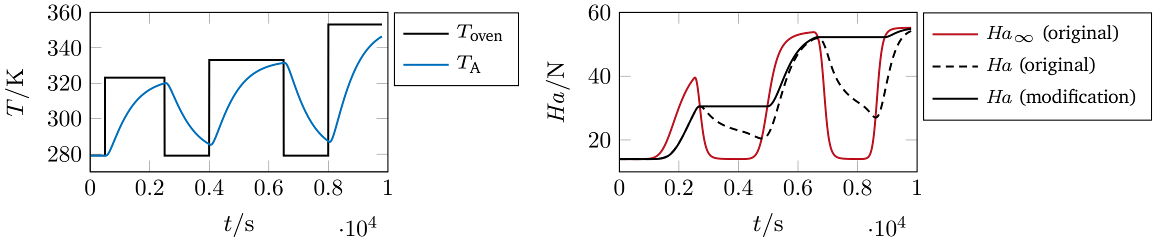

Figure 4.13. Mitigating the reversible behavior of the original model at decreasing temperatures with the proposed modification. Modified reprint with permission of Pham [188].

4.2. Conclusions from the food model analyses

The sensitivity analyses aim to estimate the sensitivity to variations in the heat and mass transfer coefficients compared to alterations of food-specific modeling terms. In summary, the hygroscopic, capillary-porous media model for potatoes has a medium-to-strong sensitivity to variable heat and mass transfer coefficients compared to the residual sensitivities that are presented. The sensitivity of the mass transfer coefficient β_{tot} to a 20% variation is in the same order of magnitude as the sensitivity to other model changes, such as transport properties (studies 5–14 and 20) or individual contributions of fluxes (studies 17–19). In terms of temperature, a 20% variation of the heat transfer coefficient (studies 3–4) is in the same sensitivity range as the food-specific model variations (studies 15, 16 and 21). Only a low-to-medium sensitivity can be established concerning variable carbohydrate properties and low sensitivity to variable water properties (studies 5–14). Studies 19 and 20 demonstrate a low sensitivity of the energy equation to mass fluxes and variable composition of the food. A weak coupling of the model to Darcy flow (and its related transport quantities, e.g., temperature-dependent viscosity) is observable in studies 17 and 18. These findings align with the discussion of negligible over-pressures for convective heating scenarios in [54]. Consequently, forthcoming analyses of the model, particularly in a conjugate setting, do not focus too much on pressures. In contrast, the model shows a strong dependence on capillary water and binary gas fluxes (studies 15–16), variable composition in effective conductivity (study 21) and accurate evaporation modeling (studies 22–28). The latter should be excluded from the sensitivity comparison with variable heat and mass transfer coefficients, as the radical changes to the evaporation modeling invalidate the model. However, these tests reveal a plausible behavior of the model (e.g., failure), when key model elements are removed.

Summarizing the findings of the soft-matter model sensitivity study, one can observe a strong sensitivity on heat transfer coefficients (studies 1–4) compared to all other performed variations (studies 5–13). The model has a low-to-medium sensitivity to water diffusivity (studies 5–6) or variable composition and temperature-dependent transport coefficients (studies 9–13), except for variable thermal conductivities. These findings are similar to the hygroscopic, capillary-porous media model results. The sensitivity study reveals a strong sensitivity concerning the modeled swelling pressure flow and the corresponding variables (e.g., μ_{w}) in the mass conservation equation. However, there is negligible sensitivity concerning the convective fluxes in the energy conservation equation (studies 15–16). This finding contradicts claims of non-negligible convective energy transport in [228], as discussed in the previous section. Testing the model for plausibility, one can observe — surprisingly — a low sensitivity to water activity (study 8), although a_{w} typically should determine the evaporative losses. On the other hand, one can observe a strong sensitivity concerning the modeled skin mass transfer coefficient and the corresponding variables, e.g., $b(T)$. Generally, the investigated model for the convective heating of chicken meat contains fitted model parameters, e.g., the equations for G' and C_{eq}. The temperature trajectories, especially at boiling temperatures, are enforced artificially by modifying the evaporative losses through β_{skin}. The model generalization remains an open question, as the swelling pressure mechanism is fitted to reproduce experimental temperature and moisture content data. At the same time, the evaporation is modified to artificially enforce temperature cut-offs at boiling temperatures. Indeed, [229] reports problems in predicting conditions beyond the boiling point. In conclusion, the sensitive, fitted behavior of the model does not qualify the model to be directly suitable for conjugate simulations. Whereas the formation of a glassy skin may be relevant for simulations in general, how the skin behavior could be included in a conjugate setting remains an open question. On the contrary, the hygroscopic, capillary-porous media model shows plausible behavior based on the validation, the investigation of the working mechanisms and the results of the sensitivity study. It does not apply empirical modeling approaches at the boundary condition (e.g., skin coefficients), and it was rigorously derived from first principles. The modeling of crucial parameters, such as capillary diffusivity and permeability, are aligned with experimental data as closely as possible. Contrasting both models, the hygroscopic, capillary-porous media model seems to be more plausible and suitable for conjugate simulations. However, the soft-matter model for chicken meats reveals its merits in combination with the matching models to predict the final sensory qualities of interest. Consequently, the soft-matter model is employed for the MPC case studies in Chapter 6. Therefore, ROMs of the soft-matter model are derived in Chapter 5. Likewise, the proposed data-driven ROM methodology is cross-validated with the hygroscopic, capillary-porous media model in a conjugate setting.

As the state of the art revealed, food science literature focuses on the exact modeling of the interactions within the food and less with its surroundings. The sensitivity study and leaving-out model terms demonstrate that some modeling aspects in food models have a relatively moderate influence on the simulation outcome, e.g., the modeling of water activity (for the soft-matter model), mass diffusivities, variable compositions or temperature-dependent transport properties. On the other hand, the heat transfer coefficient is a sensitive parameter in both models. However, both investigated models lump radiation and convection in the form of a constant value over space and time. It appears advantageous to improve the modeling of the thermal interaction with the food's surroundings with a conjugate heat and mass CFD simulation, which is the aim in Sec. 4.3.

4.3. Conjugate simulations of thermal food processing

This section aims to construct and analyze a conjugate thermal food processing model. It allows a comparison of models applying a heat transfer coefficient and models employing conjugate heat transfer. Their respective influence on the trajectories of temperature, moisture concentration, vapor concentration and pressure inside of the food is of primary interest. Similar to the benchmarks of the food models at the beginning of this chapter, this section performs plausibility checks of the conjugate simulation model concerning convective and radiative heat transfer in the oven cavity. Finally, the hygroscopic, capillary-porous media model for potatoes is investigated in a conjugate setting, where a fully coupled simulation of thermal food processing in a convection oven is performed. This chapter closes with conclusions from the conjugate heat transfer simulations.

4.3.1. Thermal fluid flow and radiation benchmarks

The thermal processing of food in a convection oven is dominated by two physical effects: convection and radiation. For testing the simulation setup, the process is split up into standard cases where sufficient experimental data exists: the flow of hot air over a flat plate (representing oven walls and baking tray), the flow over a cylinder (representing the food item) and radiative heat exchange in a cavity enclosing an ellipsoid (representing a simplified radiative heat exchange of convection oven and food item). A particular focus is put on the plausibility and accuracy of the thermal fluid flow simulations, as they may be affected by the selected turbulence model (see Sec. 2.1.2) or the applied FEM stabilization methods (see Sec. 3.1.2).

Flow over a flat plate

The study of flow over a flat heated plate is well investigated theoretically and experimentally [156, 204, 268]. Empirical formulations exist for the local Nusselt number $Nu_x = \alpha\, x/\kappa$ from analogy considerations with the boundary layer theory [16, 128]:

$$Nu_x = 0.0296\, Re_x^{4/5}\, Pr^{1/3}\,, \tag{4.6}$$

$$Re_x = \frac{\rho\, U x}{\mu}\,, \tag{4.7}$$

$$Pr = \frac{c_p\, \mu}{\kappa}\,, \tag{4.8}$$

where Re_x is the local Reynolds number, Pr is the Prandtl number and U is the free stream velocity. Note that the temperature-dependent fluid properties are evaluated at a hypothetical

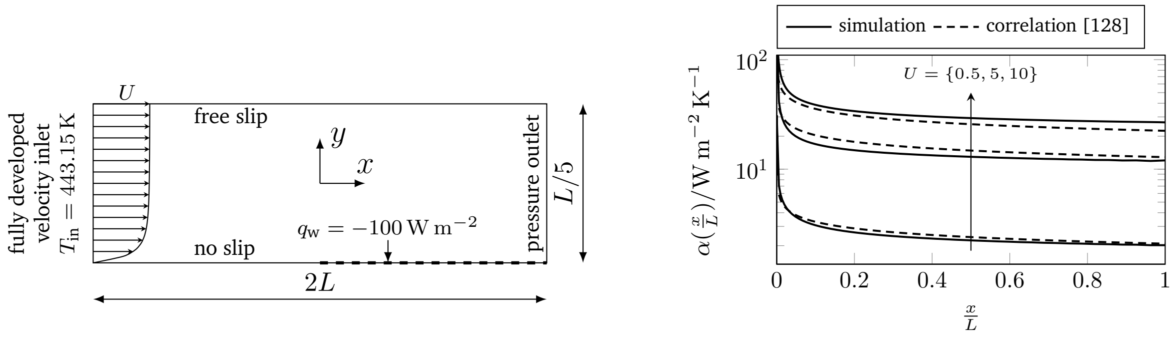

(a) Problem dimensions.

(b) Local heat transfer coefficient.

Figure 4.14. Benchmark of hot air flow over a cooled flat plate.

Table 4.6. Simulation metrics for the benchmark cases.

Metric	Flow over flat plate	Flow over cylinder	Radiative heat exchange
Mesh size	$h_{\text{max}} = 1 \times 10^{-1}\,\text{m}$	$h_{\text{max}} = 1 \times 10^{-2}\,\text{m}$	$h = 1 \times 10^{-2}\,\text{m}$
First inflation layer height	$h_1 = 2.5 \times 10^{-5}\,\text{m}$	$h_1 = 1 \times 10^{-6}\,\text{m}$	-
Average wall distance	$y^+ = 0.16$	$y^+ = 0.02$	-
Inflation layer stretch factor	1.05	1.2	-
Number of inflation cells	50	20	-
Scaled residual	$R < 5 \times 10^{-5}$	$R < 5 \times 10^{-5}$	$R < 1 \times 10^{-14}$
GCI [208] fine grid error	$E_{\text{GCI}} = 0.03\%$	$E_{\text{GCI}} = 0.15\%$	-

average film temperature $T_f = (T_{\text{wall}} + T_{\text{bulk}})/2$.

Figure 4.14a depicts the employed problem to investigate the predictability of the local heat transfer coefficient with a conjugate approach. Dry air with variable transport properties from [250] is utilized as a medium. The k–ω SST model with low-Re wall resolution is used to model turbulence. A *fully developed flow* boundary condition is given at the inlet, see Fig. 4.14a for an illustration of the velocity profile. Essentially, COMSOL Multiphysics extends the channel virtually to the left to allow the flow to develop a boundary layer. On the left half of the problem domain, hence for negative abscissae, the flow is not exposed to heat transfer at the boundaries and the velocity boundary layer of the fluid is given the possibility to stabilize. At $x/L = 0$ ($L = 5\,\text{m}$), the lower wall is cooled with a constant heat flux q_{w} and the thermal boundary layer forms (thickness $\delta_{\text{w}} \ll L/5$). The execution of the simulations again follows good CFD practice (e.g., see [77, 88]). Key metrics are given in Tab. 4.6. The free stream velocities $U \in [0.5, 10]\,\text{m}\,\text{s}^{-1}$ ($Re \in [1.62 \times 10^5, 3.31 \times 10^6]$) cover the spectrum of wind speeds in a convection oven of maximum $10\,\text{m}\,\text{s}^{-1}$ [49].

Figure 4.14b illustrates the reasonably good agreement of the simulated local heat transfer coefficient $\alpha(\frac{x}{L})$ with the empirical relation given in [128] with relative errors ranging within $E_{\text{map}} = 6$–12.9%. Moreover, the figure already underlines why constant, averaged heat transfer coefficients should not be employed when local heat transfer effects or varying free-stream conditions are investigated. Note that the turbulence model and the empirical correlation are designed for fully turbulent cases and cannot accurately model the transition from laminar to

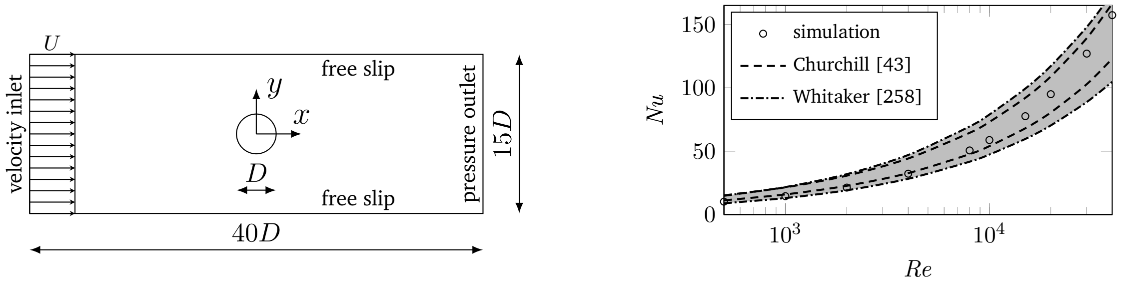

(a) Problem dimensions ($D = 0.12\,\mathrm{m}$).

(b) Comparison with two correlations and their respective error bounds.

Figure 4.15. Problem setup and comparison of flow over a cylinder simulations with two empirical correlations.

turbulent boundary layers, compare with [156] for a discussion. The onset of the transition also depends on the free-stream turbulence level, which is set to a medium value of $I_\mathrm{T} = 5\%$ for the present simulation.

Flow over a cylinder

The flow over a cylinder test case reasonably mimics hot air flow over a food item. Figure 4.15a illustrates the problem setup and key metrics of the simulated test case. The domain dimensions, mesh generation and simulation parameters again follow good CFD practice, see Tab. 4.6 for key metrics. The free stream velocity is $U \in [0.5, 10]\,\mathrm{m\,s^{-1}}$ ($Re \in [5 \times 10^2, 4 \times 10^4]$), and the free stream turbulence level is set to a medium value of $I_\mathrm{T} = 5\%$. Coherent structures of the von Kármán vortex street are resolved with a URANS approach and then appropriately averaged over at least ten periods. Figure 4.15b illustrates that the simulation model remains within the error bounds of 20–25% of the given correlations. The relative errors of the simulations compared to the correlation by Churchill are on average $E_\text{map} = 10.1\%$. Whitaker [258] gives a $\pm 25\%$ deviation from experimental data for his correlation, represented by the grey area. Lienhard [156] attests the correlation by Churchill [43] an underprediction of experimental data by 20% for $Re > 4 \times 10^4$. This might explain why the simulations lie in the upper band for higher Reynolds numbers.

Surface-to-surface radiation inside a cavity

Only for simple shapes analytical solutions can be found for radiative heat exchange, see [11, 128, 169] for background reading. Solving problems with more than three surfaces typically requires solving a system of linear equations — essentially solving the radiosity method (Sec. 2.2.2) by hand. However, it is possible to treat the walls of a simplified oven cavity ($0.4\,\mathrm{m} \times 0.4\,\mathrm{m} \times 0.4\,\mathrm{m}$) without baking plates as one surface (denoted with index 2). An ellipsoid represents the food item (denoted with index 1, semi-axes $0.06\,\mathrm{m} \times 0.03\,\mathrm{m} \times 0.015\,\mathrm{m}$), which is placed at the center of the cavity, see Fig. 4.16a for an illustration of the problem. As the shape of ellipsoids is convex,

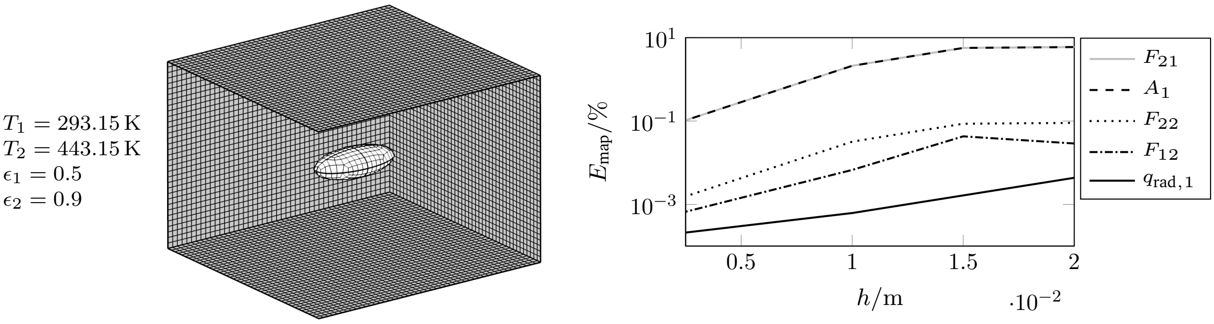

(a) Problem setup of the cavity for $h = 1 \times 10^{-2}\,\mathrm{m}$ (two walls are hidden).

(b) Relative errors of view factors, surface area and heat flux.

Figure 4.16. Relative error of the hemicube view factor calculation over mesh element size h. The most significant error is dominated by the discretization of the ellipsoid's surface area.

the self-irradiation view factor F_{11} is zero.

Following the derivation in [169], an analytical formula for the test case reads

$$F_{11} + F_{12} = 1 \Rightarrow F_{12} = 1 \quad \text{(conservation property of } F_{ij}\text{)}, \tag{4.9}$$

$$A_2 F_{21} = A_1 F_{12} \Rightarrow F_{21} = \frac{A_1}{A_2} \quad \text{(reciprocity property of } F_{ij}\text{)}, \tag{4.10}$$

$$q_{\mathrm{rad},1} = \frac{\sigma\left(T_1^4 - T_2^4\right)}{\frac{1}{\epsilon_1} + \frac{A_1}{A_2}\left(\frac{1}{\epsilon_2 - 1}\right)} \approx 883.24\,\mathrm{W\,m^{-2}} \quad \text{(energy conservation)}, \tag{4.11}$$

which holds (in its general form) for any convex object in a closed cavity. Figure 4.16b depicts the relative errors compared to the analytical solution over the surface mesh size. The hemicube view factor method operated with a default accuracy of 256 pixels. The most dominant error can be found for F_{21}, the cavity-to-ellipsoid view factor. It seems governed by the correct representation of the ellipsoid's surface area A_1 with rectangular surface elements. One can observe that the error for F_{21} closely follows the relative error of the surface area representation A_1. The error for the effective radiative heat flux $q_{\mathrm{rad},1}$ lies below $E_{\mathrm{map}} < 0.01\%$ for the surface mesh sizes of up to 2×10^{-2} m, which is well above the employed surface mesh sizes used in this work.

4.3.2. Hygroscopic capillary-porous model in conjugate flat plate configuration

This section represents an intermediate step on the path towards a conjugate convection oven model. It presents the implementation details and investigations of the hygroscopic capillary-porous model in conjugate configuration.

In the first step, the 1D implementation of the validation test case of Sec. 4.1.1 is extended to a 3D version in the *Coefficient Form PDE* module of COMSOL Multiphysics. The successful extension is ensured by running and comparing against the validation test case in x-, y- and z-direction in a pseudo-1D setup, respectively (results not shown for brevity). In the second step, the validation

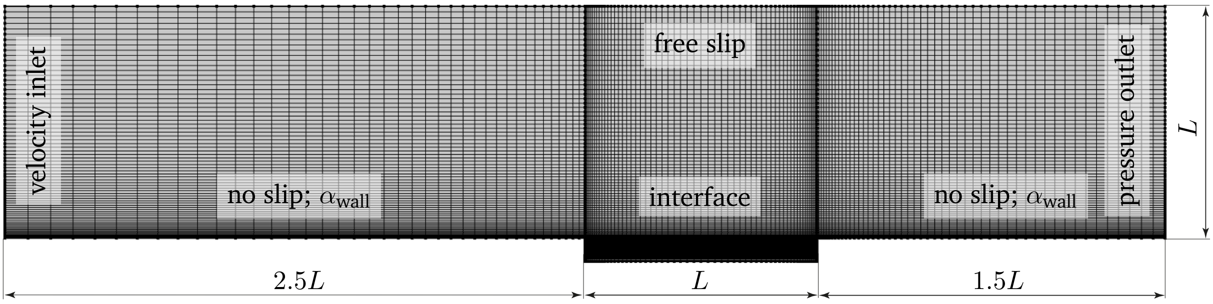

(a) Overview.

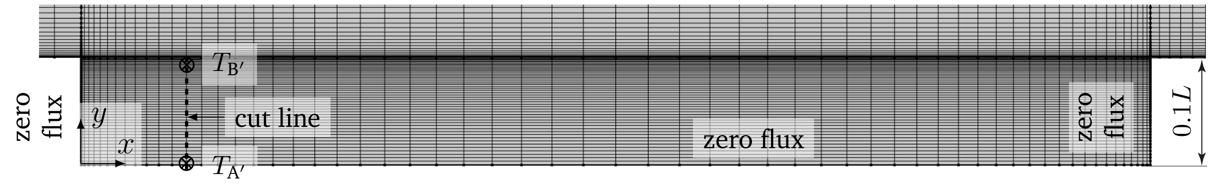

(b) Detailed view of the porous domain. Cut line and measurement positions are indicated for investigations.

Figure 4.17. The validation case of the hygroscopic capillary-porous model extended to a conjugate flat plate setup: dimensions, mesh and boundary conditions.

test case is implemented in a pseudo-2D setup in combination with the *flow over a flat plate* test case of Sec. 4.3.1. Figure 4.17 illustrates the resulting model with a potato slab of $L \times 0.1L$ ($L = 0.1\,\mathrm{m}$). The average inlet speed of a hot airflow ($T_{\text{oven}} = 450.15\,\mathrm{K}$) is held constant at $U = 5.25\,\mathrm{m\,s^{-1}}$ ($I_{\text{T}} = 5\%$) to induce an average heat transfer coefficient of $\alpha_{\text{tot}} \approx 20\,\mathrm{W\,m^{-2}\,K^{-1}}$, which is comparable to the validation test case. On the residual bottom wall of the fluid domain, $\alpha_{\text{wall}} = 15\,\mathrm{W\,m^{-2}\,K^{-1}}$ is prescribed to emulate the heat losses of a baking plate and to prevent a heating shock at the first contact point of the porous domain and the fluid domain. A no-slip condition is given at the bottom wall of the fluid domain, as no considerable obstruction of the airflow by evaporation from the porous food item (so-called blowing) is expected. The mesh design and general solver settings follow the methods described in Sec. 4.1.1 and Sec. 4.3.1.

The Richardson number

$$Ri = \frac{g\,\beta\,(T_{\text{wall}} - T_{\text{ref}})\,L}{U^2} \tag{4.12}$$

expresses the ratio of buoyant forces to inertial forces, where $T_{\text{ref}} = 448.10\,\mathrm{K}$ is the lowest average temperature in the problem domain and $T_{\text{wall}} = 450.15\,\mathrm{K}$ is the maximum temperature of a hot wall (e.g., the baking plate). For the present case, $Ri \approx 1.5 \times 10^{-4}$, which lies far below the threshold of $Ri > 0.3$ for mixed buoyant flow [230]. Consequently, no buoyant effects are considered in the conjugate simulations, and temperature-dependent viscosities are also neglected. From now on, a unidirectional coupling approach is followed for fluid-flow simulations to reduce the model's degrees of freedom during the conjugate simulation of the oven cavity and the food processing. The fluid flow of the oven cavity is pre-calculated under steady-state conditions for the average oven temperature.

The conjugate solution of temperature and vapor concentration in the cavity and the food domain is realized by treating temperature and vapor concentration as continuous fields over the cavity and food domains. Utilizing sub-nodes per domain in the *Heat Transfer in Solids and Fluids* module and the *Coefficient Form PDE* module ensures that COMSOL Multiphysics handles continuity of variables and fluxes, as introduced in Sec. 2.2.1. The energy conservation of the food model of Eq. (2.57) is ported to the *Heat Transfer in Solids and Fluids* module to make use of the built-in conjugate heat transfer capabilities of the *Nonisothermal Flow* module in the *Multiphysics* node. The food-specific modeling terms, such as $H_{\text{evap}}\,\dot{I}$ of Eq. (2.57), are included as additional volumetric source terms in the food domain.

To enable not only conjugate heat but also conjugate mass transfer, the conservation equation for water vapor must be solved both on the fluid and the porous domain. Although COMSOL Multiphysics has such a functionality in the *Moist Air* node in the *Transport of Diluted Species* module, it does not provide a distributed evaporation approach. Consequently, the conjugate mass transfer is implemented in the *Coefficient Form PDE* module. For the food domain, Eq. (2.51) is ported without changes. For the cavity, the new transport equation reads

$$\frac{\partial c_{\text{v}}}{\partial t} + v_i \frac{\partial c_{\text{v}}}{\partial x_i} = \frac{\partial}{\partial x_i}\left[\left(D_{\text{va}} + \frac{\nu_{\text{t}}}{Sc_{\text{t}}}\right)\frac{\partial c_{\text{v}}}{\partial x_i}\right]. \tag{4.13}$$

The second term on the left-hand side models the convective fluxes induced by the steady-state velocity field v_i, and the right-hand side models the diffusive mass transport of vapor in the fluid. The effective diffusivity $D_{\text{va,eff}} = D_{\text{va}} + \nu_{\text{t}}/\,Sc_{\text{t}}$ accounts for diffusion of vapor in the air ($D_{\text{va}} = 2.6 \times 10^{-5}\,\text{m}^2\,\text{s}^{-1}$) and enhanced turbulent mixing with a turbulent Schmidt number of $Sc_{\text{t}} = 0.8$ [242]. In Eq. (2.50) and Eq. (2.52), the conservation equations of liquid water and gas are left untouched and are solved exclusively on the porous domain. The boundary condition for water conservation at the top surface, Eq. (4.2), is replaced by a no flux condition without influence on the result, as water is removed exclusively by the distributed evaporation approach within the porous domain. The resulting vapor is convected away owing to the conjugate mass transfer for vapor.

For the following evaluations, the results of the conjugate simulation are evaluated at a vertical cut through the potato slab at $x = 0.01\,\text{m}$, indicated by a dashed line in Fig. 4.17b. Figure 4.18a compares the results of the conjugate simulation at the vertical cut (represented with dashed lines) with the results of the validation test case (represented with solid lines). Even for this simple conjugate setup, the variations in temperature, moisture saturation and pressure exceed the range of the sensitivity study of $\alpha_{\text{tot}} \pm 20\%$, marked with a grey band. When investigating the derived heat and mass transfer coefficients for the conjugate simulation, this is not a surprise. Although the air velocity and temperature are held constant, the derived heat transfer coefficient

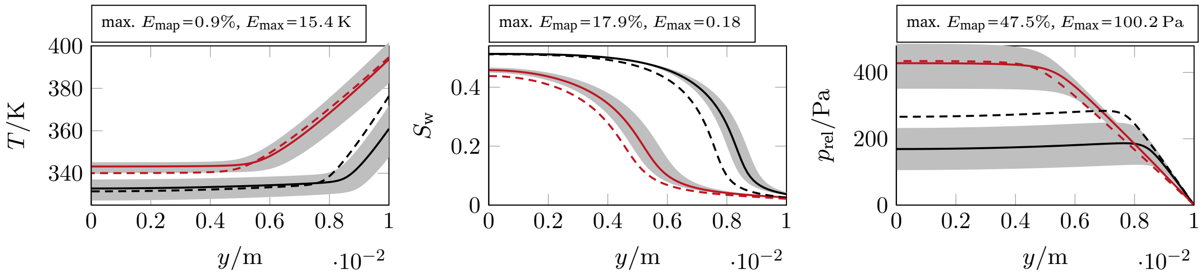

(a) Variations without considering radiation.

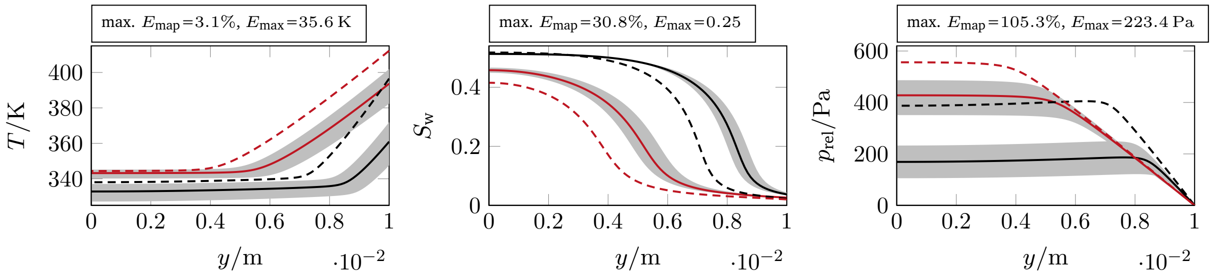

(b) Variations with considering radiation.

Figure 4.18. Comparison of conjugate flat plate setup at $x = 0.01\,\text{m}$ (dashed lines) with the transfer-coefficient-based validation case (solid lines) at $t = 20\,\text{min}$ (black) and $t = 60\,\text{min}$ (red). Deviations of $\alpha_{\text{tot}} \pm 20\%$ of the sensitivity study are represented by a gray band.

varies significantly in space and time, see Fig. 4.19a. For the first quarter of the potato slab, the coefficient varies more than 50% over time, although the preceding channel wall is pre-chilled with α_{wall}. The cause of the deviations is rooted in the temperature-dependent material properties of dry air (ρ, c_p, and κ). As the potato heats up, so does the thermal boundary layer, and heat transfer becomes less efficient owing to the decreased driving temperature gradient. A similar explanation holds for the local variation from left to right, as the hot air gets cooled during the passage over the porous food item. The derived mass transfer coefficient, calculated with Eq. (2.74), is approximately constant during the simulation, see Fig. 4.19b, as the driving material property $D_{\text{va,eff}}$ remains unchanged and given the steady-state velocity field. However, the magnitude of β_{derived} is one order higher than the estimation given in the article of the validation test case by Ni [175]. Presumably, turbulent effects, as simulated in this conjugate setup, were not considered in the empirical estimation of the mass transfer coefficient. So far, this study has demonstrated the successful extension of a food processing model into a multi-dimensional, conjugate heat and mass transfer model. The results foreshadow why the thermal processing of food should not be simulated with constant heat transfer coefficients, although geometric, temperature and fluid flow variations or thermal radiation have not been considered yet. The deviations for this simple conjugate setup exceed most of the model's sensitivities of food-specific modeling terms, recapitulate study 1–21 in Tab. 4.2.

Adding radiation for demonstration purposes to this setup with $\epsilon_{\text{wall}} = 0.9$ and $\epsilon_{\text{interface}} = 0.8$, approximately doubles the deviations in all variables, see 4.18b. With a maximum error of $35.6\,\text{K}$

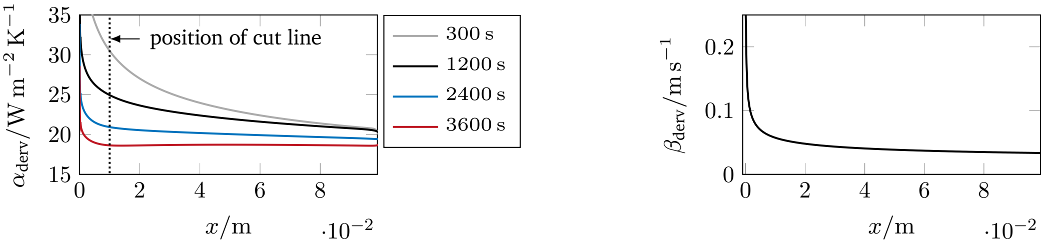

(a) Heat transfer coefficient. **(b)** Mass transfer coefficient.

Figure 4.19. Derived local heat and mass transfer coefficients from the conjugate simulation results.

in the surface temperatures and $E_{\text{map}} = 3.1\%$, the changes induced by the conjugate setup in terms of temperature are within the sensitivity range of one of the most crucial food model manipulations of the sensitivity study — the removal of evaporative source terms from the water conservation equation, see study 24 in Tab. 4.2. The deviation of $E_{\text{map}} = 30.8\%$ for the water saturation exceeds by far the maximum food model sensitivities of $E_{\text{map}} = 18.1\%$, recapitulate study 1–21 in Tab. 4.2. These results reveal that it is mandatory to consider radiation in the following derivation of the conjugate convection oven model.

4.3.3. Conjugate heat and mass thermal food processing in a convection oven

The conjugate fluid flow simulation models of Sec. 4.3.1 and the conjugate heat and mass food processing model of Sec. 4.3.2 are combined to model a hypothetical convection oven. Forced convection of non-isothermal hot air, surface-to-surface thermal radiation and the hygroscopic capillary-porous model in a conjugate configuration are utilized to model the thermal processing of two potato slices on two baking trays, see Fig. 4.20a for an illustration. Section 4.3.3.1 presents the modeling assumptions that are specifically tailored to investigate the effects of conjugate heat and mass transfer, including radiation. One designated goal of the convection oven simulations presented in Sec. 4.3.3.2 is to achieve a relative comparison of the heating effects and deliver a comparison with transfer-coefficient-based approaches. Conclusions of the convection oven simulations are given in Sec. 4.4.

4.3.3.1. Modeling assumptions

The geometry of a convection oven is inspired by standard consumer appliance, see Fig. 4.20a. In order to significantly save simulation time, a 2D model with similar dimensions is derived, see Fig. 4.20b. The impact that 2D modeling may have on the results shown, as well as an estimate of the simulation time of a 3D model, can be found in Sec. 4.4.

For representing a convection oven in a simulation model, the following modeling assumptions are made: The heating coil, the outlet grill and the ventilation system are not represented explicitly. Moreover, the geometric details of the oven, the two baking plates and the upper heating coils are simplified. This enables meshing with fewer elements. Following the usual working principle

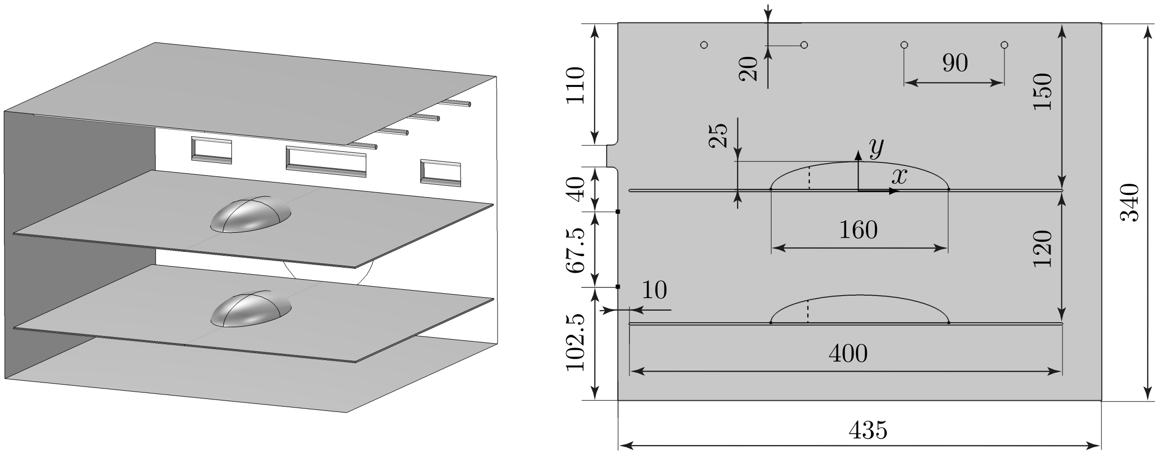

(a) 3D geometry of a convection oven inspired by a standard consumer appliance.

(b) Dimensions of the 2D model (given in mm).

Figure 4.20. Geometrical model of a conventional consumer hot air convection oven with two slices of potatoes on two separate baking plates.

of convection ovens [112], hot air is blown out of the rectangular duct into the oven cavity. A medium turbulence level of $I_\mathrm{T} = 5\%$ is set at the inlet. The velocity is chosen as $U = 5.25\,\mathrm{m\,s^{-1}}$ to induce average heat transfer coefficients comparable to the conjugate flat plate case of Sec. 4.3.2. A similarity of the conjugate flat plate and the convection oven model becomes relevant for the studies in Sec. 5.4, where this requirement is discussed in more detail. The outlet grill is modeled as a pressure outlet with zero relative pressure. Conventional convection ovens re-heat the air with heating coils mounted around a fan that blows the air back into the oven. Moreover, fresh air is continuously drawn into the cavity from the environment to renew the air. Likewise, a fume exhaust, usually located at the top of the cavity, evacuates portions of the cavity air into the surrounding kitchen [112]. These two mechanisms ensure that the hot, dry air inside of a convection oven does not saturate with fumes and steam of the food. As information is scarce on how the secondary fume exhaust system works, the following modeling approach is followed: Once air leaves the simulation domain through the outlet, it will not reenter the ducts. Thus, the modeling of a fume exhaust system is not considered.

Modeling of the plate-food contact is sophisticated. Owing to inhomogeneities and roughness of the food surface, the heat transfer partially occurs through direct contact and partially through thin films of liquids, steam or air [69, 256]. A common approach in the literature is to estimate a contact heat transfer coefficient from experimental data [69, 171, 209, 256]. As no experimental data exists for this work, plate-food contact modeling is excluded to avoid distortion of the results by loosely estimated parameters. Zero flux conditions are set on the contact line for all variables. These settings also facilitate comparing transfer-coefficient-based models (where no baking plates or oven cavities exist) with the results of the conjugate heat and mass transfer model.

Simulation of the thermal radiation requires specification of the emissivities of the participating surfaces. Oven walls and baking plates are usually manufactured from enameled sheet metal, with an emissivity of $\epsilon_{\text{enamel}} \approx 0.89$ [144, 250], which is used in this study. Heating rods are usually coated with electrically insulating ceramics, such as silicium carbide, which has $\epsilon \approx 0.8$ [190] at the operational surface temperatures of $T_{\text{rod}} \approx 1293\,\text{K}$ [3]. Almeida et al. [3] also measured the spectral emissivity of peeled potatoes, which is on average $\epsilon_{\text{pot}} \approx 0.8$.

Equation (2.29) introduced the reflected portion $\mathcal{R}$ of the incoming irradiation. This modeling assumes a purely diffuse reflection of incoming radiation. More general formulations, as implemented in COMSOL Multiphysics, also allow for specular reflection. The relative portion of specular reflection is specified as $\mathcal{R}_{\text{spec}} \in [0, 1]$. Data on the specular properties of enameled oven walls and windows is scarce. Thus, a parameter sweep for $\mathcal{R}_{\text{spec}} \in [0, 1]$ is performed for the *surface-to-surface radiation* test case of Sec. 4.3.1. The test reveals a relative deviation of maximum 0.7% on the heat flux $q_{\text{rad},1}$. Consequently, specular reflection effects are neglected. Whereas visible light can pass through the glass of an oven, a large share of thermal radiation is absorbed within the infrared band [11]. Additionally, the windows of convection ovens can be coated with reflective material to contain the thermal radiation inside the oven cavity [112]. Quartz glass and soda lime glass have an emissivity of $\epsilon \approx 0.84$–0.94 [213, 250]; therefore $\epsilon_{\text{glass}} = 0.89$ is employed for this model. The oven walls and front window are treated as well-insulated walls with a weak external heat transfer coefficient of $\alpha_{\text{ext}} = 1\,\text{W}\,\text{m}^{-2}\,\text{K}^{-1}$ with ambient temperatures of $293.15\,\text{K}$.

Utilizing a conjugate mass transfer model for water vapor raises the question of whether humidity influences the transport properties of air (κ, c_p) and whether gas radiation must be taken into account. As explained above, convection ovens continuously renew the air in the oven cavity by drawing fresh air out of the environment and evacuating moist air from the cavity [112]. Assuming a worst-case scenario of fully vapor-saturated room air at room temperature, the relative humidity inside of the cavity would fall below $\text{RH} = 0.01$ for heating the room air to $T_{\text{oven}} > 415.15\,\text{K}$. Tsilingiris [245] tabulated little influence of low humidity on the air's transport properties for the considered temperature range. Thus, the air is considered dry and is treated as an ideal gas. The temperature-dependent transport coefficients of dry air are taken from [250]. Considering the components of moist air with respect to gas radiation, only CO_2 and H_2O interact significantly with thermal radiation [11]. Those components of air exhibit relatively low partial pressures at room temperatures under standard atmospheric pressure, e.g., $p_{\text{CO}_2} \approx 39\,\text{Pa}$. The partial pressure of water vapor for $\text{RH} = 0.01$ and $T_{\text{oven}} = 415.15\,\text{K}$ is $p_{\text{H}_2\text{O}} \approx 3820\,\text{Pa}$. Textbooks such as [11, 128] tabulate the gas emissivities in relation to gas temperature, partial pressure and average beam length s_{m} that is traveled. Assuming $s_{\text{m}} \approx 0.45\,\text{m}$ for an oven cavity, one can extrapolate the gas hemispherical total emissivities $\epsilon_{\text{CO}_2} \approx 0.003$ and $\epsilon_{\text{H}_2\text{O}} \approx 0.06$ for temperatures above the boiling point. The mixture's emissivity is

$$\epsilon_{\text{g}} = \epsilon_{\text{CO}_2} + \epsilon_{\text{H}_2\text{O}} - \delta\epsilon \approx 0.063\,, \tag{4.14}$$

where the correction term $\delta\epsilon$ is negligible under atmospheric conditions [11]. To test the influence of the gases' radiative attenuation, the test case of Sec. 4.3.1 is repeated with the discrete ordinates

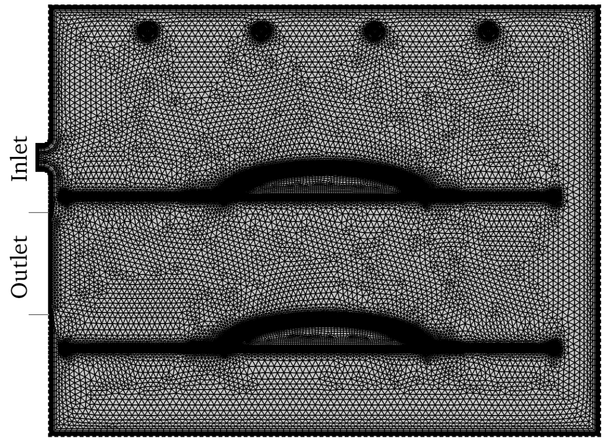

(a) Mesh overview.

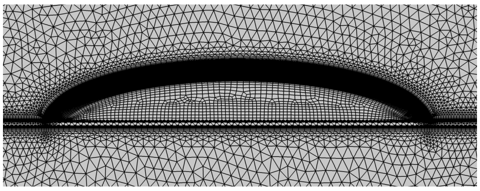

(b) Mesh detail: food item.

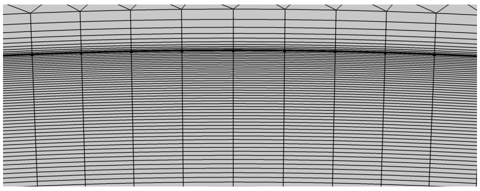

(c) Mesh detail: food-cavity interface.

Figure 4.21. Inlet and outlet positions within the 2D convection oven model and meshing details.

radiation model, a method capable of solving the radiative transport equation in participating media. With standard settings and utilizing a gas emissivity $\epsilon_{\mathrm{g}} = 0$ (i.e., non-participating gas), the method exhibited a relative error of $+1.48\%$ compared to the analytical solution. For the case of a participating air with $\epsilon_{\mathrm{g}} = 0.063$, the error is -0.56%. From these results, it can be concluded that the participation of the gas phase in the radiative heat transfer is relatively small and, thus, is neglected. This decision renders the conjugate heat and mass transfer solvable using the available computing power. The surface-to-surface radiation model induces significantly less computational load per time step than the discrete ordinates radiation model.

The element sizes and inflation layer properties of the hygroscopic capillary-porous model in conjugate flat plate configuration are utilized to mesh the 2D model, as the fine grid error was already analyzed for this similar case, see Sec. 4.3.2. Figure 4.21 gives an overview and two detailed illustrations of the resulting mesh with a maximum cell size of $h_{\mathrm{max}} = 5 \times 10^{-3}\,\mathrm{m}$. Note that the lower sides of the half-ellipsoids have no inflation layers, as the contact to and resulting heat flux from the baking plate is excluded from the investigations. Simulating $1\,\mathrm{h}$ of real time requires a solve time of $3.67\,\mathrm{h}$. The simulation model has $866\,001$ degrees of freedom and is solved with a maximum time step of $\Delta t = 5\,\mathrm{s}$.

4.3.3.2. Results of the 2D model simulations

During the first investigations of the model, the upper four heating coils do not operate. Figure 4.22 illustrates the velocities, temperatures and vapor concentrations of the conjugate heat and mass transfer model at $t = 1200\,\mathrm{s}$. One can observe that the fluid flow remains reasonably attached to the upper ellipsoid but detaches early from the lower food item owing to a more complex interaction of a secondary swirl between the outlet and the lower ellipsoid. After a heterogeneous startup phase, the oven temperature is reasonably equilibrated at $t = 1200\,\mathrm{s}$. However, differences in the food surface temperatures and water vapor concentrations can already be recognized. For

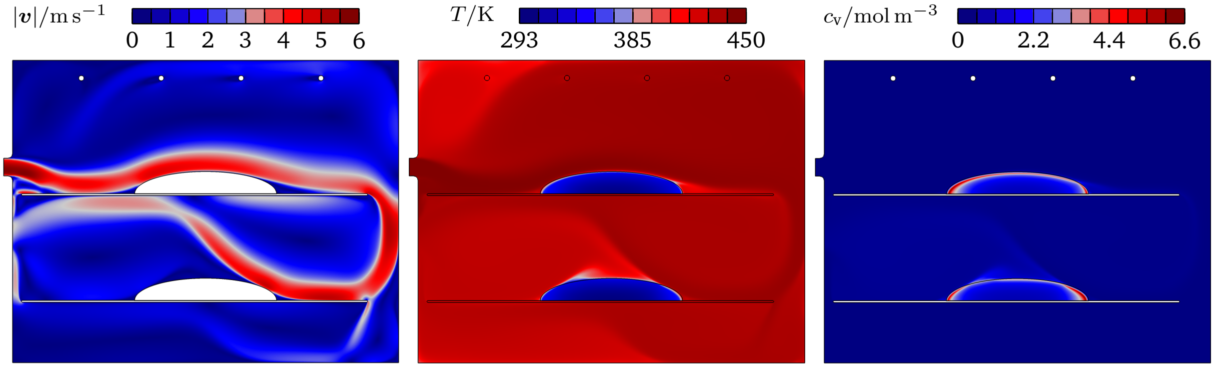

(a) Velocities. **(b)** Temperature. **(c)** Vapor concentration.

Figure 4.22. Representative field data of the conjugate thermal food processing model at $t = 1200\,\mathrm{s}$.

closer investigations, temperature, water saturation and the derived heat transfer coefficient are evaluated at the interface between the food item and oven cavity, see Fig. 4.23a. To render the comparisons fairer, the data for the lower food item is reversed in x-direction, owing to the reversed flow direction over the lower baking plate. Nonetheless, extreme variations can be observed over the boundary of the two food items and, foremost, when comparing the two food items mutually. The temperature differences between the two food items are $E_\text{map} = 7.2\%$ and $E_\text{max} = 46.3\,\mathrm{K}$. In the detached, less heated region of the lower ellipsoid, strong water saturation hot spots can be found, where crust formation may be delayed or even hindered, see central illustration in Fig. 4.23a. The forced convection around the food items induces an irregular temperature pattern. Evaluating the derived, convective heat transfer coefficient at the interface reveals local variations of $\alpha_\text{derv}(x) \in [15, 60]\,\mathrm{W\,m^{-2}\,K^{-1}}$, see the right-hand plot in Fig. 4.23a. The local variations are somewhat comparable to the values $\alpha(x_i) \in [20, 155]\,\mathrm{W\,m^{-2}\,K^{-1}}$ reported for the side faces of cuboids by Ateeque et al. [10]. Higher peak values can be explained by the fact that Ateeque et al. simulate bulk flow ($U = 4\,\mathrm{m\,s^{-1}}$) passing over the sharp edges of the cuboids.

To investigate the temporal evolution of the conjugate heat transfer, $\alpha_\text{derv}(x)$ is line-averaged at the interface and plotted over time, see Fig. 4.23b. One can observe a transient trend of the heat transfer coefficient during the first third of the simulation. At the steady-state operational state, the derived heat transfer coefficient of the upper and lower food item differs by $E_\text{map} = 34\%$. The differences between the two food items would be even more prominent when radiation is *not* considered. Figure 4.23b illustrates the average, relative radiative heat flux compared to convection over time. Whereas the upper food item receives up to 19.1% radiation, the lower item receives up to 31.6%. Indeed, radiation acts as an equilibrating mechanism inside the convection oven. The radiation of the upper baking plate heats (convective) cold spots on the lower food item.

A closer comparison of upper and lower food items can be found in Fig. 4.24a. The influences on the food-specific variables are investigated on a vertical cut through the two half ellipses, indicated by dashed lines in Fig. 4.20b. Comparing the food processing progress of the two ellipsoids results

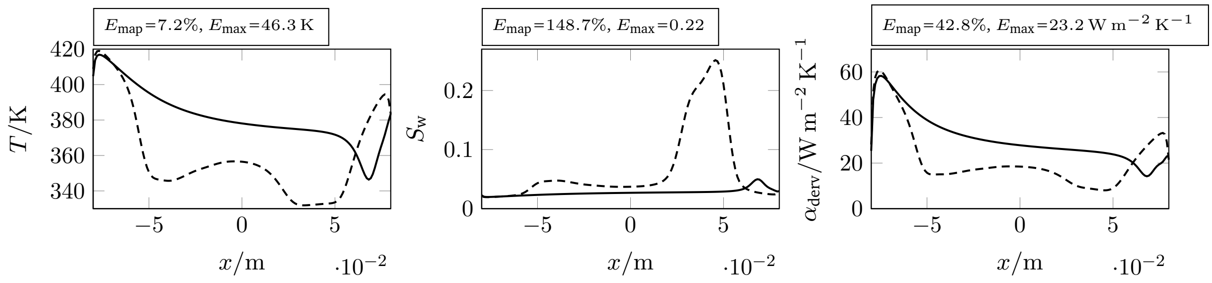

(a) Spatial evaluations at the food-cavity interface at $t = 1200\,\text{s}$.

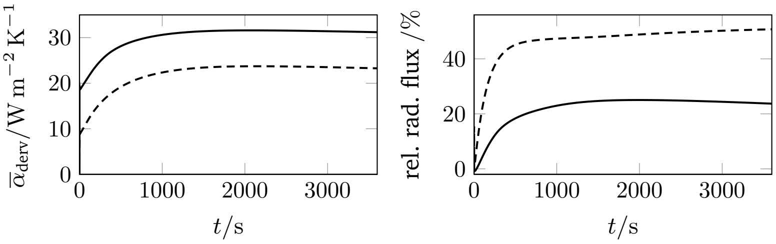

(b) Line-averaged heat transfer coefficient and relative radiative heat flux over time.

Figure 4.23. Spatial and temporal comparison of the upper (solid line) and lower food item (dashed line).

in temperature, moisture saturation and pressure deviations that clearly exceed the food modeling sensitivities of Tab. 4.2 (study 1–21). Maximum deviations of $E_{\text{max}} = 53.9\,\text{K}$ for the temperature and $E_{\text{max}} = 0.39$ for water saturations are revealed with the help of the conjugate simulation of the thermal process and food items. Enabling the upper heating rods for demonstration purposes leads to even more drastic variations between upper and lower food items, see Fig. 4.24b. The baking plate acts as a radiation shield, which results in delayed cooking progress for the lower food item.

The simple comparison of upper and lower food items in the same convection oven simulation reveals that there are no constant heat transfer coefficients in time and space. A central aim of this chapter is to compare the influences of the conjugate approach on primary variables with standard transfer-coefficient-based models. To this end, the derived, convective heat and mass transfer coefficients of the lower food item are spatially and temporally averaged to form constant coefficients: $\alpha_{\text{tot}} = 21.95\,\text{W}\,\text{m}^{-2}\,\text{K}^{-1}$ and $\beta_{\text{tot}} = 0.029\,\text{m}\,\text{s}^{-1}$. The coefficients are used on the surface of a single ellipsoid in a transfer-coefficient-based model. All other settings are identical to the benchmark test case of Sec. 4.1.1. Figure 4.25 depicts the error between the two approaches for $t = 1200\,\text{s}$ (upper row) and $t = 3600\,\text{s}$ (lower row). Dominant errors in temperature, and resulting differences in water saturation and pressures, can be found at the surface of the ellipsoid. Fewer differences can be observed at the bottom. This is not surprising since the interaction with the baking plate is not modeled, and more differences would be expected if this were the case. Local temperature variations dominate the surface and sub-surface region of the food item. For example, at the impingement point of the hot air stream (right-hand side), the temperature

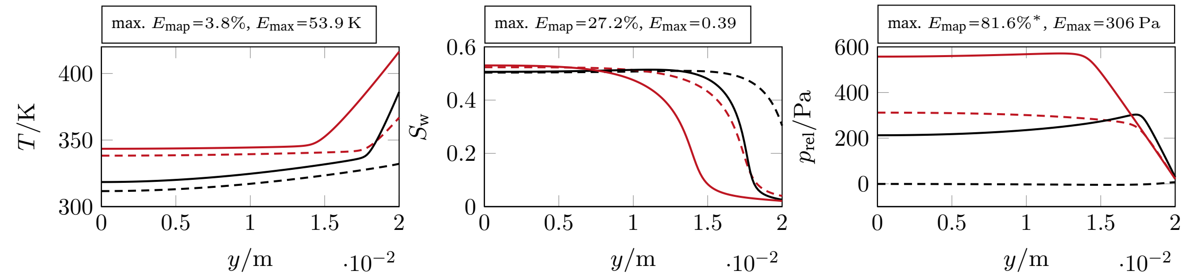

(a) Comparison at $t = 1200\,\text{s}$ (black) and $t = 3600\,\text{s}$ (red). Note that the $E_{\text{map}} = 81.6\%$ (marked with *) for pressures could only be calculated at $t = 3600\,\text{s}$ owing to devision by zero at $t = 1200\,\text{s}$.

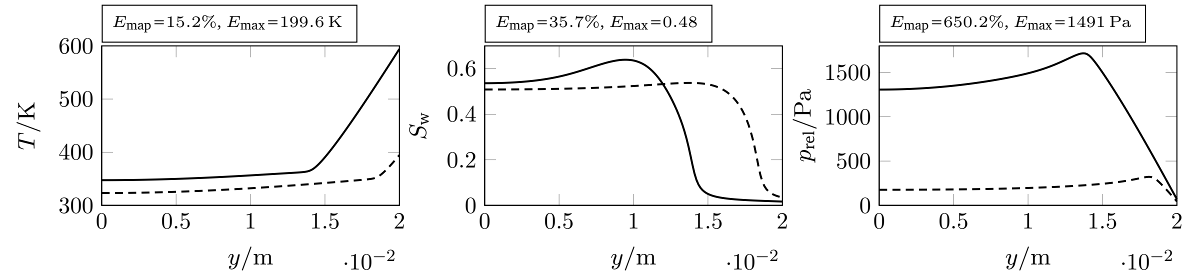

(b) Comparison at $t = 1200\,\text{s}$, with upper heating rods turned on.

Figure 4.24. Comparison of the upper (solid lines) and the lower (dashed lines) food item in conjugate configuration at vertical cut lines at $x = -0.05\,\text{m}$.

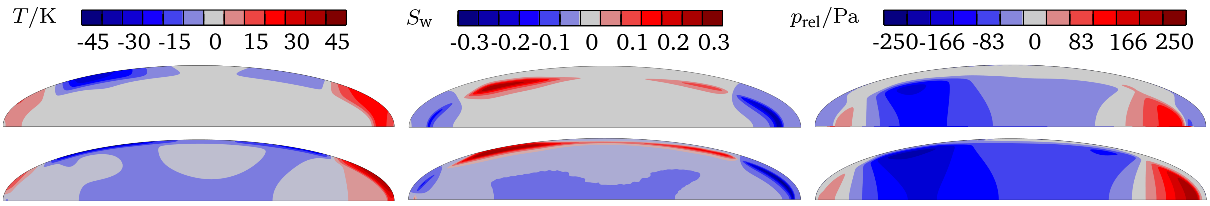

(a) Temperature. **(b)** Moisture saturation. **(c)** Pressure.

Figure 4.25. Influence of conjugate and a transfer-coefficient-based approaches on the primary food variables at $t = 1200\,\text{s}$ (upper row) and $t = 3600\,\text{s}$ (lower row). Positive values indicate a positive deviation from the transfer-coefficient-based approach.

of the conjugate model is up to $48\,\mathrm{K}$ hotter than the prediction of the model based on transfer coefficients. The resulting water saturations vary up to $E_{\text{max}} = 0.3$. Estimating surface properties, such as crusting or browning, with models based on constant heat transfer coefficients would lead to significant mispredictions.

4.4. Conclusions from the conjugate studies

Several research questions of this work can be answered with the derived conjugate simulation models. Plausibility checks with the non-isothermal benchmark cases *flow over a flat plate* and *flow over a cylinder* demonstrate that employing the k–ω SST model in combination with SUPG stabilization adequately solves conjugate heat transfer problems that are comparable to the conjugate convection oven simulations of this work. The test cases deliver trustworthy results that remain within the error bounds of empirical data for $Re \in [5 \times 10^2, 4 \times 10^4]$ (cylinder) and $Re \in [1.62 \times 10^5, 3.31 \times 10^6]$ (flat plate). Errors stemming from the numerical discretization are systematically evaluated with generalized Richardson extrapolation and are within the range of $E_{\text{GCI}} = 0.03$–0.15% for the finest grid. Errors of the radiosity method for solving surface-to-surface radiation are magnitudes lower. The *conjugate flat plate* configuration of the hygroscopic capillary-porous model demonstrates the successful development of a food processing model with combined conjugate heat and mass transfer. Free convection can be neglected because of low Richardson numbers, and consequently, a uni-directional coupling is established for air velocities and pressures. Gas radiation and specular diffusion are of minor importance when modeling radiation inside a convection oven.

Likewise, research questions concerning conjugate heat and mass transfer modeling are answered with the presented studies. The state of the art revealed that many research articles in food science and technology focus on modeling the food but treat heat and mass transfer effects of the process with rudimental methods, e.g., estimating average heat and mass transfer coefficients from empirical relations. This practice is at least debatable in light of the results highlighted within this section. In a controlled setting, the *conjugate flat plate* case demonstrates that deviations from conjugate couplings already become the most dominant on the overall simulation outcome. Without even considering the geometric variation of a food item or processing device, the maximum error in surface temperatures is $E_{\text{max}} = 15.4\,\mathrm{K}$ when the local and temporal deviations of conjugate heat transfer are not considered. Not accounting for thermal radiation leads to even more pronounced deviations of $E_{\text{max}} = 35.6\,\mathrm{K}$ for the temperatures and $E_{\text{max}} = 0.25$ for the water saturation.

The simulations of thermal food processing inside a convection oven demonstrate that there are no constant heat and mass transfer coefficients. The local heat transfer coefficient, derived from the conjugate simulations, varies strongly: $\alpha_{\text{derv}}(x) \in [15, 60]\,\mathrm{W\,m^{-2}\,K^{-1}}$. Just the positioning of food items at other places inside the oven induces a maximum temperature difference of $E_{\text{max}} = 46.3\,\mathrm{K}$ after $20\,\mathrm{min}$. Another practice observed in the literature is the estimation of a heat transfer coefficient from experimental data, where radiative and convective effects are lumped into a total heat transfer coefficient. The convection oven simulations show that the contribution of thermal radiation varies from 19.1% (upper food item) to 31.6% (lower food item) compared to convection. Moreover, a clear transient build-up phase of the radiative contribution can be identified during the first $20\,\mathrm{min}$ of the simulations. Radiation tends to fill in the gaps in heat input when convection becomes less inefficient because of increased surface temperatures of the food items. Comparing a conjugate simulation of a food item with one employing constant transfer coefficients reveals the most pronounced differences encountered within this work: The temperature locally differs up to $E_{\max} = 48\,\mathrm{K}$, which is a deviation of 30.6% compared to a possible variable range of $157\,\mathrm{K}$. The water saturations differ up to $E_{\max} = 0.3$, which is a deviation of 60% compared to a possible variable range of 0–0.5. The differences for this example could be even higher if the average heat and mass transfer coefficients were not taken from the conjugate model, but empirical correlations would have been used.

Another major consequence can be drawn from the preliminary simulation time estimations of a 3D variant of the conjugate heat and mass transfer model. Coarsely meshing one (symmetric) half of the geometry illustrated in Fig. 4.20a results in a model with 5.8×10^6 degrees of freedom. Every of the 740 time steps would approximately require $5\,\mathrm{h}$ to converge — resulting in a solve time of around 154 days. Additionally, one run of the coarsely meshed problem usually does not guarantee an acceptable solution quality that would allow drawing valid conclusions. For example, the mesh error estimation with generalized Richardson extrapolation would require solving the problem at three different mesh sizes [208]. The outlined dilemma of long simulation times of several days or even months holds for many large-scale simulation problems in the industry. Training data set sizes on the order of 10^3–10^7 [221] are unattainable in a reasonable timeframe. Even a significant increase in computing power could not render the simulations for a data set of, e.g., 100 simulations feasible for a digital twin development process. This gap shall be closed with the efficient data-driven reduced-order modeling framework presented in the next chapter.

To underpin the conclusions on convection and radiation, a 3D conjugate heat transfer simulation of the oven depicted in Fig. 4.20a is performed. All relevant parameters match the ones of the 2D model, and the effective transport properties of the food items are replaced by $\rho_{\mathrm{s}}, c_{p,\mathrm{s}}$ and κ_{s} from Tab. 4.1. The omission of food modeling enables the use of linear ansatz orders for the temperature field. Likewise, it significantly reduces the mesh refinement requirements in the porous domains. Overall, the system size is reduced to 2.02×10^6 degrees of freedom. Figure 4.26 compares the 2D results with the 3D conjugate heat transfer model results. The local convective heat transfer coefficient varies $\alpha_{\mathrm{derv}}(x) \in [8, 55]\,\mathrm{W\,m^{-2}\,K^{-1}}$ for the upper food item, which is in very good agreement with the 2D results. Comparing the relative impact of radiative heat flux, the results of the 3D simulation show an even higher spread between upper and lower food items. The 2D and 3D results of the conjugate heat and mass transfer convection oven model are probably closely resemblant. These findings also align with previous works on similar processing devices, revealing the same order of magnitude of convection and radiation effects when comparing a 2D

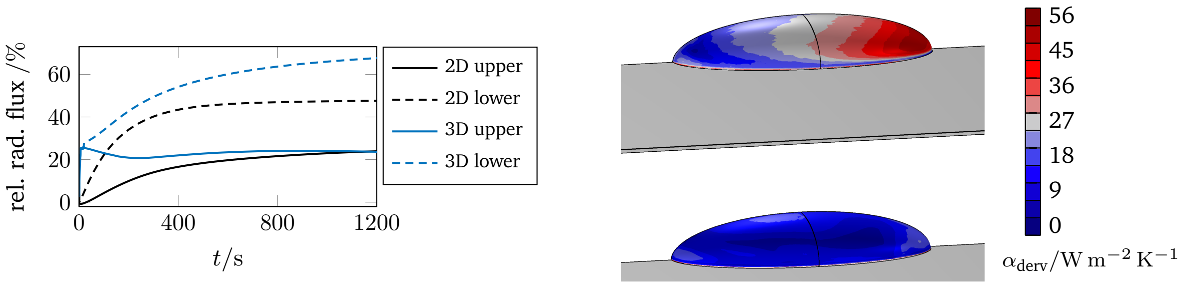

(a) Comparing the relative radiative heat flux over time from the conjugate 2D and 3D models.

(b) Spatial evaluation of the convective heat transfer coefficient at the food-cavity interface at $t = 1200\,\mathrm{s}$.

Figure 4.26. Comparison of 2D and 3D relative radiative heat flux and spatial distribution of the convective heat transfer coefficient.

and 3D model [135, 220]. In summary, simulation results produced with constant heat transfer coefficients should be scrutinized. As demonstrated, a constant, lumped heat transfer coefficient would not capture the spatial and temporal variation of radiative and convective heat fluxes. This is only possible with conjugate heat transfer simulations that include thermal radiation.

5. Reduced-order modeling studies

Digital twins must replicate their physical counterparts with minimal computational cost while retaining high accuracy and executing faster than in real time. Considering the time required for the numerical solution of the problems presented in the previous chapter, the need for reduced-order modeling becomes evident. The DynROM approach, as introduced in Sec. 3.2, is employed for the reduced-order modeling studies in this chapter. Derived data-driven ROMs with this method rely on output data of the multi-physical simulations of Chapter 4. The output data of the simulations, termed *readouts*, remain the only transport vehicle of relevant information about the problem that the data-driven ROM should replicate. This raises the question of which training data selection is appropriate, because the ROM test error is directly related to the data presented during training [115, 139]. One particularity of the DynROM method is its reduced need for training data, usually requiring less than five simulations of the reference model [8]. Consequently, the objective of this chapter is to derive a procedure for finding only one-to-two simulation data sets that ensure a training of a ROM that has low test errors.

A MATLAB code framework, called TwinLab, provides automation of the ROM studies and interfaces to COMSOL Multiphysics and ANSYS DynROM. Furthermore, TwinLab contains the main data science methods of this work, some of which are described in Sec. 5.1. Within the discipline of system identification, tailored excitation signals are utilized to extract information from a physical model. The excitation signal synthesis within TwinLab and the calculation of training data properties, termed *features*, are introduced. Moreover, the testing of the generated ROMs with so-called *global* error measures on particular *fair* data sets is motivated. Section 5.2 presents the cornerstone of ROM generation of this work: an efficient design of experiments. Its core is a proposed correlation-based selection of training data. First, the method is described in detail for the soft-matter model for meats. Subsequently, the procedure is applied to the conjugate thermal food processing model in flat plate configuration. Section 5.3 investigates the performance of the DynROM method, particularly the ODE augmentation, prediction error, extrapolatory capabilities and attainable speed-up. In Sec. 5.4, the successful reduced-order modeling of the conjugate convection oven model is demonstrated. Section 5.5 presents the conclusions from the reduced-order modeling studies and summarizes how to apply the proposed efficient design of experiments approach.

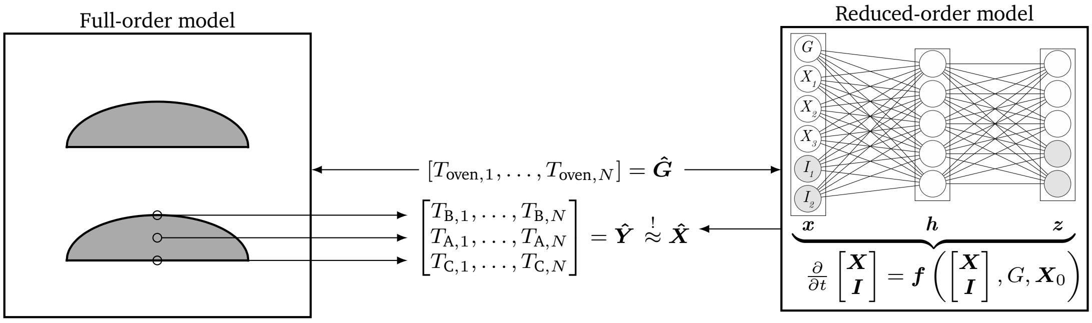

Figure 5.1. Schematic procedure for the data-driven ROM training.

5.1. The TwinLab framework

This section describes the ROM training and testing procedure and introduces the TwinLab framework. Moreover, the generation of excitation signals and their resulting properties are presented. An exemplary ROM training and testing demonstrates the derivation of six global test errors that qualify the accuracy of a ROM.

5.1.1. Model selection and training procedure within the TwinLab framework

In the previous chapter, the derivation of a conjugate heat and mass transfer simulation model of food processing is shown. Its superiority in predicting local temperature and moisture concentration differences is demonstrated. However, conjugate models are scarce in food science. Transfer-coefficient-based models enjoy great popularity in the industry and research, as highlighted in the state of the art, see Sec. 1.3. This and the following sections aim to derive a valid ROM framework for both worlds. The soft-matter model comes with consistent sensory models, as introduced in Sec. 4.1.3. Such sensory quantities are relevant for the MPC studies in Chapter 6, which rely on the ROMs found in this chapter. Consequently, the soft-matter model is prioritized for the ROM training investigations. However, a digital twin of a conjugate model is ultimately targeted, as it is believed to be more accurate than transfer-coefficient-based models. The validity of the ROM training method is thus demonstrated for the conjugate hygroscopic, capillary-porous model in a consecutive step. This proceeding proves the generality of the correlation-based training data selection for a broader class of thermal food processing models.

For the upcoming ROM studies, the validation setup of the soft-matter model of Sec. 4.1.2 is employed. The studies focus on replicating temperature probes at specific points of the full-order model, see Fig. 5.1. Investigating point data ROMs provides a condensed, minimalistic setup to closely investigate the effects of training data selection. Nonetheless, an extension to field data ROMs is demonstrated at the end of this chapter. Only temperatures are chosen for training to exclude the effects of different physics and scales in one ROM, as recommended by ANSYS [8]. The core temperatures T_A and surface temperature T_B are selected as they are considered representative of the possible temperature trajectories in the model. Core temperatures are typically monitored to control doneness. The U.S. Food and Drug Administration, for example, requires holding times of at least one second above $74\,^\circ\mathrm{C}$ [247]. Surface temperatures can be relevant for determining the temperature-dependent browning of the food item. Note that during the validation simulations of the soft-matter model, see Sec. 4.1.2, the oven temperatures are constantly high. Considering that the subsequent studies do not apply the maximum oven temperature at all times, the simulation duration is prolonged to $1400\,\mathrm{s}$ without significantly leaving the validated range of the model.

The following procedure is applied to generate one data set: A tailored excitation signal, as introduced later in this section, is handed over to the soft-matter model in COMSOL Multiphysics to vary the oven temperature $\hat{\boldsymbol{G}} = [T_{\text{oven},1}, \dots, T_{\text{oven},N}]$ over time. The readout matrix of one simulation is

$$\hat{\boldsymbol{Y}} = \begin{bmatrix} T_{\text{A},1}, \dots, T_{\text{A},N} \\ T_{\text{B},1}, \dots, T_{\text{B},N} \end{bmatrix} , \tag{5.1}$$

where N is the number of time steps. One data set consists of the unique combination of $\hat{\boldsymbol{G}}$ and $\hat{\boldsymbol{Y}}$ and is stored in a structure array within TwinLab. Each data set has a unique alphanumeric identifier which stems from the consecutive numbering in the original studies in [137, 188]. The process of excitation signal synthesis, training data generation with COMSOL Multiphysics, data management, format conversions, export for ANSYS DynROM and reimport of ROM readouts $\hat{\boldsymbol{X}}$ is centrally controlled within TwinLab. More of its functionalities are described in the following sections.

5.1.2. Excitation signal synthesis

Within the discipline of system identification, special signals are employed as an input for a physical problem. From a linear dynamics point of view, the principal "modes" of the system are "excited" by the input signal, which is why it is also referred to as an *excitation signal*. The excited transient behavior of the physical problem can be determined from the recorded output data [23, 157, 174]. Typically, two classes of excitation signals are employed for system identification: step-based and sinusoidal signals. Single-step signals provide a single jump with a certain amplitude, and pseudo-random binary sequences provide multiple jumps with alternating positive and negative amplitude. The waiting time t_hold for one state is pseudo-random [157]. Both step signals and pseudo-random binary sequences are only applied for linear system identification [174]. On the contrary, amplitude-modulated pseudo-random binary sequences (APRBS) are suitable for nonlinear system identification. They trigger different amplitude levels in a pseudo-random fashion. Jumps in the signal excite a broad range of system frequencies, and the piecewise constant sections cover low-frequency components [115, 174]. Figure 5.2a (left and center) depicts two representative APRBS signals that are used for T_oven. The illustration also shows the corresponding readouts T_A and T_B of the full-order simulation model. The synthesis of quantized

Algorithm 1 Synthesis of APRBS signals for T_{oven} [137].

```
1:  Discretize the temperature range between $T_{\text{min}} = 293.15\,\text{K}$ and $T_{\text{max}} = 473.15\,\text{K}$ into four equidistant bands
2:  Compute $T_i$ randomly in every $i^{\text{th}}$ temperature band with $i = 1, \ldots, 4$ and permute $T_i$ inside of an array
3:  Compute temperature difference $T_{\text{diff}}$ between adjacent $T_i$ inside of the array from step 2
4:  if any $T_{\text{diff}} < T_{\text{margin}} = 10\,\text{K}$ then
5:      Go to step 2
6:  end if
7:  Compute time-steps $t_i$ randomly between $t_{\text{start}}$ and $t_{\text{end}}$ with $i = 1, \ldots, 4$
8:  Compute time difference $t_{\text{diff}}$ between two adjacent time steps
9:  if any $t_{\text{diff}} < t_{\text{hold}}$ then
10:     Go to step 7
11: end if
12: Sample $T_i$ over time with $\Delta t = 5\,\text{s}$ and write out as an array $\hat{\boldsymbol{G}}$
```

APRBS signals within this work is summarized in the pseudo-code of Alg. 1. A minimum hold time $t_{\text{hold}} = 300\,\text{s}$ is set.

Nelles [114, 174] promotes the usage of sinAPRBS for system identification. Such signals consist of an APRBS base with smooth, sinusoidal transitions. Sinusoidal pieces $A\sin(2\pi f_j t) + c$ with frequencies $f_j \in [0.001, 0.01]\,\text{Hz}$ are inserted into APRBS signals to synthesize sinAPRBS within this work. The amplitudes A and the offset c are adjusted individually to fit in each APRBS step [188]. Figure 5.7 illustrates the transformation of an APRBS signal into a sinAPRBS signal with two different frequencies f_j.

Multi-sines are a superposition of s single sines

$$G(t) = \sum_{k=1}^{s} A\cos(2\pi k f_0 t + \varphi_k) + c_k \,. \tag{5.2}$$

The parameters $f_0 \in [0.001, 0.01]\,\text{Hz}$, $\varphi_k \in [0, 10]$ and $A \in [1, 30]\,\text{K}$ are chosen to match the frequency and amplitude ranges of interest. The constants c_k are adjusted such that the resulting oven temperature stays within the temperature bounds of $T_{\text{oven}} \in [293.15, 473.15]\,\text{K}$. A quantized output of Eq. (5.2) is written into the array $\hat{\boldsymbol{G}}$. A constant time step of $\Delta t = 5\,\text{s}$ provides sufficient resolution to represent the high-frequent oscillations appropriately. Data set 819, an exemplary simulation with multi-sines, can be found in Fig. 5.2a.

An excitation signal's crest factor

$$\text{Cr}(\hat{\boldsymbol{G}}) = \max_{1 \le k \le N} \frac{|\hat{G}_k|}{\text{rms}(\hat{\boldsymbol{G}})} \tag{5.3}$$

is a measure of the energy level of the excitation signal. It is sometimes maximized during system identification to increase the possible energy input into a physical system [96]. The crest factor is a possible data set feature that could correlate with a good ROM quality.

5.1.3. Data set features and global error measures

Each ROM for the upcoming studies is trained with only *one* training data set. Those ROMs are termed *1-signal ROM* hereafter. The central idea of a correlation-based training data selection is to find features of the data sets that correlate with low test errors of the 1-signal ROMs. The use of 1-signal ROMs permits features of data sets to be uniquely assigned to a ROM performance. Combinations of two data sets are investigated in Sec. 5.2.2.2. Several data set features are derived in the hope that at least one feature will correlate with low 1-signal ROM test errors. For example, simple features are the standard deviation and the mean value of T_{oven}, T_{A} and T_{B}. Moreover, various measures of the APRBS steps of Alg. 1 are calculated to serve as data set features:

$$\overline{T}_i := \text{mean}([T_1, T_2, T_3, T_4])\,, \tag{5.4}$$

$$\overline{T}_{\text{diff},i} := \text{mean}([T_{\text{diff},1}, T_{\text{diff},2}, T_{\text{diff},3}, T_{\text{diff},4}])\,, \tag{5.5}$$

$$|\overline{T}_{\text{diff},i}| := \text{mean}([|T_{\text{diff},1}|, |T_{\text{diff},2}|, |T_{\text{diff},3}|, |T_{\text{diff},4}|])\,, \tag{5.6}$$

$$\overline{T}_{\text{diff},j} := \text{mean}([T_{\text{diff},2}, T_{\text{diff},3}, T_{\text{diff},4}])\,. \tag{5.7}$$

For example, $\overline{T}_{\text{diff},i}$ can be verbalized as the *signed mean of the delta jumps of an APRBS signal*. In Fig. 5.2a, $|T_{\text{diff},2}|$ and T_2 are indicated in data set 745 to clarify their definition.

Figure 5.2 illustrates the sensitivity of training data selection for a 1-signal ROM with a short example. In Fig. 5.2a, three training data sets with identifiers 351, 745 (APRBS) and 819 (multisine) are shown. All three sets are employed individually to train a 1-signal ROM, called ROM351, ROM745 and ROM819. The testing is performed on data set 703, see Fig. 5.2b. ROM745 produces good results with a $E_{\text{rms}} = 0.7\,\text{K}$ compared to the solution of the full-order model. Conversely, ROM351 and ROM819 produce the errors $E_{\text{rms}} = 13.5\,\text{K}$ and $E_{\text{rms}} = 7.9\,\text{K}$, respectively, which are one order of magnitude larger. ROM351 and ROM745 are the worst and best-performing APRBS-trained ROMs of the upcoming study. To introduce global error measures, both ROMs are evaluated on all 165 APRBS data sets generated for the study. ROM testing on multiple test data sets renders testing more representative. For each ROM evaluation on a test data set, the test error measures E_{rms} , E_{map} , E_{max} , E_{med}, E_{iqr} and R^2, as described in Sec. 3.2.4, are calculated over all time steps. For example, the root-mean-square error of ROM745, tested on data set 298 reads

$$E_{\text{rms}} = \sqrt{\frac{1}{N}\sum_{k=1}^{N}(T^{\text{ROM745}}_{\text{B},298,k} - T_{\text{B},298,k})^2}\,, \tag{5.8}$$

where $T^{\text{ROM745}}_{\text{B},298}$ is the output of ROM745 at position B when it is excited with $T_{\text{oven},298}$. Each error measure captures the differences between test and ROM data slightly differently: linearly, quadratically, overall or locally, for example. Utilizing multiple error measures increases the chances of finding an error measure that linearly correlates with features of the training data set.

Figure 5.3 shows the histogram of the error measures when testing ROM745 and ROM351 on

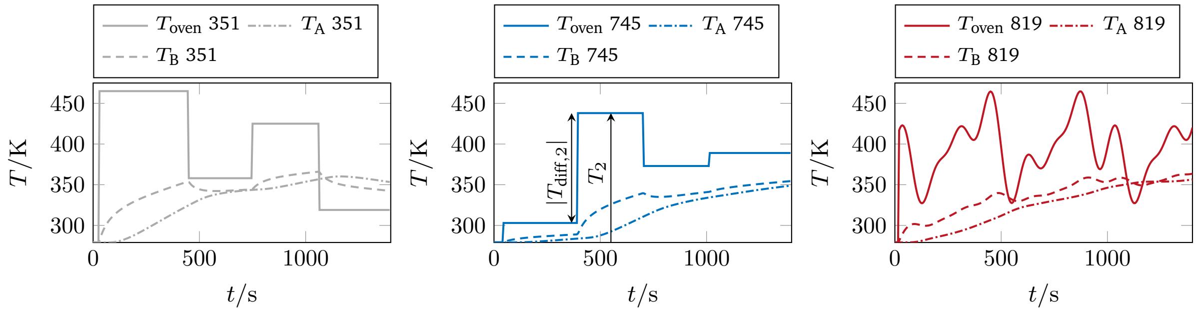

(a) Training data sets 351, 745 and 819. $|T_{\mathrm{diff},2}|$ and T_2 are indicated in data set 745 to clarify the definition of the APRBS features of Eq. (5.4)–(5.7).

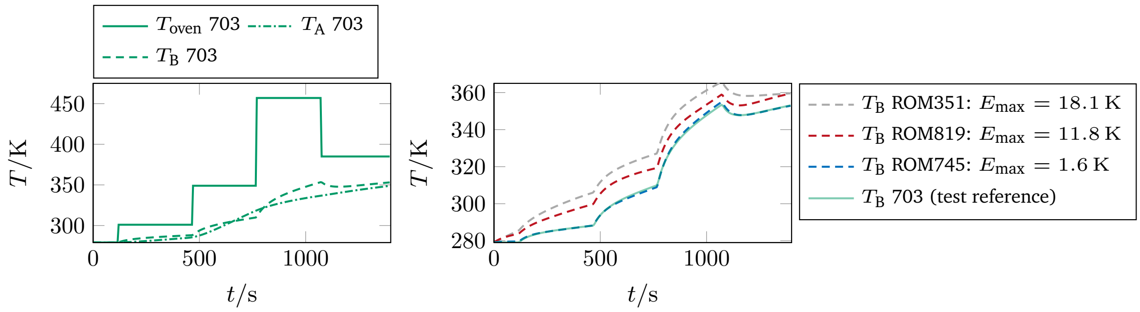

(b) Testing of the 1-signal ROMs on test data set 703.

Figure 5.2. Introductory 1-signal ROM training for data sets 351 and 745 (APRBS) and 819 (multi-sine). The sensitivity of training data selection on the resulting test error is demonstrated.

the entire group of 165 APRBS data sets. The test error measures appear normally distributed for testing on a sufficient number of data sets. Consequently, the average of the error measures is taken to obtain six global error measures per testing of a 1-signal ROM. The global error measures are denoted with an overline, e.g., $\overline{E}_{\mathrm{rms}}$. Figure 5.3 indicates the global error measures for ROM351 and ROM745 with dashed lines. The TwinLab framework includes the functionality to calculate the data set features, test ROMs on test data and calculate the global error measures.

5.1.4. Reduced-order model training and test groups

ROM training and testing must follow an objective study design to render the study outcomes statistically significant. For this study, a fixed complexity of $i = 2$ of the DynROM method, recall Sec. 3.2.2, ensures equal training conditions. Repeating ROM training within DynROM always resulted in the same ROM training error.

It is of central interest in reduced-order modeling that trained ROMs can generalize on yet unknown data sets. In other words, ROMs should show validity in a defined variable range of the full-order model output, which test data should objectively represent. One finding of this work is that a purely random choice of test data sets is not representative of the output space of the full-order model. Hence, a different approach is taken to select appropriate *fair* test data.

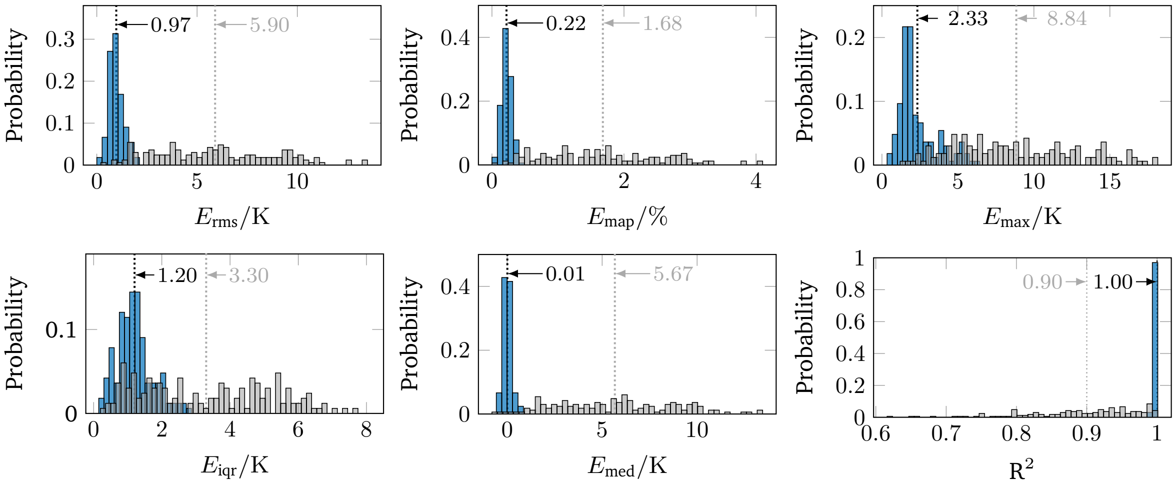

Figure 5.3. Distribution of error measures for 1-signal ROM351 (gray) and 1-signal ROM745 (blue), evaluated on all APRBS signals. Dotted lines mark the value of the global error measures for the respective ROM [137].

To avoid misunderstandings with the term *data set*, a group of several data sets used for ROM testing is termed *test group* hereafter. To define fair test groups more precisely, consider APRBS signals, as they serve well as instructive examples. Algorithm 1 generates APRBS signals for T_{oven} in a pseudo-random way. Figure 5.4a (top) depicts a histogram of the APRBS amplitudes of all data sets. The amplitudes appear sufficiently equally distributed (dark gray bars). However, the medians of each data set (bright grey bars) show a normal-like distribution. This tendency can also be found in the resulting amplitudes of surface temperatures T_{B} (blue bars) and their medians per data set (bright grey bars), see Fig. 5.4a (bottom). The serial execution of four pseudo-random oven temperatures in the physical model can be interpreted as a random experiment with four dice. The sum of the dice has a normal distribution.

Cross-validation is a common approach that separates the available data sets into train and test groups. Usually, following the standard concept of k-fold cross-validation, all remaining APRBS data sets would serve as the test group for 1-signal ROMs. However, this test group would advantage 1-signal ROMs that are trained with a data set whose median of the surface temperatures $\mathrm{med}(T_{\mathrm{B}})$ is close to the medians of the test group. Taking the average of all error measures to form the global error measures would thus pronounce operational conditions that are close to the medians of the test data. Consequently, 1-signal ROMs would receive the feedback that they would generalize well on all APRBS data sets. However, it is not ensured by this feedback that the 1-signal ROM performs well for the entire parameter range of the output space, i.e., also for high or low $\mathrm{med}(T_{\mathrm{B}})$. Further investigations revealed this bias for any randomly selected test group out of all 165 APRBS data sets.

The concept of befitted cross-validation recommends including expert input during the selection of test data sets [139]. In that spirit, one may postulate that fair test data sets should be uniformly

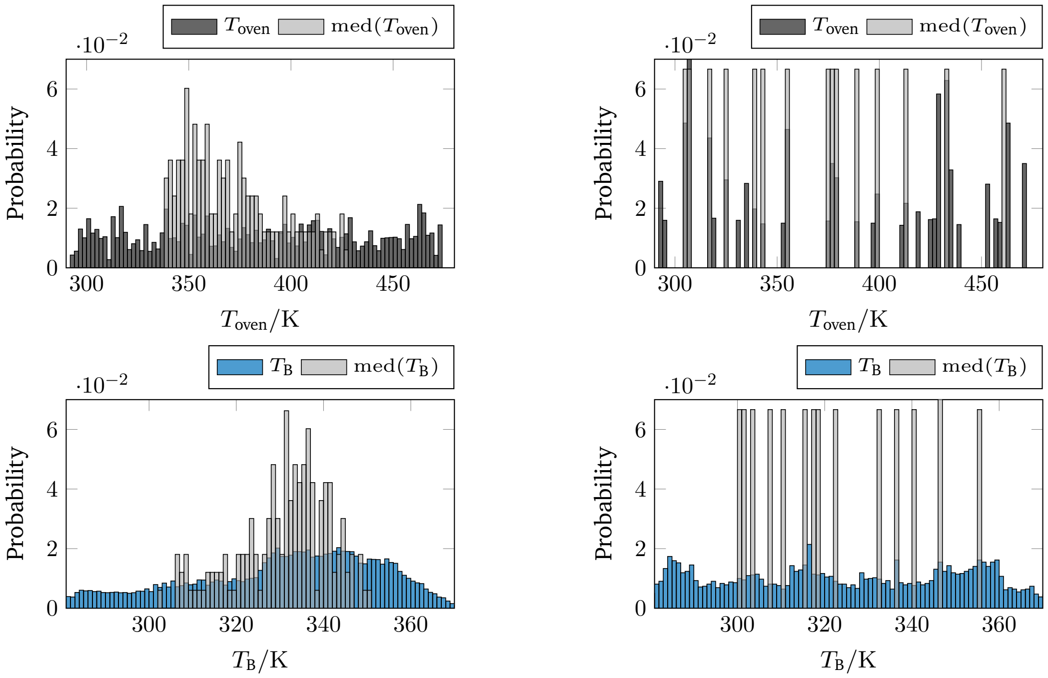

(a) Histograms of all APRBS data sets.

(b) Histograms of the fair test group AP15.

Figure 5.4. Test groups with equally distributed T_{oven} excitation signals (top left) show pronounced biased surface temperatures for testing (bottom left). Fair test groups, here AP15, show a more uniform distribution (right) [137].

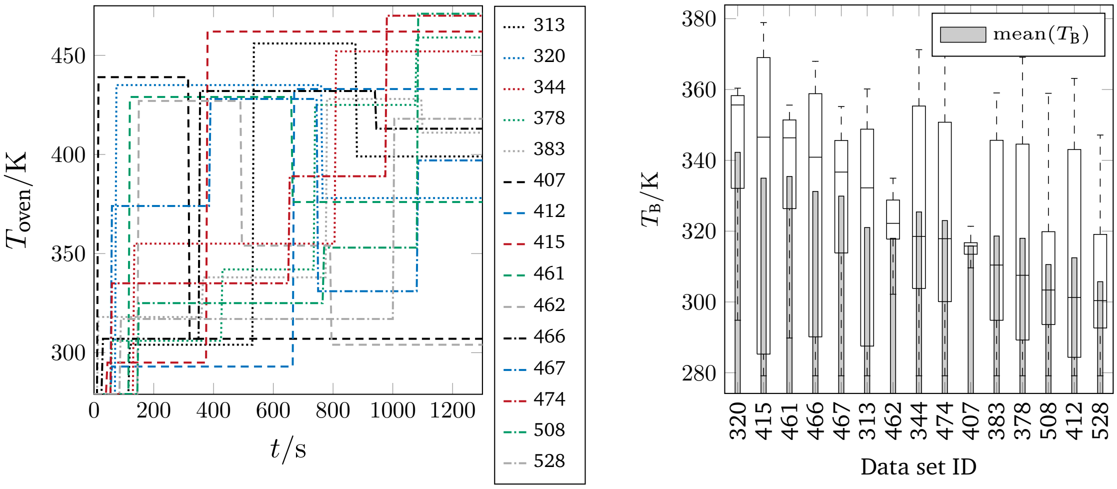

(a) Oven temperature trajectories over time.

(b) Boxplots of corresponding surface temperatures.

Figure 5.5. Fair APRBS test group AP15. The horizontal lines in the boxplots indicate the median. The box represents the interquartile range. The whiskers contain the data within 1.5 times the IQR.

distributed with respect to $\mathrm{med}(T_\mathrm{B})$. With a null hypothesis, “the observations T_B of a test group come from a uniform distribution”, the selection of a test group is automated based on a χ^2 test (probability $p = 0.05$, number of bins $n_\mathrm{bins} = 6$). Per excitation signal type, the algorithm randomly selects 15 data sets as a test group and tests it against the null hypothesis. The process repeats until the hypothesis is fulfilled. The test groups are termed AP15 (15 APRBS signals), sinAP15 (15 sinAPRBS signals), and MS15 (15 multi-sines signals). Figure 5.4b depicts the histograms of T_oven and T_B of AP15. They show a considerably more equal distribution of amplitudes and medians than Fig. 5.4a. The remaining test sets are presented in Appendix A to ensure better readability of this chapter. Figure 5.5a illustrates the good coverage of operational oven conditions for AP15. Furthermore, a boxplot in Fig. 5.5b gives an impression of the median, interquartile range and mean of the T_B readout per data set.

For the efficient design of experiments studies, 165 APRBS with four steps, 85 sinAPRBS, 55 multi-sine, ten single-sine and ten single-step data sets are generated. As will be discussed in the following sections, APRBS signals proved to be the most promising excitation signals during the course of the investigations. This explains the different sizes of the groups. Note that the study assumes that an intelligent convection oven can not only heat the air inside its cavity but also cool it, e.g., by excessively adding room air and evacuating hot air through the fume exhaust. Be it heating or cooling, the sudden APRBS steps for T_oven cannot be realized by real convection ovens. Nevertheless, APRBS serve well for the *entirely digital* data-driven reduced-order modeling. During the testing of ROMs, sinAPRBS signals for T_oven can better emulate the delayed thermal behavior of convection ovens. Mixed operational usage of the model is emulated with a test group consisting of the addition of AP15, sinAP15, and MS15.

5.2. Efficient design of experiments

The introductory example in Fig. 5.2 illustrates that certain data sets convey more information about the physical system to a 1-signal ROM than others during reduced-order modeling. Now that training and testing conditions are defined, this section presents the efficient design of experiments approach. The underlying correlation-based training data selection routine closes the gap in the literature of finding or synthesizing very few, “best-possible” training data sets for data-driven reduced-order modeling. Whereas the term design of experiment is standard in system identification, the added attribute *efficient* shall convey the conceptional idea of a minimalistic but effective training data set. The method is one of the cornerstones of the digital twin framework derived in this thesis and was published in part in [137].

5.2.1. Excitation signal type comparisons

A first pre-selection is performed to identify which excitation signal type is best suited for the reduced-order modeling of the concerning multi-physical simulations. All synthesized APRBS,

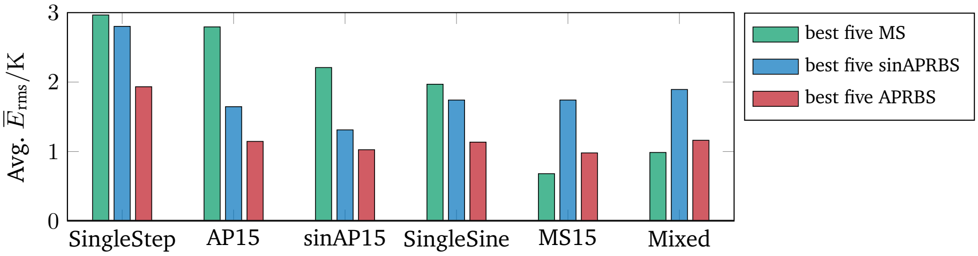

Figure 5.6. The global error measure $\overline{E}_{\mathrm{rms}}$ averaged for the five ROMs of their (excitation signal) kind, respectively. Testing is performed on six different test groups. APRBS signals perform best considering the average error on all test groups [137].

sinAPRBS, and multi-sines are utilized for training a 1-signal ROM. Each ROM is tested on AP15, sinAP15, MS15, the mixed test group and on the single steps and single sines test groups to calculate $\overline{E}_{\mathrm{rms}}$. A cluster of five data sets per excitation signal type could be identified with the lowest 1-signal ROM test errors on all test groups. The average of $\overline{E}_{\mathrm{rms}}$ for each cluster is depicted as ordinate in Fig. 5.6. Corresponding test group names can be found as the abscissa. The multi-sine-trained ROMs perform best on the MS15 test group but worse than APRBS-trained ROMs on the step-based test groups. APRBS-trained ROMs perform best on AP15, single steps, single sines and sinAP15. The latter emulates best the conditions inside a convection oven.

Figure 5.6 reveals that the best five sinAPRBS perform worse than the best five APRBS on all test sets. As APRBS and sinAPRBS are closely related, a further study tests the influence of the sinusoidal transitions in sinAPRBS on the test error. The best 15 APRBS signals are transformed into sinAPRBS signals, one with a fast and one with a moderate transition frequency, respectively. Figure 5.7 illustrates the transformation for the APRBS signal 745.

Although the changes to T_{oven} and T_{B} are minor, the test errors are considerably different, see Tab. 5.1 for a compilation of test error measures. Decreasing speeds of the sinusoidal transitions of sinAPRBS signals degrade the test error measures for the corresponding 1-signal ROMs. One possible explanation can be found in systems and control theory. Rapid signals, such as steps, are known to excite the broadest frequency range of a system. This property is taken from APRBS when sinusoidal transitions are inserted. Observe how T_{B} is marginally smoothed out during the transition, which seems to make a surprisingly considerable impact during the data-driven reduced-order modeling. Based on these results, the focus is laid on APRBS signals for the forthcoming sections.

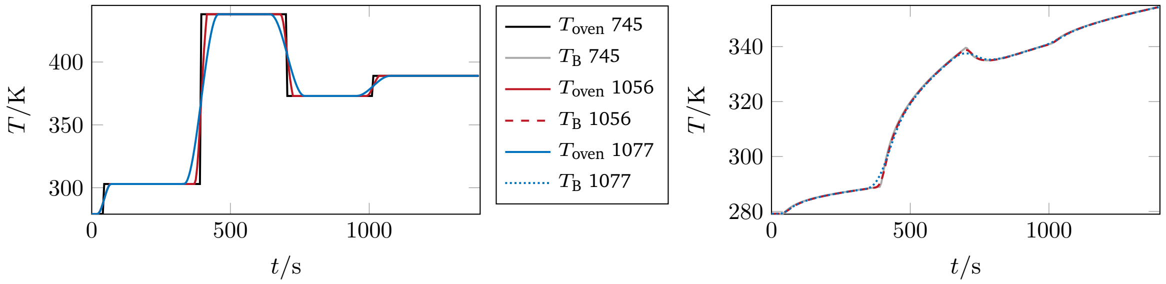

Figure 5.7. Transformation of APRBS signal 745 to a fast and slow sinAPRBS signal and corresponding full-order model readouts for T_{B} [137].

Table 5.1. Global error measures of 15 APRBS 1-signal ROMs and their transformed fast and slow sinAPRBS 1-signal ROMs (testing on AP15; similar trends for other test sets) [137].

Type Speed	APRBS -	sinAPRBS fast	 slow
$\overline{E}_{\text{rms}}$/K	1.63	2.32	2.90
$\overline{E}_{\text{map}}$/%	0.38	0.58	0.67
$\overline{E}_{\text{max}}$/K	3.91	4.79	6.22
$\overline{E}_{\text{med}}$/K	0.15	0.48	0.14
$\overline{E}_{\text{iqr}}$/K	1.64	2.46	3.36
R^2	0.99	0.97	0.94

5.2.2. Correlation-based training data selection

This section investigates correlations between APRBS data set features and 1-signal ROM test errors. Identifying such correlation allows synthesizing training data properties that ensure low ROM test errors. At first, only 1-signal ROMs are considered. Then, the study is extended to combinations of training data sets.

5.2.2.1. Investigations for 1-signal ROMs

The following procedure is followed to find correlations between global error measures and training data features[1]. Fifty-five APRBS signals are utilized in the full-order simulation model to vary T_{oven} and to generate readouts as defined in Eq. (5.1). A priori (only evaluating the excitation signal) and a posteriori (considering excitation signal or system output or both) features, as introduced in Sec. 5.1.3, are calculated for each data set. After that, each data set is utilized for training a 1-signal ROM. The median of all training errors, that is, the root-mean-square of the difference between ROM and training data set output, is $0.22\,\text{K}$, and the standard deviation is $0.14\,\text{K}$. As defined in Sec. 5.1.3, six global error measures are derived from testing the 1-signal ROMs on AP15, sinAP15 and MS15. There is hardly any correlation ($R = 0.096$) between training

---

[1] Originally, the study was performed with all signal types. This study description is tailored to APRBS for brevity, as the most significant correlations can be found here.

error and global test measures, where R is the Pearson correlation coefficient. Consequently, the training error has no significant effect on the study outcomes concerning the global error measures of the ROMs. The Pearson correlation matrix is employed to reveal correlations between training data features and global test error measures. Table 5.2 shows this matrix for testing on AP15. The testing on sinAP15 and MS15 can be found in Appendix A. Numbers close to a magnitude of one imply a strong correlation, highlighted in bold fonts.

The most significant correlation is found for $\mathrm{std}(T_\mathrm{B})$, which is an a posteriori feature. A value of $R = -0.76$ for the correlation between $\mathrm{std}(T_\mathrm{B})$ and $\overline{E}_\mathrm{rms}$ decodes to *high standard deviations in the surface temperatures of the full-order model correlate with low 1-signal ROM test errors.* For better visual interpretation, Fig. 5.8 depicts the correlation between $\mathrm{std}(T_\mathrm{B})$ and $\overline{E}_\mathrm{rms}$ on the test sets AP15 and sinAP15, where each marker symbolizes the evaluation of one 1-signal ROM. In the class of a priori training data features, $\overline{T}_{\mathrm{diff},j}$ also shows a good correlation to error measures, see Fig. 5.8c. It reveals that APRBS signals with a globally ascending trend result in lower global ROM test errors. Remember that $\overline{T}_{\mathrm{diff},j}$ is the mean signed sum of delta jumps of an APRBS signal, where the first jump is excluded from the calculation. The correlations for $\mathrm{std}(T_\mathrm{B})$ and $\overline{T}_{\mathrm{diff},j}$ are a good example of how physical particularities of a model find their way into the efficient design of experiments for data-driven reduced-order modeling through the search for correlations. One possible interpretation may be that the excessive triggering of the modeled skin effect of the soft-matter model at high oven temperatures renders the training data set not representative. The majority of data sets remain below the boiling point, see Fig. 5.4a for example. Indeed, high values for $\mathrm{std}(T_\mathrm{B})$ similarly abstract this physical requirement, as it demands the training data set to not exclusively trigger high surface temperatures. Moreover, a high standard deviation in surface temperatures can only be attained when oven temperatures are varied more dynamically. This encourages the inclusion of the maximum possible operational conditions in one training data set. The fact that this target cannot be achieved with having high standard deviations in T_oven ($R = -0.12$) demonstrates the complexity of appropriate training data synthesis for nonlinear models.

All in all, the found correlations now facilitate the synthesis or pre-selection of training data under the proposition that $\mathrm{std}(T_\mathrm{B})$ and $\overline{T}_{\mathrm{diff},j}$ should have high values. The best five training signals for a 1-signal ROM are marked in red in Fig. 5.8. Additionally, the red circle indicates the place of promising training data for a 1-signal ROM. Signal 745 is the best training data set for a 1-signal ROM, not only within the class of APRBS but also overall. It is synthesized with the knowledge of the required features of the excitation signal. Also not by chance, signal 745 is chosen as an example in the previous section. The data set is illustrated in Fig. 5.2a, and the distribution of errors can be found in Fig. 5.3. It is also revisited during the benchmarks of DynROM in Sec. 5.3.

Some remarks: Note that more markers can be found on the left half of the plots. The study commenced with an initial set of 30 pseudo-random training cases. As soon as correlations started to reveal, further data sets were synthesized that have high $\mathrm{std}(T_\mathrm{B})$ to confirm the hypothesis

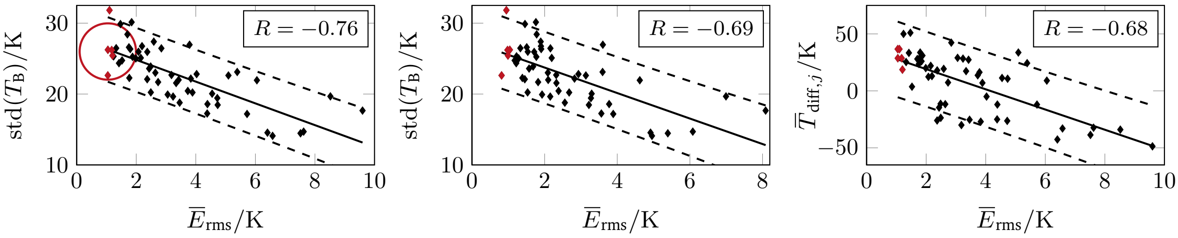

(a) Testing on AP15. **(b)** Testing on sinAP15. **(c)** Testing on AP15.

Figure 5.8. Correlations of signal features and $\overline{E}_{\mathrm{rms}}$ of 1-signal ROMs for APRBS (♦) and best 5 APRBS (♦) training data sets. Solid and dashed lines are the linear regression curve and $p = 0.95$ bounds. The red circle indicates the position of 1-signal ROMs with low test errors.

Table 5.2. Pearson correlation matrix between error measures (rows) and training data features (columns) for APRBS 1-signal-ROMs (testing on AP15). $\mathrm{std}(T_{\mathrm{B}})$ shows the best a posteriori correlation whereas $\overline{T}_{\mathrm{diff},j}$ is a potential a priori signal feature.

Measure	$\overline{T}_i$	$\overline{T}_{\mathrm{diff},i}$	$\overline{T}_{\mathrm{diff},j}$	$\lvert\overline{T}_{\mathrm{diff},i}\rvert$	$\overline{T}_{\mathrm{oven}}$	$\mathrm{std}(T_{\mathrm{oven}})$	$\mathrm{Cr}(T_{\mathrm{oven}})$	$\mathrm{std}(T_{\mathrm{A}})$	$\mathrm{std}(T_{\mathrm{B}})$
$\overline{E}_{\mathrm{rms}}/\mathrm{K}$	0.18	−0.39	**−0.68**	0.40	0.33	−0.12	−0.13	−0.05	**−0.76**
$\overline{E}_{\mathrm{map}}/\%$	0.20	−0.38	**−0.69**	0.43	0.35	−0.11	−0.14	−0.06	**−0.78**
$\overline{E}_{\mathrm{max}}/\mathrm{K}$	0.13	−0.47	**−0.69**	0.33	0.25	−0.13	−0.10	0.03	**−0.70**
$\overline{E}_{\mathrm{med}}/\mathrm{K}$	0.19	−0.37	**−0.72**	0.50	0.35	−0.09	−0.13	−0.11	**−0.83**
$\overline{E}_{\mathrm{iqr}}/\mathrm{K}$	0.31	−0.07	**−0.32**	0.23	0.36	−0.02	−0.07	−0.08	**−0.37**
R^2	−0.23	0.40	**0.60**	−0.29	−0.37	0.13	0.14	−0.08	**0.61**

more robustly and to find even better training data. The presented correlation trends hold not only for the data sets AP15 and sinAP15 but also for testing on other, additional APRBS and sinAPRBS data sets. It is also worth noting that $\overline{E}_{\mathrm{med}}$ shows slightly higher correlations than $\overline{E}_{\mathrm{rms}}$. The cancelation of positive and negative errors while averaging E_{med} for $\overline{E}_{\mathrm{med}}$ may cause doubts about the suitability of this error measure. However, it could be shown that the medians are normally distributed, compare Fig. 5.3. Hence, the average of the mean errors indicates if the ROM somewhat under- or overpredicts the output values of the full-order model.

Note that this section focuses on correlations that have been found and not on those that have not been found, although the latter outnumber the former. Moreover, note that systems and control literature sometimes suggest a uniform coverage of the model input space [174] or output space [237] to ensure good ROM training data. Implementing the input space coverage measure for the soft-matter model and demonstrating how high coverages do *not* guarantee low test errors can be exclusively found in [137].

5.2.2.2. Combination of training signals

Having found one good training data set directly raises the question of how to select a second training partner data set that enriches the accuracy of the ROM training. This section proposes a

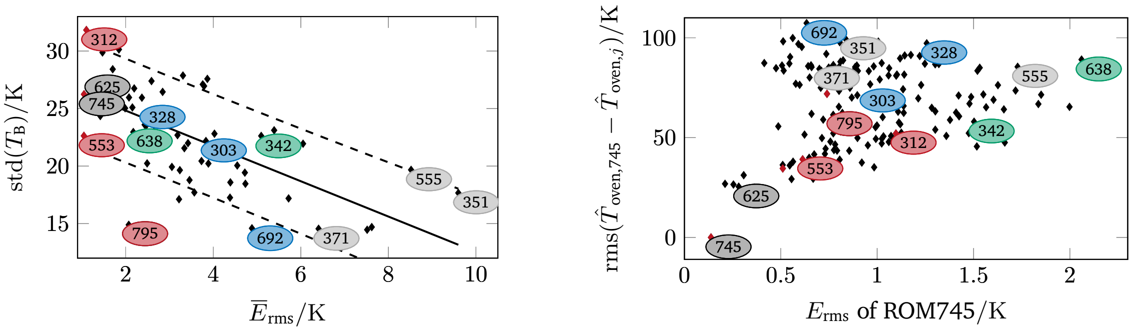

(a) Test errors of all 1-signal ROMs on AP15.

(b) Signal similarity to 745 over E_rms of ROM745.

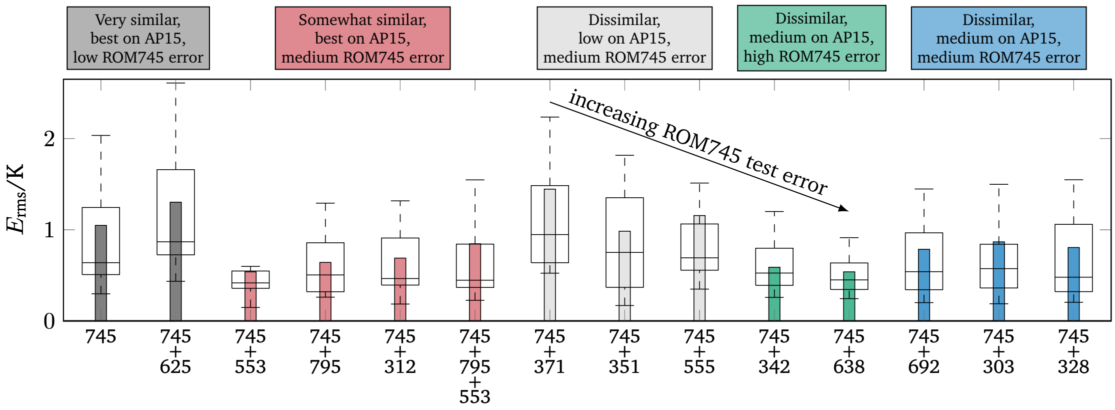

(c) Boxplots and average (bars) test errors of ROMs trained with various data set combinations. Testing is performed on AP15. Errors show the same trends also for MS15 and sinAP15.

Figure 5.9. Combinations of the best 1-signal ROM training data set 745 with other data sets: data sets that perform best on AP15 (left side of (a)) and that are sufficiently dissimilar to signal 745 (ordinate of (b)) are a good training partner furnishing low test errors on AP15.

procedure to find training partner data sets based on similarities to the 1-signal ROM. From now on, the limit of $i = 2$ is removed, and only the ROM complexity producing the lowest test error is chosen. A closer investigation of the influence of complexities can be found in Sec. 5.3.1.

Hereafter, various training partner selection routines are checked for plausibility with the help of Fig. 5.9, where several decision support tools are aggregated. Figure 5.9a is a version of Fig. 5.8a, where the data sets under consideration are now labeled and grouped with a color coding. Figure 5.9c shows $\overline{E}_\mathrm{rms}$ (bars), and the distribution of E_rms (boxplots) on AP15 of the *2-signal ROMs*. The headings of the following paragraphs are the hypotheses on how to find a training partner data set. Their naming is consistent with the naming of the boxes and the corresponding color coding in Fig. 5.9.

Very similar to 745, best performance on AP15, low ROM745 error: One intuitive approach is selecting a data set as a training partner that is also a successful training data set for a 1-signal ROM.

A measure for the similarity of an excitation signal j with APRBS 745 is $\mathrm{rms}(\hat{T}_{\text{oven},745} - \hat{T}_{\text{oven},j})$, plotted as the ordinate in Fig. 5.9b. A second tool to facilitate the selection of a training partner is the test error of the 1-signal ROM745 on all the other APRBS data sets individually, plotted as the abscissa in Fig. 5.9b. The 1-signal ROM745 has one of the lowest test errors on test set 625. This is not entirely surprising, as data set 625 (color-coded in black) is very similar to data set 745 in terms of oven temperatures, indicated by the low y-position in Fig. 5.9b. Likewise, 1-signal ROM625 is one of the best 1-signal ROMs on AP15, see Fig. 5.9a. Given both similarity to data set 745 and the good performance of 1-signal ROM745, selecting signals 745 and 625 as training partners, however, is a disadvantageous choice. Combining both signals increases the test error instead of decreasing it, compare the black section of Fig. 5.9c. Data set 625 does not add new information to the training. It may instead enforce over-fitting of the ROM to the specific, similar operational conditions of the data sets 745 and 625.

Somewhat similar to 745, best performance on AP15, medium ROM745 error: Despite the example above, it might still be a reasonable approach to combine training data sets that train accurate 1-signal ROMs on their own. However, a certain level of data set dissimilarity and a medium test error of the base ROM745 on those data sets should be guaranteed, compare the red color-coded cases in Fig. 5.9. The ROM745+553 almost halves the test error to $\overline{E}_{\text{rms}} = 0.54\,\mathrm{K}$ and has a considerably low error spread in the replication of the full-order model — the best result in this study on AP15. Also, the combination of data set 745 with medium similar, but best-performing multi-sine 1-signal ROM795 training data set produces decent results of $\overline{E}_{\text{rms}} = 0.64\,\mathrm{K}$ on AP15.

Nonetheless, combining all three signals does not increase model quality, compare the case ROM745+795+553. Figure 5.9b can be understood as a similarity map of data sets. Placing the second training data set close to a cluster of points seems to enrich the ROM training. However, as discussed in the following hypotheses, it is not as easy as it appears.

Dissimilar to 745, medium or low performance on AP15 , medium ROM745 error: Another intuitive approach to selecting a training partner is choosing a data set different from the base data set 745 in terms of the oven temperature. Yet, improving ROM quality is not guaranteed with this procedure. Consider, e.g., highly dissimilar data sets with a medium performance as 1-signal ROMs (color-coded in blue). Those training partner data sets cannot considerably improve the ROM quality. The same unproductive trend can be found for the combination with highly dissimilar data sets that train poor 1-signal ROMs (color-coded in light gray).

Somewhat similar to 745, medium performance on AP15, high ROM745 error: Adding data sets as training partners where E_{rms} of ROM745 is high seems to be a good choice (color-coded in green). The trend of decreasing test error medians of the light gray and green training signals (see trend arrow in Fig. 5.9c) leads to the assumption that the training improvement increases with increasing test error of 1-signal ROM745 (abscissa in Fig. 5.9b).

Generally, one can identify the trend that suitable training partner candidates can be found on the main diagonal of Fig. 5.9b (red and green cases). A certain level of dissimilarity has to be assured to be a successful training partner — hence, this is not the case for data set 625, as discussed before. Based on this study, one can suggest that a training partner data set should at least provide medium-quality 1-signal ROMs, have a certain level of dissimilarity to the base training data set in terms of oven temperatures, and the base-signal ROM should have elevated test errors on the potential partner data set.

5.2.3. Application to the hygroscopic capillary-porous media model

The efficient design of experiments method is now applied to the hygroscopic capillary-porous media model. It allows for investigating how the procedure adapts to different physical models. The conjugate heat and mass food processing model of Sec. 4.3.2 is utilized to provide a reasonably comparable setting. One core temperature probe $T_{\mathrm{A}'}$ is taken at $(x, y) = (0.01, 0)\,\mathrm{m}$ and one surface temperature probe $T_{\mathrm{B}'}$ is taken at $(x, y) = (0.01, 0.009)\,\mathrm{m}$. In an economized study setup, 165 APRBS and 35 multi-sine signals (among which are AP15 and MS15) are used to generate training data sets with the full-order model. Then, training of 1-signal ROMs is performed with 90 APRBS-excited data sets and a fixed complexity $i = 2$. Correlations are tested and found on the groups AP15, MS15 and all 165 APRBS data sets. The data set utilized for the training of the respective 1-signal ROM is excluded from the test groups. Data sets consisting of sinAPRBS, single sine, and single step excitation signals are not considered, as low errors on AP15 also showed low errors on sinAP15, single sines and single steps in Sec. 5.1.4.

Table 5.3 tabulates the Pearson correlation matrix between error measures (rows) and training data features (columns). The most significant correlation exists between $\overline{T}_{\text{diff},i}$ and $\overline{E}_{\text{med}}$ with $R = 0.76$ when testing is performed on all APRBS signals. In contrast to the correlations for the soft-matter model, the correlations on AP15 and MS15 are slightly less ($R = 0.67$). A possible cause is AP15 and MS15 not being perfectly tailored for the hygroscopic capillary-porous media model. Promising candidates for good 1-signal ROMs can be found at $\overline{E}_{\text{med}} \approx 0\,\mathrm{K}$ and $\overline{T}_{\text{diff},i} \approx 25\,\mathrm{K}$, as indicated by a red circle in Fig. 5.10a. ROM450 is one of the best 1-signal ROMs with $\overline{E}_{\text{rms}} = 1.58\,\mathrm{K}$, see Fig. 5.10c. Choosing a suitable training partner with the similarity chart in Fig. 5.10b further reduces the error of the respective 2-signal ROM to $\overline{E}_{\text{rms}} = 0.97\,\mathrm{K}$ for $T_{\mathrm{B}'}$, see markers in Fig. 4.17b. Lower test errors for the core temperature $T_{\mathrm{A}'}$ of $\overline{E}_{\text{rms}} = 0.71\,\mathrm{K}$ indicate that surface temperatures are more complex to replicate, presumably owing to the evaporation effects that are active in the surface region. Complexities higher than $i = 2$ do not increase the ROM test error in this particular example. The effect of complexities is investigated more closely in the next section, together with other particularities of the DynROM method. All in all, this short repetitive example demonstrates how the efficient design of experiments method flexibly adapts to the physics of other models. It is considered plausible that correlations change when different models are investigated.

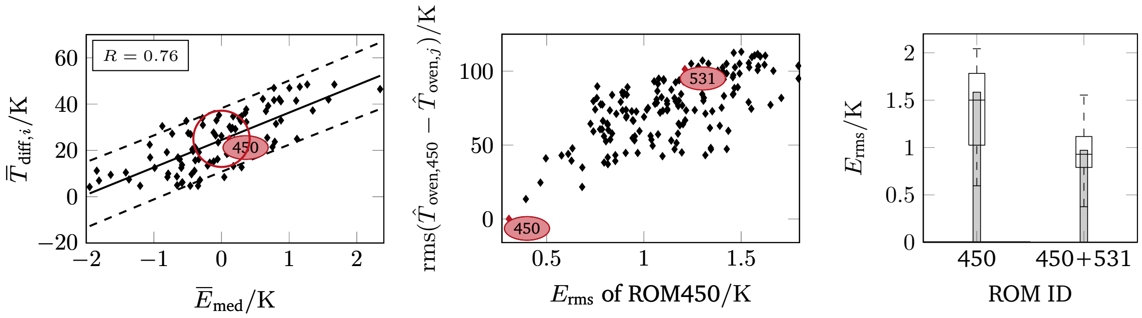

(a) Selection of a 1-signal ROM. **(b)** Selection of a training partner. **(c)** Test errors.

Figure 5.10. Efficient design of experiments for the conjugate hygroscopic capillary-porous media model. The red circle indicates the position of 1-signal ROMs with low test errors. Testing is performed on all APRBS data sets.

Table 5.3. Pearson correlation matrix between error measures (rows) and training data features (columns) for APRBS 1-signal-ROMs. $\overline{T}_{\text{diff},i}$ shows the best correlation with $\overline{E}_{\text{med}}$. Testing is performed on all APRBS data sets.

Measure	$\overline{T}_i$	$\overline{T}_{\text{diff},i}$	$\overline{T}_{\text{diff},j}$	$\lvert\overline{T}_{\text{diff},i}\rvert$	$\overline{T}_{\text{oven}}$	$\text{std}(T_{\text{oven}})$	$\text{Cr}(T_{\text{oven}})$	$\text{std}(T_{\text{A}})$	$\text{std}(T_{\text{B}})$
$\overline{E}_{\text{rms}}$/K	0.21	**0.47**	**0.37**	−0.17	0.26	0.04	−0.10	−0.05	0.22
$\overline{E}_{\text{map}}$/%	0.23	**0.44**	**0.34**	−0.16	0.27	0.05	−0.10	−0.04	0.18
$\overline{E}_{\text{max}}$/K	0.15	**0.50**	**0.40**	−0.18	0.18	0.03	−0.08	−0.09	0.22
$\overline{E}_{\text{med}}$/K	0.21	**0.76**	**0.57**	0.11	0.21	0.07	0.02	−0.29	0.26
$\overline{E}_{\text{iqr}}$/K	0.19	**0.38**	**0.32**	−0.21	0.23	0.02	−0.11	0.02	0.22
R^2	−0.14	**-0.48**	**-0.42**	0.17	−0.16	−0.02	0.07	0.07	−0.23

5.3. Benchmarks of the DynROM method

As the state of the art revealed, this work is one of the first to employ and especially investigate the properties of the DynROM method in detail. The influence of complexity (ODE augmentation), extrapolation capabilities, speed-up and prediction accuracy are investigated with the soft-matter model hereafter.

5.3.1. The influence of reduced-order model complexity

As introduced in Sec. 3.2.2, one particularity of DynROM lies in adding i free variables to the ODE system to better learn the nonlinear behavior in the data. The free variables are added iteratively to reduce the error during training [8]. So far, the 1-signal ROM study considered a fixed complexity $i = 2$. Indeed, hardly any 1-signal ROM could be trained beyond $i = 2$, and it is often unstable if $i = 3$ was reached. Presumably, positive poles of the ODE system lead to unstable system dynamics when the method reaches an over-learned state. As this behavior does not appear as strong for the 2-signal ROM study, one can assume that DynROM needs more than one training data set to not over-learn at low complexities. Figure 5.11 depicts the test errors over

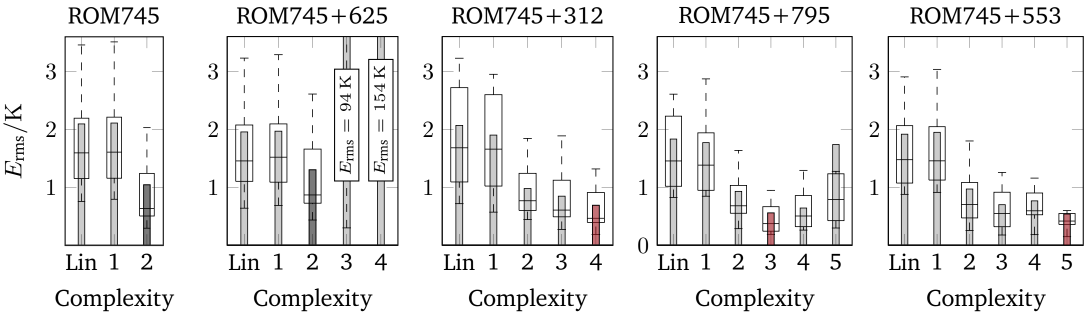

Figure 5.11. Influence of complexity i on the ROM test error. Lin represents a linear ROM. A usual error-decreasing trend for increasing i (ROM745, ROM745+312, ROM745+553), potential over-learning (ROM745+795), and instability (ROM745+625) are shown. Color-coded black and red bars mark the selected complexity for the 2-signal ROMs study.

ascending complexities for candidates of the 2-signal ROM study of the previous section. One can observe here that combining data sets 625 and 745 does not add sufficient new information to the training process. Utilizing both data sets for training leads to instability at higher complexities. In contrast, increasing complexity reduces the test error for good training partners by a factor of up to four compared to linear[2] ROMs (marked as “Lin” in Fig. 5.11), see cases ROM745+312 and ROM745+553. Nonetheless, choosing the highest complexity for a ROM does not always guarantee the best test errors, compare the case ROM745+795.

5.3.2. Extrapolation capabilities

ROMs with extrapolation capability are desired as they can predict results outside of their trained parameter space. Extending the oven’s temperature range to even higher or lower temperatures is not considered sensible. The time frame for transient ROMs can also be considered a trained parameter space. A test utilizes a repeated oven temperature signal 303 to investigate how a ROM behaves after $t = 1400\,\mathrm{s}$. The results show that the error remains reasonably low despite the temperatures behaving differently in the second segment. Figure 5.12 again reveals the nonlinear behavior of the physical model owing to evaporation effects. The ROMs can reasonably extrapolate this nonlinear behavior, as seen in the surface temperature evolution in 1-signal ROM745 and 2-signal ROM745+795. The root-mean-square errors are within the range of the physical validation of the soft-matter model in Sec. 4.1.2.

A build-up of prediction error can be observed when the model is applied outside the trained time window of $1400\,\mathrm{s}$. However, there is no clear trend of over- or under-prediction when transitioning from the learned to the unlearned time domain. The source of the accumulating error may be attributed to the extended nonlinear behavior of the physical model at high temperatures, where surface evaporation acts as a heat sink and keeps temperatures within the boiling range. Once

---

[2] The linear ROMs are a by-product of using DynROM. The linear ROM technology is based on time domain vector fitting techniques [8].

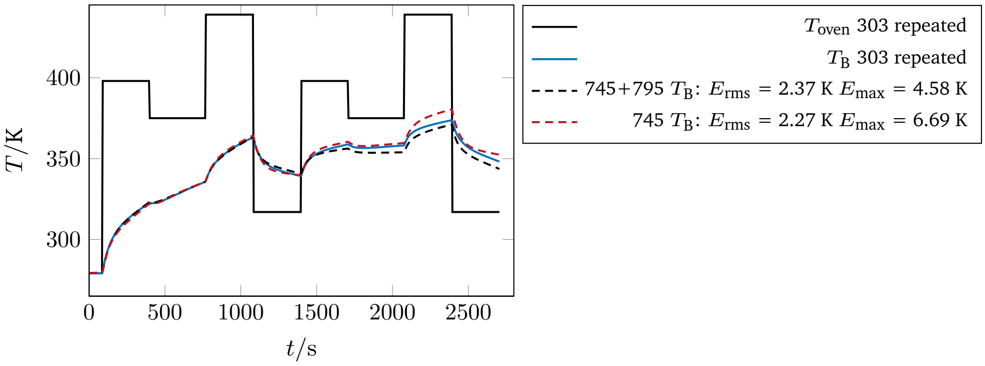

Figure 5.12. Extrapolation capability of the best 1-signal and 2-signal ROMs [137].

the surface dries out, surface temperatures can increase further. To include this behavior in the ROM, a wider time frame and higher temperatures would need to be included in the training. However, this study focused on the typical thermal processing duration of chicken fillets. Reaching core temperatures close to $100\,^{\circ}\mathrm{C}$, this simple test already leaves the sensible range of operation. Additionally, it can be concluded from this example that concatenating two excitation signals to enrich the information content of a training data set is not a practical approach. For example, the data would not include the start-up phase induced by the second signal.

5.3.3. Attainable speed-up

Speed-ups within this work are defined relative to physical process times, not the simulation times of the full-order model. A speed-up larger than unity indicates that the digital twin objectives of faster-than-real-time simulations are achieved. Table 5.4 summarizes the simulation timings of full-order models and of the corresponding ROM generated with DynROM. The numerical solutions of the validation case (a quarter section of the soft-matter model) take about $5\,\mathrm{h}$ on 20 cores of a cluster of two Intel Xeon E5-2687W v4 (3.2 GHz) processors. DynROM allows the export of synthesized ROMs in the FMU format [22], a standard model exchange format for surrogate models. The execution of the FMUs within MATLAB Simulink [241] requires approximately $0.10\,\mathrm{s}$, which translates to a speed-up of $\mathrm{Sp} \approx 3.6 \times 10^4$ with no noticeable serial computational load. When increasing the number of outputs to eight, the simulation time is still only $0.13\,\mathrm{s}$. Similar speed-ups are also achieved for field data ROMs, as discussed in Sec. 5.4.

5.3.4. Reduced-order model prediction errors

Figure 5.13 illustrates the performance of the found ROMs. Representative data sets with sinAPRBS, APRBS, and multi-sine signals are chosen for testing. Their oven temperature trajectories are depicted in Fig. 5.13a. The error measures E_{rms} and E_{max} are given in the figure legends for better comparability. Grey and blue solid lines represent the solution of the full-order model. Figure 5.13b and Fig. 5.13c show the evaluation of the best multi-sine-based and APRBS-based

Table 5.4. Comparison of simulation times and speed-up for the validation case and the conjugate convection oven simulations with ROM executions.

Type	Real time	Sim. time	Computational load	Degrees of freedom	Speed-up
3D FEM, estimation in Sec. 4.4	3600 s	est. 3700 h	parallel, full load 24 × 3.2 GHz	5.8×10^6	0.0003
3D FEM, validation case of Sec. 4.1.2	1200 s	5 h	parallel, full load 20 × 3.2 GHz	9×10^5	0.07
ROM745+795	3600 s	$\approx 0.1\,\mathrm{s}$	serial, not noticeable 1 × 3.2 GHz	5 (FMU)	36 000

1-signal ROMs: ROM795 and ROM745. Already 1-signal ROM745 shows a very good replication of the core and surface temperatures of the full-order model, achieving a test error of typically $E_{\mathrm{rms}} \approx 1\,\mathrm{K}$ on a multitude of test data sets. To further emphasize the significance of proper signal selection for ROM training, evaluations of the worst APRBS (ROM351) and multi-sine (ROM819) ROMs are also presented in Fig. 5.13b and Fig. 5.13c. The 2-signal ROM745+795 time evaluation can be found in Fig. 5.13d, displaying a characteristic $E_{\mathrm{rms}} < 0.5\,\mathrm{K}$ for the presented test signals. The 2-signal ROM745+795 performs best considering many test groups. Its global test error is as low as $\overline{E}_{\mathrm{rms}} = 0.38\,\mathrm{K}$ on MS15, $\overline{E}_{\mathrm{rms}} = 0.64\,\mathrm{K}$ on AP15 and $\overline{E}_{\mathrm{rms}} = 0.67\,\mathrm{K}$ on sinAP15. The complete error evaluations of all 2-signal ROMs on all available test groups can be found in Appendix A.4.

Table 5.5. 2-signal ROMs tested on AP15.

ID	745	+553	+795	+312	+553+795	+371	+351	+555	+638	+692	+303	+328	+342	+625
Complexity	2	5	4	4	3	3	4	3	5	4	3	3	4	2
$\overline{E}_{\mathrm{rms}}/\mathrm{K}$	1.05	**0.54**	0.64	0.69	0.85	1.45	0.98	1.16	0.54	0.79	0.87	0.81	0.59	1.30
$\overline{E}_{\mathrm{map}}/\%$	0.22	**0.12**	0.14	0.14	0.16	0.29	0.20	0.27	0.13	0.15	0.16	0.16	0.14	0.28
$\overline{E}_{\mathrm{max}}/\mathrm{K}$	2.63	**1.31**	1.67	1.73	2.70	3.99	2.70	2.28	1.41	2.29	2.71	2.29	1.36	3.20
$\overline{E}_{\mathrm{med}}/\mathrm{K}$	0.07	**0.07**	−0.19	0.02	0.03	0.01	0.13	−0.63	−0.04	−0.07	−0.02	−0.06	−0.12	0.01
$\overline{E}_{\mathrm{iqr}}/\mathrm{K}$	1.25	**0.62**	0.64	0.73	0.80	1.31	1.05	1.43	0.51	0.73	0.75	0.80	0.72	1.44
R^2	1.00	**1.00**	1.00	1.00	1.00	0.99	1.00	0.99	1.00	1.00	1.00	1.00	1.00	1.00

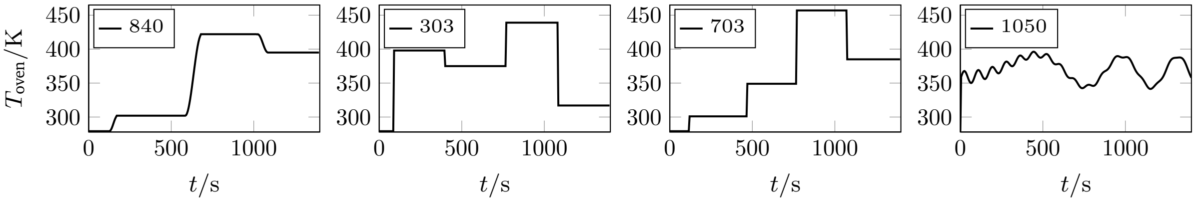

(a) Test data sets.

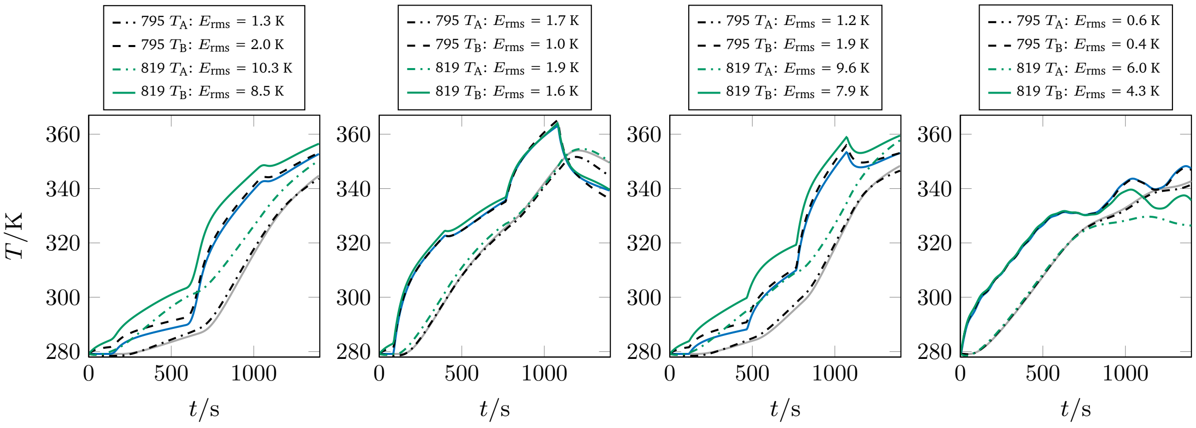

(b) Testing of best (795) and worst (819) multi-sine 1-signal ROM.

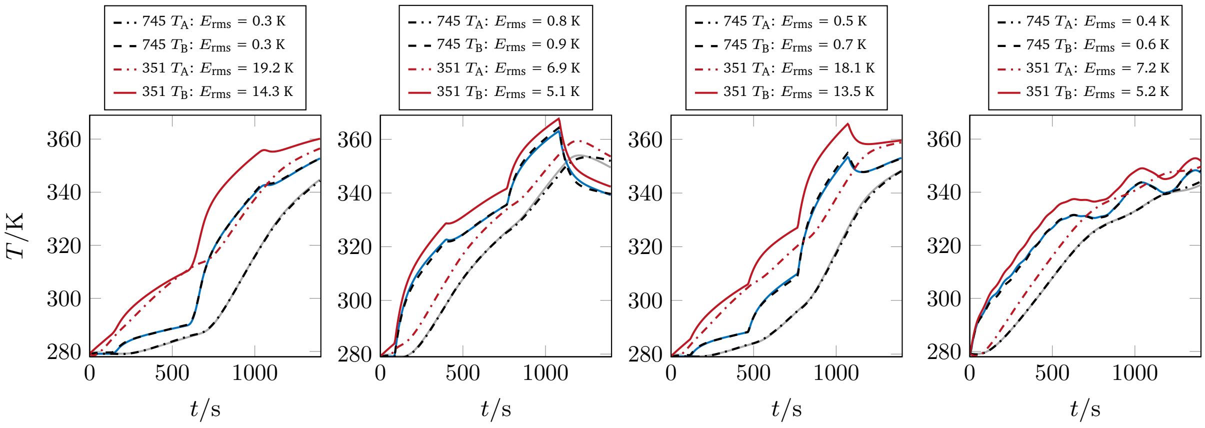

(c) Testing of best (745) and worst (351) APRBS 1-signal ROM.

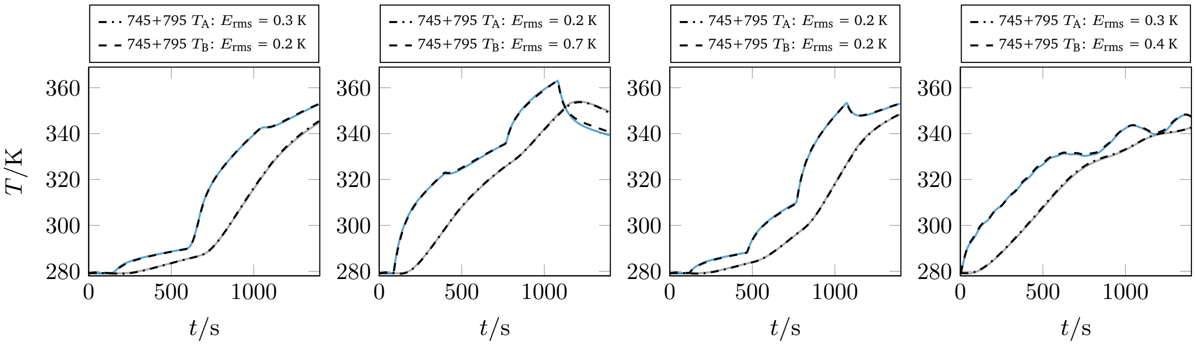

(d) Testing of ROM745+795.

Figure 5.13. Time evaluation of representative ROMs on selected test signals. The full-order model solutions T_A and T_B are represented by the grey and blue solid lines [137].

5.4. Field data reduced-order modeling

The previous sections demonstrate the derivation of ROMs for specific readout points of a full-order model. In certain MPC scenarios, it might be interesting to have access to field data as well. This section extends the ROM generation to field data with the SVD-based approach presented in Sec. 3.2.3. It investigates how the extension influences the accuracy and simulation time requirements of the generated ROM. Moreover, it embeds the generation of field-data ROMs into the proposed efficient design of experiments procedure.

5.4.1. Field data reduced-order model benchmarks

The following benchmarks of the field data ROMs are performed for the convection oven model from Sec. 4.3.3. Particularly, the temperature field of the lower food item shall be replicated by a ROM. The food item is spatially discretized into $n = 4649$ points in space defined by the vertices of the finite elements. A fixed time step of $\Delta t = 10\,\mathrm{s}$ with $N = 140$ time steps defines the resolution of the readout in time. Compared to the ROM studies for readouts at two distinct points, significantly higher efforts are required concerning the field data generation of the readout data $\hat{\boldsymbol{Y}} \in \mathbb{R}^{n \times N}$, data storage, ROM training and ROM testing time. Consequently, instead of training 1-signal ROMs from all available data sets, only apparently suitable ROMs are chosen to prove the proposed procedure and to investigate the performance of the DynROM method. Testing is performed on an economized test group consisting of AP15 enriched by 15 additional APRBS data sets. The resulting test group passes the χ^2 test of Sec. 5.1.4 for surface temperatures of the ellipse. So far, data exchange between COMSOL Multiphysics, TwinLab (MATLAB) and DynROM is conducted with text files containing comma-separated values (CSV). TwinLab is extended with an interface to read and write binary snapshot data to handle the increased data set sizes better. TwinLab writes out the 2D or 3D field data as binary snapshot files (*.bin) for DynROM and imports the evaluations of the ROM (performed in DynROM) back into the data structure in TwinLab for the error calculations.

5.4.1.1. Field data ROM accuracy

Section 3.2.3 explains the approach within DynROM that is used to reduce the readout size. Keep in mind that a SVD is performed for $\hat{\boldsymbol{Y}} \in \mathbb{R}^{n \times N}$ and a rank r representation is found:

$$\hat{\boldsymbol{Y}}_{n,N} \approx \tilde{\boldsymbol{Y}}_{n,N} = \boldsymbol{U}_{n,r} \boldsymbol{\Sigma}_{r,r} \boldsymbol{V}^*_{r,N} = \boldsymbol{U}_{n,r} \boldsymbol{C}_{r,N} \,, \tag{5.9}$$

where $\boldsymbol{U}_{n,r}$ contains purely spatial mode shape vectors and $\boldsymbol{C}_{r,N}$ contains r transient mode shape coefficients on its rows. By default, DynROM selects r such that the SVD's relative root-mean-square error for $\tilde{\boldsymbol{Y}}_{n,N}$ is below 0.1%. Figure 5.14 depicts the time-dependent mode shape coefficients[3]

---

[3] Unfortunately, ANSYS DynROM does not provide access to the spatial modes, nor does it allow to export the ROM output for the mode shape coefficients.

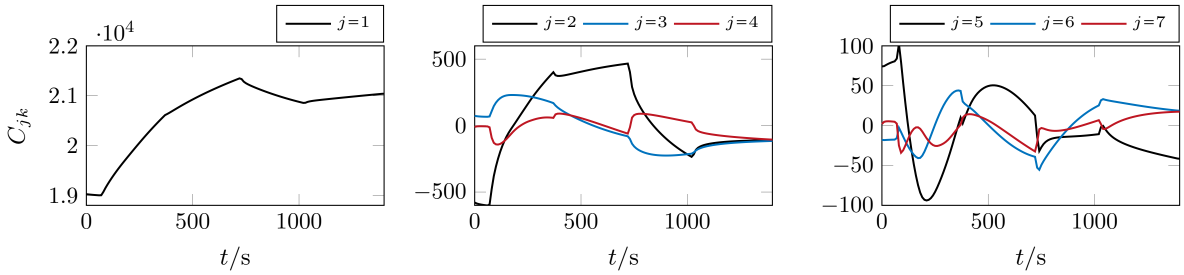

Figure 5.14. Mode shape coefficients for a rank-7 representation with relative errors less than 0.1% on data set 450.

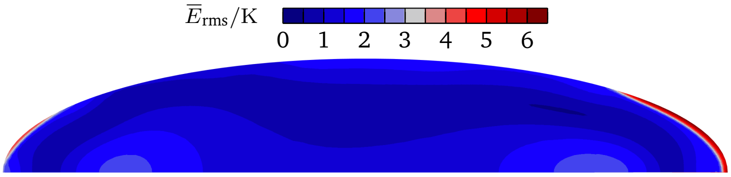

(a) Rank-3 ROM: $\mathrm{rms}(\overline{E}_{\mathrm{rms}}(x_i)) = 1.60\,\mathrm{K}$.

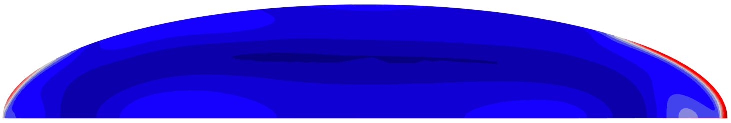

(b) Rank-7 ROM: $\mathrm{rms}(\overline{E}_{\mathrm{rms}}(x_i)) = 1.69\,\mathrm{K}$.

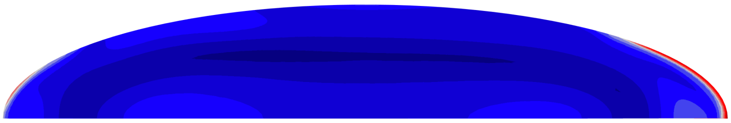

(c) Rank-20 ROM: $\mathrm{rms}(\overline{E}_{\mathrm{rms}}(x_i)) = 1.60\,\mathrm{K}$.

Figure 5.15. Influence of the SVD rank r on the ROM accuracy at a constant complexity of $i = 3$ for the 2-signal ROM450+531.

for the data set 450 at this default error setting, which results in a rank-7 representation. The coefficients are ordered by magnitude as rows in $\boldsymbol{C}_{r,N}$. A three-order decrease in magnitude can be seen from the first mode to the three last modes in Fig. 5.14. Moreover, the transient trajectory of the last mode coefficients has more complicated patterns than the coefficients of the first. Replicating these patterns might be a challenge for the DynROM method.

The findings above raise the question of how the choice of rank influences the accuracy of the ROM. Whereas $r = 3$ yields a relative root-mean-square error for $\tilde{\boldsymbol{Y}}_{n,N}$ of 0.48%, $r = 7$ and $r = 20$ yield errors of 0.089% and 0.013%, respectively. Figure 5.15 illustrates the influence of these three rank-r representations on the ROM error. The root-mean-square error over time, denoted as $\overline{E}_{\mathrm{rms}}(x_i)$, results from testing on one test data set. The isocontours in Fig. 5.15 represent the average of $\overline{E}_{\mathrm{rms}}(x_i)$ over all 30 test data sets. In the subcaption, $\mathrm{rms}(\overline{E}_{\mathrm{rms}}(x_i))$ is given to coin the error into one error measure over space and time. One can observe a slight difference in the error distribution from coarse patterns in Fig. 5.15a to slightly more granular patterns in

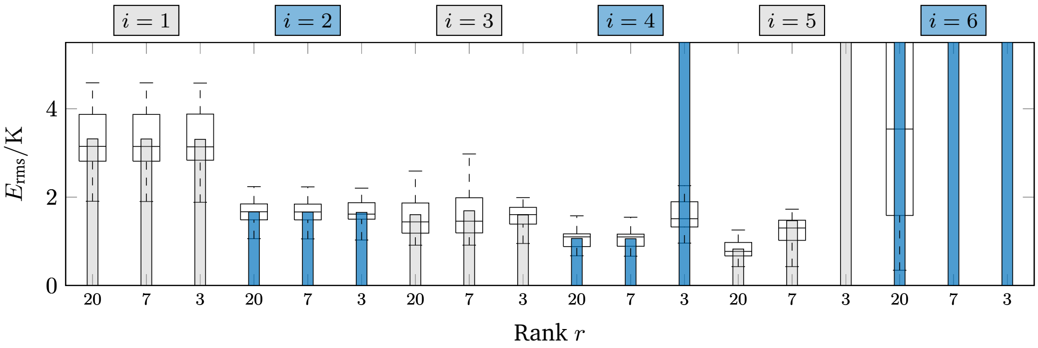

Figure 5.16. Combined interaction of rank and complexity that influence the ROM accuracy. ROMs with the same complexity are grouped in ascending order from left to right. Bars represent the average of the error measure $\text{rms}(\overline{E}_{\text{rms}}(x_i))$ on the test group. Boxplots indicate the distribution of $\text{rms}(\overline{E}_{\text{rms}}(x_i))$.

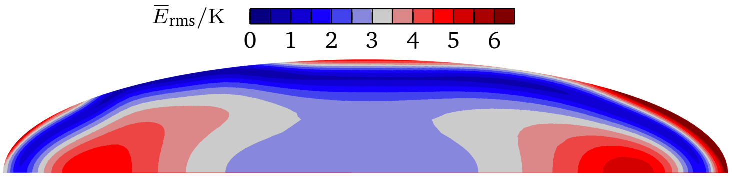

(a) Complexity $i = 1$: $\text{rms}(\overline{E}_{\text{rms}}(x_i)) = 3.32\,\text{K}$. Error contours clipped at $6\,\text{K}$. Maximum error is $15\,\text{K}$.

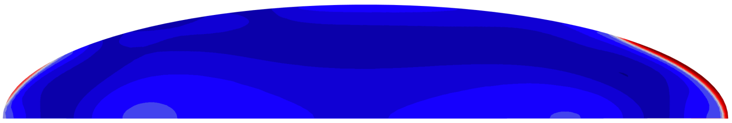

(b) Complexity $i = 2$: $\text{rms}(\overline{E}_{\text{rms}}(x_i)) = 1.67\,\text{K}$.

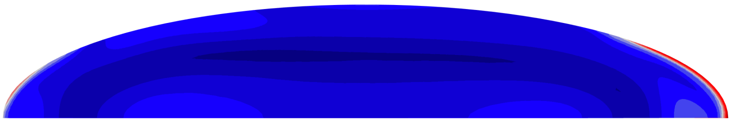

(c) Complexity $i = 3$: $\text{rms}(\overline{E}_{\text{rms}}(x_i)) = 1.60\,\text{K}$.

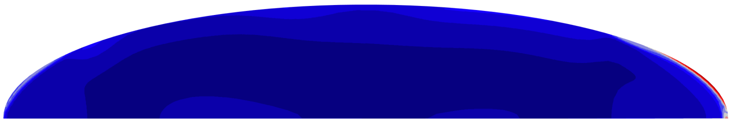

(d) Complexity $i = 4$: $\text{rms}(\overline{E}_{\text{rms}}(x_i)) = 1.06\,\text{K}$.

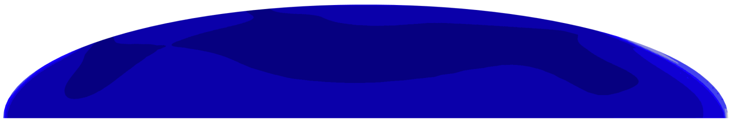

(e) Complexity $i = 5$: $\text{rms}(\overline{E}_{\text{rms}}(x_i)) = 0.83\,\text{K}$.

Figure 5.17. High complexities employed within the DynROM approach allow training ROMs with exceptionally low test errors.

Fig. 5.15b and Fig. 5.15c. The occurrence of dark red areas on the right-hand side is slightly reduced with increasing rank. However, no clear trend can be established for the overall error measure $\mathrm{rms}(\overline{E}_{\mathrm{rms}}(x_i))$ that varies from $1.60\,\mathrm{K}$ to $1.69\,\mathrm{K}$ and back to $1.60\,\mathrm{K}$. Investigating the rank together with the complexity i of the ROM is more instructive. Indeed, $i = 3$ is chosen for Fig. 5.15, as this is the highest complexity where the rank-3 ROM does not show instabilities in the form of highly deviating solution trajectories. Figure 5.16 depicts the error levels of the ROMs when both rank r and complexity i are considered. ROMs with the same complexity are grouped in ascending order from left to right. One can observe a trend of reduced error levels when increasing the complexity from 1 to 5. This behavior agrees with the findings in Sec. 5.3.1. Up to a complexity of $i = 3$ the rank r does not significantly influence the error. For $i = 4$, the rank-3 ROM becomes unstable for selected test data sets. This can be seen from the mean being biased by one outlier ROM evaluation with values far outside the variable range. The median and interquartile range remain less sensitive to the single outlier. For $i = 5$, the ROM with rank $r = 20$ can be trained to even lower test error measures. Figure 5.17 depicts the average for all stable rank-20 cases of the 2-signal ROM450$+$531. Up to a complexity of 4, the ROMs struggle to replicate the hotter zones of the food item caused by the conjugate simulation of the convection oven and food item. At $i = 5$, those zones are captured with very high accuracy. Here, the combination of increased rank and high complexity seem to interact in a sweet spot. The error of the ROM remains below $1\,\mathrm{K}$ for large portions of the domain, and the global error measure is $\mathrm{rms}(\overline{E}_{\mathrm{rms}}(x_i)) = 0.83\,\mathrm{K}$, which can be considered a remarkably good result given the fact that testing is performed on 30 representative and fair data sets. The error is reduced by a factor of four compared to the ROM with $i = 1$. For $i = 6$, a threshold for error reduction is reached. Although the training error is still reduced for $i = \{5, 6\}$ (results not shown), the corresponding ROMs become highly unstable during testing. Presumably, over-fitting to the dedicated training data entails a loss of generality and ROM stability. Considering that the rank r determines the number of states of the DynROM ODE system (plus the number of free variables), one may conclude that the selection of $i < r$ ensures better stability of a ROM until a certain threshold is reached and instabilities of the ROM start to appear. Depending on the patterns in the field data, it may be beneficial to increase the rank of the SVD such that higher complexities and even lower ROM test errors can be attained.

5.4.1.2. Field data ROM run times

One may suspect that switching to field data ROMs would entail significant performance losses compared to point data ROMs. Fortunately, this is not the case because of the SVD. The time requirements to execute a point data ROM do not differ significantly for field data ROMs. Only the mode shape coefficients $\hat{\boldsymbol{C}}_{r,N}$ must be replicated with an ODE time stepping scheme. The maximum number of mode shapes is 20 in the benchmarks above. A corresponding execution time of such ROM is $0.37\,\mathrm{s}$ on average. The decompression to field data is the algebraic expression $\hat{\boldsymbol{X}}_{n,N} = \boldsymbol{U}_{n,r}\hat{\boldsymbol{C}}_{r,N}$. Such matrix-vector products and potential further algebraic expressions to obtain derived quantities of interest, e.g., the average surface temperature, are not too computationally expensive. If secondary food variables are of interest within an MPC task, the ODEs of Sec. 2.3.3 must be integrated in time while utilizing the temperature trajectories generated by the ROM. Simulations of $1400\,\mathrm{s}$ of real time in 20 points would require additional $0.30\,\mathrm{s}$ on the same hardware (ODE45 solver, fixed time step $\Delta t = 10\,\mathrm{s}$, serial execution within MATLAB). Whereas the 20 points of interest might be sufficient for many applications, other scenarios might rely on field data for the secondary variables. The simulation for one secondary variable with the entire temperature field requires additional $23\,\mathrm{s}$. Here, it would be worth a try to train additional ROMs for the secondary variables. Studies by Pham [188] suggest that ROMs that include secondary variables and temperatures have reduced output quality compared to ROMs with only temperatures. Consequently, a tradeoff between accuracy and speed must be found.

5.4.2. Efficient design of experiments for field data reduced-order models

The discussions in Sec. 4.3.3 elaborate how simulations of realistic-sized multi-physical, coupled problems can easily take weeks or months to solve on modern cluster PCs. Consequently, the training data generation of field data ROMs makes use of the forerunner concept: Instead of again performing the (time-consuming) correlation search with the full-order model of the convection oven, one can resort to the correlations already found on a reduced-size simulation model. This forerunner model may be a by-product of the simulation model development. In computational engineering, one would seldom derive a new simulation model directly with all physical couplings, employing a fine mesh and the problem's detailed geometry. Instead, the individual components of the model are validated step-by-step. They are assembled into a model of smaller size and dimension. This procedure is followed in Chapter 4. The hygroscopic capillary-porous model in conjugate flat plate configuration can be considered a forerunner of the convection oven model. All required physical models are present, but geometric particularities are not considered. Not by chance, comparable average heat transfer conditions are simulated in the conjugate flat plate model and in the convection oven model. Thus, the simplified setup serves as the forerunner model to perform the efficient design of experiments' pre-simulations to identify correlations. In Sec. 5.2.3, data set 450 serves as good training data to generate a 1-signal ROM. ROM361 lies in the midrange, and ROM483 is one of the worst, stable 1-signal ROMs. A good training partner for ROM450 is data set 531, as identified with the proposed similarity chart in Fig. 5.10. Table 5.6

Table 5.6. Similar error trends for point and field data ROMs. Comparison of one top, mid and end-range ROM of the flat plate case and the 2D convection oven case, respectively.

		Conj. flat plate at B'			Convection oven field data		
Training data	Complexity	$\overline{E}_{\mathrm{rms}}/\mathrm{K}$	$\overline{E}_{\mathrm{iqr}}/\mathrm{K}$	$\overline{E}_{\mathrm{map}}/\%$	$\mathrm{rms}(\overline{E}_{\mathrm{rms}}(x_i))/\mathrm{K}$	$\mathrm{rms}(\overline{E}_{\mathrm{iqr}}(x_i))/\mathrm{K}$	$\mathrm{rms}(\overline{E}_{\mathrm{map}}(x_i))/\%$
450+531	5	–	–	–	0.83	0.51	0.18
450+531	2	0.97	1.10	0.25	1.66	1.30	0.37
450	2	1.58	1.58	0.30	1.94	1.45	0.46
361	2	2.47	2.97	0.58	2.01	1.47	0.47
483	2	5.29	4.75	1.18	2.64	2.53	0.62

summarizes the corresponding error measures. The same error trends persist for the convection oven field data ROMs. One can assume that correlations and good training partners found on the forerunner model are also valid for the convection oven problem. Exploiting this association of models would require only one-to-two simulations of the physical problem in full geometric representation to derive a 2-signal ROM.

5.5. Conclusions from the reduced-order modeling studies

The research presented in this chapter demonstrates that data-driven reduced-order modeling is a powerful method for developing accurate and efficient digital twins for industrial applications. The employed methodology is not dependent on modeling software. With only one-to-two training data sets, data-driven ROMs having high accuracy and speed-up can be created. The proposed efficient design of experiments supports selecting appropriate training data sets.

Summary and conclusions concerning the ROM performance

The ROMs presented in this chapter can provide significant speed-ups compared to real time. This results in suitable tools for on-device MPC. Attainable speed-ups for point data ROMs of up to eight outputs are approximately $\mathrm{Sp} \approx 3.6 \times 10^4$ with characteristic solution times of one-tenth of a second — without imposing a noticeable computational cost on a single-core processor. In less than half a second, field data ROMs with 4649 points in space and 140 points in time can reproduce the output of full-order models. Besides the significant speed-up, the data-driven ROMs show excellent test accuracy on large, representative test data groups. In particular, root-mean-square errors for the best point data ROM are 0.30–$0.74\,\mathrm{K}$, depending on the test group, and $0.83\,\mathrm{K}$ for the field data ROM. Compared to the variable range of 279.15–$450.15\,\mathrm{K}$, this is a relative error of 0.18–0.49%. The accuracy achieved by the ROMs is superior to the accuracy achieved by the hygroscopic, capillary-porous food model ($E_{\mathrm{rms}} = 0.9\,\mathrm{K}$) or the validation error of the soft-matter model ($E_{\mathrm{rms}} = 2.4$–$3.4\,\mathrm{K}$). Particularly, the field data ROM can capture the highly heterogenous temperature fields stemming from the conjugate simulation of heat and mass transfer inside a convection oven, see Fig. 4.25 and Fig. 5.17. The neural ODE augmentation mainly attains the high accuracy, which involves adding i free variables to the ROM ansatz. Compared to linear ROMs, this reduces the average test error by a factor of four. A lower complexity than the maximum possible should be employed to ensure ROM stability. A clear sweet spot for accuracy and stability is often identifiable when testing is performed on large enough test groups. Choosing a sufficient number of outputs, such as 4–8 probe locations for point data ROMs or 7–20 mode shape coefficients for field ROMs, improves ROM training. When the ODE ansatz has more state variables and more than one training data set, it is possible to apply a higher complexity i while being numerically stable. This holds especially for field data ROMs, where high complexities keep accuracy remarkably high, and the underlying SVD ensures a low computational load of the ROM.

In general, generating field data ROMs can be considered a “chicken–egg” problem. Suppose only five-to-ten derived variables of interest are evaluated within an MPC environment. In that case, it is questionable whether field data ROMs are required. A good alternative might be to train those derived variables directly as a point-data ROM. It would not require performing the SVD, the rank-r compression, the mode shape replication with ROMs, the decompression and the final calculation of the derived variables from the ROM’s field data. This might be an unnecessary chain of errors that can be circumvented with point data ROMs.

Three limitations of the DynROM method could be identified during the studies. First, the initial condition present in the training data must be identical. Owing to the black-box nature of ANSYS DynROM, trained ROMs always begin their output at the initial conditions of the training data. From a practical point of view, this does not represent an obstacle to deriving digital twins of thermal food processing. Usually, food is stored at controlled temperatures before processing. Additionally, one could enhance the digital twin concept by training various ROMs at different initial conditions. Only a few megabytes of storage are needed to store point data ROMs exported in the FMU format.

Second, the trained ROMs depend on the initial values of the free variables. A start from different values for the state variables would also require specifying appropriate initial conditions for the free variables. Without knowing an appropriate initial condition, the latter specification for the free variables is not yet possible in DynROM. On request, ANSYS acknowledges the issue and considers addressing it in future releases. The restart of a ROM from defined initial conditions is often needed during MPC tasks. A solution to this issue is proposed in Chapter 6.

Third, to avoid obscuring the training process, ANSYS suggests training only outputs of the same physical unit. However, preliminary tests by the author and Pham [188] indicate that mixing physical units within one ROM might not necessarily decrease its quality. In certain combinations, this might even be beneficial. The co-learning of temperature for a ROM of secondary variables could enhance the training effect, as the temperature might serve as a latent variable in the ODE system. In other cases, e.g., co-learning of water concentration together with temperatures, the accuracy of the temperature predictions is decreased compared to a temperature-only training run. These findings have the potential for future exploration.

Summary and conclusions concerning the efficient design of experiments

The proposed efficient design of experiments closes the gap in how to select only a few appropriate training data sets to obtain accurate ROMs. It correlates features of training data with error measures of 1-signal ROMs. Acknowledging such trends, good training data sets can be selected, or even better ones can be generated.

When selecting a suitable excitation signal type, one must distinguish ROM training, testing, and operation. In this work, ROM training is most successful with APRBS-excited data sets. However, a real convection oven cannot replicate the instant jumps in oven temperature. These findings oppose common recommendations in the literature, where signal types close to operational signals are suggested for training [96]. For APRBS, sinAPRBS, single-step, or single-sine test sets, APRBS-trained ROMs exhibit the lowest average test errors for the presented problems. Remarkably, APRBS-trained ROMs outperform their transformed sinAPRBS counterparts. Multi-sines may provide more suitable training signals if the operating environment is solely sinusoidal.

Testing needs to be done on fair and objective test groups. Random generation and selection of training data, such as the k-fold cross-validation, may not necessarily represent the output space equally at all positions, as demonstrated for the soft-matter model. Selecting data sets based on a χ^2 test, one can establish, e.g., a uniform distribution of the medians of the output variable. Fair test groups are beneficial for finding correlations between data set features and error measures. Besides using fair test groups, testing might also be performed with different excitation signal classes. SinAPRBS data sets most properly emulate the convection oven operating temperatures. However, testing on APRBS is considered conservative, as APRBS-trained ROMs exhibit even lower test errors on sinAPRBS test groups in this work.

The pragmatic approach of using a forerunner model allows the economized computational cost of the efficient design of experiments. An a priori search of correlations is performed on simpler forerunner models. Forerunner models can be a by-product during the usual modeling work in computational engineering, where physical, geometric and dimensional complications are tested and increased step-wise. Only one-to-two final full-order model simulations are required at the end. In this work, a similar ROM test error trend can be established between the forerunner and full-order model, given the prerequisite that both models contain identical physical models and operational conditions to ensure comparability. Future work could investigate the correlations between forerunner and full-order models more in-depth. Data and time-consuming studies could prove that correlations found in the forerunner concept also hold for the full-order model.

Correlations between data set features and ROM test errors vary depending on the physical model. Whereas high standard deviation in surface temperatures can serve as a good feature to select training data for the soft-matter model, derived properties of the APRBS signal serve as better features for the hygroscopic, capillary-porous model. Recommendations in literature to maximize coverage of input or output space of a data set [174, 237] cannot be confirmed. Investigations presented in [137] demonstrate that no beneficial correlation between input space coverage and ROM test error could be found for the soft-matter model.

Notably, low correlation values in the Pearson correlation matrix only indicate that no *linear* correlation exists. However, one might observe nonlinear dependencies between data set features and error measures. This limitation is partly lifted in this work through the choice of error measures, of which some behave linearly or quadratically in a local or global sense. Similarly, nonlinear data set features could be derived in future research. Nonetheless, the pre-search is not in vain even if no correlation can be found for any feature and error measure. The performed parameter sweep can serve to select the best training data set that exists. Likewise, independent of whether a correlation can be established, a similarity chart for the best 1-signal ROM facilitates the selection of additional data sets that enrich the ROM accuracy. An appropriate partner data set shows dissimilarity to the base data set, and elevated mutual 1-signal ROM test error levels should be considered to select potential training partner data sets. Moreover, all viable training partners should create excellent 1-signal ROMs.

Based on the results in this chapter, the following practical summary of the efficient design of experiments can be given in the style of a checklist:

I. Validate the physics and ensure the numerical accuracy of simulation on a geometrically simpler, potentially 2D, forerunner model.

II. Select and generate excitation signals that are appropriate for the problem at hand

   A. APRBS signals can be a good starting point for nonlinear system identification unless testing and application are exclusively sinusoidal. Here, consider multi-sines.

   B. For APRBS synthesis, divide the maximum overall process time into a manageable number of input steps/operational conditions (such as four steps in this study, considering the largest time constant of the model).

   C. Simulate the forerunner model with a significant number of random signals, e.g., $50-100$, to gather sufficient data sets covering the desired operating conditions.

III. Consider the usage of fair test data groups

   A. Check whether a group of test data sets might bias the error feedback of 1-signal ROMs.

   B. Data set selections based on χ^2 tests can furnish fair test groups if the desired distribution of the outputs is known.

   C. Consider sinAPRBS as an appropriate test signal if the physical process device cannot realize the immediate steps of the input signal (such as the thermal lag of convection ovens).

IV. Establish the efficient design of experiments in TwinLab

   A. Design and calculate data set features. This work's features might give inspiration for new, potentially nonlinear features.

   B. The data sets should be filtered based on their features, such as $\mathrm{std}(T_\mathrm{B})$ in this work. When a priori features are yet unknown, perform a random selection.

   C. $10-20$ data sets should at least be employed to train a preliminary 1-signal ROM each. The complexity should be selected to be moderate, such that stability is ensured.

   D. Derive global error measures of the 1-signal ROMs.

   E. Search for correlations between error measures and data set features and design better data sets with the knowledge of what features correlate with low ROM test errors.

   F. Choose the best 1-signal ROM as the base case.

   G. Select potential training partners with a similarity chart for the base 1-signal ROM, e.g., based on signal dissimilarity and the base case 1-signal ROM test error on the residual data sets.

H. Good training partners have at least medium dissimilar excitation signals. Furthermore, the base case 1-signal ROMs should at least show medium test errors on the potential training partners. The latter should also provide high-quality 1-signal ROMs.
I. Train 2-signal ROMs with training partners and test the ROM errors.
J. Repeat combinations of training partners until the test error stagnates.

V. Exploit the similarity between the forerunner and finished (3D) full-order models. Simulate 1-2 data sets of the final full-order model and train the corresponding ROM.

6. Model predictive control studies

This chapter briefly demonstrates the potential of physics-based, data-driven digital twins for developing advanced control algorithms. In an exclusively virtual setup, the predictions of the accurate surrogate models are employed to control the inner temperature of a convection oven. The core of the intelligent control approach entails an MPC algorithm. MPC is among the most popular closed-loop approaches for advanced process control [72]. The theoretical foundations and a condensed description of the implementation in MATLAB can be found in Sec. 6.1. It also introduces a proposed sub-optimization approach, which allows utilizing FMUs with fixed initial conditions. Section 6.2 demonstrates how the MPC algorithm deals with the remaining model/reality mismatch. Moreover, the MPC algorithm is exposed to challenging scenarios where autonomous decision-making is mandated. Conclusions from the presented use cases on the assets of physics-based, data-driven digital twins are drawn in Sec. 6.3.

6.1. A digital-twin-based model predictive control algorithm

The presented MPC solution approach and the decision-making scenarios were conceptualized and implemented for this thesis. Dorer [73] was given parts of the problem and wrote the first version of the code during his master's thesis in 2021. However, the results presented in this chapter were produced using a thoroughly revised version of the original code, including corrected loss functions, streamlined parameterization and optimizer selection for accuracy and speed, and improved FMU readouts at higher sampling rates to increase the prediction accuracy. In addition, an automatic command line call of the COMSOL model mimics the real process. Instead of using section-wise constant oven temperatures in the model call, the thermally delayed behavior of a convection oven temperature is emulated with a PT_1 block.

6.1.1. Control vector parameterization and model predictive control

This section briefly introduces the concepts of optimal control, control vector parameterization and MPC. The theoretical foundations are taken from [72, 108, 152], where the reader is referred to for further reading. Optimal control is an open-loop control algorithm that relies on a process model. Prior to the start of the process, an optimal control approach determines a set of control variables that optimizes the performance of a dynamical system model. The optimization is realized by minimizing a cost function that includes desired process targets. A direct solution method for an optimal control problem is approximating the control variables with a polynomial over time.

The approximation coefficients are then employed as design variables in a (in this case) nonlinear optimization problem. The simplest form of this so-called control vector parameterization approach utilizes constant subsections within the control signal.

Consider the benchmark setup of thermal processing of chicken meat, as presented in Sec. 4.1.2. Oven temperature set points $T_{\text{set},k}$ are the design variables. Those must remain within the sensible range of oven temperatures $T_{\text{set},k} \in [291.15\,\text{K}, 450.15\,\text{K}]$. A more realistic temperature trajectory is obtained in this work by superposing a PT_1 model to each set point. A PT_1 block consists of a proportional gain (P) and a first-order time lag (T_1). The step response of the oven temperature between t_k and t_{k+1} reads:

$$T_{\text{oven}}(t) = T_{\text{set},k} + (T_{\text{set},k+1} - T_{\text{set},k}) \left(1 - \exp^{-(t-t_k)/\tau}\right) , \tag{6.1}$$

where $\tau = 60\,\text{s}$ is the estimated time constant of the oven and $T_{\text{set},k+1} - T_{\text{set},k}$ is the gain. Figure 6.1 (center) illustrates the resulting exponential trajectories for T_{oven}. To give the emulated PT_1-behavior the possibility to equilibrate, the time window of $1000\,\text{s}$ is divided into four MPC time steps. To ensure sufficient pathogen inactivation, it is required as a safety constraint that the core temperature $T_{\text{A}}\left(t_{\text{end}}\right)$ reaches $T_{\text{A,safe}} = 347.15\,\text{K}$ at the end of the process [247]. The final moisture concentration $M_{\text{db}}\left(t_{\text{end}}\right)$ and the final texture $Ha\left(t_{\text{end}}\right)$ can be considered as possible process variables subject to optimization. If the moisture concentration and the hardness shall reach certain end values $M_{\text{db,end}}$ and Ha_{end}, the nonlinear optimization problem reads:

$$\min_{T_{\text{set},k}} \quad J = w_{Ha}\left[Ha\left(t_{\text{end}}\right) - Ha_{\text{end}}\right]^2 + w_M\left[M_{\text{db}}\left(t_{\text{end}}\right) - M_{\text{db,end}}\right]^2 , \tag{6.2}$$

$$\text{s.t.} \quad T_{\text{A,safe}} - T_{\text{A}}\left(t_{\text{end}}\right) \leq 0 , \tag{6.3}$$

$$291.15\,\text{K} \leq T_{\text{set},k} \leq 450.15\,\text{K} , \tag{6.4}$$

where $w_{Ha} = 10$ and $w_M = 3$ are the weights of the penalty terms chosen to be most suitable for the presented use cases. Internally, all variables are treated with a unity-based normalization. The process end time is termed t_{end}. A maximization of moisture concentration and minimization of hardness is realized by setting the moisture concentration and hardness to their initial values ($M_{\text{db, end}} = 0.76$ and $Ha_{\text{end}} = 14\,\text{N}$). The optimal control policy of oven temperature set points is determined by numerically solving the constrained optimization problem in Eq. (6.2)–(6.4).

The optimal control approach presented so far is carried out only once before the start of the process. It cannot cope with model/reality mismatch and unexpected disturbances. Closure of the control loop is achieved by recomputing the optimal control problem at discrete times during the process. For example, at a time t_k, the optimization is performed again for the remaining future temperature setpoints.

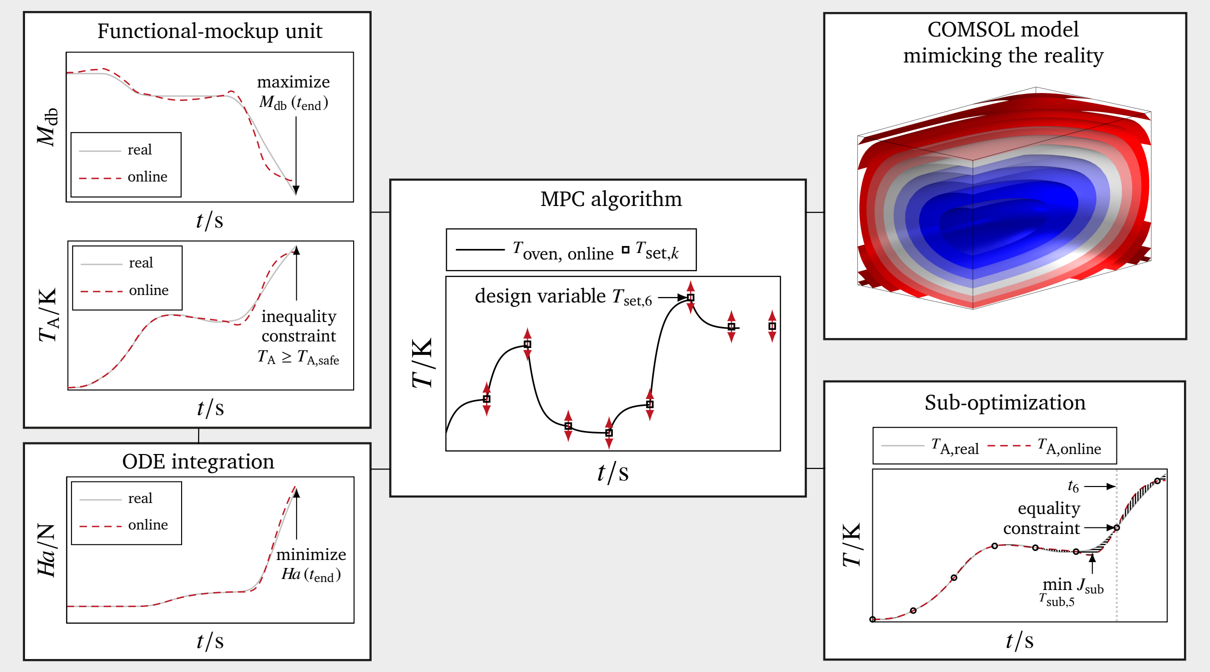

Figure 6.1. Digital-twin-based model predictive control approach.

Note that the loss function presented here is based on rough common sense estimates of what would be a plausible target. It serves to demonstrate what an intelligent MPC-based control algorithm might look like. The focus of upcoming studies lies on the accuracy and speed-up, as well as the computational approach that allows to apply FMUs in the context of MPC. However, generating enhanced loss functions would certainly require further expert input from food scientists and practitioners. Browning parameters within the loss function would possibly mandate different oven temperature trajectories. Additional power-related loss parameters could be added to explicitly account for energy savings.

6.1.2. Circumventing fixed initial conditions with a sub-optimization

During an MPC step at t_k, actual measurements of the process variables (if available) can be fed to the model to improve future predictions. Namely, the model for core temperatures could be initialized at t_k with the actual core temperatures from the measurements. As concluded in Sec. 5.5, the FMUs stemming from ANSYS DynROM possess hardcoded initial conditions. For this reason, the FMUs cannot be reinitialized at later points in time. Simulating the FMU with the previously realized oven setpoints inherently induces a difference between predicted and real core temperature, which comes from the inaccuracy of the ROM. A sub-optimization is conceptualized to still benefit from the measured values. At t_k, the last realized setpoint in the control vector could not, of course, be changed because it lies in the past. However, it can be altered for the model run. Therefore, the last oven temperature setpoint $T_{\mathrm{set},k-1}$ is artificially changed to $T_{\mathrm{sub},k-1}$, which minimizes the difference between real measurement and model prediction for T_{A} between t_{k-1} and t_k. An additional equality constraint requires that the two values equal at t_k. The corresponding sub-optimization problem reads:

$$\min_{T_{\text{sub},k-1}} \quad J_{\text{sub}} = \int_{t_{k-1}}^{t_k} \left(T_{\text{A}}\left(t\right) - T_{\text{A,real}}\left(t\right)\right)^2 \mathrm{d}t\,, \tag{6.5}$$

$$\text{s.t.} \quad T_{\text{A}}\left(t_k\right) - T_{\text{A,real}}\left(t_k\right) = 0\,, \tag{6.6}$$

$$291.15\,\text{K} \leq T_{\text{sub},k-1} \leq 500.15\,\text{K}\,. \tag{6.7}$$

6.1.3. Numerical procedure

One run of the MPC algorithm is initialized by solving the optimal control problem for all oven temperature set points. Under the assumption of a convex loss function, a global optimum is sought for the problem in Eq. (6.2)–(6.4). In a first heuristic step, the genetic algorithm *ga* (two generations, EliteCount = 5) is utilized to find a good initial guess for the design variables. The initial guess is further refined with the gradient-based local optimizer *fmincon* employing the sequential quadratic programming (sqp) algorithm. The latter is recommended because of its rapid convergence for medium-size optimization problems [240].

At $t_k \in \{250\,\text{s}, 500\,\text{s}, 750\,\text{s}\}$, each MPC step starts with a sub-optimization step, respectively: The oven temperature setpoint of the previous control step is artificially optimized such that the model output $T_{\text{A}}\left(t_k\right)$ matches best the real core temperature $T_{\text{A,real}}$. Then, the residual, future design variables $T_{\text{set},k}$ are updated within the MPC optimization. Given that the previously determined control vector already provides a good initial guess for both the sub-optimization and the MPC optimization, the local optimization algorithm *fmincon* (sqp) is employed again. As no explicit gradient of the FMU with respect to the design variables is available, the gradient is reconstructed with forward finite differences by *fmincon*. Preliminary parameter tests identified robust optimizer settings (TolX = 1×10^{-5} ; TolFun = 1×10^{-6}). The parameters of the finite difference stencil could be left at standard settings.

Whenever a design variable changes during optimization, the FMU of ROM745+795 is automatically simulated in MATLAB Simulink with the optimizer-defined oven temperature trajectory. The explicit ODE45 algorithm (RelTol = 1×10^{-6}) provides the temporal solution of the FMU within MATLAB Simulink. In the absence of a real process, the simulation model within COMSOL Multiphysics mimics reality in the presented virtual MPC setup. Notice that the validation error of this model is $E_{\text{rms}} = 2.38\,\text{K}$ for the core temperatures. At every grid point $t_k \in \{250\,\text{s}, 500\,\text{s}, 750\,\text{s}, 1000\,\text{s}\}$, an updated trajectory of the oven temperature is computed. The algorithm then automatically calls the COMSOL model and queries the real core temperature trajectory. Note that the time delay between the measurement of reality and the subsequent run time of the re-optimization is not reflected in the following demonstration as it is quite small.

6.2. Application scenarios for autonomous thermal food processing

In the following, two selected decision-making scenarios are presented. The first one highlights how efficiently the derived digital twin acts within the MPC algorithm when it operates within its trained temperature range and time horizon. The second scenario forces the digital twin to leave this time horizon to ultimately adapt to new optimization targets during operation. Nevertheless, the algorithm masters this challenge with success.

6.2.1. Mitigation of the reduced-order model error during undisturbed operation

A digital twin is mandated to be a highly accurate reflection of a process. However, there is always some mismatch between the model and reality. This baseline case demonstrates how the sub-optimization and the MPC routine mitigate the mismatch between the ROM and the underlying full-order model.

As motivated earlier, a COMSOL model mimics the reality in the presented virtual setup. Since the numerical solution errors of the simulation model are shown to be negligibly small, the only significant error source is the test error of ROM745+795, which is $0.30–0.74\,\mathrm{K}$ depending on the test set. Figure 6.2 illustrates trajectories and statistics on the baseline case with ROM745+795. The realized trajectory $T_{\mathrm{oven,online}}$ by the MPC algorithm does not differ significantly from the pre-calculated offline policy $T_{\mathrm{oven,offline}}$. This is a strong indicator of a low model error. Further evidence confirming this hypothesis is provided by the performance of the sub-optimization algorithm, which applies only minor adjustments (red x-markers) compared to the realized set points (black squares) to keep $T_{\mathrm{A,online}}$ (FMU model) aligned with $T_{\mathrm{A,real}}$ (COMSOL model). Consequently, the predictions and the realization for the texture parameter Ha are also almost identical. Note that ROM745+795 is not only trained to reproduce T_{A} and T_{B}, but also M_{db}. Its reproduction is required inside of the loss function. Figure 6.2 illustrates the accuracy of the prediction, which only misses reality by $E_{\mathrm{max}} = 0.01$. However, a slight unphysical rise in M_{db} is also observable during the first third of the prediction. One MPC step takes maximum $t_{\mathrm{MPC}} + t_{\mathrm{sub}} \approx 3.73\,\mathrm{s}$ to be solved on one core of an Intel Xeon E5-2687W v4 (3.2 GHz) processor. This corresponds to a feedback delay of 1.5% compared to the MPC step length of $250\,\mathrm{s}$. Like all steps, the total time of the second MPC step is strongly dominated by the time required to realize the model runs and the subsequent solutions of the ODE for hardness. Here, it becomes evident that the fast and precise control of the virtual convection oven only becomes possible thanks to the accurate and fast-solving ROM. For example, if the ROM required $12.5\,\mathrm{s}$ to replicate one of the 21 model calls, the duration of the MPC algorithm would already exceed the time window of one MPC step. In summary, minor mismatches stemming from reduced-order modeling are mitigated efficiently by the sub-optimization and the MPC algorithm.

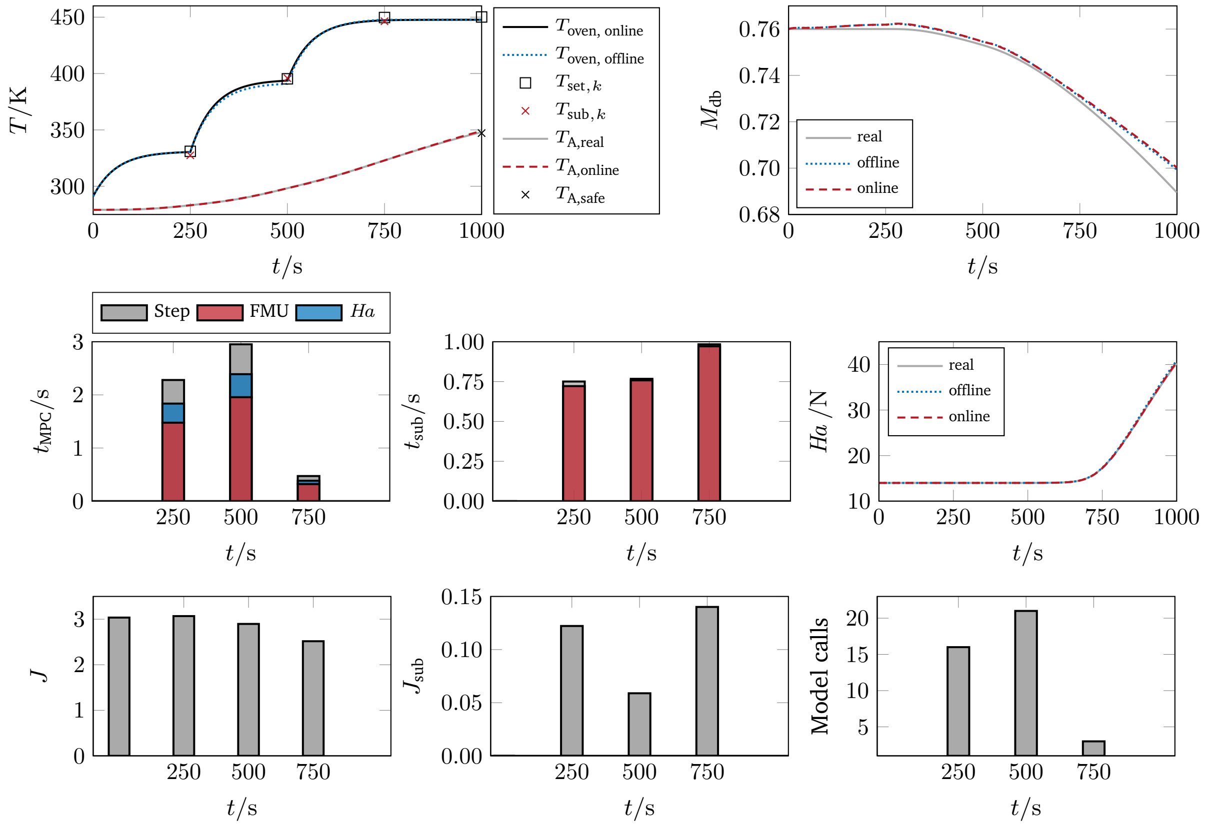

Figure 6.2. Baseline case demonstrating the mitigation of the ROM error with MPC and sub-optimization.

6.2.2. Change of end time during operation

To challenge the MPC algorithm, several scenarios are conceptualized. In analogy to the SAE J3016 levels of driving automation [216], mainly scenarios for autonomy levels 4 and 5 are developed. This means that the process does not demand the operator to take over control despite challenging environmental conditions. Instead, the algorithm masters the situation on its own. For example, short-term power failures were emulated, or target variables such as Ha_{end} were manipulated within physically reasonable limits during operation. Still achieving the required goals, the MPC algorithm successfully reacted to these disturbances. Preliminary results can be found in [73]. One of the most challenging scenarios is presented here: After $500\,\text{s}$ of the run, the required end time is changed to $t_{\text{end}} = 1800\,\text{s}$. This case requires a complete re-optimization of the existing and newly added design variables, which is a potential complication for the gradient-based optimizer. By analogy to SAE J3016, this scenario would correspond to a level-5-autonomy case as the underlying ROM must operate outside its trained model duration of $1400\,\text{s}$ without human help.

Figure 6.3 shows the progression of the control and process variables and illustrates additional statistics of the run. First, the optimal control algorithm plans the same sequence as for the

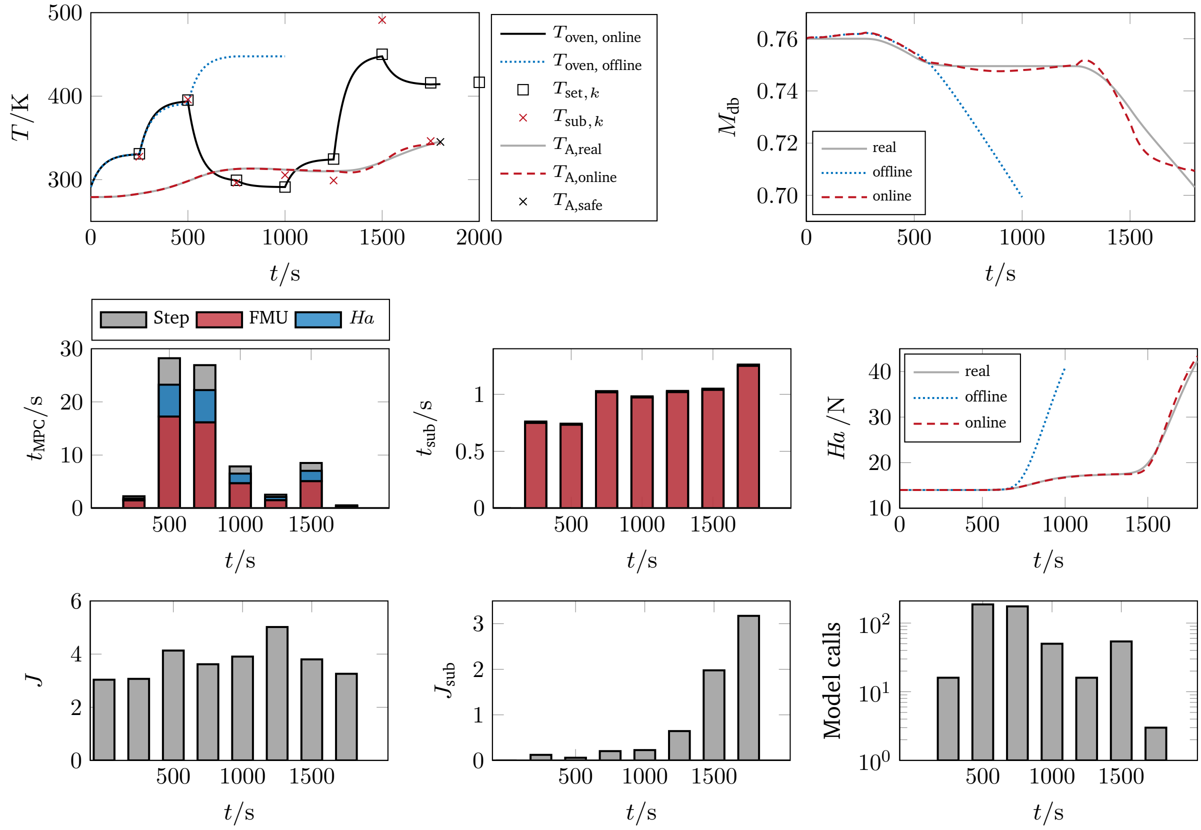

Figure 6.3. Change of process end time to $t_{\text{end}} = 1800\,\text{s}$ before executing the MPC step at $t_k = 500\,\text{s}$.

baseline case (blue dotted line). The MPC algorithm takes over this trajectory again until the time $t_k = 500\,\text{s}$. Now, before calculating the future design parameters, the end time is changed. Accordingly, further entries extend the control vector for $t_k = \{1250\,\text{s}, 1500\,\text{s}, 1750\,\text{s}, 2000\,\text{s}\}$ with initial guesses $T_{\text{set},k} = 300\,\text{K}$. The chosen end time of $t_{\text{end}} = 1800\,\text{s}$ serves to demonstrate that the algorithm can also realize end times outside the grid points. To this end, another degree of freedom is inserted at $t_k = 2000\,\text{s}$.

The sub-optimization approach is increasingly challenged from $t_k = 1000\,\text{s}$ onward. Manipulations become necessary to keep the course of $T_{\text{A,online}}$ in agreement with reality. This can also be seen in J_{sub}, which increases visibly towards the end, as the mismatch can no longer be compensated entirely. Although the grid points still match, more vigorous manipulations become necessary to bridge the thermal lag of the model between $T_{\text{oven, online}}$ to the core temperature $T_{\text{A,online}}$. Thus, the superposed waveform of the online solution stems exclusively from the sub-optimization. The solution would presumably be smoother if the ROM could be initialized at arbitrary initial conditions. This example also illustrates why finer time grids are unsuitable for the sub-optimization approach. In shorter time windows, the manipulation may no longer be effective.

Overall, the algorithm masters this challenge successfully. It adjusts promptly to the new situation: In the MPC steps at $t_k = 500\,\mathrm{s}$ and $t_k = 750\,\mathrm{s}$, the oven temperature is lowered before finishing the food up to the new end time. Compared to the offline predicted value of $J = 3.04$ at the preliminary end time of $t_{\text{end}} = 1000\,\mathrm{s}$, the loss function only slightly increases to a final value of $J = 3.26$. The moisture concentration is slightly better after $1800\,\mathrm{s}$ than in the offline prediction. Meanwhile, the final value of Ha increased only marginally by $1.49\,\mathrm{N}$. The most critical MPC step at time $t_k = 500\,\mathrm{s}$ requires $28.96\,\mathrm{s}$ for its calculation (including sub-optimization), although the FMU model and the ODE for Ha are both run 187 times, respectively. In total, the ROM is executed 501 times in this scenario, and the FMU simulation time accumulates to only $46.6\,\mathrm{s}$.

6.3. Conclusions from the model predictive control studies

The examples shown provide a good impression of the great potential that accurate and fast-solving digital twins offer for advanced control scenarios. It becomes clear why digital twins may by no means operate only in real time to achieve process autonomy. Only multiple, complete predictions of possible future scenarios enable algorithms like the MPC shown here to make good decisions autonomously. If these predictions should be realized on existing process hardware and software, particularly computationally inexpensive models are required. Feedback delay can be significantly reduced if only slight re-optimizations are required. The number of model runs can be effectively reduced by saving optimization iterations. In return, few optimization iterations are only needed if the model error is as small as possible. In line with the digital twin philosophy, a model with utmost accuracy is needed. Note that all calculations of the MPC algorithm, the FMU model calls, and the ODE integration for Ha are executed in serial on a single processor. MATLAB operates inherently serial if no further action is taken. The parallelization of the FMU executions and the ODE integrations show potential for even further acceleration.

7. Summary, contributions and outlook

Autonomous processes employing artificial intelligence may contribute to a paradigm shift towards more sustainable economies. Digital twins symbolize the endeavor to render simulation insights also available to the process in operation, allowing the process control algorithms to make better-informed, autonomous decisions [177, 253]. Digital-twin-based control algorithms may optimize thermal food processing in terms of reduced wastage, improved food quality and safety, and the economization of energy input. This thesis is one of the few publications that aim to implement digital twin methodology within food science holistically, fulfilling essential requirements of highly accurate predictions that are supplied much faster than in real time. It supplies a technological building block to enable autonomous thermal food processing with digital twins. The computational framework is designed to be readily applicable within the industry, independent of the modeling approach and simulation software. Owing to its reduced computational costs, the digital twin can be deployed directly on the control unit of a processing appliance. There, it offers knowledge about unknown food process variables, such as core temperature, moisture content, or texture, by replicating a detailed multi-physical simulation model. The latter couples the governing heating effects, such as convection and radiation, with a food processing model. Employing a fast ROM of the model enables an MPC algorithm to evaluate multiple future scenarios. Consequently, the algorithm can plan its optimal oven temperature trajectory to meet user requirements for specific moisture content, safe core temperatures, texture, and process end time.

Conjugate heat and mass transfer simulations better capture product-process relationships

Using physics-based models as a foundation for accurate digital twins is a central pillar of this work. First, this entails employing a mechanistic food model with as few fitting parameters as possible to potentially provide better generalization outside the validation setup. Second, it requires capturing the thermal processing with a conjugate heat and mass transfer model, a practice seldom found in food science literature.

To demonstrate the impact of a conjugate model in this thesis, a thermal process (non-isothermal flow of air and thermal radiation) is coupled with a mechanistic food processing model developed by Datta et al. [55, 175]. For hot air flow over a flat food item, the conjugate couplings induce significant deviations in primary variables, such as $E_{\text{max}} = 15.4\,\mathrm{K}$ for the temperature. The derived heat transfer coefficient varies more than 50% over space and time, although air velocity and temperature are constant. Adding thermal radiation leads to even more pronounced deviations of

$E_{\text{max}} = 35.6\,\text{K}$ for the temperature and $E_{\text{map}} = 30.8\%$ for the water saturation. Such deviations would not be captured by models employing constant transfer coefficients. Within a hypothetical convection oven model, the derived heat transfer coefficient at the food surface varies significantly with $\alpha_{\text{derv}} \in [15, 60]\,\text{W}\,\text{m}^{-2}\,\text{K}^{-1}$. Comparing two food items within the oven reveals that the temperature locally differs up to $E_{\text{max}} = 48\,\text{K}$ (30.6% relative error), whereas the water saturations differ up to $E_{\text{max}} = 0.3$ (60% relative error). The conjugate convection oven simulations reveal that the contribution of thermal radiation compared to convection varies from 19.1% to 31.6% depending on the position of the food item. The radiative heat flux also has an explicitly transient behavior.

In the presented food models, it becomes apparent how much attention is dedicated to modeling the mechanistic effects within the food accurately, e.g., with Darcy and capillary fluxes, binary diffusion, distributed evaporation, water activity, temperature-dependent material parameters, porosity or permeability. In contrast, constant transfer coefficients are employed to model the interaction with the thermal process or the surroundings. In light of the results discussed above, the practice of validating the food models with constant transfer coefficients is at least questionable — especially when food model parameters are fitted such that the model output matches the experimental data. In the end, one can assume that the fitted food model parameters may compensate for erratic heat and mass transfer modeling during validation. Notice that empirical correlations from literature rely on experiments for single, hypothetical configurations that typically do not match the complex conditions within a realistic convection oven setup. Lumped heat transfer coefficients cannot capture the spatial and temporal variation of radiative and convective heat fluxes, as presented in the convection oven model. Moreover, when radiation is present, mass transfer coefficients derived from analogy considerations lose their validity [66]. The sensitivity study conducted in this work gives insight into the relative proportions of the physical effects within the food and those of the convective and radiative heating. The changes induced by the conjugate flat plate setup are within the sensitivity range of one of the most crucial food model manipulations: removing the evaporative source terms from the water conservation equation. Additionally, the position-dependent effects of local convection and radiation within the convection oven become the most dominant on the overall simulation outcome.

This work demonstrates that the conjugate coupling of convection and radiation to a food processing model better captures the mutual cause-and-effect relationships of process variables and heating mechanisms than transfer-coefficient-based approaches. The concepts presented here could inspire the development of more conjugate food processing models. Indeed, this thesis may pave the way for many possible directions regarding future research; the experimental validation of the conjugate simulation model could be a starting point. Using low-order ansatz functions to decrease the degrees of freedom in the simulation model potentially renders a 3D model solvable within reasonable time frames. To this extent, mainly the distributed, non-equilibrium evaporation approach requires the use of high-order ansatz functions. The complications faced in this work are in agreement with Datta's comment on implementing the evaporation model in COMSOL

Multiphysics: *“Thus, complexities resulting from rapid evaporation in porous media (a physics that is not typically built-in) will continue to be a challenge even in such apparently flexible codes”* [54]. This might explain why the *Moist Air* module within COMSOL Multiphysics employs a different evaporation model. The effects on the primary variables would need proper investigation before a switch could be made to the module.

Besides solving the 3D model, many additional engineering problems must be addressed to transfer the concept to actual appliances. On the process side, the heating coil, the ventilation system and the fume exhaust system would need explicit modeling. Investigating different velocities and the effects of recirculating moist air could be a promising approach. Higher steam concentrations may require air to be considered as a participating medium within the radiative heat exchange, which in return implies significantly higher computational cost when employing the discrete ordinates method. Considering the significant impact of radiation within this work, a promising path would be the derivation of a coupled model that relates the local emissivities, e.g., to the surface browning. Ibarra et al. [126] reported emissivities of chicken fillets that vary during cooking from 0.91 to 0.64. Almeida et al. [3] investigated the spectral emissivities of peeled potatoes.

Concerning food processing modeling, first efforts towards more robust models aim to capture the heterogenous shapes and material properties of the food items [197]. To account for the position dependence of heating effects and the overall loading of the oven, a pragmatic approach is to guide the end-user on where to place the food items. Multiple ROMs could then capture the placement combinations. The efficient design of experiments would certainly help to keep the simulation efforts manageable. The DynROM method allows for shape morphing, an interesting feature that could capture the variability in the size of the food items.

Training of accurate, data-driven ROMs with only one-to-two training data sets

Long computational times and the high cost of transient, large-scale simulation problems are hurdles that must be overcome for digital twins based on physical models. Data-driven reduced-order modeling is a promising approach that adapts to a multitude of simulation approaches, be it in commercial, open-source or custom software. ROMs that employ neural networks to model transient problems have not yet reached awareness in food science. The research presented in this work demonstrates that neural ODEs are a powerful method for developing accurate and efficient ROMs. Attainable speed-ups for point data ROMs with eight outputs are approximately $\mathrm{Sp} \approx 3.6 \times 10^4$ with characteristic solution times of one-tenth of a second without imposing a noticeable computational cost on a single-core processor. In less than half a second, field data ROMs with 4649 points in space and 140 points in time can reproduce the output of full-order models. Besides the significant speed-up, the data-driven ROMs provide excellent test accuracy on large, representative test data groups. The root-mean-square errors are 0.30–$0.74\,\mathrm{K}$ for the best point data ROM and $0.83\,\mathrm{K}$ for the field data ROM. This is a relative error of 0.18–0.49% compared to the variable range. In particular, the accuracy achieved by the ROMs is superior to the accuracy achieved by the benchmark of the hygroscopic, capillary-porous food model ($E_{\mathrm{rms}} = 0.9\,\mathrm{K}$) or the validation error of the soft-matter model ($E_{\mathrm{rms}} = 2.4$–$3.4\,\mathrm{K}$). The ODE augmentation within DynROM reduces the average test error by a factor of four compared to linear ROMs. Future work could also examine the applicability of the proposed efficient design of experiments for other variants of ROMs, such as the augmented neural ODEs by Dupont et al. [74] or the Runge–Kutta neural networks by Zhuang et al. [265]. Likewise, investigating mixed physics during ROM training to utilize the latent variable effect shows potential for future exploration.

The proposed efficient design of experiments attempts to answer how to select only a few appropriate training data sets to obtain accurate ROMs. When selecting a suitable excitation signal type, one must distinguish ROM training, testing, and operation. In this work, ROM training is most successful with APRBS-excited data sets. SinAPRBS data sets most properly emulate the convection oven operating temperatures during ROM testing. Testing of the ROMs is performed on so-called fair data sets that are selected with a χ^2 test. A full-order model is considered too slow for multiple preliminary simulations, as it typically may take days or weeks to solve numerically. An a priori search of correlations on simpler forerunner models enables the economized computational cost of the efficient design of experiments. Forerunner models can be a by-product during the usual modeling work in computational engineering, where physical, geometric and dimensional complications are tested and increased step-wise. The Pearson correlation matrix reveals correlations between training data set properties and corresponding ROM prediction errors for the forerunner model. Acknowledging such trends, good training data sets can be selected, or even better ones can be generated. Different correlations between data set features and ROM test errors can be found for differing physical models. The approach somewhat adapts to the model by searching for correlations, as demonstrated for the transfer-coefficient-based soft-matter model and the conjugate hygroscopic, capillary-porous model. Occasionally, there might be no *linear* correlation between any data set feature and ROM test error. This limitation is partly lifted through the choice of error measures, some of which behave linearly or quadratically in a local or global sense. Likewise, nonlinear data set features or nonlinear correlations could be sought in future research. In this work, a similar ROM test error trend can be established between the forerunner and the full-order model, given the prerequisite that both models contain identical physical models and operational conditions to ensure comparability. Only one-to-two final full-order model simulations are required at the end, making the proposed design of experiments efficient. Future work could pursue a more in-depth investigation of the correlations between forerunner and full-order models. Data and time-consuming studies could prove that correlations found in the forerunner concept also hold for the full-order model.

The inclined reader may question why the DynROM approach does not directly resort to experimental data and thus avoids the tedious detour via modeling and simulation. This is certainly a valid approach for a few simple cases. However, one may miss the predictive power of the models for quantities that cannot be determined easily or economically with experiments. Looking at a large amount of geometry and material data variability, a break-even point for the modeling efforts is quickly reached. Moreover, one is rewarded with a deeper understanding of the underlying physics. In food science, physics-based models exceed observation-based models in insights and predictive capability [55, 58].

Physics-based, data-driven digital twins enable thermal food processing autonomy

The designed MPC algorithm of this thesis is unique in food science and technology literature. Operating with information from highly accurate, multi-physical simulations within an MPC environment sets new standards in accuracy, as the errors of the digital twin are less than the model validation errors of the food model. Unprecedented efficiency of the ROM is characterized by lean computational cost and simulation times of 0.1–$0.5\,\mathrm{s}$ for $1\,\mathrm{h}$ of real time. From the up to 501 model runs within the MPC algorithm, it becomes evident why the solutions of the digital twin must be generated much faster than in real time. The limitations of fixed initial conditions of the FMUs of the DynROM method are circumvented with a pragmatic sub-optimization approach, such that the FMU can also run during operation and not only at the beginning of the process. All in all, employing the ROM within the MPC environment echoes the core digital twin spirit of virtually reflecting a physical process with utmost accuracy while interacting in real time to perform bi-directional data exchange. The presented digital twins based on a conjugate simulation model of realistic dimension and application do not trade off accuracy and speed, contrary to the expectations discussed in recent food science literature [161, 253].

So far, the underlying food model validation errors are more extensive than those introduced by the ROMs. Besides, the food models have only been validated for constant operating conditions, not dynamic oven temperature paths. Hence, future interdisciplinary research projects need to bring the domains of computational engineering and food science closer together to develop even more accurate simulation models. The developed framework is ready to contribute to an overall validation to render the digital-twin-based autonomy of thermal food processing a reality. A worthwhile application scenario is the use of digital twins within a so-called *combination heating* appliance: Such a cooking device could employ multiple heating modes, such as convection, infrared or microwave radiation, to tailor the final quality of the product in terms of texture, flavor, temperature and moisture distribution while reducing the cooking time by up to 40% [112, 199].

Contributions and outlook

The code framework TwinLab provides helpful automation of the data-driven ROM generation from simulation data. Excitation signal generation, test group selection based on χ^2 tests, data set feature determination and global test error calculation are fully automated. Code for batch simulations of full-order models in COMSOL Multiphysics or ANSYS Fluent considerably reduces data handling and user-interaction efforts. Although the interfaces to these two software tools already cover a large share of the CFD and multi-physics community, APIs to open-source software such as OpenFOAM would also be an option in future releases. Likewise, the import and export of training data and readouts to and from ANSYS DynROM could be extended to other data-driven ROM methods within the open-source domain.

The proposed efficient design of experiments can be applied to a variety of industrial or academic problems where simulations take too long to generate large amounts of training data. Adhering to a universal data-driven ROM approach is valuable when simulating the full-order model within commercial software. The pragmatic proposition of the correlation-based training data selection on a forerunner model may serve as guidance. It can inspire the development of training approaches for data-driven ROMs with only a few data sets. Researchers are invited to extend the approach with novel data set features or nonlinear correlation-seeking.

Overall, the digital twin framework within this thesis contributes to shifting the perspective on digital twins towards the autonomy of processes. This is a stride that has not yet been fully appreciated in the literature on digital twins. To some extent, the presented digital twin concept at the device level can be understood as a counter-concept to the *internet of things*, in which the sensorization of the processes and connection to the cloud is often a dogma. Not every state of a process can be captured with a sensor. For system-critical control algorithms, it might be desired to stay offline and still benefit from digital twin knowledge within modern control algorithms. Be it offline or online, encrypted FMUs as large as a few megabytes facilitate the safe deployment of the digital twins at scale. Software updates, such as improved ROMs after retraining, can be supplied easily. As only a ROM is shipped to the devices, the manufacturer's intellectual property (the multi-physical simulation model) does not leave the company premises.

This work demonstrates the application of physics-based, data-driven digital twins for thermal food processing. A relevant application area that corresponds closely with physics is the optimal operation of fuel cells, which requires modeling a porous medium, fluid flow, heat exchange, and additional reaction kinetics. Mobile applications are expected to emerge, e.g., within the transportation sector, where digital twins can provide intelligent control to achieve the optimal operating window of fuel cells. Even for problems of a different physical nature, the proposed framework can contribute to many endeavors where physics-based, data-driven digital twins might improve the autonomy of processes.

A. Test and training data for ROMs

A.1. Fair test groups

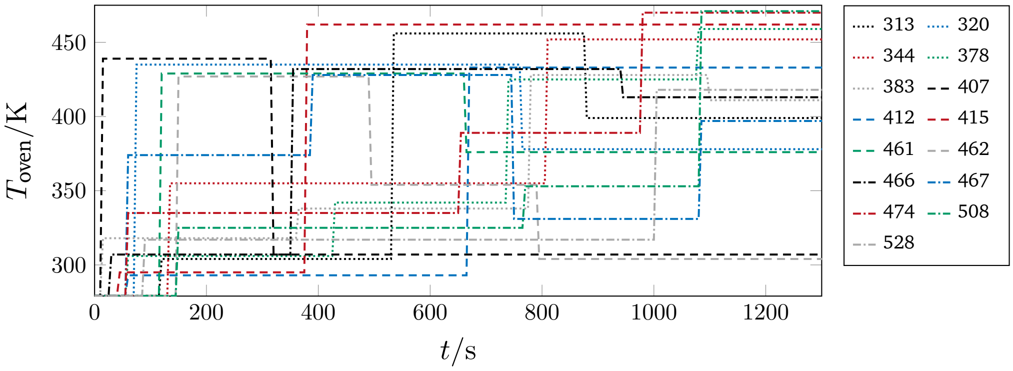

(a) Fair APRBS test group AP15.

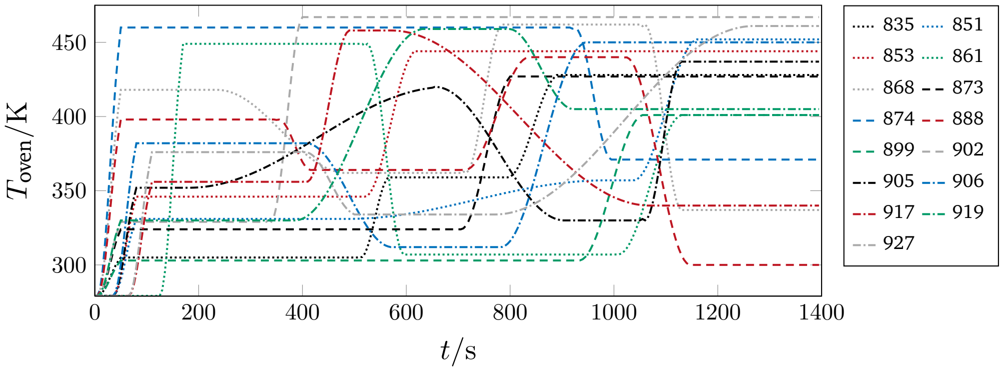

(b) Fair sinAPRBS test group sinAP15.

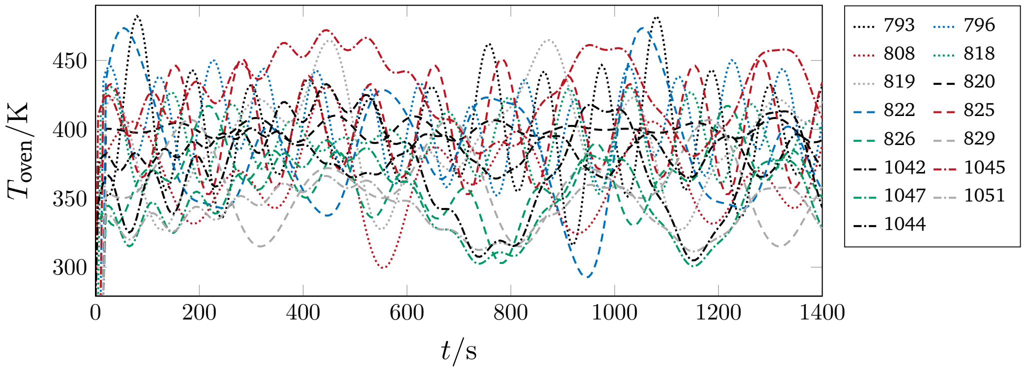

(c) Fair multi-sine test group MS15.

Figure A.1. Fair test groups.

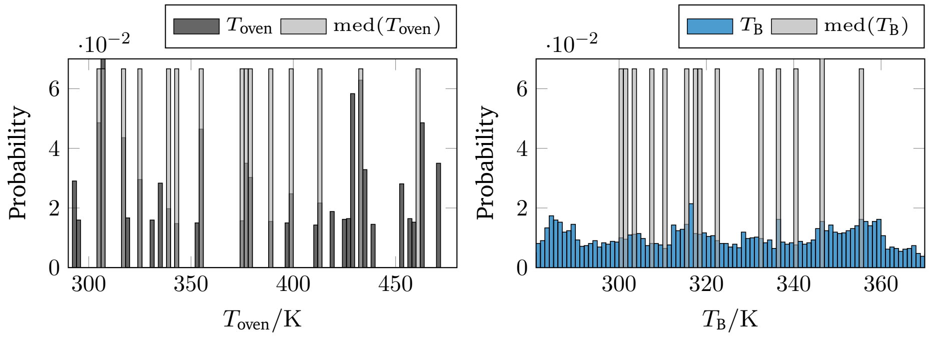

Figure A.2. Fair APRBS test group AP15 [137].

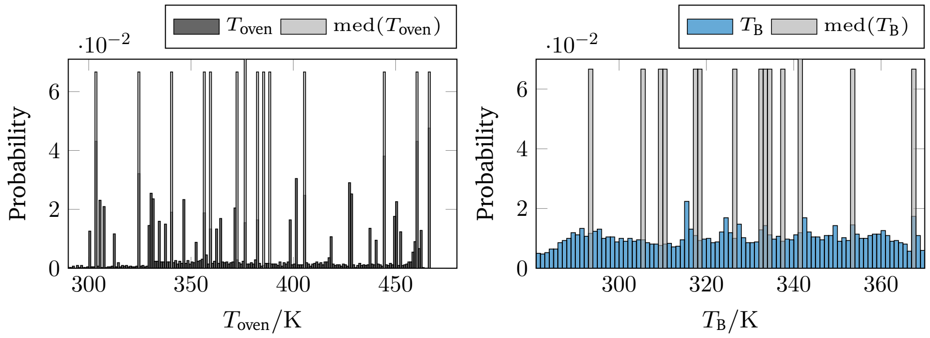

Figure A.3. Fair sinAPRBS test group sinAP15.

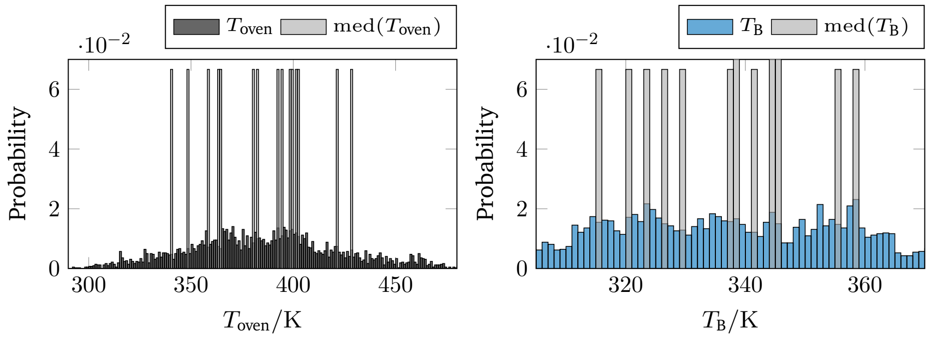

Figure A.4. Fair multi-sine test group MS15.

A.2. Excitation signals of the best training data sets

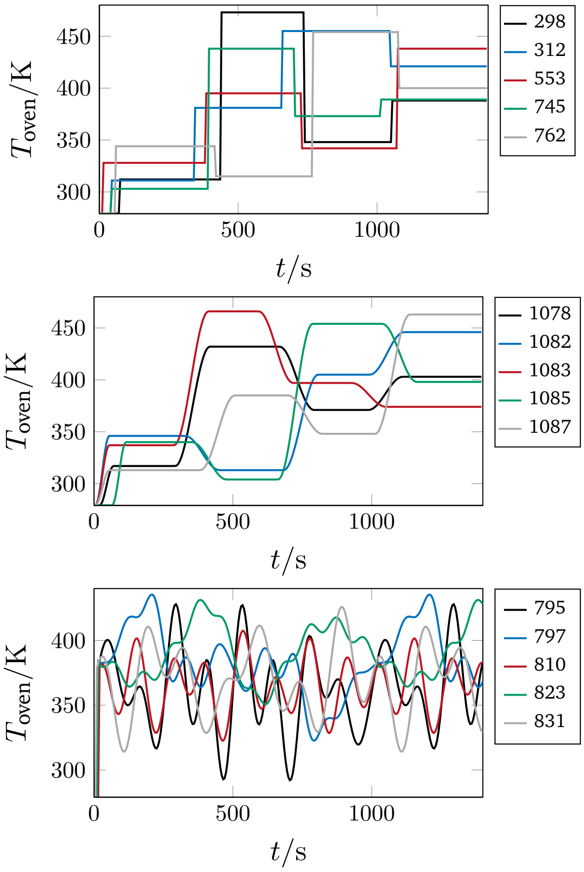

Figure A.5. Excitation signals of the best five APRBS, sinAPRBS and multi-sine training data sets.

A.3. Pearson correlation matrices

Table A.1. Correlations between error measures (rows) and data set features (columns) for APRBS 1-signal-ROMs (test group: AP15).

Measure	$\overline{T}_i$	$\overline{T}_{\text{diff},i}$	$\overline{T}_{\text{diff},j}$	$\lvert\overline{T}_{\text{diff},i}\rvert$	$\overline{T}_{\text{oven}}$	$\mathrm{std}(T_{\text{oven}})$	$\mathrm{Cr}(T_{\text{oven}})$	$\mathrm{std}(T_{\text{A}})$	$\mathrm{std}(T_{\text{B}})$
$\overline{E}_{\text{rms}}/\text{K}$	0.18	–0.39	–0.68	0.40	0.33	–0.12	–0.13	–0.05	–0.76
$\overline{E}_{\text{map}}/\%$	0.20	–0.38	–0.69	0.43	0.35	–0.11	–0.14	–0.06	–0.78
$\overline{E}_{\text{max}}/\text{K}$	0.13	–0.47	–0.69	0.33	0.25	–0.13	–0.10	0.03	–0.70
$\overline{E}_{\text{med}}/\text{K}$	0.19	–0.37	–0.72	0.50	0.35	–0.09	–0.13	–0.11	–0.83
$\overline{E}_{\text{iqr}}/\text{K}$	0.31	–0.07	–0.32	0.23	0.36	–0.02	–0.07	–0.08	–0.37
$\overline{\mathrm{R}}^2$	–0.23	0.40	0.60	–0.29	–0.37	0.13	0.14	–0.08	0.61

Table A.2. Correlations between error measures (rows) and data set features (columns) for APRBS 1-signal-ROMs (test group: sinAP15).

Measure	$\overline{T}_i$	$\overline{T}_{\text{diff},i}$	$\overline{T}_{\text{diff},j}$	$\lvert\overline{T}_{\text{diff},i}\rvert$	$\overline{T}_{\text{oven}}$	$\mathrm{std}(T_{\text{oven}})$	$\mathrm{Cr}(T_{\text{oven}})$	$\mathrm{std}(T_{\text{A}})$	$\mathrm{std}(T_{\text{B}})$
$\overline{E}_{\text{rms}}/\text{K}$	0.10	–0.45	–0.68	0.28	0.22	–0.14	–0.11	0.01	–0.72
$\overline{E}_{\text{map}}/\%$	0.16	–0.43	–0.69	0.34	0.29	–0.13	–0.12	0.00	–0.74
$\overline{E}_{\text{max}}/\text{K}$	–0.04	–0.52	–0.64	0.15	0.04	–0.17	–0.07	0.05	–0.64
$\overline{E}_{\text{med}}/\text{K}$	0.18	–0.43	–0.75	0.48	0.34	–0.08	–0.13	–0.05	–0.81
$\overline{E}_{\text{iqr}}/\text{K}$	0.04	–0.25	–0.30	–0.08	0.04	–0.12	–0.01	0.08	–0.28
$\overline{\mathrm{R}}^2$	–0.15	0.42	0.64	–0.28	–0.30	0.14	0.12	–0.04	0.68

Table A.3. Correlations between error measures (rows) and data set features (columns) for APRBS 1-signal-ROMs (test group: MS15).

Measure	$\overline{T}_i$	$\overline{T}_{\text{diff},i}$	$\overline{T}_{\text{diff},j}$	$\lvert\overline{T}_{\text{diff},i}\rvert$	$\overline{T}_{\text{oven}}$	$\mathrm{std}(T_{\text{oven}})$	$\mathrm{Cr}(T_{\text{oven}})$	$\mathrm{std}(T_{\text{A}})$	$\mathrm{std}(T_{\text{B}})$
$\overline{E}_{\text{rms}}/\text{K}$	0.03	0.07	–0.05	–0.09	0.04	0.05	0.07	–0.15	–0.18
$\overline{E}_{\text{map}}/\%$	0.12	0.02	–0.11	–0.02	0.14	0.04	0.03	–0.08	–0.21
$\overline{E}_{\text{max}}/\text{K}$	–0.21	0.12	0.07	–0.21	–0.20	0.08	0.12	–0.24	–0.10
$\overline{E}_{\text{med}}/\text{K}$	0.07	–0.56	–0.67	0.29	0.19	–0.03	–0.07	0.17	–0.53
$\overline{E}_{\text{iqr}}/\text{K}$	–0.12	0.20	0.18	–0.30	–0.17	0.13	0.17	–0.19	0.11
$\overline{\mathrm{R}}^2$	–0.17	0.34	0.44	–0.15	–0.26	0.07	0.10	–0.14	0.41

A.4. Global error measures of the best 2-signal ROMs

Table A.4. Testing on AP15.

ID	745	+553	+795	+312	+553+795	+371	+351	+555	+638	+692	+303	+328	+342	+625
Complexity	2	5	4	4	3	3	4	3	5	4	3	3	4	2
$\overline{E}_{\mathrm{rms}}$/K	1.05	0.54	0.64	0.69	0.85	1.45	0.98	1.16	0.54	0.79	0.87	0.81	0.59	1.30
$\overline{E}_{\mathrm{map}}$/%	0.22	0.12	0.14	0.14	0.16	0.29	0.20	0.27	0.13	0.15	0.16	0.16	0.14	0.28
$\overline{E}_{\mathrm{max}}$/K	2.63	1.31	1.67	1.73	2.70	3.99	2.70	2.28	1.41	2.29	2.71	2.29	1.36	3.20
$\overline{E}_{\mathrm{med}}$/K	0.07	0.07	−0.19	0.02	0.03	0.01	0.13	−0.63	−0.04	−0.07	−0.02	−0.06	−0.12	0.01
$\overline{E}_{\mathrm{iqr}}$/K	1.25	0.62	0.64	0.73	0.80	1.31	1.05	1.43	0.51	0.73	0.75	0.80	0.72	1.44
R^2	1.00	1.00	1.00	1.00	1.00	0.99	1.00	0.99	1.00	1.00	1.00	1.00	1.00	1.00

Table A.5. Testing on MS15.

ID	745	+553	+795	+312	+553+795	+371	+351	+555	+638	+692	+303	+328	+342	+625
Complexity	2	5	4	4	3	3	4	3	5	4	3	3	4	2
$\overline{E}_{\mathrm{rms}}$/K	0.91	0.56	0.38	0.59	0.67	1.31	0.62	0.79	0.79	0.58	0.82	0.60	0.63	0.87
$\overline{E}_{\mathrm{map}}$/%	0.20	0.14	0.09	0.14	0.13	0.29	0.14	0.19	0.18	0.12	0.16	0.13	0.15	0.19
$\overline{E}_{\mathrm{max}}$/K	2.37	1.33	0.98	1.34	2.05	3.21	1.48	1.71	1.94	1.54	2.38	1.65	1.39	2.12
$\overline{E}_{\mathrm{med}}$/K	−0.07	0.26	0.07	−0.01	0.12	−0.05	0.17	−0.10	0.48	0.07	−0.12	0.17	0.06	−0.06
$\overline{E}_{\mathrm{iqr}}$/K	0.98	0.62	0.44	0.62	0.65	1.16	0.66	1.02	0.49	0.56	0.69	0.56	0.80	1.02
R^2	1.00	1.00	1.00	1.00	1.00	0.99	1.00	1.00	1.00	1.00	1.00	1.00	1.00	1.00

Table A.6. Testing on sinAP15.

ID	745	+553	+795	+312	+553+795	+371	+351	+555	+638	+692	+303	+328	+342	+625
Complexity	2	5	4	4	3	3	4	3	5	4	3	3	4	2
$\overline{E}_{\mathrm{rms}}$/K	1.31	0.73	0.67	0.78	1.33	1.94	1.18	1.01	0.80	0.95	1.19	1.00	0.64	1.55
$\overline{E}_{\mathrm{map}}$/%	0.28	0.16	0.14	0.16	0.25	0.40	0.24	0.23	0.17	0.18	0.22	0.19	0.14	0.34
$\overline{E}_{\mathrm{max}}$/K	3.02	1.64	1.52	1.89	3.46	4.63	2.91	2.28	2.04	2.67	3.26	2.62	1.54	3.52
$\overline{E}_{\mathrm{med}}$/K	0.25	0.21	0.02	0.06	0.36	0.47	0.31	−0.36	0.31	0.09	0.17	0.21	−0.00	0.16
$\overline{E}_{\mathrm{iqr}}$/K	1.64	0.82	0.80	0.83	1.44	2.28	1.39	1.24	0.69	0.90	1.22	1.04	0.72	1.95
R^2	1.00	1.00	1.00	1.00	0.99	0.99	1.00	1.00	1.00	1.00	1.00	1.00	1.00	1.00

Table A.7. Testing on mixed test group (AP15+sinAP15+MS15).

ID	745	+553	+795	+312	+553+795	+371	+351	+555	+638	+692	+303	+328	+342	+625
Complexity	2	5	4	4	3	3	4	3	5	4	3	3	4	2
$\overline{E}_{\mathrm{rms}}$/K	0.97	0.57	0.47	0.59	0.86	1.49	0.81	0.88	0.80	0.74	0.94	0.71	0.58	1.06
$\overline{E}_{\mathrm{map}}$/%	0.21	0.13	0.11	0.14	0.16	0.31	0.17	0.21	0.17	0.15	0.18	0.15	0.14	0.24
$\overline{E}_{\mathrm{max}}$/K	2.29	1.28	1.13	1.30	2.44	3.62	1.92	1.88	2.10	1.99	2.59	1.80	1.30	2.41
$\overline{E}_{\mathrm{med}}$/K	0.11	0.19	0.00	0.02	0.12	0.09	0.21	−0.27	0.27	0.03	−0.01	0.12	−0.04	0.15
$\overline{E}_{\mathrm{iqr}}$/K	1.12	0.66	0.53	0.70	0.90	1.52	1.00	1.06	0.59	0.77	0.89	0.77	0.73	1.33
R^2	1.00	1.00	1.00	1.00	1.00	0.99	1.00	1.00	1.00	1.00	1.00	1.00	1.00	1.00

Table A.8. Testing on all APRBS data sets.

ID	745	+553	+795	+312	+553+795	+371	+351	+555	+638	+692	+303	+328	+342	+625
Complexity	2	5	4	4	3	3	4	3	5	4	3	3	4	2
$\overline{E}_{\mathrm{rms}}/\mathrm{K}$	0.97	0.67	0.72	0.72	0.65	0.99	0.70	1.22	0.70	0.54	0.54	0.52	0.64	1.11
$\overline{E}_{\mathrm{map}}/\%$	0.22	0.16	0.16	0.16	0.14	0.23	0.16	0.28	0.15	0.11	0.12	0.12	0.14	0.26
$\overline{E}_{\mathrm{max}}/\mathrm{K}$	2.33	1.55	1.68	1.85	1.85	2.50	1.89	2.82	1.71	1.51	1.61	1.57	1.61	2.67
$\overline{E}_{\mathrm{med}}/\mathrm{K}$	0.01	0.30	-0.18	-0.04	0.13	0.17	0.20	-0.49	0.14	-0.03	-0.15	0.04	-0.04	-0.25
$\overline{E}_{\mathrm{iqr}}/\mathrm{K}$	1.20	0.59	0.70	0.84	0.66	1.08	0.86	1.35	0.64	0.56	0.56	0.53	0.70	1.17
R^2	1.00	1.00	1.00	1.00	1.00	1.00	1.00	1.00	1.00	1.00	1.00	1.00	1.00	1.00

Table A.9. Testing on 55 sinAPRBS data sets.

ID	745	+553	+795	+312	+553+795	+371	+351	+555	+638	+692	+303	+328	+342	+625
Complexity	2	5	4	4	3	3	4	3	5	4	3	3	4	2
$\overline{E}_{\mathrm{rms}}/\mathrm{K}$	0.93	0.61	0.65	0.74	0.69	1.02	0.75	1.23	0.77	0.55	0.57	0.57	0.67	1.10
$\overline{E}_{\mathrm{map}}/\%$	0.22	0.15	0.14	0.15	0.15	0.23	0.16	0.27	0.18	0.11	0.12	0.13	0.15	0.26
$\overline{E}_{\mathrm{max}}/\mathrm{K}$	2.20	1.33	1.55	1.84	1.83	2.44	1.89	2.75	1.74	1.47	1.56	1.52	1.60	2.51
$\overline{E}_{\mathrm{med}}/\mathrm{K}$	0.08	0.24	0.00	0.04	0.21	0.20	0.25	−0.29	0.21	0.05	0.05	0.11	0.00	−0.05
$\overline{E}_{\mathrm{iqr}}/\mathrm{K}$	1.18	0.60	0.70	0.81	0.70	1.14	0.87	1.49	0.73	0.56	0.60	0.59	0.69	1.40
R^2	1.00	1.00	1.00	1.00	1.00	1.00	1.00	0.99	1.00	1.00	1.00	1.00	1.00	1.00

Table A.10. Testing on 10 single sines data sets.

ID	745	+553	+795	+312	+553+795	+371	+351	+555	+638	+692	+303	+328	+342	+625
Complexity	2	5	4	4	3	3	4	3	5	4	3	3	4	2
$\overline{E}_{\mathrm{rms}}/\mathrm{K}$	0.65	0.44	0.30	0.57	0.24	0.73	0.46	0.58	0.65	0.43	0.44	0.30	0.56	0.71
$\overline{E}_{\mathrm{map}}/\%$	0.14	0.12	0.08	0.15	0.06	0.19	0.12	0.13	0.17	0.10	0.10	0.07	0.13	0.17
$\overline{E}_{\mathrm{max}}/\mathrm{K}$	1.57	0.89	0.64	1.04	0.73	1.51	0.97	1.39	1.13	0.99	1.02	0.71	1.16	1.68
$\overline{E}_{\mathrm{med}}/\mathrm{K}$	-0.17	0.32	0.17	0.05	0.03	-0.37	0.17	0.22	0.65	0.08	-0.18	0.10	0.05	-0.02
$\overline{E}_{\mathrm{iqr}}/\mathrm{K}$	0.65	0.55	0.32	0.73	0.26	0.52	0.62	0.61	0.48	0.61	0.25	0.33	0.71	0.97
R^2	1.00	1.00	1.00	1.00	1.00	1.00	1.00	1.00	1.00	1.00	1.00	1.00	1.00	1.00

Table A.11. Testing on 10 single step data sets.

ID	745	+553	+795	+312	+553+795	+371	+351	+555	+638	+692	+303	+328	+342	+625
Complexity	2	5	4	4	3	3	4	3	5	4	3	3	4	2
$\overline{E}_{\mathrm{rms}}/\mathrm{K}$	1.75	1.07	0.74	0.96	2.37	3.64	1.62	1.31	1.81	1.75	2.56	1.68	0.73	1.64
$\overline{E}_{\mathrm{map}}/\%$	0.38	0.25	0.16	0.21	0.41	0.70	0.32	0.31	0.29	0.31	0.45	0.33	0.17	0.37
$\overline{E}_{\mathrm{max}}/\mathrm{K}$	3.68	1.87	1.64	1.80	6.10	8.34	3.47	2.72	5.92	4.85	6.49	3.52	1.62	3.11
$\overline{E}_{\mathrm{med}}/\mathrm{K}$	0.78	0.52	-0.03	0.08	0.30	0.78	0.44	-0.74	0.10	0.09	0.36	0.37	-0.31	0.83
$\overline{E}_{\mathrm{iqr}}/\mathrm{K}$	1.98	1.27	1.00	1.35	2.59	4.22	2.13	1.54	1.24	1.81	2.76	2.11	0.94	2.21
R^2	1.00	1.00	1.00	1.00	0.98	0.96	0.99	0.99	0.98	1.00	0.99	1.00	0.99	1.00

References

[1] S. G. Agrawal and R. N. Methekar. “Mathematical model for heat and mass transfer during convective drying of pumpkin”. In: *Food and Bioproducts Processing* 101 (2017), pp. 68–73.

[2] AIAA Digital Engineering Integration Committee. *Digital twin: Definition & value. An AIAA and AIA position paper*. Tech. rep. American Institute of Aeronautics and Astronautics, 2020.

[3] M. Almeida, K. Torrance, and A. Datta. “Measurement of optical properties of foods in near- and mid-infrared radiation”. In: *International Journal of Food Properties* 9.4 (2006), pp. 651–664.

[4] A. Alonso et al. “Event-based dynamic optimization for food thermal processing: High-quality food production under raw material variability”. In: *Food and Bioproducts Processing* 127 (2021), pp. 162–173.

[5] A. A. Alonso et al. “Real time optimization for quality control of batch thermal sterilization of prepackaged foods”. In: *Food Control* 32.2 (2013), pp. 392–403.

[6] American Society of Heating, Refrigerating and Air-Conditioning. *2014 ASHRAE Handbook – Refrigeration (SI edition)*. ASHRAE, 2014.

[7] ANSYS, Inc. *ANSYS CFX-Solver Theory Guide – Release 2020 R2*. Available online, accessed on 04 December 2022. URL: https://www.ansys.com/.

[8] ANSYS, Inc. *ANSYS Twin Builder – Release 2020 R2*. Available online, accessed on 04 December 2022. URL: https://www.ansys.com/.

[9] A. Arias-Mendez et al. “Quality and safety driven optimal operation of deep-fat frying of potato chips”. In: *Journal of Food Engineering* 119.1 (2013), pp. 125–134.

[10] M. Ateeque et al. “Numerical modeling of convective drying of food with spatially dependent transfer coefficient in a turbulent flow field”. In: *International Journal of Thermal Sciences* 78 (2014), pp. 145–157.

[11] H. D. Baehr and K. Stephan. *Heat and mass transfer*. 3rd. Springer, 2011.

[12] J. Baillieul and T. Samad, eds. *Encyclopedia of systems and control*. Springer, 2015.

[13] G. Barbosa-Cánovas et al. *Water activity in foods: Fundamentals and applications*. Institute of Food Technologists Series. Wiley, 2020.

[14] J. Bear. *Dynamics of fluids in porous media*. American Elsevier Publishing Company, 1972.

[15] J. Bear and M. Corapcioglu. *Fundamentals of transport phenomena in porous media*. Martinus Nijhoff Publishers, 1984.

[16] A. Bejan and A. Kraus. *Heat transfer handbook*. Wiley, 2003.

[17] P. Benner et al., eds. *Model order reduction – System- and data-driven methods and algorithms*. De Gruyter, 2021.

[18] C. Bernardeschi et al. “Co-simulation of a model predictive control system for automotive applications”. In: *Software Engineering and Formal Methods. SEFM 2021 Collocated Workshops*. Ed. by A. Cerone et al. Springer International Publishing, 2022, pp. 204–220.

[19] R. B. Bird, W. E. Stewart, and E. N. Lightfoot. *Transport phenomena*. 2nd. Wiley, 2007.

[20] N. Bixler. *NORIA – A finite element computer program for analyzing water, vapor, air, and energy transport in porous media*. Tech. rep. SAND84–2057, UC-70. Sandia National Laboratories, 1985.

[21] M. J. Blikra, D. Skipnes, and A. H. Feyissa. “Model for heat and mass transport during cooking of cod loin in a convection oven”. In: *Food Control* 102 (2019), pp. 29–37.

[22] T. Blochwitz et al. “The functional mockup interface for tool independent exchange of simulation models”. In: *Proceedings from the 8th International Modelica Conference, Dresden, Germany* (2011).

[23] C. Bohn and H. Unbehauen. *Identifikation dynamischer Systeme – Methoden zur experimentellen Modellbildung aus Messdaten*. Springer, 2016.

[24] L. Boscaglia et al. “Numerically based reduced-order thermal modeling of traction motors”. In: *IEEE Transactions on Industry Applications* 57.4 (2021), pp. 4118–4129.

[25] E. Bottani and A. Volpi. “An analytical model for cooking automation in industrial steam ovens”. In: *Journal of Food Engineering* 90.2 (2009), pp. 153–160.

[26] M. Bourne. *Food texture and viscosity: Concept and measurement*. Academic Press, 2002.

[27] K. E. Brenan, S. L. Campbell, and L. R. Petzold. *Numerical solution of initial-value problems in differential-algebraic equations*. Society for Industrial and Applied Mathematics, 1995.

[28] L. Brescia and R. Moreira. “Modelling and control of a continuous frying process: A simulation study: Part I: Dynamic analysis and system identification”. In: *Food and Bioproducts Processing* 75.1 (1997), pp. 3–11.

[29] A. N. Brooks and T. J. Hughes. “Streamline upwind/Petrov-Galerkin formulations for convection dominated flows with particular emphasis on the incompressible Navier–Stokes equations”. In: *Computer Methods in Applied Mechanics and Engineering* 32.1 (1982), pp. 199–259.

[30] P. N. Brown, A. C. Hindmarsh, and L. R. Petzold. “Using Krylov methods in the solution of large-scale differential-algebraic systems”. In: *SIAM Journal on Scientific Computing* 15.6 (1994), pp. 1467–1488.

[31] B. Broyart and G. Trystram. “Modelling of heat and mass transfer phenomena and quality changes during continuous biscuit baking using both deductive and inductive (neural network) modelling principles”. In: *Food and Bioproducts Processing* 81.4 (2003), pp. 316–326.

[32] S. Bruin and K. Luyben. “Drying of food materials : A review of recent developments”. In: *Advances in drying, Vol.1*. Ed. by A. Mujumdar. 1980.

[33] N. P. Brunton, D. A. Cronin, and F. J. Monahan. “Volatile components associated with freshly cooked and oxidized off-flavours in turkey breast meat”. In: *Flavour and Fragrance Journal* 17.5 (2002), pp. 327–334.

[34] S. L. Brunton and J. N. Kutz. *Data-driven science and engineering: Machine learning, dynamical systems, and control*. 2nd. Cambridge University Press, 2022.

[35] P. Caccavale, M. V. De Bonis, and G. Ruocco. “Conjugate heat and mass transfer in drying: A modeling review”. In: *Journal of Food Engineering* 176 (2016), pp. 28–35.

[36] M. Calka et al. “Machine-learning based model order reduction of a biomechanical model of the human tongue”. In: *Computer Methods and Programs in Biomedicine* 198 (2021), p. 105786.

[37] E. Catmull. “A subdivision algorithm for computer display of curved surfaces”. PhD thesis. University of Utah, 1974.

[38] H. Chang, J. Carpenter, and R. Toledo. “Modeling heat transfer during oven roasting of unstuffed turkeys”. In: *Journal of Food Science* 63.2 (1998), pp. 257–261.

[39] C. Chen, J. Twycross, and J. M. Garibaldi. “A new accuracy measure based on bounded relative error for time series forecasting”. In: *PLoS One* 12.3 (2017).

[40] H. Chen, B. P. Marks, and R. Y. Murphy. “Modeling coupled heat and mass transfer for convection cooking of chicken patties”. In: *Journal of Food Engineering* 42.3 (1999), pp. 139–146.

[41] T.-C. Chen. “The technical impact of Moore’s law.” In: *IEEE solid-state circuits society newsletter* 20.3 (2006).

[42] Y. Choi and M. R. Okos. “Effects of temperature and composition on thermal properties of foods”. In: *Food Engineering and Process Applications* 1 (1986), pp. 93–101.

[43] S. W. Churchill and M. Bernstein. “A correlating equation for forced convection from gases and liquids to a circular cylinder in crossflow”. In: *Journal of Heat Transfer* 99.2 (1977), pp. 300–306.

[44] M. A. Clark et al. “Global food system emissions could preclude achieving the 1.5 ° and 2 °C climate change targets”. In: *Science* 370 (2020), pp. 705–708.

[45] M. F. Cohen and D. P. Greenberg. *The hemi-cube – a radiosity solution for complex environments*. Tech. rep. Cornell University, 1985.

[46] COMSOL AB. *COMSOL Multiphysics 6.1 CFD Module User’s Guide*. Available online, accessed on 05 December 2022. URL: https://doc.comsol.com/6.1/docserver/.

[47] COMSOL AB. *COMSOL Multiphysics 6.1 Reference Manual. Available online, accessed on 05 December 2022.* URL: https://doc.comsol.com/6.1/docserver/.

[48] COMSOL AB. *Heat transfer: conservation of energy.* Available online, accessed on 05 December 2022. URL: https://www.comsol.de/multiphysics/heat-transfer-conservation-of-energy.

[49] Constructa-Neff Vertriebs-GmbH. *Was ist der Unterschied zwischen Heißluft, Umluft und CircoTherm®?* Available online, accessed on 01 January 2023. URL: https://www.neff-home.com/de/neff-entdecken/produkt-design-highlights/funktionen-von-a-z/circotherm.

[50] Y. Dadmohammadi and A. K. Datta. “Prediction of effective moisture diffusivity in plant tissue food materials over extended moisture range”. In: *Drying Technology* 38.16 (2020), pp. 2202–2216.

[51] Y. Dadmohammadi and A. K. Datta. “Food as porous media: a review of the dynamics of porous properties during processing”. In: *Food Reviews International* 38.5 (2022), pp. 953–985.

[52] A. Datta. “Hydraulic permeability of food tissues”. In: *International Journal of Food Properties* 9.4 (2007), pp. 767–780.

[53] A. Datta. “Porous media approaches to studying simultaneous heat and mass transfer in food processes. I: Problem formulations”. In: *Journal of Food Engineering* 80.1 (2007), pp. 80–95.

[54] A. Datta. “Porous media approaches to studying simultaneous heat and mass transfer in food processes. II: Property data and representative results”. In: *Journal of Food Engineering* 80.1 (2007), pp. 96–110.

[55] A. Datta. “Toward computer-aided food engineering: Mechanistic frameworks for evolution of product, quality and safety during processing”. In: *Journal of Food Engineering* 176 (2016), pp. 9–27.

[56] A. Datta and H. Ni. “Infrared and hot-air-assisted microwave heating of foods for control of surface moisture”. In: *Journal of Food Engineering* 51.4 (2002), pp. 355–364.

[57] A. Datta and V. Rakesh. “Principles of microwave combination heating”. In: *Comprehensive Reviews in Food Science and Food Safety* 12.1 (2013), pp. 24–39.

[58] A. Datta and A. Halder. “Status of food process modeling and where do we go from here (synthesis of the outcome from brainstorming)”. In: *Comprehensive Reviews in Food Science and Food Safety* 7.1 (2008), pp. 117–120.

[59] A. Datta et al. “Soft matter approaches as enablers for food macroscale simulation”. In: *Faraday Discussions* 158 (2012), pp. 435–459.

[60] M. V. De Bonis, P. Caccavale, and G. Ruocco. “Convective control to microwave exposure of moist substrates. Part I: Model methodology”. In: *International Journal of Heat and Mass Transfer* 86 (2015), pp. 943–949.

[61] T. Defraeye. “Advanced computational modelling for drying processes – A review”. In: *Applied Energy* 131 (2014), pp. 323–344.

[62] T. Defraeye, B. Blocken, and J. Carmeliet. “Analysis of convective heat and mass transfer coefficients for convective drying of a porous flat plate by conjugate modelling”. In: *International Journal of Heat and Mass Transfer* 55.1 (2012), pp. 112–124.

[63] T. Defraeye and A. Radu. “Convective drying of fruit: a deeper look at the air-material interface by conjugate modeling”. In: *International Journal of Heat and Mass Transfer* 108 (2017), pp. 1610–1622.

[64] T. Defraeye and A. Radu. “Insights in convective drying of fruit by coupled modeling of fruit drying, deformation, quality evolution and convective exchange with the airflow”. In: *Applied Thermal Engineering* 129 (2018), pp. 1026–1038.

[65] T. Defraeye, P. Verboven, and B. Nicolai. “CFD modelling of flow and scalar exchange of spherical food products: Turbulence and boundary-layer modelling”. In: *Journal of Food Engineering* 114.4 (2013), pp. 495–504.

[66] T. Defraeye et al. “Convective heat and mass transfer modelling at air–porous material interfaces: Overview of existing methods and relevance”. In: *Chemical Engineering Science* 74 (2012), pp. 49–58.

[67] T. Defraeye et al. “Digital twins probe into food cooling and biochemical quality changes for reducing losses in refrigerated supply chains”. In: *Resources, Conservation and Recycling* 149 (2019), pp. 778–794.

[68] T. Defraeye et al. “Digital twins are coming: Will we need them in supply chains of fresh horticultural produce?” In: *Trends in Food Science & Technology* 109 (2021), pp. 245–258.

[69] A. Dhall. “Multiphase transport in deformable phase-changing porous materials”. PhD thesis. Cornell University, 2011.

[70] A. Dhall et al. “Radiative heat exchange modeling inside an oven”. In: *AIChE Journal* 55.9 (2009), pp. 2448–2460.

[71] J. S. Dickson. “Control of salmonella typhimurium, listeria monocytogenes, and escherichia coli 0157:h7 on beef in a model spray chilling system”. In: *Journal of Food Science* 56.1 (1991), pp. 191–193.

[72] R. Dittmar and B.-M. Pfeiffer. “Modellbasierte prädiktive Regelung in der industriellen Praxis”. In: *at - Automatisierungstechnik* 54.12 (2006), pp. 590–601.

[73] D. Dorer. “Echtzeit modellprädikative Regelung zur Realisierung autonomer Prozesse”. MA thesis. Technical University of Darmstadt, 2022.

[74] E. Dupont, A. Doucet, and Y. W. Teh. “Augmented neural ODEs”. In: *Advances in Neural Information Processing Systems*. Ed. by H. Wallach et al. Vol. 32. Curran Associates, Inc., 2019.

[75] EN ISO/CIE 11664-4. *Colorimetry — Part 4: CIE 1976 L*a*b* colour space*. Norm. CIE International Commission on Illumination, June 2019.

[76] T. Eppinger et al. “Increase food production efficiency using the executable digital twin (xdt)”. In: *Chemical Engineering Transactions* 87 (2021), pp. 37–42.

[77] ERCOFTAC. “Industrial computational fluid dynamics of single-phase flows”. In: *ERCOFTAC Best Practice Guidelines*. 2000.

[78] A. Erriguible et al. “Modeling of heat and mass transfer at the boundary between a porous medium and its surroundings”. In: *Drying Technology* 23.3 (2005), pp. 455–472.

[79] A. Erriguible et al. “Simulation of vacuum drying by coupling models”. In: *Chemical Engineering and Processing: Process Intensification* 46.12 (2007), pp. 1274–1285.

[80] European Commision. *European Green Deal 2030*. 2019.

[81] C.-S. Fen et al. “Knudsen and molecular diffusion coefficients for gas transport in unconsolidated porous media”. In: *Soil Science Society of America Journal* 75.2 (2011), pp. 456–467.

[82] J. Ferziger and M. Peric. *Numerische Strömungsmechanik*. Springer, 2008.

[83] A. H. Feyissa. “Robust modelling of heat and mass transfer in processing of solid foods”. PhD thesis. Technical University of Denmark, 2011.

[84] A. H. Feyissa, K. V. Gernaey, and J. Adler-Nissen. “3D modelling of coupled mass and heat transfer of a convection-oven roasting process”. In: *Meat Science* 93.4 (2013), pp. 810–820.

[85] T. Fischer et al. “Nonlinear model predictive control of a thermal management system for electrified vehicles using FMI”. In: *Proceedings of the 12th International Modelica Conference, Prague, Czech Republic, May 15-17, 2017*. 132. Linköping University Electronic Press. 2017, pp. 255–264.

[86] P. J. Flory and J. Rehner. “Statistical mechanics of cross-linked polymer networks II. swelling”. In: *The Journal of Chemical Physics* 11.11 (1943), pp. 521–526.

[87] M. Fortes and M. Okos. “Drying theories: Their bases and limitations as applied to foods and grains”. English. In: *Advances in drying, Vol.1*. Ed. by A. Mujumdar. 1980.

[88] J. Franke et al. “Best practice guideline for the CFD simulation of flows in the urban environment”. In: *COST Action 732 Quality Assurance and Improvement of Microscale Meteorological Models*. 2007.

[89] C. Gear. “Simultaneous numerical solution of differential-algebraic equations”. In: *IEEE Transactions on Circuit Theory* 18.1 (1971), pp. 89–95.

[90] E. Glaessgen and D. Stargel. “The digital twin paradigm for future NASA and U.S. air force vehicles”. In: *53rd AIAA/ASME/ASCE/AHS/ASC Structures, Structural Dynamics and Materials Conference*. American Institute of Aeronautics and Astronautics, 2012.

[91] S. M. Goñi and V. O. Salvadori. “Prediction of cooking times and weight losses during meat roasting”. In: *Journal of Food Engineering* 100.1 (2010), pp. 1–11.

[92] I. J. Goodfellow, Y. Bengio, and A. Courville. *Deep learning*. MIT Press, 2016.

[93] M. Gräber, J. Fritzsche, and W. Tegethoff. “From system model to optimal control-a tool chain for the efficient solution of optimal control problems”. In: *Proceedings of the 12th International Modelica Conference, Prague, Czech Republic, May 15-17, 2017*. 132. Linköping University Electronic Press. 2017, pp. 249–254.

[94] M. Gräber et al. “Using functional mock-up units for nonlinear model predictive control”. In: *Proceedings of the 9th International MODELICA Conference; September 3-5; 2012; Munich; Germany*. 076. Linköping University Electronic Press. 2012, pp. 781–790.

[95] M. Grieves and J. Vickers. “Digital twin: Mitigating unpredictable, undesirable emergent behavior in complex systems”. In: *Transdisciplinary Perspectives on Complex Systems: New Findings and Approaches*. Ed. by F.-J. Kahlen, S. Flumerfelt, and A. Alves. Springer International Publishing, 2017, pp. 85–113.

[96] M. Gringard and A. Kroll. “On the parametrization of APRBS and multisine test signals for the identification of nonlinear dynamic TS-models”. In: *2016 IEEE Symposium Series on Computational Intelligence (SSCI)*. 2016, pp. 1–8.

[97] W. Gruyters et al. “Modelling cooling of packaged fruit using 3D shape models”. In: *Food and Bioprocess Technology* 11.11 (2018), pp. 2008–2020.

[98] A. Guidi and L. Castigliego. “Poultry meat color”. In: *Handbook of Poultry Science and Technology*. John Wiley & Sons, Ltd, 2010, pp. 359–388.

[99] T. Gulati and A. K. Datta. “Enabling computer-aided food process engineering: Property estimation equations for transport phenomena-based models”. In: *Journal of Food Engineering* 116.2 (2013), pp. 483–504.

[100] T. Gulati and A. K. Datta. “Mechanistic understanding of case-hardening and texture development during drying of food materials”. In: *Journal of Food Engineering* 166 (2015), pp. 119–138.

[101] T. Gulati and A. K. Datta. “Coupled multiphase transport, large deformation and phase transition during rice puffing”. In: *Chemical Engineering Science* 139 (2016), pp. 75–98.

[102] T. Gulati, H. Zhu, and A. K. Datta. “Coupled electromagnetics, multiphase transport and large deformation model for microwave drying”. In: *Chemical Engineering Science* 156 (2016), pp. 206–228.

[103] P. Guo, P. O. Dusadeerungsikul, and S. Y. Nof. “Agricultural cyber physical system collaboration for greenhouse stress management”. In: *Computers and Electronics in Agriculture* 150 (2018), pp. 439–454.

[104] H. Hadiyanto et al. “Control vector parameterization with sensitivity based refinement applied to baking optimization”. In: *Food and Bioproducts Processing* 86.2 (2008), pp. 130–141.

[105] E. Hairer, S. Nørsett, and G. Wanner. *Solving ordinary differential equations II: Stiff and differential-algebraic problems*. Springer, 1996.

[106] A. Halder and A. K. Datta. “Surface heat and mass transfer coefficients for multiphase porous media transport models with rapid evaporation”. In: *Food and Bioproducts Processing* 90.3 (2012), pp. 475–490.

[107] A. Halder, A. Dhall, and A. K. Datta. “Modeling transport in porous media with phase change: Applications to food processing”. In: *Journal of Heat Transfer* 133.3 (2010).

[108] J. Han, Y. Hu, and S. Dian. “The state-of-the-art of model predictive control in recent years”. In: *IOP Conference Series: Materials Science and Engineering* 428.1 (2018), p. 012035.

[109] G. Hauke and T. Hughes. “A unified approach to compressible and incompressible flows”. In: *Computer Methods in Applied Mechanics and Engineering* 113.3 (1994), pp. 389–395.

[110] K. He et al. “Deep residual learning for image recognition”. In: *2016 IEEE Conference on Computer Vision and Pattern Recognition (CVPR)*. 2016, pp. 770–778.

[111] HEA – Fachgemeinschaft für effiziente Energieanwendung e.V. *Herde und Backöfen: Anwendung*. Available online, accessed on 05 December 2022. URL: https://www.hea.de/fachwissen/herde-backoefen/anwendung.

[112] HEA – Fachgemeinschaft für effiziente Energieanwendung e.V. *Herde und Backöfen: Aufbau und Funktion*. Available online, accessed on 05 December 2022. URL: https://www.hea.de/fachwissen/herde-backoefen/elektroherde-aufbau-und-funktion.

[113] HEA – Fachgemeinschaft für effiziente Energieanwendung e.V. *Herde und Backöfen: Marktdaten*. Available online, accessed on 05 December 2022. URL: https://www.hea.de/fachwissen/herde-backoefen/marktdaten.

[114] T. O. Heinz and O. Nelles. “Vergleich von Anregungssignalen für Nichtlineare Identifikationsaufgaben”. In: *Proceedings 26. Workshop Computational Intelligence*. KIT Scientific Publishing, 2016, pp. 139–158.

[115] T. O. Heinz and O. Nelles. “Iterative excitation signal design for nonlinear dynamic black-box models”. In: *Procedia Computer Science* 112 (2017), pp. 1054–1061.

[116] T. O. Heinz and O. Nelles. “Excitation signal design for nonlinear dynamic systems with multiple inputs – A data distribution approach”. In: *at - Automatisierungstechnik* 66.9 (2018), pp. 714–724.

[117] E. Henrichs et al. “Can a byte improve our bite? An analysis of digital twins in the food industry”. In: *Sensors* 22.1 (2022).

[118] J. Hesthaven and S. Ubbiali. “Non-intrusive reduced order modeling of nonlinear problems using neural networks”. In: *Journal of Computational Physics* 363 (2018), pp. 55–78.

[119] A. C. Hindmarsh et al. “Sundials: Suite of nonlinear and differential/algebraic equation solvers”. In: *ACM Trans. Math. Softw.* 31.3 (2005), pp. 363–396.

[120] C. Ho and S. Webb. *Gas transport in porous media*. Theory and Applications of Transport in Porous Media. Springer Netherlands, 2006.

[121] S. Hochreiter et al. “Gradient flow in recurrent nets: the difficulty of learning long-term dependencies”. In: *A Field Guide to Dynamical Recurrent Neural Networks*. Ed. by S. C. Kremer and J. F. Kolen. IEEE Press, 2001.

[122] S. Hochreiter and J. Schmidhuber. “Long short-term memory”. In: *Neural computation* 9.8 (1997), pp. 1735–1780.

[123] A. Honchar. *Neural ODEs: breakdown of another deep learning breakthrough.* Available online, accessed on 04 January 2023. URL: https://towardsdatascience.com/neural-odes-breakdown-of-another-deep-learning-breakthrough-3e78c7213795.

[124] K. Hornik. “Approximation capabilities of multilayer feedforward networks”. In: *Neural Networks* 4.2 (1991), pp. 251–257.

[125] Y. Huang, A. D. Whittaker, and R. E. Lacey. “Neural network prediction modeling for a continuous, snack food frying process”. In: *Transactions of the ASAE* 41.5 (1998), pp. 1511–1517.

[126] J. G. Ibarra, Y. Tao, and J. S. A. J. Cardarelli. “Cooked and raw chicken meat: Emissivity in the mid-infrared region”. In: *Applied Engineering in Agriculture* 16.2 (2000), pp. 143–148.

[127] L. Imsland, P. Kittilsen, and T. S. Schei. “Model-based optimizing control and estimation using modelica model”. In: *Modeling, Identification and Control* 31.3 (2010), pp. 107–121.

[128] F. P. Incropera et al. *Fundamentals of heat and mass transfer*. 6th. Wiley, 2006.

[129] IPCC. “Summary for policymakers.” In: *Climate Change and Land: An IPCC special report on climate change, desertification, land degradation, sustainable land management, food security, and greenhouse gas fluxes in terrestrial ecosystems*. Ed. by P. Shukla et al. In press, 2019.

[130] H. Isleroglu and S. Beyhan. “Prediction of baking quality using machine learning based intelligent models”. In: *Heat and Mass Transfer* 56.7 (2020), pp. 2045–2055.

[131] H. Isleroglu, T. Kemerli, and F. Kaymak-Ertekin. “Effect of steam-assisted hybrid cooking on textural quality characteristics, cooking loss, and free moisture content of beef”. In: *International Journal of Food Properties* 18.2 (2015), pp. 403–414.

[132] *Automation systems and integration – Digital twin framework for manufacturing – Part 1: Overview and general principles*. Standard. International Organization for Standardization, 2021.

[133] M. U. Joardder, C. Kumar, and M. Karim. “Multiphase transfer model for intermittent microwave-convective drying of food: Considering shrinkage and pore evolution”. In: *International Journal of Multiphase Flow* 95 (2017), pp. 101–119.

[134] M. Kannapinn. *The digital twin for thermal fluid-structure interaction in the context of cooking modeling – Concept paper*. Tech. rep. Technical University of Darmstadt, Graduate School Computational Engineering, 2018.

[135] M. Kannapinn and M. Schäfer. “Endeavouring intelligent process self-control by employing digital twin methodology: Proof-of-concept study for cooking applications”. In: *CADFEM ANSYS Simulation Conference*. 2019.

[136] M. Kannapinn and M. Schäfer. “Autonomous cooking with digital twin methodology”. In: *14th World Congress on Computational Mechanics (WCCM) and ECCOMAS Congress 2020*. Ed. by F. Chinesta et al. 2021.

[137] M. Kannapinn, M. K. Pham, and M. Schäfer. “Physics-based digital twins for autonomous thermal food processing: Efficient, non-intrusive reduced-order modeling”. In: *Innovative Food Science & Emerging Technologies* 81 (2022), p. 103143.

[138] W. M. Kays. “Turbulent Prandtl Number—Where Are We?” In: *Journal of Heat Transfer* 116.2 (1994), pp. 284–295.

[139] R. S. Kenett et al. “Self-supervised cross validation using data generation structure”. In: *Applied Stochastic Models in Business and Industry* (2022), pp. 1–16.

[140] F. A. Khan, C. Fischer, and A. G. Straatman. “Numerical model for non-equilibrium heat and mass exchange in conjugate fluid/solid/porous domains with application to evaporative cooling and drying”. In: *International Journal of Heat and Mass Transfer* 80 (2015), pp. 513–528.

[141] F. A. Khan and A. G. Straatman. “A conjugate fluid-porous approach to convective heat and mass transfer with application to produce drying”. In: *Journal of Food Engineering* 179 (2016), pp. 55–67.

[142] M. I. H. Khan et al. “Machine learning-based modeling in food processing applications: State of the art”. In: *Comprehensive Reviews in Food Science and Food Safety* 21.2 (2022), pp. 1409–1438.

[143] C. Kim et al. “Design, implementation, and evaluation of an output prediction model of the 10 MW floating offshore wind turbine for a digital twin”. In: *Energies* 15.17 (2022), p. 6329.

[144] KLEIBER Infrared GmbH. *Emissionsgradtabelle.* Available online, accessed on 05 January 2023. URL: https://www.kleiberinfrared.com/index.php/de/amanwendungen/emissionsgrade.html.

[145] T. Kondakci and W. Zhou. “Recent applications of advanced control techniques in food industry”. In: *Food and Bioprocess Technology* 10.3 (2017), pp. 522–542.

[146] A. Koulouris, N. Misailidis, and D. Petrides. “Applications of process and digital twin models for production simulation and scheduling in the manufacturing of food ingredients and products”. In: *Food and Bioproducts Processing* 126 (2021), pp. 317–333.

[147] C. Kumar et al. “Multiphase porous media model for intermittent microwave convective drying (IMCD) of food”. In: *International Journal of Thermal Sciences* 104 (2016), pp. 304–314.

[148] C. Kumar et al. “A porous media transport model for apple drying”. In: *Biosystems Engineering* 176 (2018), pp. 12–25.

[149] C. Kumar et al. “Investigation of intermittent microwave convective drying (IMCD) of food materials by a coupled 3D electromagnetics and multiphase model”. In: *Drying Technology* 36.6 (2018), pp. 736–750.

[150] D. Kuzmin, O. Mierka, and S. Turek. “On the implementation of the $k-\epsilon$ turbulence model in incompressible flow solvers based on a finite element discretisation”. In: *International Journal of Computing Science and Mathematics* 1.2-4 (2007), pp. 193–206.

[151] S. Langsrud et al. “Cooking chicken at home: Common or recommended approaches to judge doneness may not assure sufficient inactivation of pathogens”. In: *PLoS One* 15.4 (2020), pp. 1–27.

[152] J. P. Lars Grüne. *Nonlinear model predictive control – Theory and algorithms*. 2nd. Springer, 2016.

[153] J. H. Lee. “Model predictive control: Review of the three decades of development”. In: *International Journal of Control, Automation and Systems* 9.3 (2011), pp. 415–424.

[154] J. Li et al. “A recurrent self-evolving fuzzy neural network predictive control for microwave drying process”. In: *Drying Technology* 34.12 (2016), pp. 1434–1444.

[155] X.-J. Li, B.-G. Zhang, and W.-J. Li. “Microwave-vacuum drying of wood: Model formulation and verification”. In: *Drying Technology* 26.11 (2008), pp. 1382–1387.

[156] J. H. Lienhard IV and J. H. Lienhard V. *A heat transfer textbook*. 5th. Dover Publications, 2019.

[157] L. Ljung. *System identification – Theory for the user*. 2nd. Prentice Hall PTR, 1999.

[158] J. Lu et al. “Neural-ODE for pharmacokinetics modeling and its advantage to alternative machine learning models in predicting new dosing regimens”. In: *iScience* 24.7 (2021), p. 102804.

[159] Y. Lu et al. “Digital twin-driven smart manufacturing: Connotation, reference model, applications and research issues”. In: *Robotics and Computer-Integrated Manufacturing* 61 (2020), p. 101837.

[160] A. Luikov. “Systems of differential equations of heat and mass transfer in capillary-porous bodies”. In: *International Journal of Heat and Mass Transfer* 18.1 (1975), pp. 1–14.

[161] M. Madoumier et al. “Towards a holistic approach for multi-objective optimization of food processes: A critical review”. In: *Trends in Food Science & Technology* 86 (2019), pp. 1–15.

[162] F. Marra, M. V. De Bonis, and G. Ruocco. “Combined microwaves and convection heating: A conjugate approach”. In: *Journal of Food Engineering* 97.1 (2010), pp. 31–39.

[163] M. Martinez-Diaz and F. Soriguera. “Autonomous vehicles: Theoretical and practical challenges”. In: *Transportation Research Procedia* 33 (2018). XIII Conference on Transport Engineering, CIT2018, pp. 275–282.

[164] W. L. McCabe, J. C. Smith, and P. Harriott. *Unit operations of chemical engineering*. McGraw-hill, 2005.

[165] F. R. Menter. “Two-equation eddy-viscosity turbulence models for engineering applications”. In: *AIAA Journal* 32.8 (1994), pp. 1598–1605.

[166] F. R. Menter, M. Kuntz, and R. Langtry. “Ten years of industrial experience with the SST turbulence model”. In: *Turbulence, Heat and Mass Transfer*. 4. 2003.

[167] T. Milkievicz et al. “Modeling salmonella spp. inactivation in chicken meat subjected to isothermal and non-isothermal temperature profiles”. In: *International Journal of Food Microbiology* 344 (2021), p. 109110.

[168] Modelica Association. *Functional Mock-up Interface 2.0.* Available online, accessed on 24 February 2023.

[169] M. Modest and S. Mazumder. *Radiative heat transfer*. Elsevier Science, 2021.

[170] F. Moukalled, L. Mangani, and M. Darwish. *The finite volume method in computational fluid dynamics: An advanced introduction with OpenFOAM® and Matlab*. Fluid Mechanics and its Applications. Springer Cham, 2016.

[171] J. Moya et al. “Development and validation of a computational model for steak double-sided pan cooking”. In: *Journal of Food Engineering* 298 (2021), p. 110498.

[172] R. Murphy et al. “Heat transfer properties, moisture loss, product yield, and soluble proteins in chicken breast patties during air convection cooking”. In: *Poultry Science* 80.4 (2001), pp. 508–514.

[173] F. Nadi et al. “Numerical simulation of vacuum drying by luikov’s equations”. In: *Drying Technology* 30.2 (2012), pp. 197–206.

[174] O. Nelles. *Nonlinear system identification – From classical approaches to neural networks, fuzzy models, and gaussian processes*. 2nd. Springer International Publishing, 2020.

[175] H. Ni. “Multiphase moisture transport in porous media under internal heating of microwaves”. PhD thesis. Cornell University, 1997.

[176] H. Ni and A. K. Datta. “Heat and moisture transfer in baking of potato slabs”. In: *Drying Technology* 17.10 (1999), pp. 2069–2092.

[177] S. A. Niederer et al. “Scaling digital twins from the artisanal to the industrial”. In: *Nature Computational Science* 1.5 (2021), pp. 313–320.

[178] D. A. Nield and A. Bejan. *Convection in porous media*. 3rd. Springer, 2006.

[179] W. Nusselt. “Graphische Bestimmung des Winkelverhältnisses bei der Wärmestrahlung”. In: *VDI Zeitschrift* 72.20 (1928), p. 673.

[180] N. Oberhuber. *Fachkräftemangel - Als wären das niedere Arbeiten. ZEIT online.* Available online, accessed on 27 February 2023. URL: https://www.zeit.de/wirtschaft/2018-07/fachkraeftemangel-arbeitskraefte-arbeitsmarkt-firmenchefs-loesungen.

[181] D. I. Onwude et al. "A fully coupled multiphase model for infrared-convective drying of sweet potato". In: *Journal of the Science of Food and Agriculture* 101.2 (2021), pp. 398–413.

[182] D. I. Onwude et al. "Modelling of coupled heat and mass transfer for combined infrared and hot-air drying of sweet potato". In: *Journal of Food Engineering* 228 (2018), pp. 12–24.

[183] A. Ousegui et al. "Porous multiphase approach for baking process – Explicit formulation of evaporation rate". In: *Journal of Food Engineering* 100.3 (2010), pp. 535–544.

[184] A. Ousegui et al. "Optimal control and CFD modeling for heat flux estimation of a baking process". In: *Computers & Chemical Engineering* 38 (2012), pp. 139–150.

[185] B. Peherstorfer and K. Willcox. "Data-driven operator inference for nonintrusive projection-based model reduction". In: *Computer Methods in Applied Mechanics and Engineering* 306 (2016), pp. 196–215.

[186] S. Pepe et al. "Neural ordinary differential equations and recurrent neural networks for predicting the state of health of batteries". In: *Journal of Energy Storage* 50 (2022), p. 104209.

[187] P. Perrot. *A to Z of thermodynamics*. Oxford University Press, 1998.

[188] M. K. Pham. "Untersuchung transienter reduzierter Modelle zur Realisierung digitaler Zwillinge thermodynamischer Probleme". MA thesis. Technical University of Darmstadt, 2022.

[189] J. C. Z. Piaia et al. "Air flow CFD modeling in an industrial convection oven". In: *CFD Techniques and Thermo-Mechanics Applications*. Ed. by Z. Driss, B. Necib, and H.-C. Zhang. Springer International Publishing, 2018, pp. 1–12.

[190] S. Pidan et al. "Recombination coefficients and spectral emissivity of silicon carbide-based thermal protection materials". In: *Journal of Thermophysics and Heat Transfer* 19.4 (2005), pp. 566–571.

[191] S. B. Pope. *Turbulent flows*. Cambridge University Press, 2000.

[192] K. Prawiranto, J. Carmeliet, and T. Defraeye. "Physics-based digital twin identifies trade-offs between drying time, fruit quality, and energy use for solar drying". In: *Frontiers in Sustainable Food Systems* 4 (2021).

[193] M. Quesada-Pérez et al. "Gel swelling theories: The classical formalism and recent approaches". In: *Soft Matter* 7 (2011), pp. 10536–10547.

[194] F. Rabeler. "Mechanistic modelling of heat and mass transfer in processing of solid and semi-solid foods". PhD thesis. Technical University of Denmark, 2020.

[195] F. Rabeler and A. H. Feyissa. "Kinetic modeling of texture and color changes during thermal treatment of chicken breast meat". In: *Food and Bioprocess Technology* 11.8 (2018), pp. 1495–1504.

[196] F. Rabeler and A. H. Feyissa. "Modelling the transport phenomena and texture changes of chicken breast meat during the roasting in a convective oven". In: *Journal of Food Engineering* 237 (2018), pp. 60–68.

[197] F. Rabeler and A. H. Feyissa. “Modelling of food processes under uncertainty: Mechanistic 3D model of chicken meat roasting”. In: *Journal of Food Engineering* 262 (2019), pp. 49–59.

[198] F. Rabeler, J. L. Skytte, and A. H. Feyissa. “Prediction of thermal induced color changes of chicken breast meat during convective roasting: A combined mechanistic and kinetic modelling approach”. In: *Food Control* 104 (2019), pp. 42–49.

[199] V. Rakesh et al. “Microwave combination heating: coupled electromagnetics- multiphase porous media modeling and MRI experimentation”. In: *AIChE Journal* 58.4 (2012), pp. 1262–1278.

[200] M. Ranjbaran and A. K. Datta. “Pressure-driven infiltration of water and bacteria into plant leaves during vacuum cooling: A mechanistic model”. In: *Journal of Food Engineering* 246 (2019), pp. 209–223.

[201] A. Rasheed, O. San, and T. Kvamsdal. “Digital twin: Values, challenges and enablers from a modeling perspective”. In: *IEEE Access* 8 (2020), pp. 21980–22012.

[202] C. Ratti, G. Crapiste, and E. Rotstein. “A new water sorption equilibrium expression for solid foods based on thermodynamic considerations”. In: *Journal of Food Science* 54.3 (1989), pp. 738–742.

[203] Resolved Analytics, PLLC. *CFD software user survey results.* Available online, accessed on 06 March 2023. URL: https://www.resolvedanalytics.com/theflux/comparing-cfd-software-part-5-cfd-software-user-survey-results.

[204] W. C. Reynolds, W. M. Kays, and S. J. Kline. *Heat transfer in the turbulent incompressible boundary layer. 3 – Arbitrary wall temperature and heat flux*. Tech. rep. MEMO-12-3-58W. NASA Technical Reports, 1958.

[205] C. Rimkate et al. “Moisture sorption isotherm of chicken breast”. In: *Journal of Food Science and Agricultural Technology* 1.1 (2015), pp. 99–104.

[206] H. Ritchie and M. Roser. *United Kingdom: CO2 country profile.* Available online, accessed on 29 March 2023. URL: https://ourworldindata.org/co2/country/united-kingdom.

[207] D. Rivas et al. “Derivation of postharvest fruit behavior reduced order models for online monitoring and control of quality parameters during refrigeration”. In: *Journal of Food Process Engineering* 36.4 (2013), pp. 480–491.

[208] P. J. Roache. “Perspective: A method for uniform reporting of grid refinement studies”. In: *Journal of Fluids Engineering* 116.3 (1994), pp. 405–413.

[209] R. Rocca-Poliméni et al. “Continuous measurement of contact heat flux during minced meat grilling.” In: *Journal of Food Engineering* 242 (2019), pp. 163–171.

[210] D. Rojas-Rueda et al. “Autonomous vehicles and public health”. In: *Annual Review of Public Health* 41.1 (2020), pp. 329–345.

[211] Y. H. Roos et al. “Food engineering at multiple scales: Case studies, challenges and the future—A european perspective”. In: *Food Engineering Reviews* 8.2 (2016), pp. 91–115.

[212] R. Rosen et al. “About the importance of autonomy and digital twins for the future of manufacturing”. In: *IFAC-PapersOnLine* 48.3 (2015). 15th IFAC Symposium on Information Control Problems in Manufacturing, pp. 567–572.

[213] M. Rubin. “Optical properties of soda lime silica glasses”. In: *Solar Energy Materials* 12.4 (1985), pp. 275–288.

[214] S. Ruder. *An overview of gradient descent optimization algorithms*. Available online, accessed on 11 April 2023. 2016. URL: https://arxiv.org/abs/1609.04747.

[215] Y. Saad and M. H. Schultz. “GMRES: a generalized minimal residual algorithm for solving nonsymmetric linear systems”. In: *SIAM Journal on Scientific and Statistical Computing* 7.3 (1986), pp. 856–869.

[216] SAE On-Road Automated Driving (ORAD) committee. *SAE J3016: Taxonomy and definitions for terms related to driving automation systems for on-road motor vehicles*. Tech. rep. SAE International, 2021.

[217] P. Salagnac, P. Glouannec, and D. Lecharpentier. “Numerical modeling of heat and mass transfer in porous medium during combined hot air, infrared and microwaves drying”. In: *International Journal of Heat and Mass Transfer* 47.19 (2004), pp. 4479–4489.

[218] M. Schäfer. *Computational engineering – Introduction to numerical methods*. Springer, 2006.

[219] P. Schalbart, D. Leducq, and G. Alvarez. “Ice-cream storage energy efficiency with model predictive control of a refrigeration system coupled to a PCM tank”. In: *International Journal of Refrigeration* 52 (2015), pp. 140–150.

[220] M. Scheid. “Thermodynamische und strukturmechanische Untersuchungen von auf Kontakthitze basierenden Gartechnik-komponenten mittels Finite-Element-Methoden und numerischer Strömungssimulation”. MA thesis. Technische Universität Darmstadt, 2017.

[221] M. Schüssler, T. Münker, and O. Nelles. “Deep recurrent neural networks for nonlinear system identification”. In: *2019 IEEE Symposium Series on Computational Intelligence (SSCI)*. 2019, pp. 448–454.

[222] F. Selimefendigil, S. O. Coban, and H. F. Öztop. “Numerical analysis of heat and mass transfer of a moving porous moist object in a two dimensional channel”. In: *International Communications in Heat and Mass Transfer* 121 (2021), p. 105093.

[223] F. Selimefendigil and H. F. Öztop. “Three dimensional unsteady heat and mass transport from six porous moist objects in a channel under laminar forced convection”. In: *Applied Thermal Engineering* 183 (2021), p. 116100.

[224] K. Shoji et al. “Mapping the postharvest life of imported fruits from packhouse to retail stores using physics-based digital twins”. In: *Resources, Conservation and Recycling* 176 (2022), p. 105914.

[225] C. Shrivastava et al. “Digital twins for selecting the optimal ventilated strawberry packaging based on the unique hygrothermal conditions of a shipment from farm to retailer”. In: *Postharvest Biology and Technology* 199 (2023), p. 112283.

[226] R. P. Singh and D. R. Heldman. *Introduction to food engineering*. 5th. Academic Press, 2014.

[227] R. van der Sman. “Simple model for estimating heat and mass transfer in regular-shaped foods”. In: *Journal of Food Engineering* 60.4 (2003), pp. 383–390.

[228] R. van der Sman. “Moisture transport during cooking of meat: An analysis based on Flory–Rehner theory”. In: *Meat Science* 76.4 (2007), pp. 730–738.

[229] R. van der Sman. “Modeling cooking of chicken meat in industrial tunnel ovens with the Flory–Rehner theory”. In: *Meat Science* 95.4 (2013), pp. 940–957.

[230] E. M. Sparrow, R. Eichhorn, and J. L. Gregg. “Combined forced and free convection in a boundary layer flow”. In: *The Physics of Fluids* 2.3 (1959), pp. 319–328.

[231] J. Spurk and N. Aksel. *Fluid mechanics*. 2nd. Springer International Publishing, 2008.

[232] R. Stark and T. Damerau. “CIRP encyclopedia of production engineering – Digital twin”. In: *CIRP Encyclopedia of Production Engineering*. Ed. by S. Chatti and T. Tolio. Springer, 2019.

[233] I. Sutskever. “Training recurrent neural networks”. PhD thesis. University of Toronto, 2013.

[234] A. S. Szczesniak. “Classification of textural characteristicsa”. In: *Journal of Food Science* 28.4 (1963), pp. 385–389.

[235] E. Taghinezhad, V. Rasooli Sharabiani, and M. Kaveh. “Modeling and optimization of hybrid HIR drying variables for processing of parboiled paddy using response surface methodology”. In: *Iranian Journal of Chemistry and Chemical Engineering* 38.4 (2019), pp. 251–260.

[236] G. Tagliavini, T. Defraeye, and J. Carmeliet. “Multiphysics modeling of convective cooling of non-spherical, multi-material fruit to unveil its quality evolution throughout the cold chain”. In: *Food and Bioproducts Processing* 117 (2019), pp. 310–320.

[237] T. Talis et al. “Adaptive sampling of dynamic systems for generation of fast and accurate surrogate models”. In: *Chemie Ingenieur Technik* 93.12 (2021), pp. 2097–2104.

[238] F. Tao and Q. Qi. “Make more digital twins”. In: *Nature* 573 (2019), pp. 490–491.

[239] J. T. Teleken et al. “Mechanistic understanding of microwave-vacuum drying of non-deformable porous media”. In: *Drying Technology* 39.7 (2021), pp. 850–867.

[240] The MathWorks, Inc. *MATLAB R2021b online documentation.* Available online, accessed on 04 December 2022. URL: https://www.mathworks.com/help.

[241] The MathWorks, Inc. *MATLAB Simulink R2021b.* Available online, accessed on 04 December 2022. URL: https://www.mathworks.com/help/simulink.

[242] Y. Tominaga and T. Stathopoulos. “Turbulent Schmidt numbers for CFD analysis with various types of flowfield”. In: *Atmospheric Environment* 41.37 (2007), pp. 8091–8099.

[243] E. Tornberg. “Effects of heat on meat proteins – Implications on structure and quality of meat products”. In: *Meat Science* 70.3 (2005). 50th International Congress of Meat Science and Technology,(ICoMST), 8-13 August 2004, Helsinki, Finland, pp. 493–508.

[244] S. Trehan and L. J. Durlofsky. “Trajectory piecewise quadratic reduced-order model for subsurface flow, with application to pde-constrained optimization”. In: *Journal of Computational Physics* 326 (2016), pp. 446–473.

[245] P. Tsilingiris. “Thermophysical and transport properties of humid air at temperature range between 0 and 100 °C”. In: *Energy Conversion and Management* 49.5 (2008), pp. 1098–1110.

[246] U. S. Food and Drug Administration. *Inspection technical guides, No. 39 water activity in foods*. Tech. rep. 1984.

[247] U.S. Food and Drug Administration. *Food code*. Tech. rep. 2017.

[248] U.S. Provisional Patent Application No. 62/773 555. "Systems and methods for building dynamic reduced order physical models". Nov. 2018.

[249] M. A. Van Boekel. "Kinetic modeling of food quality: A critical review". In: *Comprehensive Reviews in Food Science and Food Safety* 7.1 (2008), pp. 144–158.

[250] VDI-Gesellschaft Verfahrenstechnik und Chemieingenieurwesen. *VDI Wärmeatlas*. Springer Vieweg, 2013.

[251] P. Verboven et al. "Computational fluid dynamics modelling and validation of the isothermal airflow in a forced convection oven". In: *Journal of Food Engineering* 43.1 (2000), pp. 41–53.

[252] P. Verboven et al. "Computation of airflow effects on heat and mass transfer in a microwave oven". In: *Journal of Food Engineering* 59.2 (2003), pp. 181–190.

[253] P. Verboven et al. "Digital twins of food process operations: The next step for food process models?" In: *Current Opinion in Food Science* 35 (2020), pp. 79–87.

[254] C. Vilas et al. "Model-based real time operation of the freeze-drying process". In: *Processes* 8.3 (2020).

[255] Vorwerk Elektrowerke GmbH & Co. KG. *thermomix TM6 Gebrauchsanleitung.* Available online, accessed on 11 April 2023. URL: https://www.vorwerk.com/de/de/c/dam-home/downloads/user-manuals/thermomix/gebrauchsanleitung_thermomix-tm6_ga_25340_02-22_V9-0.pdf.

[256] L. Wang and R. P. Singh. "Finite element modeling and sensitivity analysis of double-sided contact-heating of initially frozen hamburger patty". In: *Transactions of the ASAE* 47.1 (2004), pp. 147–157.

[257] A. Warning et al. "Porous media based model for deep-fat vacuum frying potato chips". In: *Journal of Food Engineering* 110.3 (2012), pp. 428–440.

[258] S. Whitaker. "Forced convection heat transfer correlations for flow in pipes, past flat plates, single cylinders, single spheres, and for flow in packed beds and tube bundles". In: *AIChE Journal* 18.2 (1972), pp. 361–371.

[259] S. Whitaker. "Simultaneous heat, mass, and momentum transfer in porous media: A theory of drying". In: ed. by J. P. Hartnett and T. F. Irvine. Vol. 13. Advances in Heat Transfer. Elsevier, 1977, pp. 119–203.

[260] D. Wilcox. *Turbulence modeling for CFD*. DCW Industries, Incorporated, 2006.

[261] Z. Wu et al. "Model predictive control of the grain drying process". In: *Mathematical Problems in Engineering* (2012), p. 584376.

[262] J. Zhang, A. K. Datta, and S. Mukherjee. "Transport processes and large deformation during baking of bread". In: *AIChE Journal* 51.9 (2005), pp. 2569–2580.

[263] J. Zhang and A. Datta. "Mathematical modeling of bread baking process". In: *Journal of Food Engineering* 75.1 (2006), pp. 78–89.

[264] F. Zhou et al. “Integrated energy management of a smart community with electric vehicle charging using scenario based stochastic model predictive control”. In: *Energy and Buildings* 260 (2022), p. 111916.

[265] Q. Zhuang et al. “Model order reduction based on Runge–Kutta neural networks”. In: *Data-Centric Engineering* 2 (2021), e13.

[266] O. Zienkiewicz, R. Taylor, and P. Nithiarasu, eds. *The finite element method for fluid dynamics*. Butterworth-Heinemann, 2014.

[267] O. Zienkiewicz, R. Taylor, and J. Zhu, eds. *The finite element method: Its basis and fundamentals*. Butterworth-Heinemann, 2013.

[268] A. Zukauskas and A. Slanciauskas. *Heat transfer in turbulent fluid flows*. Hemisphere Publishing Corp., 1987.